Signal and Data Processing for Terahertz Imaging

A thesis submitted to the University of Manchester for the degree of
Doctor of Philosophy in the Faculty of Engineering and Physical Sciences

2014

Miguel Angel Bañuelos Saucedo

School of Electrical and Electronic Engineering

LIST OF CONTENTS

Word count: 44220

LIST OF FIGURES

8

9

10

LIST OF TABLES

ABBREVIATIONS

ADC	Analogue-to-Digital Converter
BD	Balanced Detection
BS	Beam Splitter
CCD	Charged Coupled Device
CW	Continuous Wave
DC	Direct Current
DR	Dynamic Range
DSP	Digital Signal Processor
EFL	Equivalent Focal Lenght
ENBW	Equivalent Noise Bandwidth
EO	Electro-optic
FFT	Fast Fourier Transform
FIR	Finite Impulse Response
FTIR	Fourier Transform Infrared
FWHM	Full Width Half Maximum
GDD	Group Delay Dispersion
GPIB	General Purpose Interface Bus
GUI	Graphical User Interface
GVD	Group Velocity Dispersion
HDPE	High Density Polyethylene
ID	Iris Diaphragm
IEMN	Institut d'électronique de microélectronique et de nanotechnologie
IR	Infrared
LED	Light Emitting Diode
LIA	Lock-in Amplifier
LPF	Low Pass Filter
LT-GaAs	Low temperature GaAs
MBD	Modified Balanced Detection
ND	Neutral Density
OFCG	optical frequency comb generator
OPLL	Optical Phase-locked Loop
PC	Photoconductive
PCA	Photoconductive Antenna
PM	Parabolic Mirror
PSD	Phase Sensitive Detector
PTFE	Polytetrafluoroethylene
QCL	Quantum Cascade Laser
RC	Resistor and Capacitor
RH	Relative Humidity
SNR	Signal-to-Noise Ratio
TDS	Time Domain Spectrometry
THz-TDS	THz Time-Domain Spectrometry
TTL	Transistor-Transistor Logic
UV	Ultraviolet

ABSTRACT

This thesis presents the research made on signal and data processing for THz imaging, with emphasis in noise analysis and tomography in amplitude contrast using a THz time-domain spectrometry system. A THz computerized tomography system was built, tested and characterized. The system is controlled from a personal computer using a program developed ad hoc. Detail is given on the operating principles of the system's numerous optical and THz components, the design of a computer-based fast lock-in amplifier, the proposal of a local apodization method for reducing spurious oscillations in a THz spectrum, and the use of a parabolic interpolation of integrated signals as a method for estimating THz pulse delay. It is shown that our system can achieve a signal-to-noise ratio of 60 dB in spectrometry tests and 47 dB in tomography tests.

Styrofoam phantoms of different shapes and up to 50x60 mm is size are used for analysis. Tomographic images are reconstructed at different frequencies from 0.2 THz to 2.5 THz, showing that volume scattering and edge contrast increase with wavelength. Evidence is given that refractive losses and surface scattering are responsible of high edge contrast in THz tomography images reconstructed in amplitude contrast. A modified Rayleigh roughness factor is proposed to model surface transmission scattering. It is also shown that volume scattering can be modelled by the material's attenuation coefficient. The use of 4 mm apertures as spatial filters is compared against full beam imaging, and the limitations of Raleigh range are also addressed. It was estimated that for some frequencies between 0.5 THz and 1 THz the Rayleigh range is enough for the tested phantoms. Results on the influence of attenuation and scattering at different THz frequencies can be applied to the development of THz CW imaging systems and as a point of departure for the development of more complex scattering models.

DECLARATION

No portion of the work referred to in this thesis has been submitted in support of an application for another degree or qualification of this or any other university or other institution of learning.

COPYRIGHT STATEMENT

i. The author of this thesis (including any appendices and/or schedules to this thesis) owns certain copyright or related rights in it (the "Copyright") and s/he has given The University of Manchester certain rights to use such Copyright, including for administrative purposes.

ii. Copies of this thesis, either in full or in extracts and whether in hard or electronic copy, may be made only in accordance with the Copyright, Designs and Patents Act 1988 (as amended) and regulations issued under it or, where appropriate, in accordance with licensing agreements which the University has from time to time. This page must form part of any such copies made.

iii. The ownership of certain Copyright, patents, designs, trade marks and other intellectual property (the "Intellectual Property") and any reproductions of copyright works in the thesis, for example graphs and tables ("Reproductions"), which may be described in this thesis, may not be owned by the author and may be owned by third parties. Such Intellectual Property and Reproductions cannot and must not be made available for use without the prior written permission of the owner(s) of the relevant Intellectual Property and/or Reproductions.

iv. Further information on the conditions under which disclosure, publication and commercialisation of this thesis, the Copyright and any Intellectual Property and/or Reproductions described in it may take place is available in the University IP Policy (see http://documents.manchester.ac.uk/DocuInfo.aspx?DocID=487), in any relevant Thesis restriction declarations deposited in the University Library, The University Library's regulations (see http://www.manchester.ac.uk/library/aboutus/regulations) and in The University's policy on Presentation of Theses.

ACKNOWLEDGMENTS

To my parents, for their love, their example and their courage. To my siblings, because I know that no matter what they will be always with me.

To Universidad Nacional Autónoma de México, for granting me a leave for studying this PhD. To CONACYT, for granting me a scholarship for doing these studies.

To the EPS-CONACYT program, its coordinator Dr. Teresa Alonso Rasgado and all the persons involved in it.

To my supervisor, Prof. Krikor B. Ozanyan, I really appreciate your guidance, and I really enjoyed our discussions.

To Dr. Paul Wright, Dr. Alisdair Macperson, Dr. Med BenYezzar and Dr. DeChang Dai, experimental officers from SISP group the former, and Photon Science Institute the others. Your help and advice was really valuable, and appreciate the short conversations and discussions that we had.

To the amazing parallel worlds.

To all my friends.

To the Centro de Ciencias Aplicadas y Desarrollo Tecnológico, Universidad Nacional Autónoma de México.

To México.

LIST OF PUBLICATIONS

1. Banuelos-Saucedo, M. A., Ozanyan, K.B. Fast response lock-in amplifier. In: 8th IEEE International Symposium on Instrumentation and Control Technology, ISICT 2012; London; United Kingdom; 11-13 July 2012; Pages 122 – 125. DOI: 10.1109/ISICT.2012.6291623

2. Ozanyan, K., Banuelos-Saucedo, M., Wright, P., Young, J., Stringer M., Wang, Q., Zhang, Y., Miles, B. Measurements of THz pulse delay in sooty flames. In: IOP Photon 12 Conference; 3-6 September 2012; Durham, UK.

3. Darabkhani, H.G., Banuelos-Saucedo, M., Young, J., Stringer, M., Wright, P., Wang, Q., Zhang, Y., Miles, R.E., Ozanyan, K.B. Sensing in sooting flames: THz time-domain spectroscopy and tomography. In: IEEE SENSORS 2012 - Proceedings; 28-31 Oct 2012; Taipei, Taiwan. Pages 1-4. DOI: 10.1109/ICSENS.2012.6411257

4. Cantoral Ceballos, J. A., Wood, M. P., Nurgiyatna, N., Banuelos-Saucedo, M. A., Wright, P., Ozanyan, K. B. Hard-field Tomography Imaging in Secondary Contrast. In: Sensors and Their Applications XVII; 16-18 Sep 2013; Dubrovnik, Croatia. DOI:10.1088/1742-6596/450/1/012033

5. Banuelos-Saucedo, M. A., Ozanyan, K.B. Hard-field THz Tomography in Amplitude Contrast. IEEE SENSORS 2014 Conference. *Accepted*.

THE AUTHOR

Miguel Angel Bañuelos Saucedo received the Bachelor degree in Mechanical and Electrical Engineering from the Universidad Nacional Autónoma de México (UNAM) in 1993, with a thesis entitled: Design and development of an evaluation system for the 80535 microcontroller. In 1997, he received the MSc degree in Electrical Engineering from the same university with a thesis entitled: Design and development of an analogue neurocomputer. Since 1994, he has been working with the Electronics Group at the Centre of Applied Sciences and Technological Development (UNAM) as an Academic Technician. He was head of the Electronics Group from 1999 to 2007. In 2010, he was granted a leave for studying his PhD at the University of Manchester. His teaching experience includes undergraduate courses on Control Systems, and Analogue Electronics at the Faculty of Engineering (UNAM). He has been involved in the development of several instruments that include: instrumentation for soil mechanics studies, human cardiac valve prosthesis testing and clinical diagnosis.

1 INTRODUCTION

The THz band is a region in the electromagnetic spectrum covering frequencies between 0.1 THz and 10 THz (see Figure 1-1). The development in ultrashort pulse laser technology, along with the appearance of THz emitters and detectors in the late eighties, made it possible to explore the unique spectroscopy and imaging characteristics of this band of radiation. The THz band is situated between the microwave and infrared frequencies and was traditionally known as the THz gap, because of the lack of instrumentation suitable for work at these frequencies.
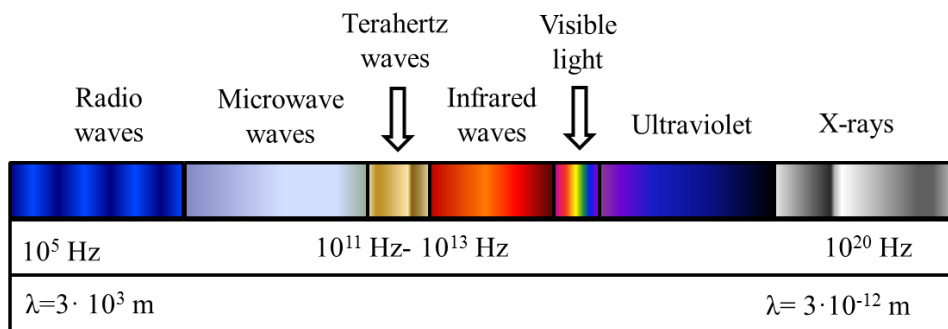
Figure 1-1. The electromagnetic spectrum.

THz frequencies present two important properties: first, they are able to penetrate some materials like paper, textiles, or plastics, which make them suitable for non-destructive evaluation; and second, many molecules present strong absorption and therefore can be identified by non-contact spectrometry. An advantage is that THz radiation is non-ionizing, making it safer to use for material inspection than X-rays. Among the applications that have been explored using THz waves are: explosive detection, pharmaceutical drugs control, corrosion inspection, structural defects detection, security inspection, spectroscopy and tomography imaging. As a limitation, THz radiation is absorbed by water molecules and this has restricted the development of long range communication systems, long range chemical identification, and medical tomography

applications, due to the water content in air and human body. However, short range communications and chemical identification are possible.

Terahertz systems can be divided in two: pulsed wave and continuous wave (CW). Pulsed systems generate a broadband signal that is suitable for spectroscopy and it can be generated and detected by a THz time-domain spectrometry (THz-TDS) system. THz-TDS systems were developed in the late eighties after the invention of the Auston switch [1], which is a semiconductor device capable of generating and detecting THz radiation, and the availability of near-infrared ultrashort pulse laser sources. Generation and detection of pulsed THz radiation is also possible by electro-optical techniques. A THz-TDS system produces and detects a broadband radiation pulse. The detected pulse can be analysed using fast Fourier Transform (FFT) to obtain the spectrum of the signal. Since all phase information is preserved, it is possible to estimate the attenuation coefficient and the refractive index of a material without involving Kramers-Kronig relations. THz CW waveforms produce a narrow band signal that is usually generated by using photomixing techniques or cryogenically cooled quantum cascade lasers (QCL). Both THz Pulsed and CW systems are suitable for performing spectrometry, imaging and tomography.

THz spectroscopy applications appear to constitute a mature field and it has been applied to different types of materials including: polymers, semiconductors, ceramics, gases and oils [2]. THz imaging applications evolved from 2D to complete 3D tomography. One of the firsts application examples of THz imaging was presented in 1996 by Mittleman *et al*[3], who estimated the moisture content in a leaf using time-of-flight contrast. An in-depth review on THz tomography was published in 2004 by S. Wang et al [4]. In this paper, authors underline the scattering phenomena occurring at THz frequencies and present a diffraction tomography reconstruction of three rectangular sections of a polyethylene tube.

THz imaging can be based on both transmission and reflection and several applications have been demonstrated in areas such as: security (inspection of luggage or postal mail), explosive detection, paper, polymers, food and pharmaceutical industries, paints and coatings defect identification, structure analysis of ceramics and composites, thickness of

24

pharmaceutical tablet coatings, structural defects in semiconductors, interconnection defects in integrated circuits, gas flame analysis, art conservation, detection of epithelial cancer as well as detection of tooth decay [5, 6]. Commercial THz spectroscopy and imaging systems are available from Teraview (UK), Toptica (Germany), Zomega (USA), and a few others. Most commercial imaging systems are 2D but 3D THz imaging systems are also available from Teraview and have small working areas (25x25 mm). The global THz market was valued at $50.2 million dollars in 2012 and it is expected to reach $195.3 million dollars in 2018 [7].

THz instruments are still very far from having a widespread use as ultrasound or X-ray equipment in medical and industrial applications. Some factors that have limited their development are the size of the components, the cost, and the speed. THz generation and detection techniques, have presented a continuous but perhaps slow progress, and there are several challenges that need further research in order to fully exploit the advantages of working in this region of the electromagnetic spectrum. Central problems to the improvement of this technology include: high power THz sources, acquisition speed and size reduction. Besides these, THz imaging and tomography have to address particular problems such as: image resolution, etalon effects and scattering.

Over the past 25 years, research on THz systems has drawn a growing interest and it is not a coincidence that one of the most downloaded papers in April 2014 from the Journal of the Optical Society of America B was the work of Grischkowsky et al (1990) on THz time-domain spectroscopy [8]. Most of the research presented in this dissertation is based on a THz-TDS system.

1.1   Overview of the problem

Many THz-TDS systems are relatively slow because their operation relies on the movement of a motorized optical delay-line. Several alternatives have been proposed to address this problem, including the use of asynchronous optical sampling. However, a faster sampling doesn't necessarily imply an improvement in signal-to-noise ratio (SNR).

If a progress is made in a conventional THz-TDS system regarding SNR performance, it would have the potential of being applied on different implementations of a TDS system.

A method for detection of pulsed THz waveforms is the electro-optical sampling. This method uses a balanced photodetector that works in conjunction with a lock-in amplifier. In a typical system, the balancing operation is done before the synchronous demodulation provided by the lock-in amplifier. It is an open question whether this arrangement is optimal or it can be outperformed by a system doing the operations in reverse order, that is, applying a synchronous demodulation first and then the balancing operation. It is also possible to think that a digital balancing algorithm may be able to reduce the noise levels. An improvement in signal-to-noise ratio of the THz-TDS system based on modifications to the detection section would be independent of the operation of the optical delay-line and could be applied to systems with a different optical sampling approach; moreover, this will represent an advantage not only in spectroscopy measurements but also in imaging applications.

A THz-TDS system can be used to determine the spectral absorption of some material to THz radiation, and also to determine its attenuation coefficient and refractive index. With some modifications it is also possible to scan an object and produce a tomography image. On one side, if amplitude contrast is used, the reconstructed image will have information on object's spatial distribution of attenuation coefficients. On the other side, if time-of-flight contrast is used, the image will contain information on object's spatial distribution of refractive index. When working in amplitude contrast, if a Fourier analysis is carried out, an image can be separated in its frequency components, which may provide more detailed information on the composition of the object. This capability hasn't been properly exploited since most imaging systems work in time-of-flight contrast.

System portability is an important issue not only for THz spectrometry systems but for imaging and tomography systems, and semiconductor QCL are a very promising option for the generation of THz radiation from a small device. The most powerful type of THz QCLs operate a temperatures below 200 K, but recently, a 160 μW QCL @ 3.51 THz operating at room temperature has been demonstrated in [9]. By comparison, in a typical

THz-TDS systems THz power emissions are in the nW to µW range [10], but they are broadband which limits the power content of individual frequency components. It can be expected that the role of THz CW systems will be substantial in future solutions for portable THz systems. If such systems are to include imaging and tomography applications, further work is needed to understand the properties and limitations of acquiring images at THz frequencies. In order to identify potential applications it would be of interest to determine if there are specific limitations: in size, material composition or shape; to the imaging task. A tomography system is able to produce a 3D reconstruction of an object and this provides greater information than a 2D imaging systems at the cost of longer scanning times. However, a tomography system is an excellent platform for studying beam propagation phenomena since the test object is analysed from different angles.

A THz-TDS system can be used as an approximation for studying the operation of narrow band sources. In a THz-TDS system, an image is generated by broadband THz pulses. Line integrals acquired in amplitude contrast can be Fourier transformed to produce reconstructed images for one or several frequency components and therefore producing an image of limited bandwidth. In this way, any insight gained by analysing such images can be extended to interpret the operation of CW systems.

In summary, two problems have been identified: first the need to improve the signal-to-noise ratio performance of current THz-TDS systems as a way of facilitating faster data acquisition speeds. Typical THz-TDS systems have a SNR=70 dB [11] with up to SNR=100 dB @ 0.4 THz been reported in commercial THz-TDS systems [12]). Second, the need to characterize the limits and opportunities that imaging in amplitude contrast present as a step towards the development of portable THz imaging instruments.

1.2 Objectives of the research

The operation of present and future THz systems will be improved if any of the following objectives is achieved:

- To increase the signal-to-noise ratio in a conventional THz-TDS system by modifying the electronic instrumentation and signal processing associated to a balanced detection/synchronous demodulation scheme. Any improvement will be evaluated by measuring the signal-to-noise ratio using standard techniques and comparing it against the values obtained from an unmodified configuration.

- To define rules of utilization of the different parts of the THz spectrum for imaging of objects depending on their material and geometrical properties, by taking advantage of the spectral character of the THz-TDS measurement. The definition of such rules will be supported by experimental tests and simulations.

In order to achieve these, a conventional THz-TDS system capable of spectrometry and tomography test was built from scratch and characterized using methods reported in the published literature. This required the study of all its parts, from optical and THz components, to data acquisition, signal-to-noise ratio estimation, digital lock-in amplifiers, signal processing, development of computer-based instrumentation, and tomography image reconstruction and analysis. Techniques were developed for the mounting and alignment of all optical and THz components.

1.3   Summary of novelties and achievements

In the present dissertation, the following novelties are introduced:

- A method for reducing spurious oscillations in a THz spectrum using local apodization of the time-domain signal.

- A digital lock-in amplifier using a cumulative averager as filter

- The use of the Equivalent Noise Bandwidth (ENBW) figure of merit, which is of common use in analogue electronics, was used for performance evaluation of a digital lock-in amplifier with a finite impulse response (FIR) filter for the first time (to our knowledge).

- The use of a parabolic interpolation on integrated signals for estimating pulse delay in THz analysis of sooty flames

- The use of spatial filtering for reducing scattering effects in amplitude based THz tomography systems

- An analysis of THz tomography images in amplitude contrast using different frequency components.
- A scattering and attenuation model based on modified Fresnel equations for THz tomography in amplitude contrast.

This research also includes the following achievements:

- Mounting and alignment of a THz Time-domain spectroscopy system from scratch and without specific previous training. This includes:
  - o Design of a dry air Perspex chamber.
  - o Design of a triple cuvette for liquid samples for comparing two samples in the same test and a third chamber to work as a reference. This is useful because changing the samples requires the opening of the dry air chamber.
- Signal-to-noise characterization of the THz TDS system, and positive comparison against systems reported in the literature.
- An alternative configuration for balanced detection with a third beam working as reference.
- Implementation of a lock-in amplifier using a data acquisition module and a LabVIEW program with custom filtering.
- Development of a computer program (LabVIEW) for a THz TDS system with control of a second translation stage for linear scan of samples, or for controlling sample position.
- Design and construction of a rotation stage for performing tomography, based on a DC servo motor.
- Development of a computer program (LabVIEW) for a THz Tomography system which includes the following main characteristics:
  - o Setting up time-constant of an attached commercial lock-in amplifier and reading of antenna photocurrent form digital multimeter using GPIB communication.
  - o Generate a separate file for each pulse scan for avoiding memory saturation problems.
  - o Present real time data, and display spectrum after each scan.

- Several data analysis programs (MATLAB) including:
  - Time-domain and spectrum plots of THz pulsed signals.
  - Signal-to-noise ratio analysis.
  - Refractive index and attenuation coefficient calculation.
  - 3D frequency plot of linear sample scans.
  - Tomography reconstruction using a graphical user interface (GUI) with selectable gain, frequency, filtering, interpolation and windowing.
  - Video generation of a sequence of tests.

1.4 Thesis outline

This dissertation is divided in six chapters plus one appendix. In chapter I, an introduction to THz technology and some of its applications is given. It also comprises the overview of the problem, the objectives of the research, a summary of achievements and novelties and a general outline of the text.

Chapter 2 describes in detail the operation of a THz time-domain spectrometry system. After introducing the most common THz sources and detectors, and optics, it makes emphasis in photoconductive antenna emitters and electro-optical detection of THz pulses. It also covers the balanced detection and synchronous demodulation.

Chapter 3 gives a brief description of the layout and assembling of the THz-TDS system before presenting the steps followed for characterizing the system. It introduces a novel method for reducing spurious oscillations in a THz spectrum by using local apodization of the time-domain signal. It also explains a method for estimating the THz pulse delay using parabolic interpolation of the integrated time-domain signal. This method was used to measure the delay on sooty flames produced by a constant methane flow and a controlled air flow. The chapter also reports on some modifications that were carried out in order to improve the operation of the optical delay-line and beam focusing for imaging tests. An analysis of the signal-to-noise ratio of the system is made using a methodology found in the literature. The operation of a digital fast lock-in amplifier is introduced and its performance is analysed using the Equivalent Noise Bandwidth. Once that the THz-

TDS system was characterized some spectroscopy tests on dielectric transformer oil were carried out in order to try to detect a difference between a virgin oil sample and other with accelerated ageing. Finally, the performance of some alternative configurations for the balanced detection and synchronous demodulation is explained.

Chapter 4 presents the basics of THz continuous wave generation using photomixing techniques. It also describes the experimental setup and presents the results of a simple emission test.

Chapter 5 introduces the theory of computerized tomography and then it proceeds to explain the design and construction of a THz tomography system. Details on the developed computer-based instrumentation and programs used to analyse and reconstruct images are also given. Reconstructed images, using amplitude contrast, of phantoms made of Styrofoam are presented and discussed. Refraction losses presented by the images are modelled using Fresnel equations and the scattering losses using the Rayleigh roughness factor. A scattering factor for transmission in rough surfaces is introduced as a way of explaining high levels of contrast obtained in the edges of reconstructed images. A simulation is presented using experimental data on refractive index, attenuation factor and roughness factor of the Styrofoam.

Chapter 6 summarizes the conclusions of the research and suggests potential future work. Additionally, an appendix presenting some details on alignment procedures of the THz-TDS system is included.

2 TERAHERTZ TIME-DOMAIN SPECTROMETRY

2.1 System overview

Spectroscopy is a technique for studying materials using electromagnetic waves [13], in particular, it tries to measure a frequency dependent behaviour in some specific region of the electromagnetic spectrum. Different instruments have been developed to perform ultraviolet (UV) spectrometry, visible spectrometry, or infrared spectrometry [14].

Terahertz Time-domain spectrometry (THz-TDS) is a technique that uses ultrashort laser pulses to generate and sample a broadband THz radiation pulse. The THz pulse is reconstructed from a sequence of space and time sampling measurements. The use of a Fast Fourier Transform (FFT) produces information about the spectrum of the pulse. Applications for this technology range from material identification and characterization, to imaging and tomography [2, 4, 15-22]. In Figure 2-1, a THz absorption spectrum of air is shown. The red arrows point to some of the water vapour absorption lines. The strong absorption produced by water vapour may limit THz applications in communication systems or substance identification at distance [23].
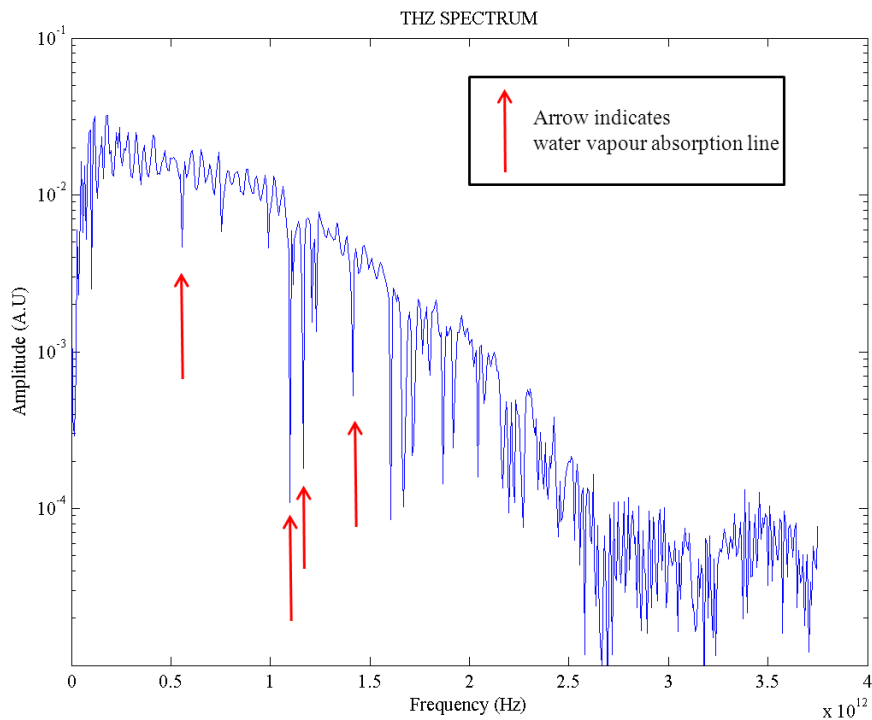
Figure 2-1. THz absorption spectrum of air. Arrows point to water vapour absorption lines at 0.557, 1.097, 1.163, and 1.410 THz.

THz-TDS systems are capable of measuring electric field instead of intensity [24].Thus, as opposite to other techniques like FTIR (Fourier transform infrared) spectroscopy, phase information is preserved and not just the power spectrum. THz-TDS has a typical bandwidth between 2 and 5 THz and a frequency resolution of 50 GHz [16]. It also presents a typical dynamic range and SNR between 60 dB and 80 dB.
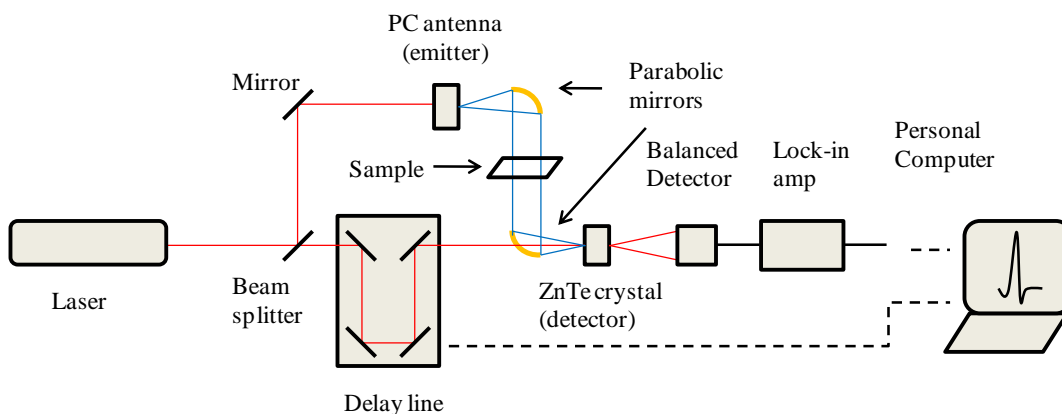
Figure 2-2. Block diagram of a TDS system.

A schematic diagram of a TDS system is shown in Figure 2-2. A 800 nm 150 ns ultrashort pulse beam generated by a Ti:sapphire modelocked laser, with a repetition rate of 76 MHz is used. These kind of lasers are especially suited for driving GaAs emitters and detectors [18], because the photon energy of a 800 nm wavelength (1.55 eV) is just above the energy gap of the semiconductor (1.43 eV). This is a technology and is widely used in THz systems, despite the fact that it is very sensitive to changes in optical alignment and mechanical vibration.

In the TDS system, the laser pulse is passed through a beam splitter with a theoretical ratio of 80:20. The higher power component is applied to the emitter antenna (pump beam) and the other is used as a probe beam. A beam sampler with a 99:1 ratio was considered but alignment was very difficult since the 1% beam was hard to see with a laser card. Nevertheless, the laser power impinging on the GaAs photoconductive (PC) antenna was enough to operate it close to its maximum photocurrent operating point.

The generated THz pulse can have a duration of less than 1 ps. This is too fast to be acquired; therefore an undersampling technique is used. This technique relies on the fact that the pulse is generated repeatedly at 76 MHz. A fast interaction with the probe beam laser pulse provides with high temporal resolution of a fraction of ps [24]. The probe beam is synchronized with the THz pulse and a train of pulses are received by a low frequency bandwidth photoreceiver, which produces an averaged output (see Figure 2-3). Changing the sampling delay produces a sample of a different point in the THz waveform (see Figure 2-4). The time position of the sampling pulse is shifted by an opto-mechanical delay line and after several steps, a waveform representing the THz electrical field can be reconstructed. There is no absolute reference to time, but the relative time difference between probe and pump pulsed is used to reconstruct a time frame.
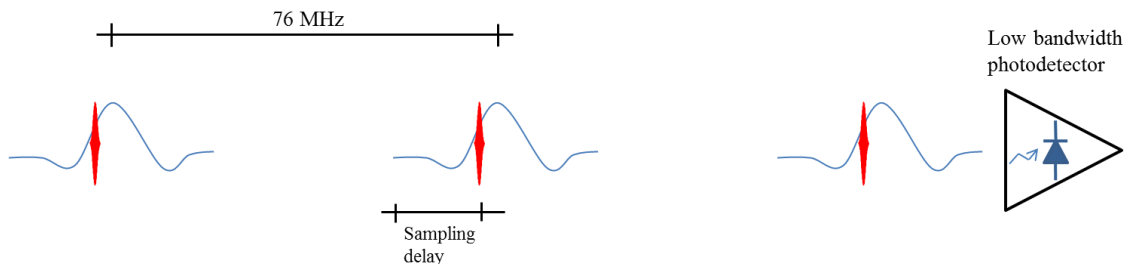
Figure 2-3. Undersampling of a THz pulse.
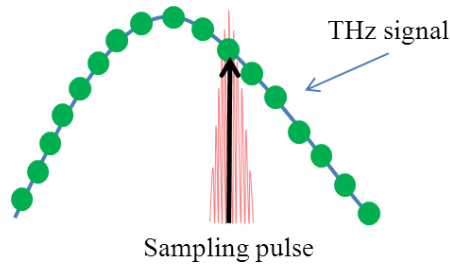
Figure 2-4. Sampling in a TDS system.

2.2 Terahertz generation

There are several techniques available for producing Terahertz including: optical rectification, difference frequency generation, transient photoconductive switching, and photomixing [25]. The first two rely on the optical properties of a nonlinear crystal, while the remaining use a photoconductive antenna (PCA). PCAs where developed in the 80's [1] and remain one of the most important devices for generating THz waves specially in TDS systems, even when there are other devices available, such as electro-optic (EO) crystals [26]. PCAs have a high efficiency which allows them to operate from a 10 mW average power Ti:sapphire mode locked laser oscillator, while EO crystal may require ten times as much power [26]. However, EO crystal do produce a broader bandwidth [18].

Optical rectification and difference frequency generation use the properties of a second order non-linear crystal to produce Terahertz radiation. If a femtosecond laser pulse is applied to a second order non-linear crystal, a broadband Terahertz pulse will be generated with a waveform resembling the envelope of the incoming laser pulse in an optical rectification process. In difference frequency generation, two continuous wave lasers operating at slightly different frequencies interact over the crystal for producing the THz radiation, which correspond to the modulation [25, 27, 28] (see Figure 2-5). A limitation of non-linear crystals is that they present phonon absorption and Etalon effects which produce blind spots with poor SNR at some specific frequency bands.
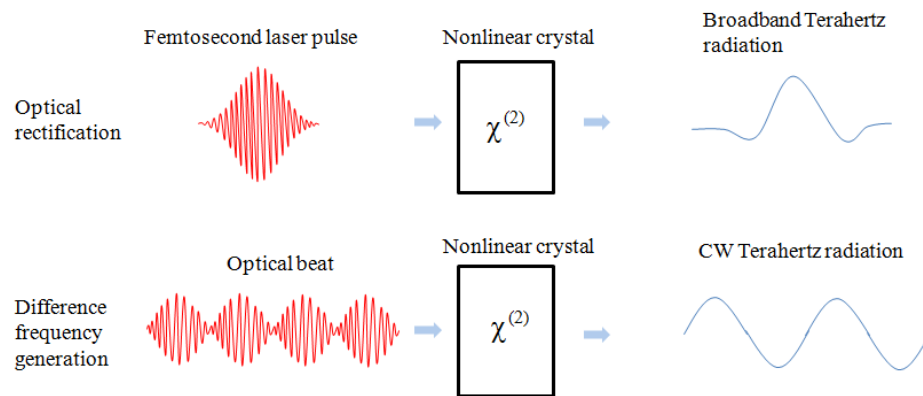
Figure 2-5. Terahertz generation in nonlinear media [25].

Transient photoconductive switching and photomixing are techniques useful to generate Terahertz radiation using photoconductive antennas. In the former, a femtosecond laser pulse is applied to the gap between two electrodes, the carriers generated are accelerated by a bias voltage. Photocurrent changes as a function of laser beam intensity, and a broadband Terahertz pulse is produced. In photomixing, two laser beams with different frequency are used to produce a CW Terahertz radiation [25] (see Figure 2-6).
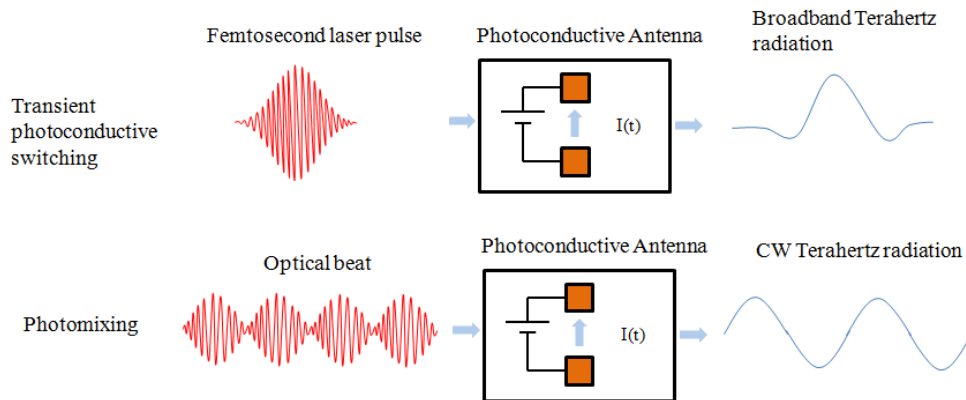
Figure 2-6. THz radiation from accelerated electrons [25].

2.2.1   Photoconductive switching

Photoconductive switching is a method for generating THz radiation in which an electric circuit is "closed" by a laser pulse. This switching produces a rapid movement of electric

carriers that generate THz radiation (Figure 2-7). This type of device is also known as the Auston Switch [1]. It has been reported that photoconductive antennas can generate up to 40 µW output power [29].
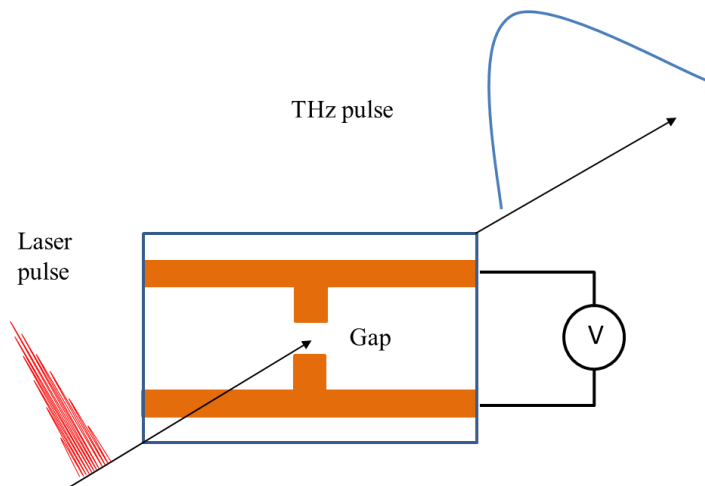
Figure 2-7. A dipole photoconductive antenna.

A PCA consist of a pair of electrodes deposited over a semiconductor substrate, for example, low temperature GaAs (LT-GaAs). This material has a breakdown field of approximately 500 kV/cm and is considered one of the best choices for photoconductive devices.

Our implementation uses a large aperture LT-GaAs PCA (Figure 2-9A). The distance between electrodes is not specified in the datasheet, but it is estimated to be larger than 500 µm. The electrodes are biased by a 160 V DC power supply.

The bias voltage produces an electrical field between the electrodes (Figure 2-8A). When an ultrashort laser pulse, with an energy above the band gap of the semiconductor (E_g=1.43 eV for GaAs), arrives to the gap between the electrodes, carriers (electrons and holes) gain enough energy to migrate from the valence band to the conduction band (Figure 2-8B). In our case, the laser pulse has a wavelength of 800 nm which translates to a photon energy of 1.55 eV. The static field accelerates the carriers (Figure 2-8C), generating a broadband Terahertz pulse (Figure 2-8D). The radiated pulse has a linear polarization parallel to the direction of the electrode electric field [30].
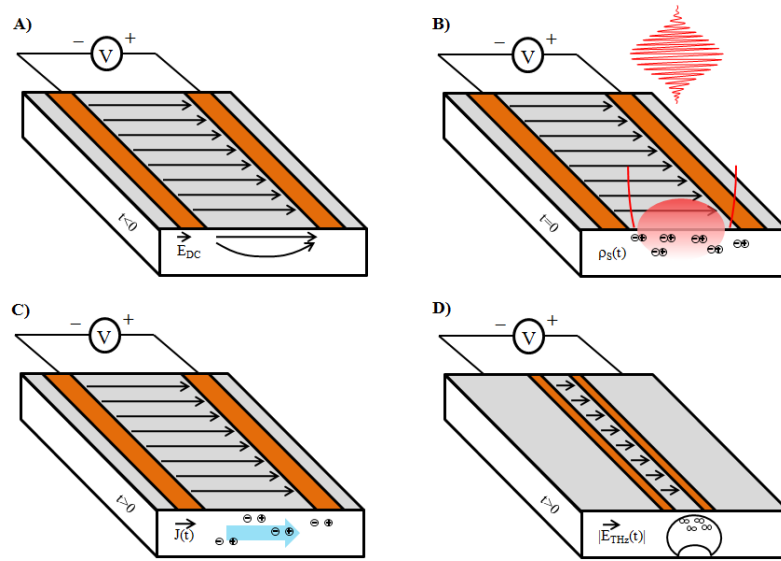
Figure 2-8. The mechanism of photoconductive switching [31].

Apart from the basic two parallel electrodes PCA, several configurations have been developed, which try to increase efficiency (Figure 2-9). Among this models are dipole, bow-tie, butterfly, spiral and interdigitated arrays [32-35]. Parallel configuration generates THz radiation polarized in the direction of the bias voltage, but dipole configuration generates around 7% of lateral polarization, and 25% in the case of an offset dipole [36] (see Figure 2-10). It has been reported that a small spot close to the anode produces more THz power than illuminating the whole gap [36, 37].
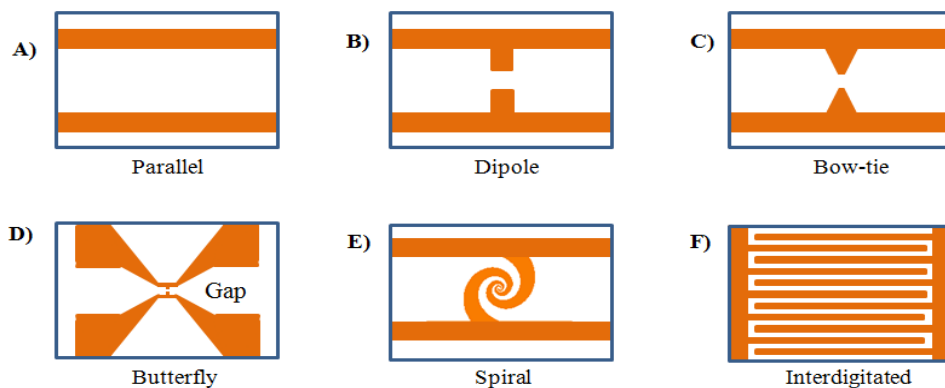
Figure 2-9. Photoconductive antenna architectures.
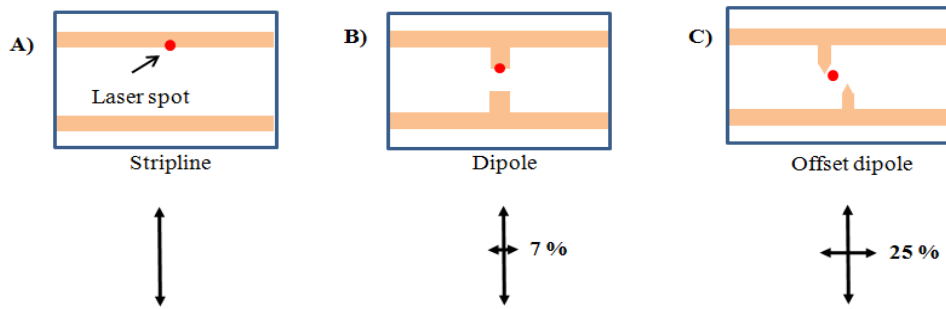
Figure 2-10. Effect on polarization of THz radiation from antenna structure [36].

The parallel or strip line (Figure 2-9A) has a high bandwidth emission close to 5 THz. The dipole antenna (Figure 2-9B), is a very common configuration and it has a spectral distribution of 3 THz. The bow-tie has increased emissions but at frequencies lower than the dipole configuration [32].

In a parallel configuration, electrodes can be separated by 50 μm to 500 μm, and a femtosecond laser pulse can be focused to form a 10 μm spot near the positive electrode [24, 38]. It has been reported that dipole antennas with gaps of 10 μm, 20 μm and 30 μm have almost the same spectral response but with larger signal amplitudes than produced by larger dipoles [32].

In a GaAs PCA, radiation power radiated into the substrate can be twelve times stronger than into free space [39]. In order to avoid this problem, it is a very common approach to add a silicon hyperhemispherical lens to the back of the PCA to collimate or to avoid high divergence of the THz radiation [18]. However, radiation pattern will be affected by any misalignment of the silicon lens.

InP semiconductor presents an energy band gap similar to that of GaAs (E_g=1.27 eV for InP) and it has been used to develop photoconductive antennas which have presented a 30 THz bandwidth but with half the SNR of a GaAs antenna due to lower resistivity [40]
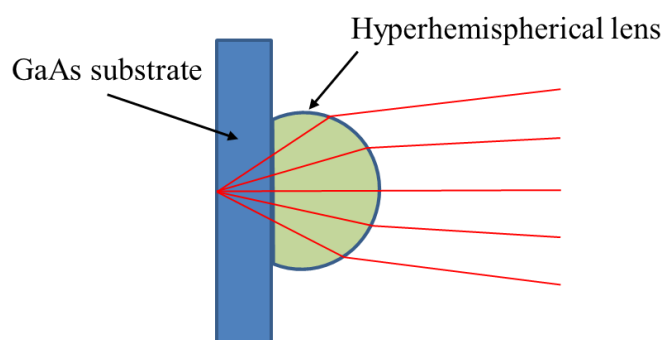
Figure 2-11. PCA with a hyperhemispherical lens.

2.3 Terahertz detection

Terahertz detectors can be classified in coherent and incoherent techniques. Coherent detectors are capable of measuring amplitude and phase information, and incoherent detectors measure only intensity. Electro-optic sampling, photoconductive switching and photomixing are all coherent detection techniques and they use the same laser light source for generation and detection (Figure 2-12). In our system, as will be described in detail in later paragraphs, electro-optic sampling (an example of coherent detection) is used.

 Photoconductive switching as a method for generating a THz signal has already been described; however, the photoconductive switching can be also used to detect a THz pulse. In this case, a THz signal induces a current in a photoconductive gap when a laser probe pulse arrives and the current generated is proportional to the THz amplitude. The shape of the THz pulse is obtained by varying the time delay between the THz pulse and the optical probe, using the undersampling technique depicted in Figure 2-4.

Photomixing also uses the photoconductive switching effect of the receiver antenna, but in this case, photocurrent depends on the phase difference between the envelope of the optical probe and the THz signal. Electro-optic sampling is described in section 2.3.1.
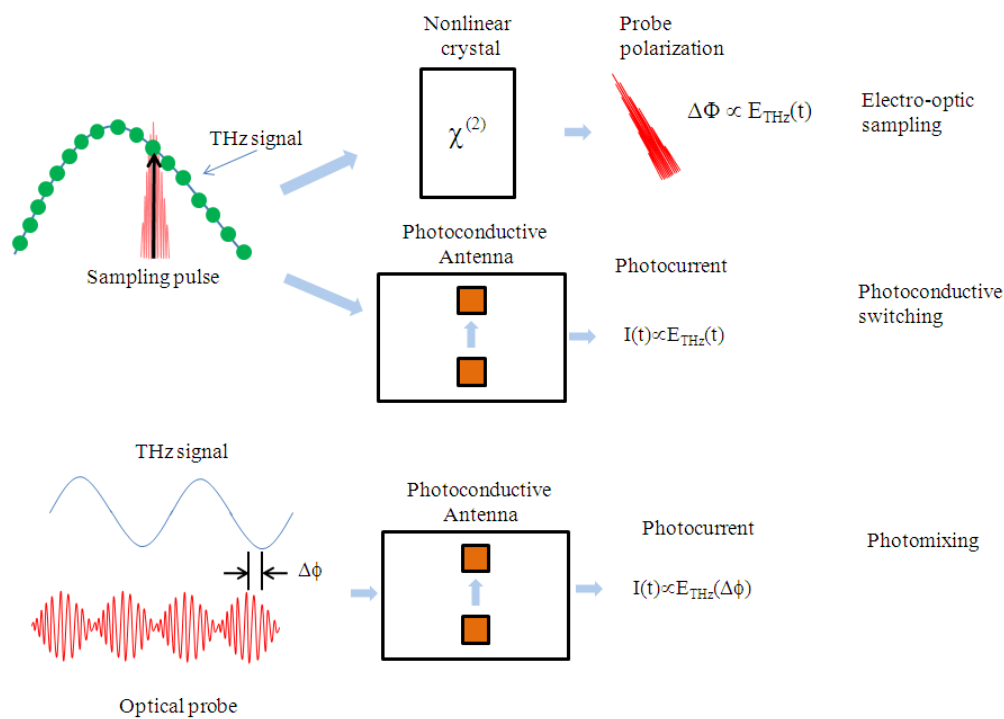
Figure 2-12. Coherent Terahertz detection methods.

PCA detectors have the same different configurations as PCA emitters. According to Batop Optoelectronics (http://www.batop.de/) the recommended use for different photoconductive antennas is summarized in Table 2-1.

Type of antenna	Emmiter	Detector	Broadband	High power
Butterfly	+	++	+	+
Dipole	++	+	++	-
Bow-tie	+	++	+	+
Interdigitated	++	+	++	++

Table 2-1. Recommended use for PCAs.

Photoconductive detectors based on InP have shown higher responsivity and better SNR at low gating laser powers than [41]. Incoherent THz detectors are usually a type of thermal sensors, for example: bolometers, Golay cells and Pyroelectric devices. These devices have an absorbing element which transforms electromagnetic radiation to heat [42]. A bolometer has an electrical resistance thermometer which has greater sensitivity

when operated at cryogenic temperatures. In a Golay cell, absorbed radiation is transferred to a small volume of gas. A change in internal pressure deflects a membrane with a mirror attached and thus varying the amount of light that is produced by a LED and collected in a photodiode. Pyroelectric detectors are made of pyroelectric material in which a change in electric charge is produced by a temperature change [25, 42, 43]. Thermal sensors are slow, because the absorbing element must reach thermal equilibrium before a measurement can be made.

2.3.1 Electro-optical sampling

In electro-optic sampling, the polarization of a probe beam is changed by the presence of a THz electrical field. This polarization change, which is proportional to the THz electrical field, is measured and used to reconstruct the actual THz waveform. In other words, an electrical field (THz radiation) causes a change in the refractive index (induced birefringence) of an electro-optic crystal. This phenomenon is also known as the Pockels effect. A linearly polarized laser beam is subject to phase retardation $\Delta\phi$, causing it to become elliptically polarized with its intensity components Ix and Iy modified as [39]

$$
\begin{aligned}
I_x &\approx \frac{I_0(1 - \Delta\emptyset)}{2} \\
I_y &\approx \frac{I_0(1 + \Delta\emptyset)}{2}
\end{aligned}
\tag{2-1}
$$

and the THz field intensity is proportional to the difference I_s between these components

$$
I_s = I_y - I_x = I_0\Delta\emptyset \propto E_{THz} \tag{2-2}
$$

Electro-optical sampling can measure the amplitude and phase of THz pulses with high precision ($<10^{-2}$ rad) [39]. It has been suggested that electro-optical sampling requires less power, has equivalent signal to noise ratio, has more bandwidth and is more stable and easier to align than PCA detection [44]. Among electro-optical crystals, ZnTe is the best candidate for THz detection with 800 nm pulsed lasers [45] and is suitable for measurements from sub-Terahertz to tens of THz [27].

The use of electro-optical detection produces a compromise between the sensitivity and the frequency response [46]. Thinner EO sensors have a broader frequency response, but with smaller sensitivity, since there is a short interaction distance [27]. A thicker crystal has a higher sensitivity but a reduced bandwidth caused by group velocity dispersion. For thinner crystals, a shorter pulse would be recommended for an increased resolution [47]. For our system, a 2 mm thick ZnTe crystal is used which provides a high signal and a bandwidth below 10 THz [48]. The electro-optical sampling procedure is depicted in Figure 2-13. The THz pulse and the laser probe pulse are focused inside the EO crystal. It is important that both the THz pulse and the laser probe pulse share the same polarization and are correctly oriented with the EO crystal (see Figure 2-14). The laser probe pulse is vertically polarized. After going through a quarter wave plate, the beam becomes circularly polarized. The polarization components are separated by means of a Wollaston prism, but without the presence of a THz pulse, both components are equal. Subtracting them produces a zero result. However, if a THz pulse is present, an induced birefringence is produced inside the EO crystal producing an elliptically polarized beam after the quarter wave plate. Separating the vertical and horizontal components of the beam with the Wollaston prism produces a signal which is proportional to the THz electrical field.
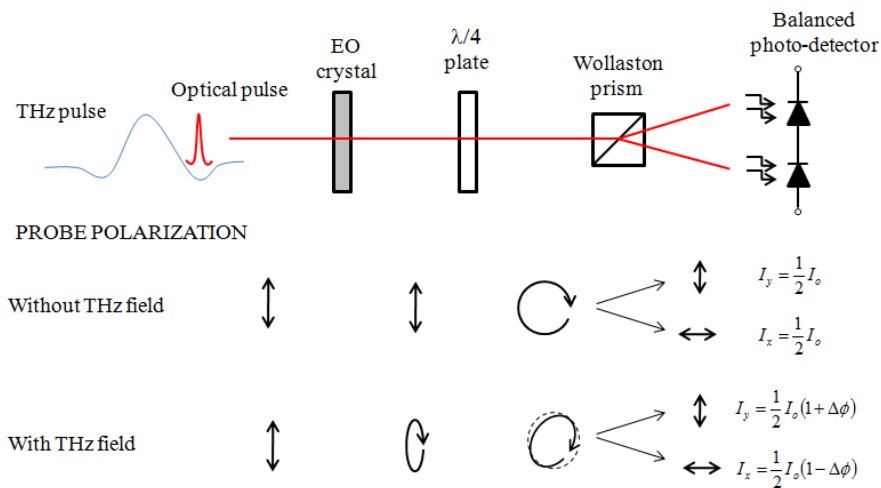
Figure 2-13. Detection of a THz pulse by electro-optical sampling [39].

[1 $\bar{1}$ 0]

ZnTe
Crystal

Probe
beam

[1 1 0]

THz
beam
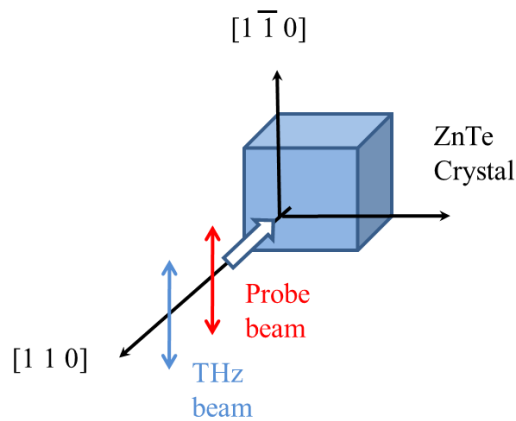
Figure 2-14. Electro-optic sampling in a ZnTe Crystal.

In order to improve the signal to noise ratio in this type of experiments it is almost indispensable to use a lock-in amplifier. For that purpose a mechanical wheel chopper is usually added to the pump or the probe beam.

2.4   Terahertz optics

There are two types of Terahertz optical components in the system. The Si lens attached to the PCA emitter antenna which was discussed above, and the parabolic mirrors. An important effect that should be considered in Terahertz optics is diffraction, which becomes important, since the wavelength of Terahertz radiation is not negligible compared to the size of the optical components [18].

2.4.1   Parabolic mirrors

Our initial setup uses two parabolic mirrors, one for collimating the Terahertz radiation generated by the photoconductive antenna, and the second is used to focus the Terahertz beam on the ZnTe crystal detector. The former is needed to collimate the THz radiation, since otherwise the beam will continually diverge, reducing the power density, the latter is needed to focus the THz beam on the crystal detector in order to facilitate its detection.

The metallic off-axis parabolic mirrors used are for this functions. This type of mirror is generated by cutting a section of a parabolic mirror, as can be seen in Figure 2-15. The reflected focal length plays an important role in setting the relative position of the emitter antenna and the ZnTe crystal detector.
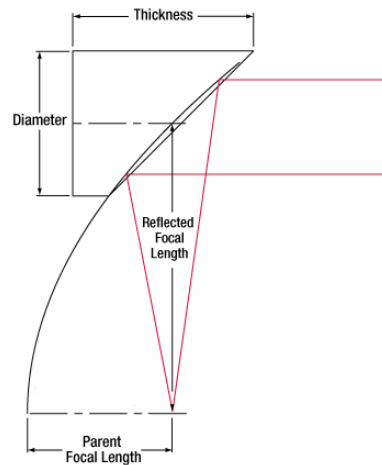
Figure 2-15. Off-axis parabolic mirror. Reproduced from [49].

2.5 Ultrafast mirrors

In an ultrafast laser system, it is important to avoid pulse broadening effects as the laser beam goes through the different components. Our system uses several ultrafast mirrors which are specifically designed to work with ultrafast laser pulses.

A laser pulse is made of several frequency components, each of these components can experiment a difference in velocity as they travel through an optical component (or are reflected by a mirror). Group velocity dispersion (GVD) is a measure of this difference. Since femtosecond laser pulses have a large bandwidth, GVD is an important issue. The broadening effect of a laser pulse is depicted in Figure 2-16. Laser mirrors should have a

broad operating wavelength range and linear phase versus frequency (low reflectance Group Delay Dispersion, GDD).
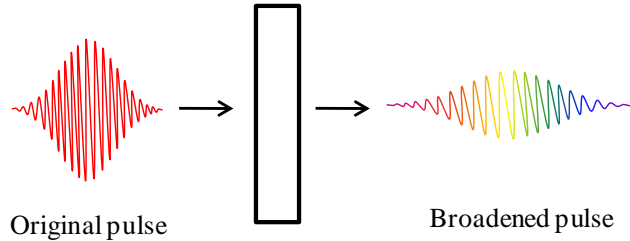
Figure 2-16. Broadening of a femtosecond pulse.

For implementing the system, there were several mirrors model 10B20UF.25 from Newport (£188.00) at our disposal. Newport's mirror has been designed to operate specifically at 800 nm, and particular attention has been put to its GVD specifications. As can be seen in Figure 2-17, at 800 nm, GVD is almost negligible. Alternatives to this mirror are Thorlabs Ultrafast Mirror for femtosecond pulsed laser UFM10R (£95.50) and Thorlabs Broadband Dielectric Mirrors BB1-E03 (E03 coating) (£51.82), and is been considered as a cheaper replacement. Thorlabs UFM10R mirror has a GVD of around -50 fs^2 @ 800 nm, whereas Thorlabs BB1-E03 mirror has a very high GVD close to -1000 fs^2 @ 800 nm, therefore UMF10R is a good option but BB1-E03 may be is unsuitable, since it may generate too much broadening.
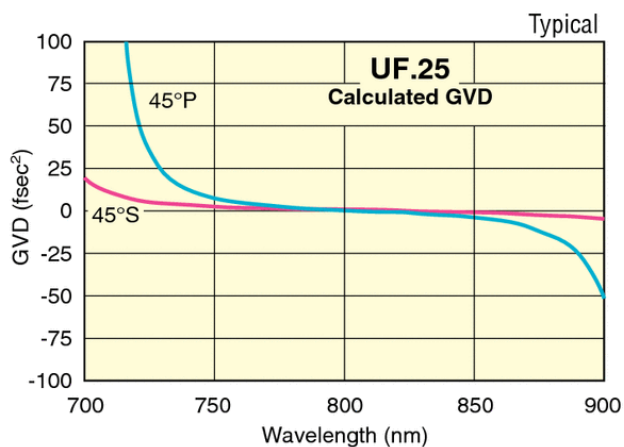
Figure 2-17. Newport Broadband Mirror GVD vs. λ. Reproduced from [50].
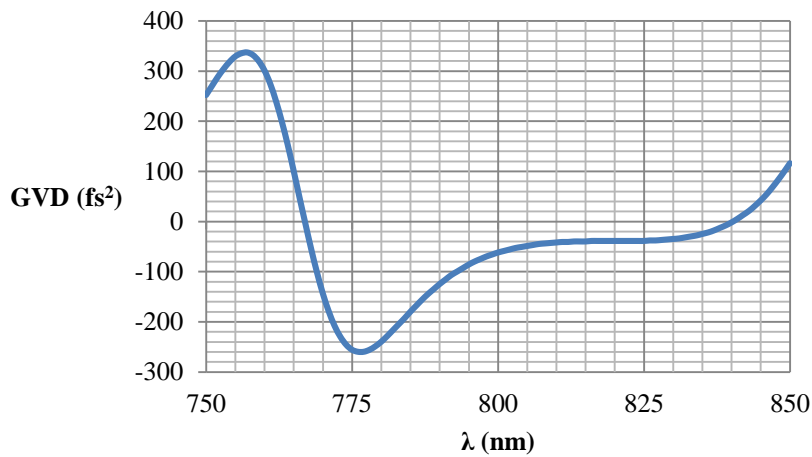
Figure 2-18.Thorlabs Ultrafast mirror (UFM10R) GVD vs. λ.
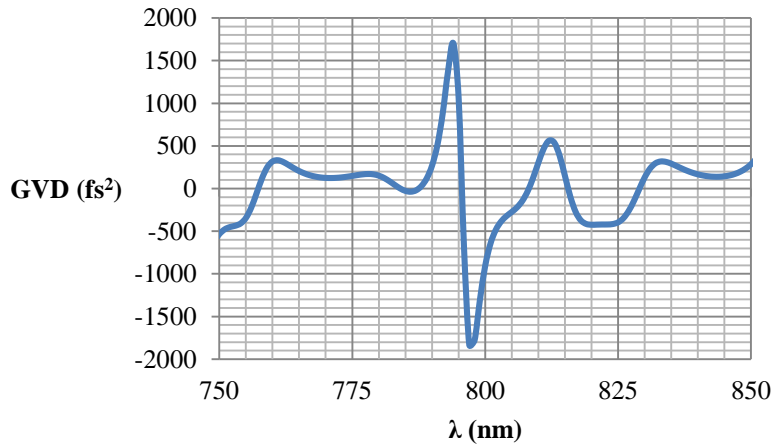
Figure 2-19. Thorlabs –E03 broadband dielectric coating GVD vs. λ.

In order to determine whether a BB1-E03 mirror is suitable, an estimation of its broadening effect can be developed. Supposing a Gaussian pulse envelope, the theoretical broadening for the pulse is given by [51]

$$\tau_{out} = \tau_{in} \sqrt{1 + \left(\frac{4\ln2 \cdot GVD}{\tau_{in}^2} \right)^2} \qquad (\ 2.3)$$

In Figure 2-20, the theoretical broadening effect for a 50 fs, 150 fs and a 200 fs laser pulse has been plotted. Broadening is higher for a 50 fs pulse, but negligible for 150 fs or 200

fs pulse even at GVD as high as 1000 fs^2. Therefore, since the system has a 150 fs pulse, it can be concluded that Thorlabs BB1-E03 mirrors are suitable for the system.
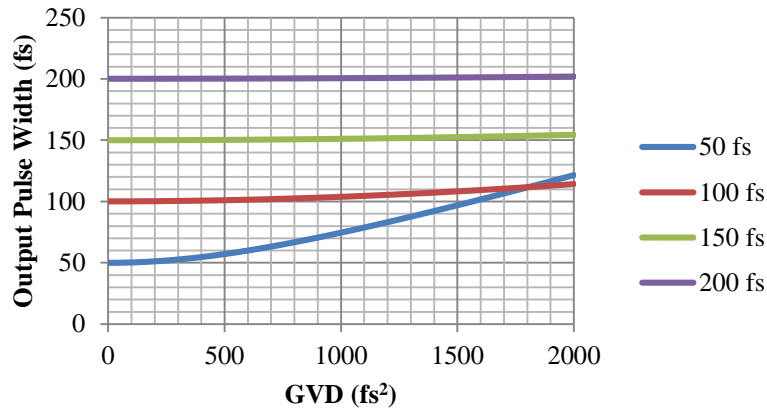
Figure 2-20. Output pulse width vs. GVD.

2.6 Auxiliary optics

Other optical components also used in the system include: a beamsplitter, focusing lenses, a waveplate, and a Wollaston prism.

2.6.1 Beamsplitter

A beamsplitter is an optical device that divides a beam in two. A Newport 10RQ00UB.2 ultrafast laser beam sampler was selected and it has 20% reflectance for a P-polarized beam at an angle of incidence of 45 °. It is used to produce an 80% pump beam and a 20% probe beam. A P-polarized beam has its electrical field parallel to the plane of incidence whereas an S-polarized beam has it perpendicular (*senkrecht* in German) to that plane.
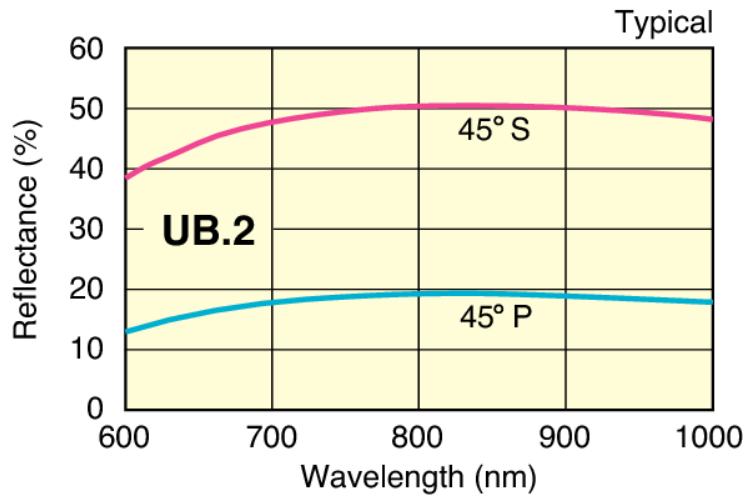
Figure 2-21. Reflectance an ultrafast beam sampler. Reproduced from [52].

2.6.2 Focusing lenses

Focusing lenses are required in a THz-TDS system for concentrate optical power in a small area. Using a lens to focusing a femtosecond pulse produces some broadening due to GVD effects, with a group delay dispersion proportional to the length of the material (see Figure 2-22) [53].
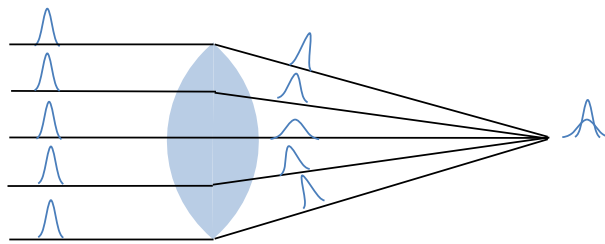
Figure 2-22. Effect of GVD in focusing a femtosecond pulse [53].

GVD depends on the index of refraction of the material n and wavelength λ, and is given by

$$GVD = \frac{\lambda^3}{2\pi c^2}\left(\frac{d^2 n}{d\lambda^2}\right) \qquad (2.4)$$

50

The lenses selected are made from BK7 material. In Figure 2-23, the effect of broadening for an 800 nm pulse through a 20 mm of BK7 is shown. Since the laser produces a 150 fs pulse, expected broadening effects are minimal.
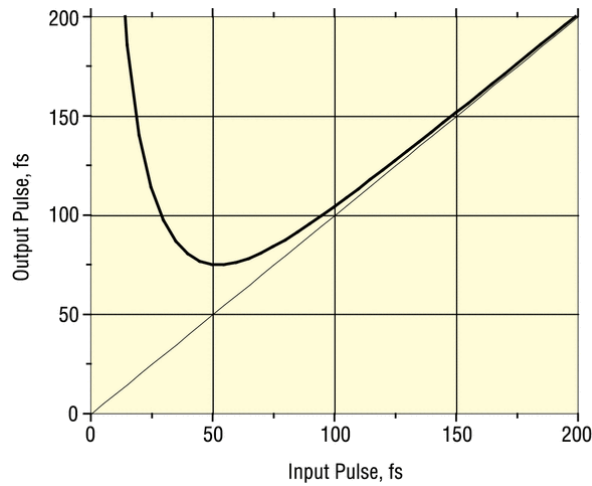
Figure 2-23. Broadening of an 800 nm femtosecond pulse after propagating in 20 mm of BK7. Reproduced from [54].

2.6.3 Wave plates

A waveplate (also called retarder) is an optical device that modifies the polarization of a beam. A halfwave plate will change the relative polarization angle of beam by 2θ, where θ is the rotation angle of the waveplate with respect to the fast axis of the plate (see Figure 2-24). A quartewave plate will change a linearly polarized beam in a circular polarized or a circular polarized beam in a linearly polarized if it arrives at 45 ° with respect to the fast or slow axis.
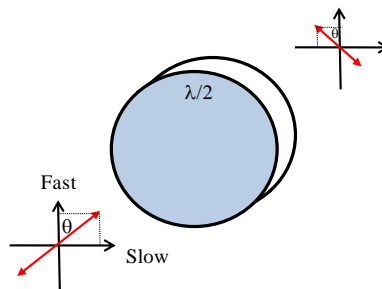
Figure 2-24. Halfwave plate rotates a linearly polarized beam.
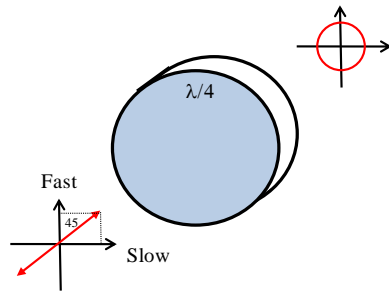
Figure 2-25. Quarterwave plate transforms a linearly polarized beam into a circularly polarized one.

2.6.4 Wollaston prism

The Wollaston prism is a polarized beamsplitter made of an ensemble of two calcite or quartz prisms. It separates orthogonal components of a beam by an angle between 15° and 45° [55]. The Thorlabs WP10 Wollaston prism has a wavelength range from 320 nm to 2.3 µm, and a damage threshold of 1 W/cm^2, making it suitable for the intended application.
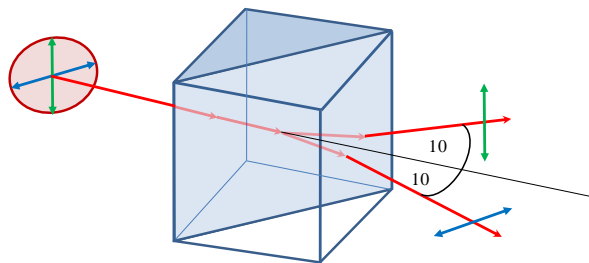
Figure 2-26. Wollaston prism.

2.7 Balanced optical detection

A balanced optical detector is a device used to reduce common mode noise generated by a laser source. In one of its simplest forms, it consists of a pair of photodetectors. Their photocurrents are subtracted and amplified to produce an output voltage, as shown in Figure 2-27.
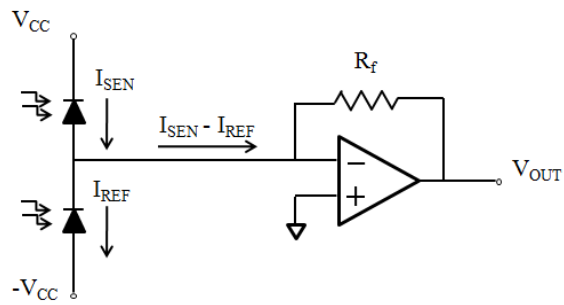
Figure 2-27. Difference photocurrent amplifier.

The basic idea behind a balanced optical detector is to split the laser source in two beams, usually in a 50/50 ratio, in order to send one to the sample to be analysed, and to use the second as a reference. It is usually configured in the setup shown in Figure 2-28. A laser beam of power P_o is divided by a beam splitter in $P_1=\beta P_o$, and $P_2=(1-\beta)P_o$ where $0<\beta<1$ is the splitting ratio. $P_{SIG}=\alpha P_2$ is the signal detected after being attenuated by the sample, α is the attenuation factor and P_{REF} is the reference signal. In a typical situation, a neutral density filter (ND) is required to compensate for the attenuation produced by the sample. After this compensation, the output voltage will be proportional to small variations in the absorption produced by the sample.
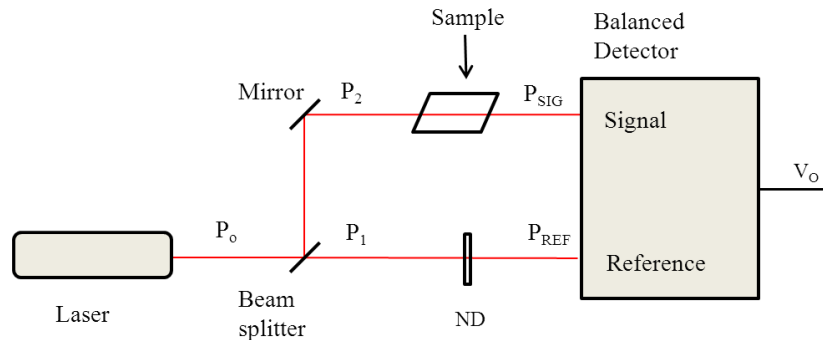
Figure 2-28. Schematic diagram for an optical balanced detection system.

In order to explain the operation of the balanced detector, the trivial case shown in Figure 2-29, will be first considered. In this case, there is no sample in the laser beam path, and the splitting ratio is 50%. Photocurrent is then

$$I_{SIG} = I_2 + I_{CM}$$
$$I_{REF} = I_1 + I_{CM}$$

(2-5)

53

Where I_{CM} is the common mode current produced by the laser common mode.

If signals are subtracted, the common mode signal is cancelled out.

$$I_{SIG} - I_{REF} = I_2 - I_1 \qquad (2\text{-}6)$$
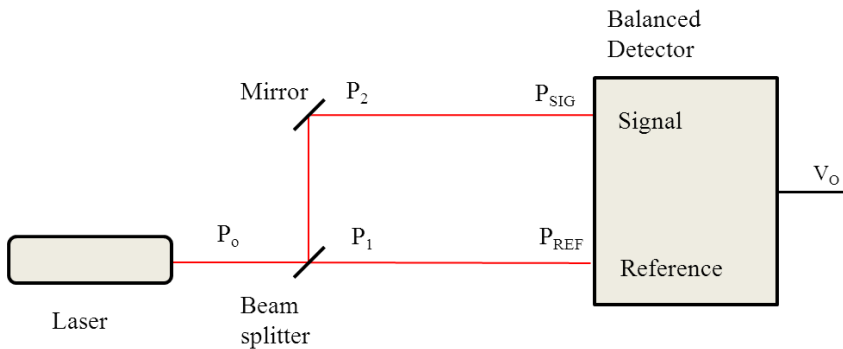
Figure 2-29. Balanced detector. Trivial case.

If now a sample with attenuation factor α (see Figure 2-30) is introduced

$$\begin{aligned} I_{SIG} &= \alpha(I_2 + I_{CM}) \\ I_{REF} &= I_1 + I_{CM} \end{aligned} \qquad (2\text{-}7)$$

Subtracting the signals gives

$$I_{SIG} - I_{REF} = \alpha I_2 - I_1 + I_{CM}(\alpha - 1) \qquad (2\text{-}8)$$

where the common mode signal can no longer be cancelled, because of the unbalance introduced by the sample.

In order to recover the balance, a ND filter is introduced as shown in Figure 2-28. If we define α_{ND} and α_S the attenuation factors produced by the ND filter and the sample respectively,
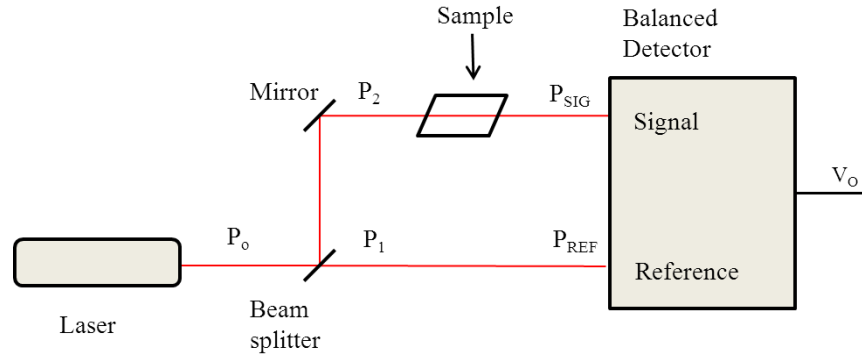
Figure 2-30. Balanced detector with sample.

$$I_{SIG} = \alpha_S(I_2 + I_{CM})$$
$$I_{REF} = \alpha_{ND}(I_1 + I_{CM})$$

(2-9)

Then

$$I_{SIG} - I_{REF} = \alpha_S I_2 - \alpha_{ND} I_1 + I_{CM}(\alpha_2 - \alpha_{ND})$$

(2-10)

where common mode signal can be cancelled if $\alpha_S = \alpha_{ND}$, and we get

$$I_{SIG} - I_{REF} = \alpha_{ND}(I_2 - I_1)$$

(2-11)

This configuration needs constant adjustment of the relative strengths of signal and reference beam in order to obtain a good noise cancelation and signal-to-noise ratio achieved is around 20 dB [56]. For avoiding this continuous manual adjustment, some techniques to implement an automatic electronic balancing have been proposed [57-59]. The idea is to add some gain control mechanism to one of the photodetectors. This can be done using a divider, but analogue dividers are very noisy and prone to instability. Gain-bandwidth behaviour requires a 1 MHz divider to achieve a 40 dB noise reduction at 10 kHz bandwidth [60]. Instead of that, an analogue multiplier or a multiplying digital-to-analogue converter can be used. None of these solutions is suitable for a THz TDS system, since the signal to be processed is a differential one, and changing the gain on one of the branches will spoil the measurement.

2.8   Lock-in amplifier

A lock-in amplifier is an instrument that relies on phase sensitive detection to reduce the amount of noise in a measurement. It is widely used in optical systems. A brief description of its operating principles will be given in the following paragraphs.

A basic light measurement problem is depicted in Figure 2-31. A light source passes through a sample and a photodetector converts the incoming light in an electrical signal. The signal is amplified and displayed on a meter. The lecture is a measure of the amount of light that is transmitted through the sample [61].
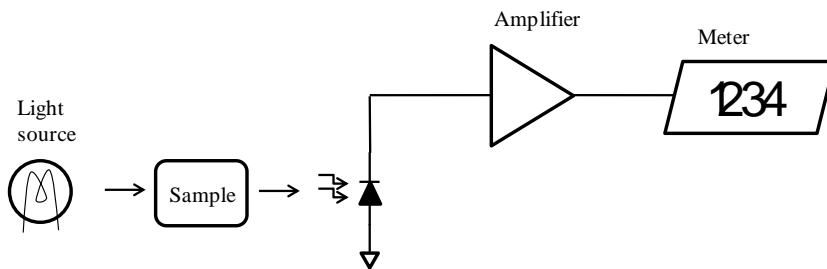
Figure 2-31. Simple light measurement system [61].

In many cases, low frequency noise may mask the measurement. The signal has a low-frequency content with an amplitude smaller than the level of noise present in the system (see Figure 2-32A). This situation can be improved if the signal is modulated (for example, using an optical chopper in the beam path), as shown in Figure 2-33. Electronic semiconductor devices are affected by defects in the crystal lattice, interaction between carriers, surface energy states and imperfect contacts, these phenomena gives rise to a type of noise that presents a frequency response approximated by 1/f, and is called flicker noise or excess noise [62]. Modulating the signal to frequency f_0 and avoiding the flicker noise region (1/f noise) produces a major improvement in signal to noise ratio (Figure 2-32B), since now the signal amplitude is greater than the noise. In order to recover the signal, a highly selective band-pass filter and a rectifier are required; however, it is difficult to build bandpass filters with a Q (quality factor) higher than some 100's. Moreover, minor variations in chopper speed may generate error measurements caused by mismatch between chopper (modulation) frequency and filter centre frequency. The

rectifier also poses a problem since it rectifies the noise as well, producing a DC level in the meter. These problems can be tackled by using a phase sensitive detector (PSD).
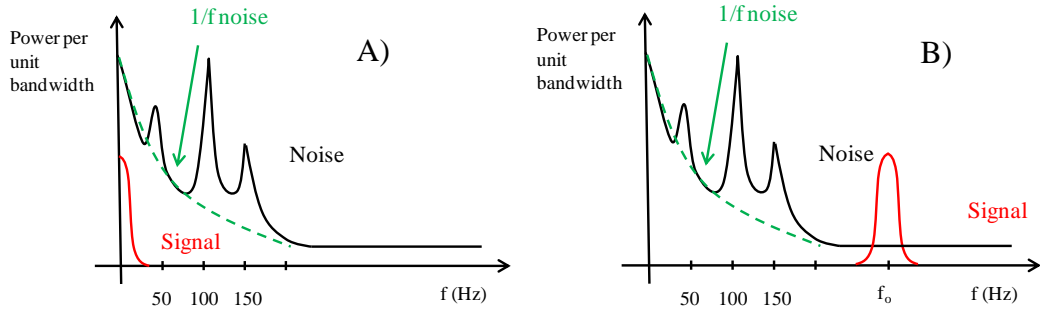
Figure 2-32. Noise distribution. A) Low frequency signal. B) High frequency signal [61].
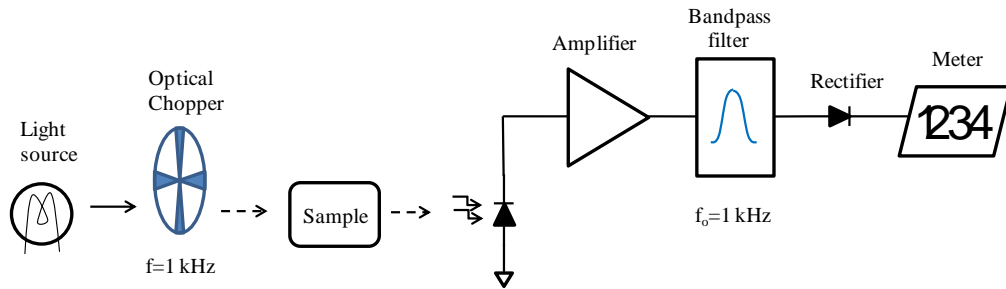
Figure 2-33. Shifting the signal frequency by modulation [61].

A PSD is shown in Figure 2-34. The rectifier has been replaced by a synchronous switch and the bandpass filter by an RC circuit. A reference signal, which can be obtained from the control circuitry of the chopper, is used to rectify the input signal with the switch (half wave rectifier). The noise will pass unrectified to the RC circuit, since noise is not synchronized with the reference signal. The RC circuit averages the noise, contributing to its reduction. The circuit behaves like a bandpass filter and quality factors above 1000 are easily achieved. Any drift in chopper frequency, will be followed by the switch (lock-in), in turn adjusting the central frequency of the equivalent bandpass filter.
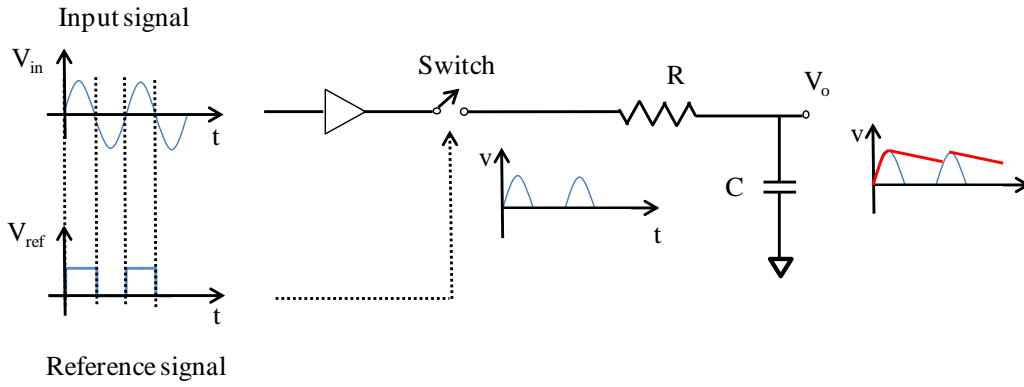
Figure 2-34. Phase sensitive detector [61].

For the circuit to operate properly, it is mandatory that the reference signal and input signal have identical phase. Since this is not the general case a second PSD can be added but with its reference signal shifted 90° (quadrature). A block diagram for the modified lock-in amplifier is shown in Figure 2-35. Besides the second PSD, a second filter and a magnitude module are required. For example, having two reference sinusoidal signals I and Q given by

$$I = V_r\sin(\omega_r t + \theta_r), \quad Q = V_r\sin(\omega_r t + \theta_r + \pi/2) \qquad (2.12)$$

which can be generated by a phase-locked loop (PLL), from a input signal S

$$S = V_s\sin(\omega_s t + \theta_s) \qquad (2.13)$$

multipliying both reference signals by the input signal

$$V_1 = S \cdot I = \frac{V_s V_r}{2}[\cos(\omega_s t - \omega_r t + \theta_s - \theta_r) \\ - \cos(\omega_s t + \omega_r t + \theta_s + \theta_r)] \qquad (2.14)$$

$$V_2 = S \cdot Q = \frac{V_s V_r}{2}[\cos(\omega_s t - \omega_r t + \theta_s - \theta_r - \pi/2) \\ - \cos(\omega_s t + \omega_r t + \theta_s + \theta_r + \pi/2)] \qquad (2.15)$$

considering the frequency of signal and references equal, $\omega_s=\omega_r=\omega$, then

$$V_1 = \frac{V_s V_r}{2} [\cos(\theta_s - \theta_r) - \cos(2\omega t + \theta_s + \theta_r)] \qquad (2.16)$$

$$V_2 = \frac{V_s V_r}{2} [\cos(\theta_s - \theta_r - \pi/2) - \cos(2\omega t + \theta_s + \theta_r + \pi/2)] \qquad (2.17)$$
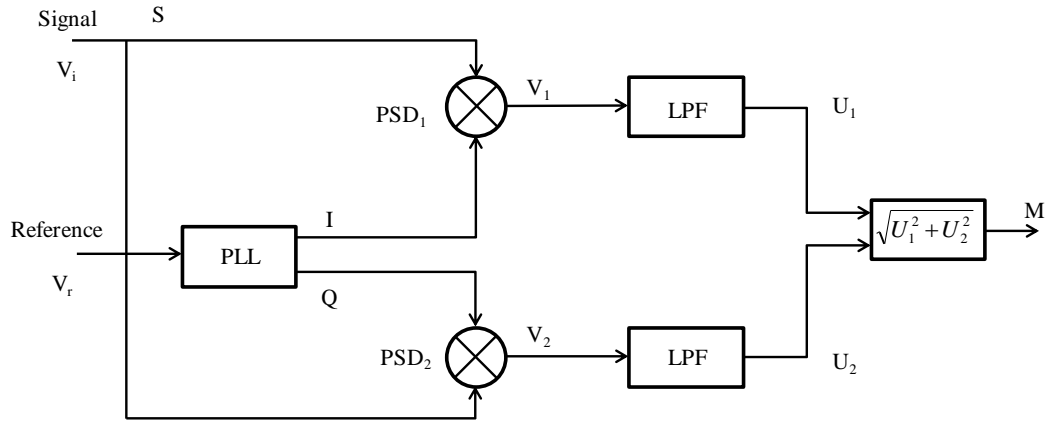
Figure 2-35. Dual phase lock-in amplifier [63].

Therefore, V_1 and V_2 are composed of a DC component and a 2ω frequency component. After the low-pass filters signals U_1 and U_2 are defined by

$$U_1 = \frac{V_s V_r}{2} \cos(\theta_s - \theta_r) \qquad (2.18)$$

$$U_2 = \frac{V_s V_r}{2} \cos(\theta_s - \theta_r - \pi/2) = \frac{V_s V_r}{2} \sin(\theta_s - \theta_r) \qquad (2.19)$$

calculating

$$M = \sqrt{U_1^2 + U_2^2} \qquad (2.20)$$

$$M = \sqrt{\left(\frac{V_s V_r}{2}\right)^2 \cos^2(\theta_s - \theta_r) + \left(\frac{V_s V_r}{2}\right)^2 \sin^2(\theta_s - \theta_r)} \qquad (2.21)$$

then

$$M = \frac{V_s V_r}{2} \qquad (2.22)$$

where the DC component M is proportional to the signal amplitude V_s. This expression only gives positive values. If the recovered signal has positive and negative values then the phase can be calculated from

$$\varphi = arctan\left(\frac{U_1}{U_2}\right) \qquad (2\text{-}23)$$

Some digital implementations of the lock-in amplifier have been reported [63, 64]. An improved architecture in terms of hardware has been proposed by García et al in [64], where they use a multiplexer to avoid using two low-pass filters. Their implementation operates at 180 kHz and reportedly achieves a SNR of 55 dB using a 16 bit ADC. For comparison, a commercial digital lock-in amplifier such as Stanford Research SR830 has a specification of 76 dB SNR.

2.9 Summary

In this chapter, the main building components of a THz-TDS system have been presented. The configuration has a PCA as emitter and a ZnTe crystal as detector; therefore more attention was paid to these components in particular. A good understanding of the operating principles of the components is the best starting point to build, adjust and test the system. It is important to understand the concept of photoconductive switching to avoid problems with focusing and alignment of the emitter antenna. The detection involves a very singular adjustment procedure; therefore we needed to study the principles of electro-optical sampling, which involves the use of a quarterwave plate, a Wollaston prism and a balanced photodetector.

The possible broadening effects produced by lenses and mirrors were of particular concern. Several mirrors with different specs were available, but not in enough number to use just a single type of them. It was demonstrated that GVD is minimal, due to the use of a relatively wide 150 fs pulse.

The balanced detector and the lock-in amplifier needed a more detailed review, since signal-to-noise ratio depends highly on these components.

After building the first TDS system as shown in Figure 2-2, several modifications were pursued in order to improve its performance, and to make it able to do THz tomography. This work and its results will be described in the following chapters.

3 THz-TDS SYSTEM IMPLEMENTATION

3.1 Introduction

In the previous chapter, the basic operating principles of a Terahertz Time-domain spectrometry system were covered. This chapter will focus on the construction, testing and improvement of this system.

There is no unique solution regarding the implementation of a THz-TDS system, different arrangements can be envisaged just by selecting the type and characteristics of the emitter, detector, optical components, and THz focusing elements. Moreover, many important details regarding mounting procedures are not covered neither in journal papers nor in specialized books. Therefore, an iterative process was followed, supported by the previous study of the constituting components of the system, in order to guarantee that the system had a performance similar to systems reported in the literature.

3.2 Layout design

The first task was to design the layout of the system. The relative order of the components was suggested by the literature review. The facilities at the Photon Science Institute, where the experiment was to be installed, consisted of two optical tables joined in a "T" configuration (Figure 3-1). The laser source was installed at the rear part of the first table, and the THz-TDS was to be installed in the second table, because of lack of space in the first one. Stability of this arrangement is difficult to control though it may be improved by the use of some sort of mechanical joint, for example with a stainless steel plate [65]. Since the laser source was more than 5 meters away from the TDS experiment, there was some concern about beam drifting. Final results showed no position drift of the laser beam, but the long distance from the laser source to the experiment does increase the sensitivity to mechanical noise.
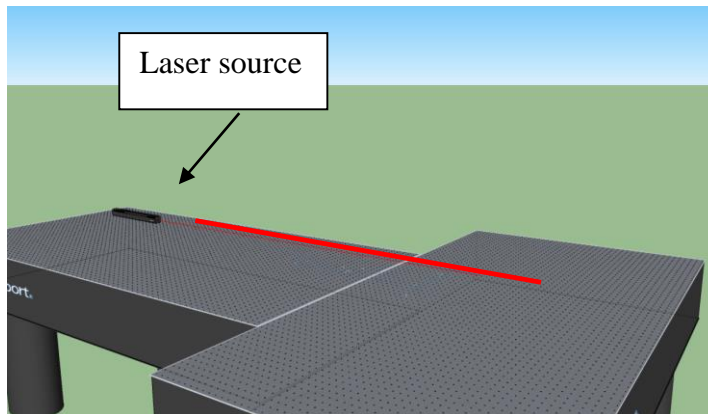
Figure 3-1.Two optical table arrangement.

The first attempt was to use the layout shown Figure 3-2. This configuration is easier to align, since many components are placed close to the side of the table. Nevertheless, the pump and probe beam paths are unbalanced, so it was realized that this was not adequate for detecting the THz radiation. Pump and beam paths must be of similar length, otherwise the THz pulse and the probe pulse will not arrive at the same time to the ZnTe crystal detector.
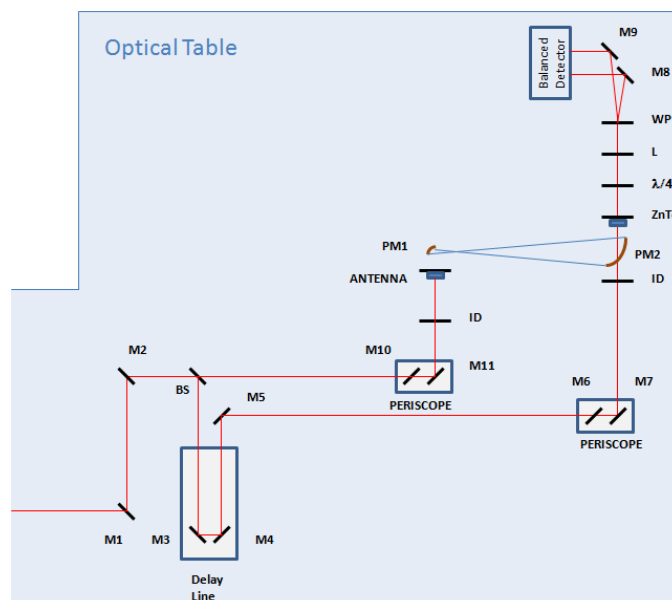
Figure 3-2. First layout.

The distance between the laser source and the experiment could amplify any alignment drift, and to prevent that, a two mirror approach is suggested in [66] [67]. Mirrors M1 and M2 are used to correct for any alignment drift from the laser source, reducing the need to make further adjustments in the rest of the system. With this idea in mind, a second layout was proposed (Figure 3-3). This time, beam path lengths are balanced. However, this configuration has a drawback: the splitting ratio of the beamsplitter BS was not right. In order to maximize THz radiation, the pump beam coming into the antenna must be more intense. The beamsplitter is a Newport 10RQ00UB.2 ultrafast laser beam sampler. According to its datasheet, for a P polarized beam, expected reflection percentage is 20% (Figure 3-4), so the strongest beam will be transmitted. In this configuration, the strongest beam needs to be reflected.
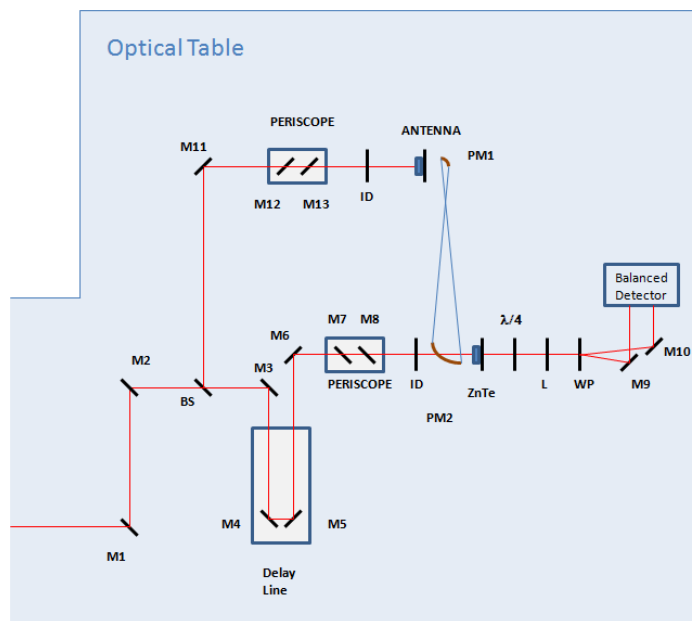
Figure 3-3. Second layout.
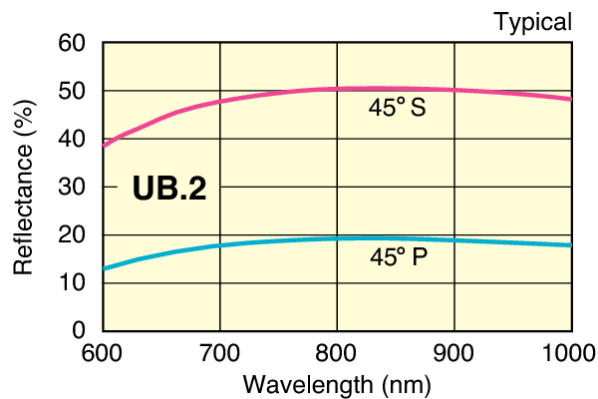
Figure 3-4. Newport 10RQ00UB.2 ultrafast laser beamsplitter reflectance curves [52].

65

3.2.1 Practical setup

The relative position of the beamsplitter had to be changed in order to steer the strongest beam towards the emitter antenna. One option could have been to add a mirror just after M2 in Figure 3-3; however, it was preferred to avoid adding components which can make the alignment more complex.

In the new setup, mirror M2 was removed, and the two mirror adjustment capabilities are lost. However, further tests showed that there was no appreciable alignment drift form the laser source, so this layout was appropriate. A schematic diagram of the layout is shown in Figure 3-5. The beam transmitted through the beamplitter (which is the strongest) goes to the emitter antenna. The periscopes have been moved and their configuration was changed in order to provide a rotation of beam polarization. In the previous arrangement (Figure 3-3), the periscopes only produce a change in beam height. In the new configuration (Figure 3-5), the periscopes also add a 90 degrees bend, which produce a change in polarization from horizontal to vertical, as depicted in Figure 3-6. The Ti-Sapphire laser produces a horizontally polarized beam, but the photoconductive antenna generates a vertically polarized beam, and the probe pulse must have the same polarization [39]. As an added benefit, mirror count was reduced by two.
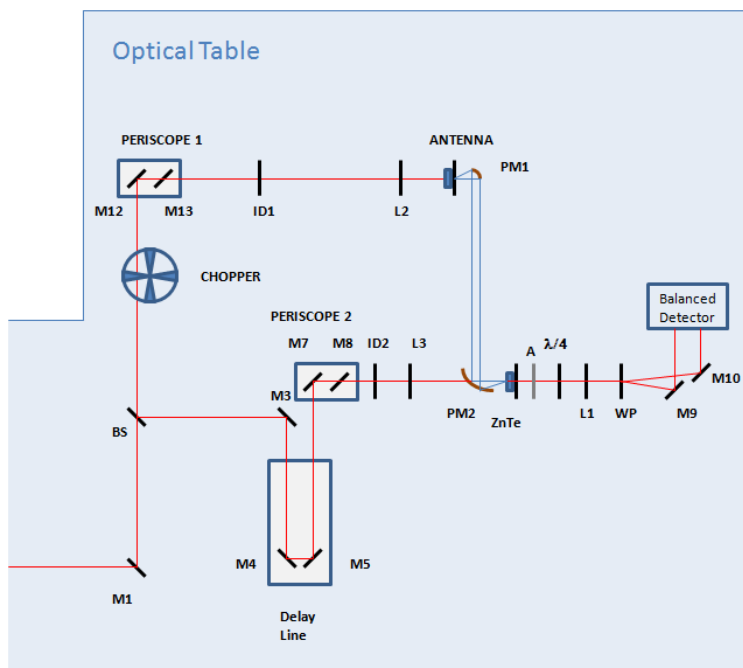
Figure 3-5. Practical layout.
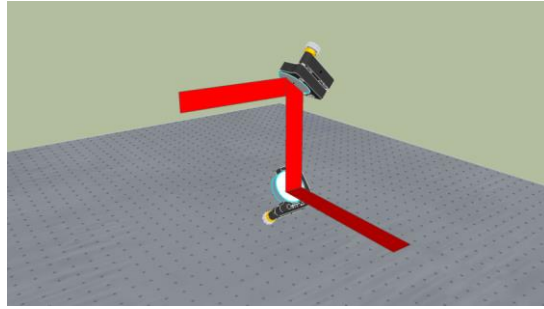
Figure 3-6. Change in polarization by using a periscope.

Three focusing lenses are used: L1 (200 mm focal length) is used to focus the beam over the optical balanced detector, L2 (100 mm focal length) is used to focus the pump beam over the photoconductive antenna and L3 (200 mm focal length) is used to focus the probe beam over the ZnTe crystal. Iris diaphragms ID1 and ID2 are used to block spurious reflections, but can also serve as intensity controls. Figure 3-7 shows two pictures of the THz-TDS system.
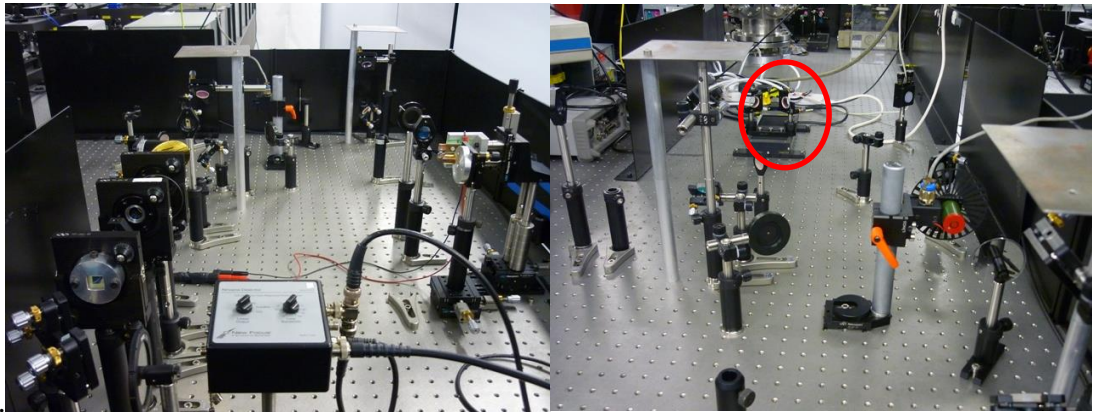
Figure 3-7. Two views of the THz-TDS. Encircled in red is the delay line.

The system setup is completed with several peripheral electronic instruments. Control and data acquisition is performed by a personal computer, with a program written in LabVIEW. The program main tasks are to control the movement of the optical delay-line, to receive the voltage reading from a lock-in amplifier and to save the readings in a text file. The lock-in amplifier (LIA) measures the output of the balanced detector, which is proportional to the THz electrical field. Several signals are monitored with an oscilloscope. Among them, the signal coming out of the balanced detector is used to

adjust the orientation of the quarter wave plate. In this configuration, it is more convenient to have the chopped beam in the pump branch, since the detecting (probe) branch remains constant and it is easier to adjust the quarter wave plate using the oscilloscope.

In Figure 3-9, a simplified flow-chart of the control program is shown. The program will move the optical delay-line one step (usually 20 μm), and then it will wait for a certain amount of time until the lecture in the lock-in amplifier has stabilized (this depends on the operating time-constant of the lock-in amplifier). The time chart will be updated after each sample. The operation will stop after a pre-defined number of steps (for example, 2048), and data will be saved to a disk file. Data is saved in a text format file, compatible with a spreadsheet. The file then can be processed using a MATLAB program (which performs a FFT) in order to generate the spectrum plots. Other functions of the program include: selection of step size, initial point position, number of steps, acquisition delay and emergency stop.
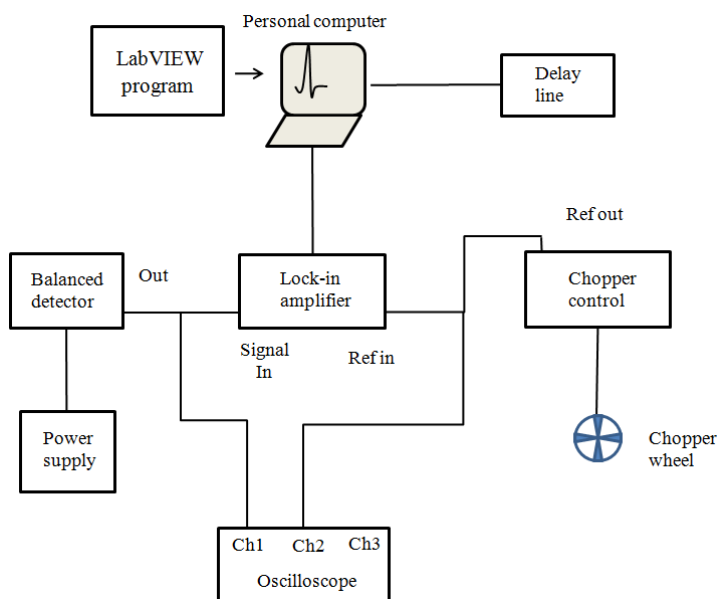
Figure 3-8. Instrument connections for the TDS system.
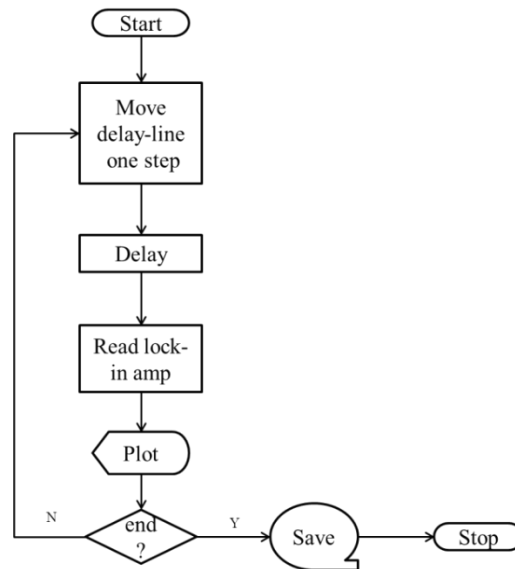
Figure 3-9. Simplified program flow-chart.

3.3   System characterization

This section is devoted to describe some of the main characteristics of the THz TDS system, as well as some operating procedures. After the initial effort of generating and detecting a THz pulse, it was important to evaluate if the systems' performance was up to the standards encountered in the literature.

3.3.1   Terahertz emission verification

The first test performed was a complete sweep of the translation stage in order to find the actual position of the THz pulse. At first, it was not possible to detect any THz pulse; therefore some experiments were performed in order to verify that there was a THz emission.

One alternative method to detect THz radiation is by using a Golay detector. A Golay detector is a "photo-acoustic" device capable of detecting infrared and Terahertz radiation. It is a very sensitive device, so any laser leakage from the Ti-Sapphire would damage the detector. The datasheet of the Golay detector was not available but information from a similar device indicates that the recommended maximum to the detector power is 10 µW

[68]. An infrared (IR) power meter (Fieldmaster, Coherent) was used to measure the leaking laser power at the point where the Golay cell was going to be installed (setup shown in Figure 3-10). Measurements proved that it was safe to use the Golay cell if a Teflon screen is placed before the device.
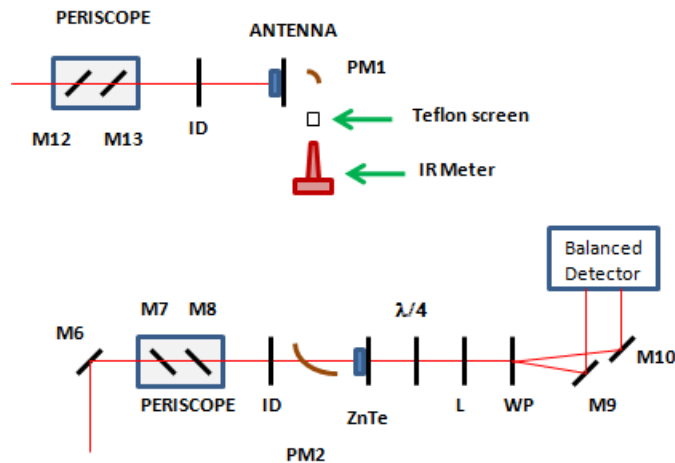
Figure 3-10 .Measuring leaking laser energy.

The IR power meter was replaced with the Golay Cell, and connected to a lock-in amplifier. A chopper wheel was also added to the setup (Figure 3-11).
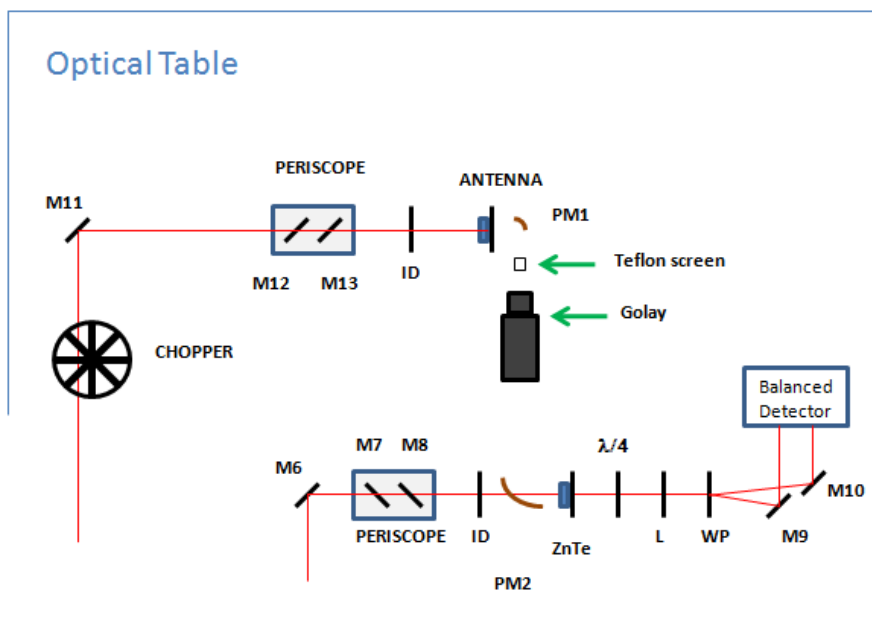
Figure 3-11. Terahertz emission measurement using a Golay cell.

We did a voltage scan of the PCA from 0 V to 160 V and the results are plotted in Figure 3-12. There is a clear linear relation between the bias voltage and the measured radiation, proving that there is THz emission.
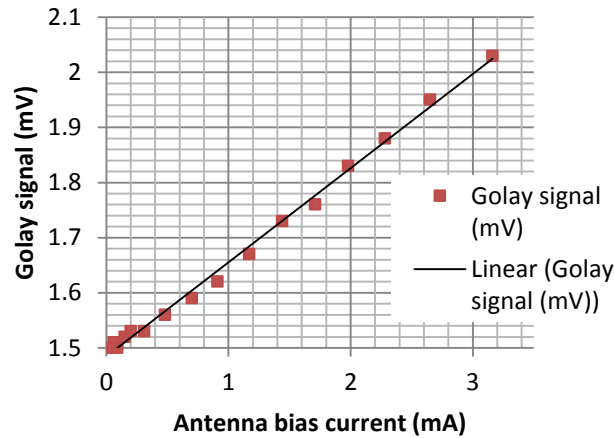
Figure 3-12. Antenna bias current vs. Golay signal plot. TDS tests

The first successful measurements of a THz spike were obtained after minor adjustments to alignment of parabolic mirrors and probe beam focus. An example of the control program windows showing the acquisition of a THz signal is presented in Figure 3-13. The complete pulse waveform is depicted in Figure 3-14. There is a second, smaller, spike at 32 ps which is due to unwanted reflexion of the THz pulse, and it is further explained in section 3.3.2. For this experiment the optical chopper was set to 1.5 kHz, and the lock-in amplifier sensitivity was set to 20 mV with a time-constant of 200 ms. 1024 data points were collected with a size step of 20 µm.
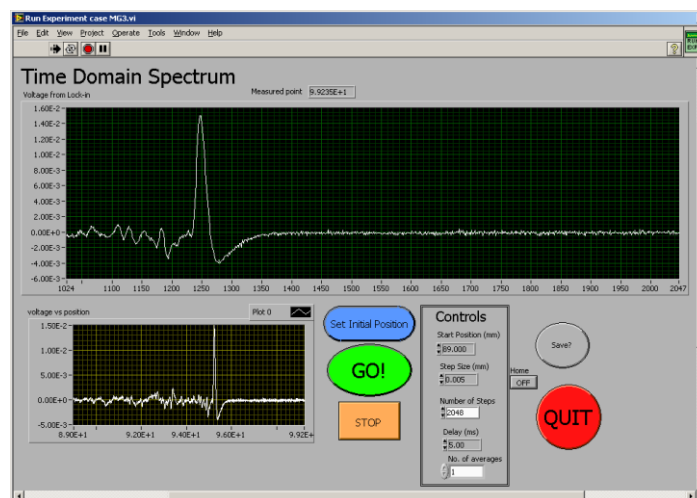
Figure 3-13. Example screen of the LabVIEW acquisition and control program.
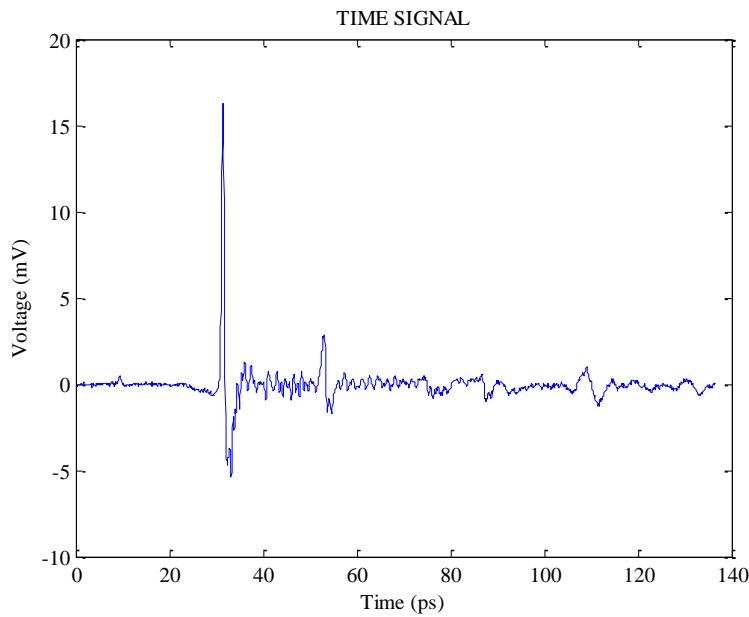
Figure 3-14. THz pulse.

A detailed experiment was carried out to obtain the full-width half-maximum (FWHM) value of the pulse as a representative way of approximating the pulse duration [69]. The shape of the pulse is strongly influenced by the alignment of system components, and the best pulse was found to have a FWHM of 0.3 ps, which is similar to the 0.25 ps reported in [70]. It is important to have a short duration pulse, since this will produce a broader frequency bandwidth.
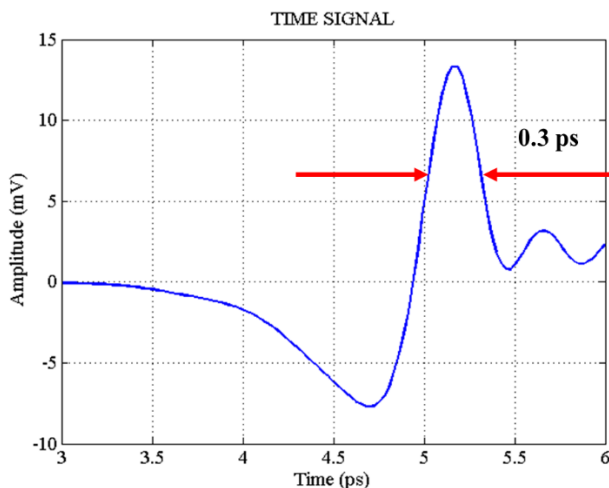
Figure 3-15. FWHM of THz pulse.

Figure 3-16 shows a THz spectrum of an air sample. Spikes at 0.557, 1.097, 1.163 y 1.410 THz and others are caused by water vapor absortion [71] . A dynamic range of 55 dB is

observed, which is to the 50 dB reported in the literature [72, 73], for a system with similar characteristics. Nevertheless, after several changes to the setup, a dynamic range close to 60 dB was attained. This value matches the one reported in the datasheet of the GaAs emitter antenna used [74].
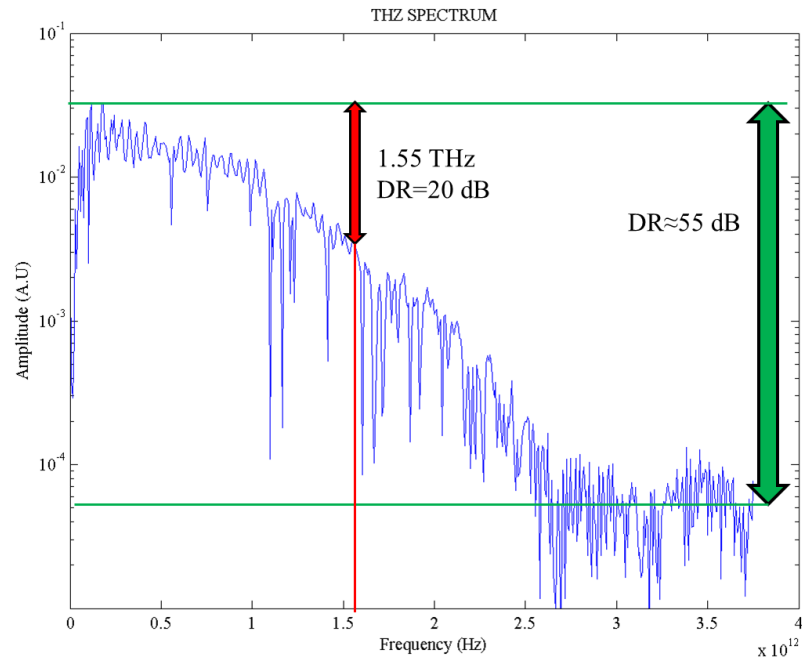
Figure 3-16. THz spectrum of an air sample.

3.3.2   Spurious oscillations

THz spectrum in Figure 3-16 presents an oscillation which appears to have a constant frequency. A more detailed version is presented in Figure 3-17. As an alternative to reduce these oscillations, the use of windowing functions was attempted; however, no improvement was accomplished. Two examples using a Hamming and Blackman windows are shown in Figure 3-18.
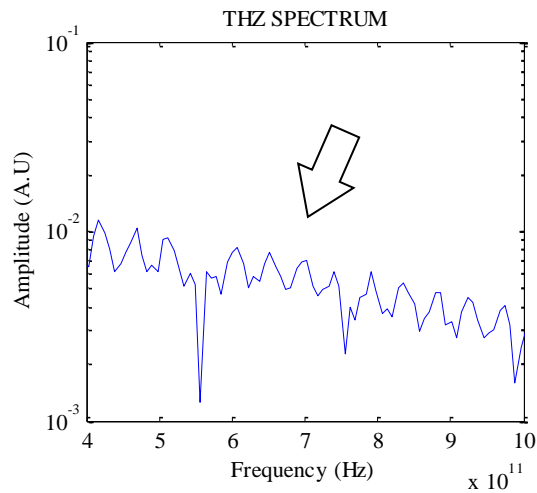
Figure 3-17. Detail of a THz spectrum showing spurious oscillations.
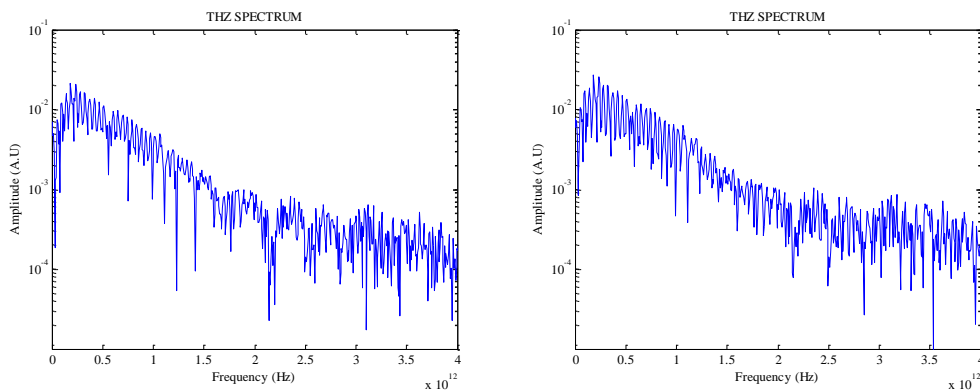
Figure 3-18. THz spectrum with Hamming window (left) and Blackman window (right).

The spurious oscillations are caused by an Etalon, which is the consequence of multiple internal reflexions inside an optical component (see Figure 3-19), and a method for reducing its effects has been presented in [75]. This method is based in convolution, but has limitations in the case of pulse spreading.
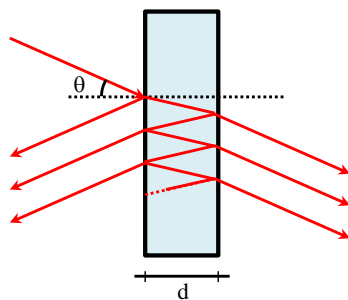
Figure 3-19. An Etalon.

The effects of the Etalon can be seen in the time domain signal of Figure 3-20, in the form of a second spike. The first spike occurs at t_1=31.42 ps, and the second spike at t_2=53.09; giving a difference Δt_{meas}= 21.67 ps. From the THz spectrum (Figure 3-21) the oscillations occur at a $\Delta f \approx 0.044$ THz. Since $\Delta f = \frac{1}{\Delta t}$, the estimated time interval is Δt_{estim}= 22.73 ps, which is similar to Δt_{meas}.

The laser pulse employed has a wavelength λ=800 nm. At this wavelength, GaAs has a refractive index n=3.6834 [76]. The laser pulse speed in the crystal is $v = \frac{c}{n}$, and the thickness of the crystal is given by

$$x = \frac{c \cdot \Delta t}{2n} = 0.8686 \; mm \qquad (3\text{-}1)$$

which is approximately the thickness of the GaAs crystal antenna. Therefore, it can be concluded that the source of the second spike, and the spurious oscillations is an Etalon produced inside the GaAs antenna.
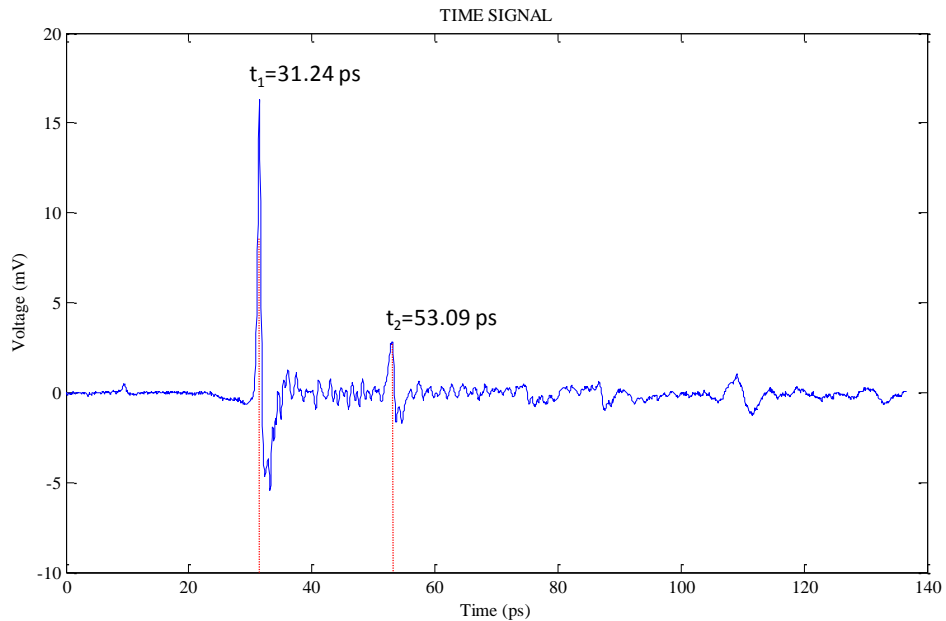
Figure 3-20. Time-domain THz signal.
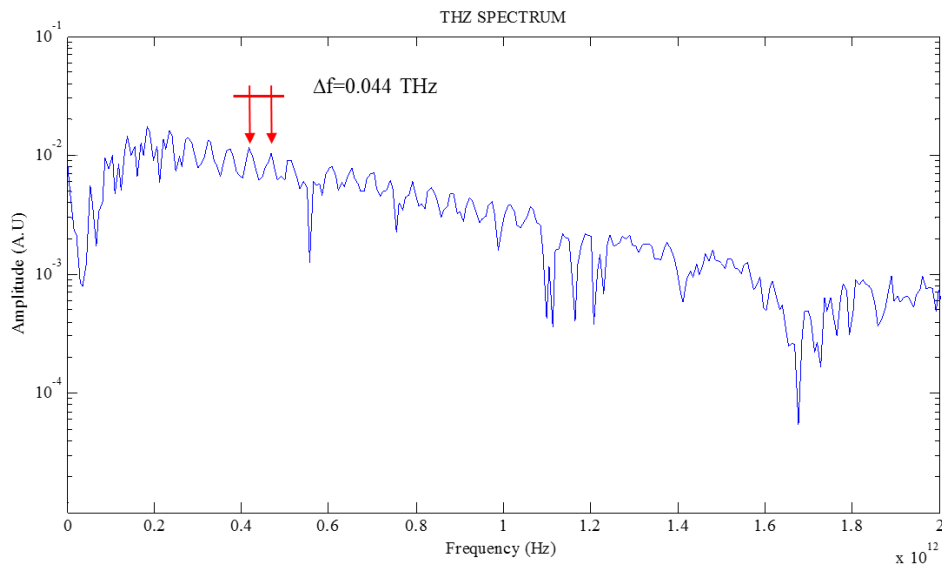
Figure 3-21. THz spectrum of ambient atmosphere.

3.3.3 Method for reducing spurious oscillations using local apodization

In order to improve the characteristics of the spectrum obtained in a THz-TDS system, time-domain signal asymmetrical apodization has been used to minimize spectrum side lobes in [77]. Also, wavelets have been applied to improve the SNR [78]. Since the spurious oscillations found in THz spectra are caused by spike echoes in the time-domain signal, we devised a method for reducing the level of oscillations by applying local apodization to the echo. The objective is to attenuate the echo without completely suppressing it, because the echo carries important information on the absorption lines and a complete suppression affects the detection of such lines. The method follows the next procedure (see Figure 3-22): First the main pulse is detected, , then the first echo is searched after a delay window, in order to avoid interpreting part of the transient response of the main pulse as an echo. A threshold is defined to identify a signal as a valid echo. Once the echo has been found, then a rectangular apodization window is defined over it. Finally, all signal data inside the window is attenuated by a preselected factor. Therefore, the method relies on the definition of four values: delay (the region where no echo is searched for), threshold (the level above a signal is considered a valid echo), window (the time frame where the apodization function will be applied), and attenuation (according to the apodization selected function). The method can be extended to detect several echoes.

76
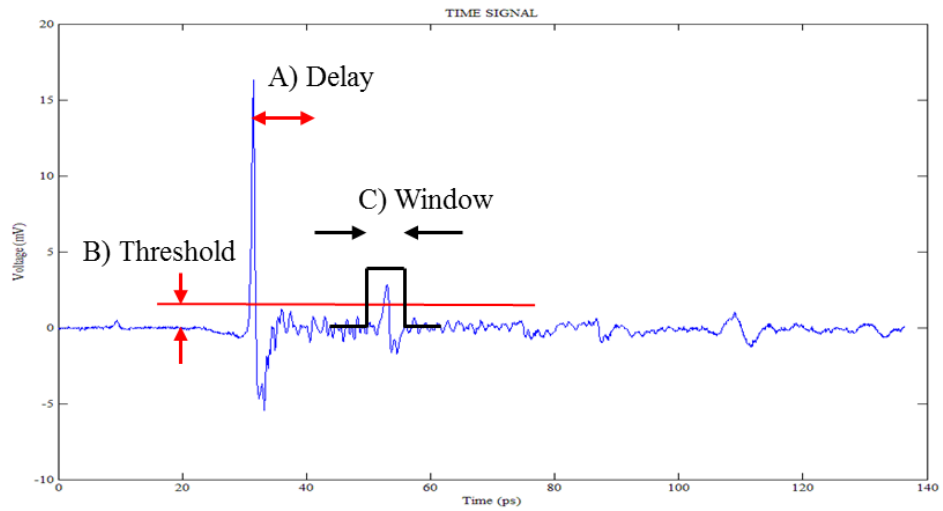
Figure 3-22. Local apodization method for reducing spurious oscillations.

An example of the results, calculated using a MATLAB program, for the THz time-domain signal of Figure 3-23 (signal with two echoes) is given in Figure 3-24. The signal corresponds to a THz pulse transmitted in free space. In this case, the two echoes produce two spurious oscillations which may cancel each other but still are visible in the blue plot of Figure 3-24. The method manages to reduce the oscillations in the spectral response with minimal interference with the water vapour absorption lines. This method could be extended to use other apodization functions such as triangular, hamming, etc.
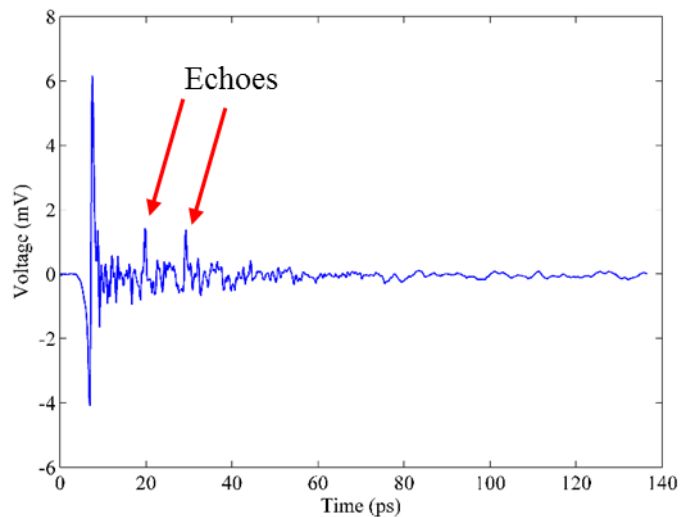
Figure 3-23. THz time-domain signal with two echoes.
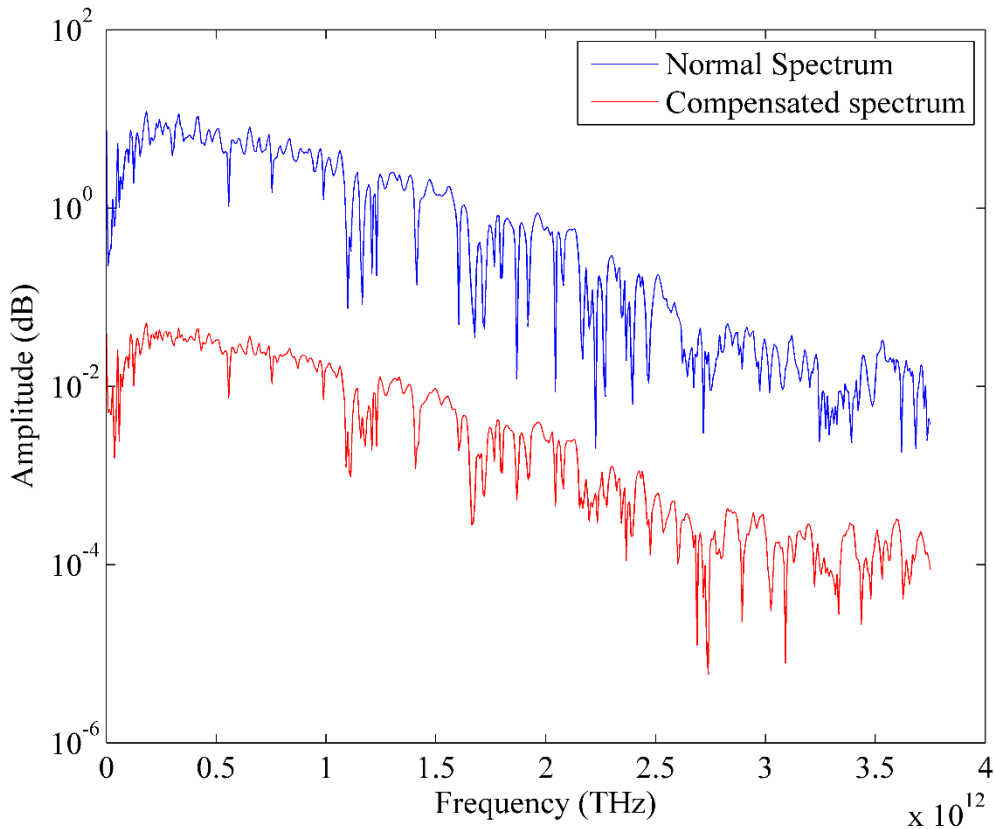
Figure 3-24. Normal signal spectrum and compensated spectrum using local apodization.

3.3.4   Power measurements

It is important to know the amount of optical power that is pumped into the antenna and used as probe beam, as it may help to repeat the installation or to compare performance with other systems. As part of the installation procedures, a map of the optical power was measured and the results are shown in Figure 3-25. Pump beam intensity is 173 mW and probe beam is 7.6 mW, but the latter result is due to the use of iris diaphragm ID4. It can be seen that beam splitting ratio is close to 20:80 as it was expected. Iris diaphragms ID1, ID2 and ID3 produce a large drop in laser power because they are limiting the size of the beam.
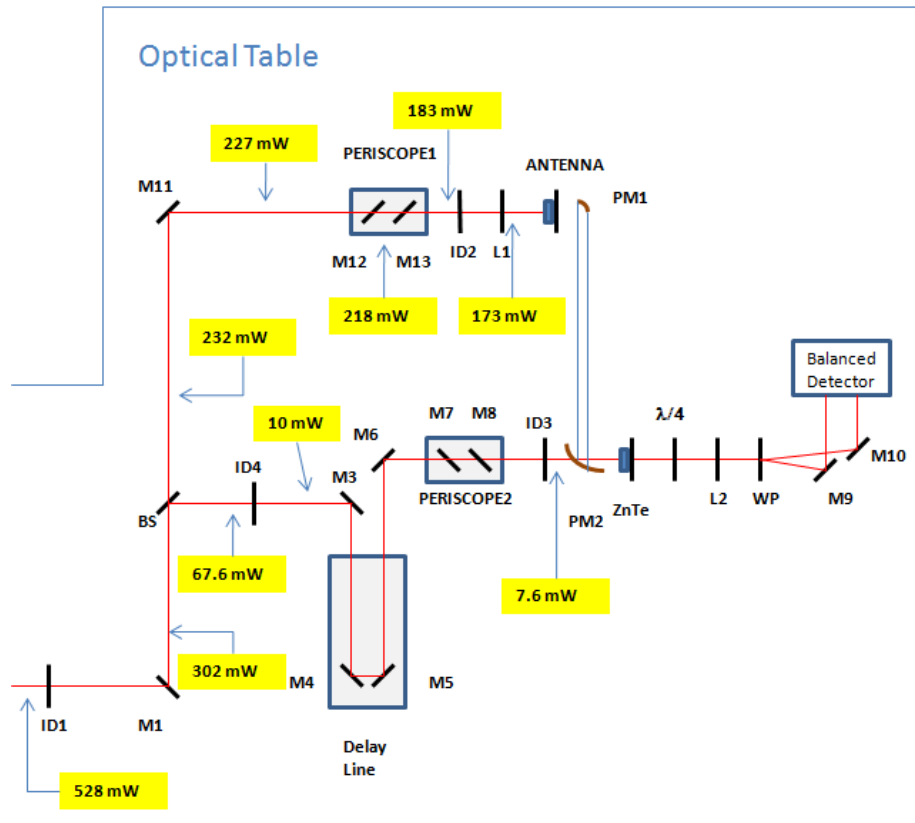
Figure 3-25. Optical power measurements.

3.3.5 Antenna without Si lens

During the development of the project, two PCA were used. The first one that was installed had a Si lens, but it was accidentally removed. This gave us the opportunity to make some tests and compare the operation with and without the Si lens. The performance of the antenna without the Si lens was tested with two different parabolic mirrors (1 inch diameter and 2 inch diameter). Given equal conditions in the rest of the setup, we measure a peak intensity of 8 mV with the 1 inch ϕ mirror and 11 mV with the 2 inch ϕ. Since both mirrors had the same equivalent focal length (EFL=50.8 mm) a fourfold increment in THz collection would be expected, but we do not have a tested model for the radiation pattern of the PCA.
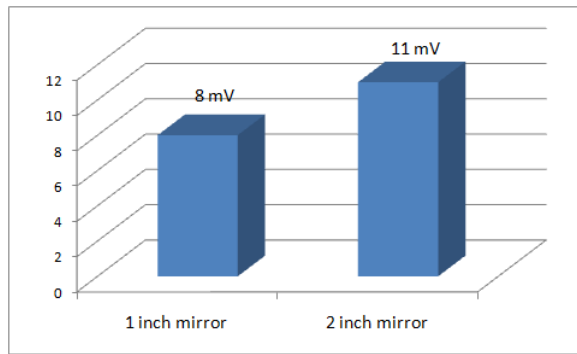
Figure 3-26. Amplitude comparison using 1 inch and 2 inch mirrors.

The Si lens was reinstalled on the PCA but as it has a virtual focal point behind the plane of the PCA, the parabolic mirror had to be placed closer, making impossible to use neither the 1 inch φ nor the 2 inch φ mirrors. A ½ inch parabolic mirror was installed instead.

The datasheet for the PCA was not available; however, according to information from Batop Optoelectronics [79], virtual focal length of the lens is given by

$$L = r(n + 1) \tag{3-2}$$

Where n is the refractive index of GaAs≈3.4, and r is the lens radius (3.5 mm). That gives L= 15.4 mm. Since EFL is 50.8 mm, the antenna must be placed 50.8-15.4= 35.4 mm apart.

 With the new configuration, the maximum peak amplitude obtained is 28 mV against 37 mV without Si lens and with a 1 inch φ mirror. In both cases the maximum amplitude is obtained by leaving the ZnTe attenuator open (ID3). Usually this will saturate the output of the balanced detector, but once that the balance condition is adjusted (by rotating the quarterwave plate), we are able to open the attenuator without the risk of saturating the balanced detector.
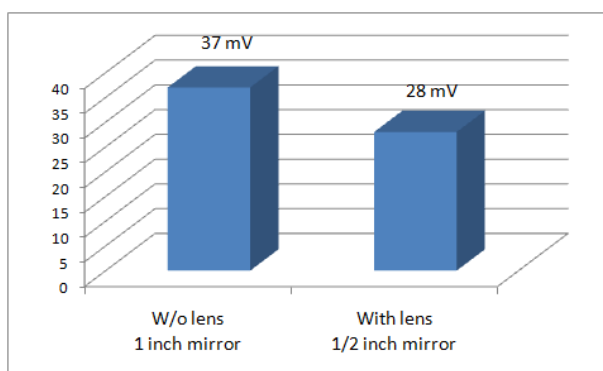
Figure 3-27. Amplitude comparison with and without Si lens.

Results are inconclusive. Since it was not possible to perform the same test for both configurations (with and without lens), it is not possible to say that the Si lens indeed helps to collect more radiation out of the antenna.

3.3.6   ZnTe orientation

For the current setup, pulse detection is optimal with the ZnTe crystal rotated at an angle of 140° (as marked on the mount) and efficiency is quickly reduced as it is moved away from that angle (Table 3-1). Each time that the crystal is rotated, a recalibration procedure have to be performed since the rays coming into the balanced detector become misaligned.

Rotation angle (degrees)	Peak amplitud (mV)	Crystal orientation
85	-0.6 (negative)	▭
135	7	
140	8	◇
145	7	
170	0.2	▯

Table 3-1. Influence of ZnTe crystal orientation in detected amplitude.

3.3.7 Pump beam polarization

The Ti-Sapphire laser produces a beam with horizontal polarization, which becomes vertical polarized after going through two periscopes, one for the pump beam, and the other for the probe beam. The THz radiation generated by the PCA is vertical polarized because that is the orientation of the bias field.

THz generation mechanism involves the transfer of energy from laser photons to electrons in the valence band in the GaAs crystal. It does not seem necessary to have any particular orientation of the pump beam polarization. With the purpose of validating this hypothesis, an experiment was set up to change pump beam polarization. A halfwave plate is placed in the pump beam path, as shown in Figure 3-28. The linear polarized pump beam will have its orientation changed by 2θ, where θ is the rotation angle of the waveplate. The waveplate is mounted in a precision rotational mount and the slow axis mark is adjusted to be horizontal.
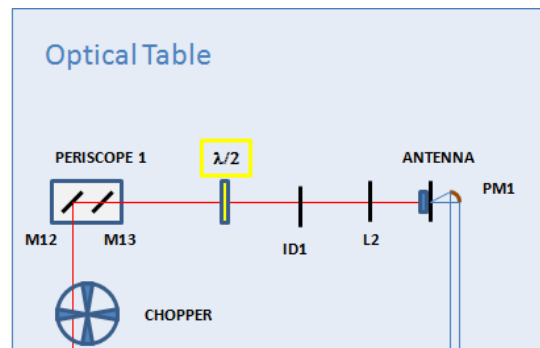
Figure 3-28. Placement of a halfwave plate in the pump beam path.

A complete 360° scan was done with 30° increment steps and the THz peak amplitude was measured. The results are plotted in Figure 3-29, where it can be seen that there is almost no variation in the peak magnitude. The minor variations can be caused by a slight misalignment of the waveplate.

A second test was made with 22.5^o steps, in order to produce a rotation of exactly 90° and the results are summarised in Table 3-2. From these results, it can be concluded that there

is no variation in applying a vertical or horizontal polarized beam to the PCA, therefore our hypothesis is correct.
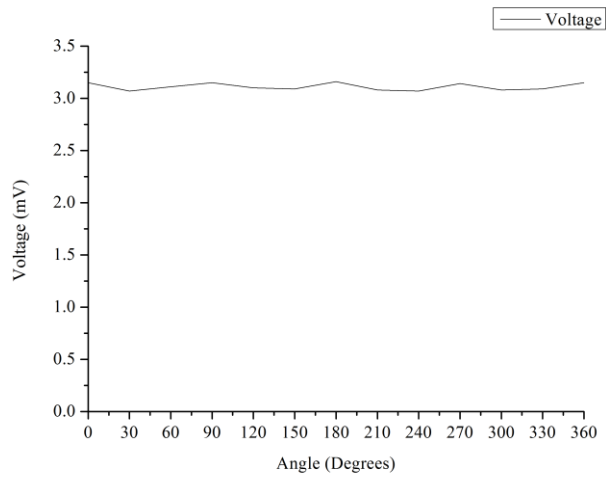
Figure 3-29. Halfwave plate rotation angle vs. peak voltage plot.

Halfwave plate Slow axis Rotation angle (degrees)	Peak amplitude (mV)	Resulting Polarization Change (degrees)
0	7.2	0
22.5	7.3	45
45	7.1	90
67.5	7.4	135
90	7.4	180

Table 3-2. Halfwave plate rotation angle and resulting polarization change.

3.3.8   Changing the probe lens position

Probe beam focusing lens L3 is at 235 mm from the ZnTe crystal (lens EFL is 200 mm). This distance was varied to see its influence in the peak amplitude detected. However, the system is very sensitive and is difficult to realign. Since the probe beam must go through a hole drilled in the parabolic mirror, there is little tolerance to misalignments. Results are depicted in Figure 3-30 and show an increase in amplitude as the lens is moved away from the ZnTe crystal. This may suggest that beam focus on the ZnTe crystal is improved as the L3 lens is moved away.
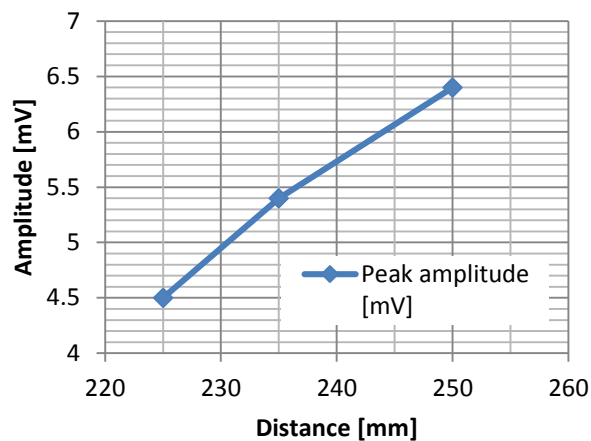
Figure 3-30. Amplitude variation vs. probe focusing lens position.

3.4 System modifications for spectroscopy tests

After doing the first tests of the systems, it was decided to modify the system in order to make it more suitable for spectroscopy tests. This modifications included: an improvement in the transient response of the delay line, adding THz optics for focusing the THz beam, and adding a chamber for performing test under a low water vapour content atmosphere.

3.4.1 Transient response of the optical delay line

Reconstruction of the THz pulse waveform requires a set of successive displacements of the optical delay line, as it was explained in Chapter 2. Each movement of the mechanism requires a sudden acceleration and breaking of the translation table which generates an oscillatory transient response. This affects the optical signal and it can be seen clearly with an oscilloscope (see Figure 3-31A). It is possible to introduce a delay in the data acquisition routine in order to avoid the transient; however this will add between 100 ms and 200 ms to each step, this is up to 3.3 minutes for a test that already is 10 minutes long (@ 1024 steps scan). A better approach would be to reduce the size of the oscillations. The transient oscillations are amplified by path length in the setup. In order to reduce the

amplitude of the transient, the delay line was moved closer to the ZnTe detector crystal. This reduced the path length between the delay line and the optical photodetector. The mirror mounts of the delay line were also changed (see Figure 3-32), as it was found that shorter and more robust ones would be a better option [80]. The improved transient response is shown in Figure 3-31B. The amplitude of the transient was reduced from 400 mV_{p-p} to 30 mV_{p-p}.
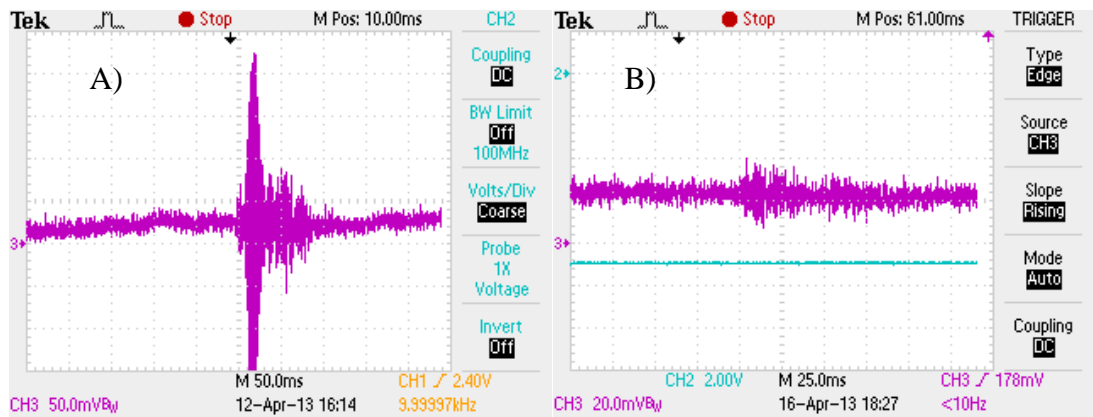
Figure 3-31. Balanced detector output showing the transient response to each step of the delay line. A) Before changes. 400 mV_{p-p} (50 mV/div vertical scale). B) After improvements. 30 mV_{p-p} (20 mV/div vertical scale).
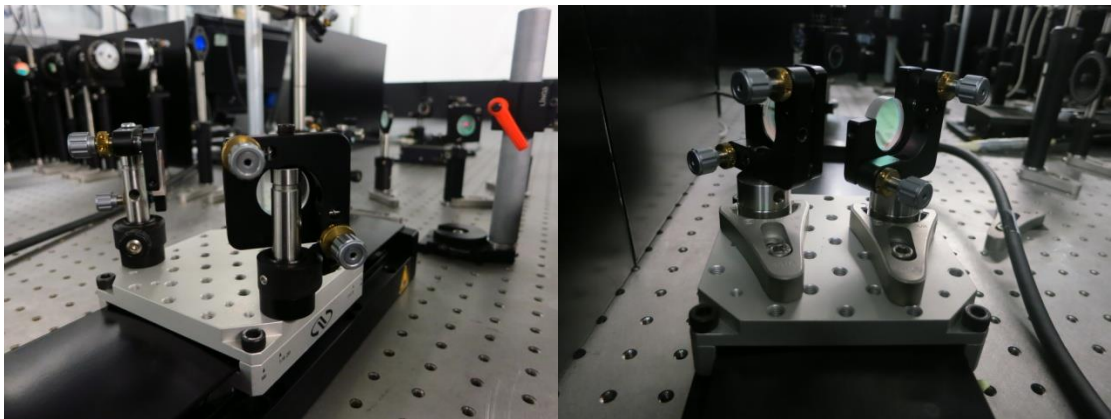
Figure 3-32. Delay line mirror mounts. Left: previous setup. Right: new setup.

3.4.2 THz beam focusing

Some examples of THz spectroscopy systems use two parabolic mirrors, and this is useful for applying a collimated beam to the sample [39, 69]. If a focused beam is required, a setup made with four parabolic mirrors or with added THz lenses is needed [16, 24, 81, 82]. The latter is also suitable for THz imaging and tomography [3, 83, 84]. A focused beam has the advantage of concentrating the beam power in a small spot, making it easier to penetrate the sample. However, when measuring the transmission properties of materials, it has been reported that a highly convergent beam can produce an overestimation in refractive index values [85].
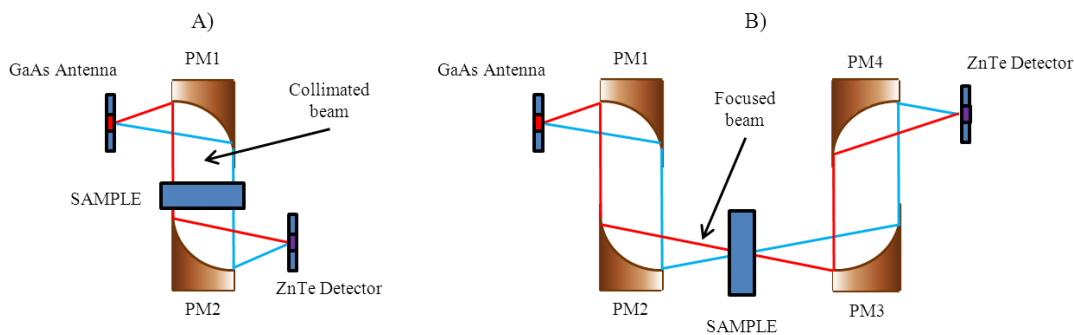
Figure 3-33. THz spectroscopy setups. A) Collimated beam. B) Focused beam.

The new setup is shown in Figure 3-34. THz optics is now formed by four parabolic mirrors PM1-PM4. The THz beam between parabolic mirrors PM1 and PM2, and between PM3 and PM4 is collimated, whereas the beam between PM2 and PM3 is focused. Al mirrors have a 2 in. diameter. The GaAs antenna does not have a Si lens attached, therefore a relatively large parabolic mirror is needed in order to collect as much THz radiation as possible. Tests with a 3 in diameter parabolic mirror didn't show any improvement and its large size and weight caused problems during alignment. The best option found was to use a 2 inches mirror, and the rest of the THz path had to be installed in a compatible way. Focusing mirrors PM2 and PM3 have an equivalent focal length (EFL) of 177 mm, and that was the longest available. This was selected in order to have enough room to put a burner chamber, in case that it were needed. In the end, the decision proved useful as there is enough space to make different types of tests, including tomography.
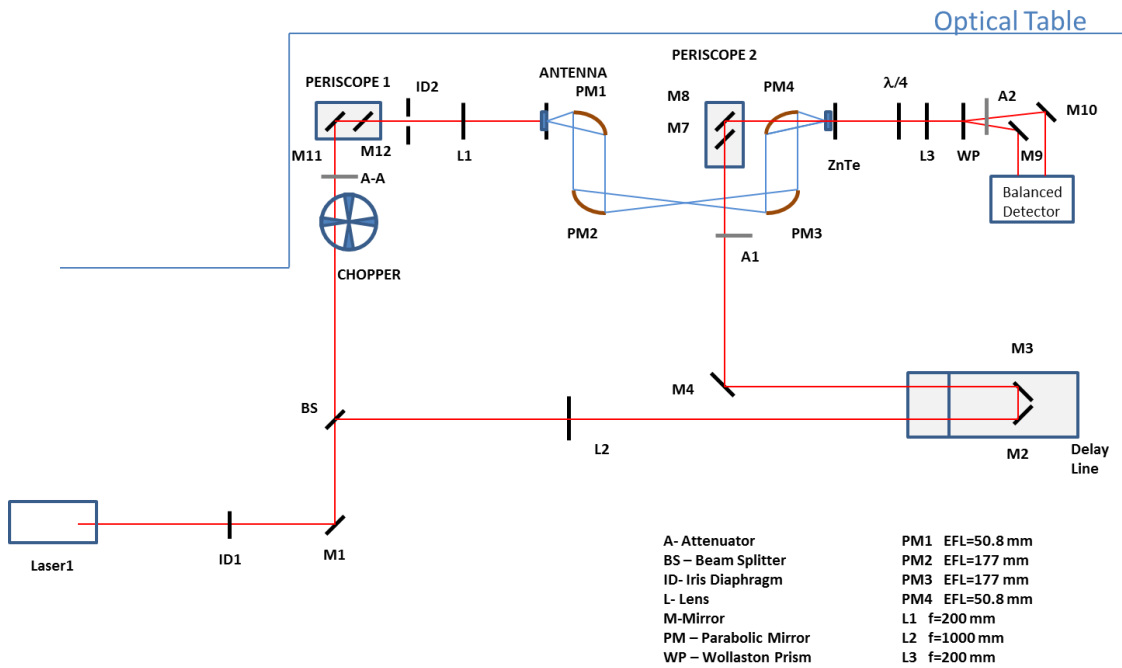
Figure 3-34. Modified layout, showing two added parabolic mirrors, and relocation of the delay line.

For testing the THz beam spot size, an iris diaphragm was placed at the centre between parabolic mirror PM2 and PM3. Distance between these two mirrors is twice their EFL, meaning that the focus point is expected to be just in the middle. The iris was closed at different apertures and the size of the THz spike was registered. As it can be seen in Figure 3-35, the pulse is able to pass without attenuation through an aperture of 5 mm, with a 4 mm aperture producing just a 10% attenuation. It was not possible to get a smaller spot, despite working several days trying to improve the alignment of the parabolic mirrors. Nevertheless, the obtained spot is adequate for spectroscopy tests.
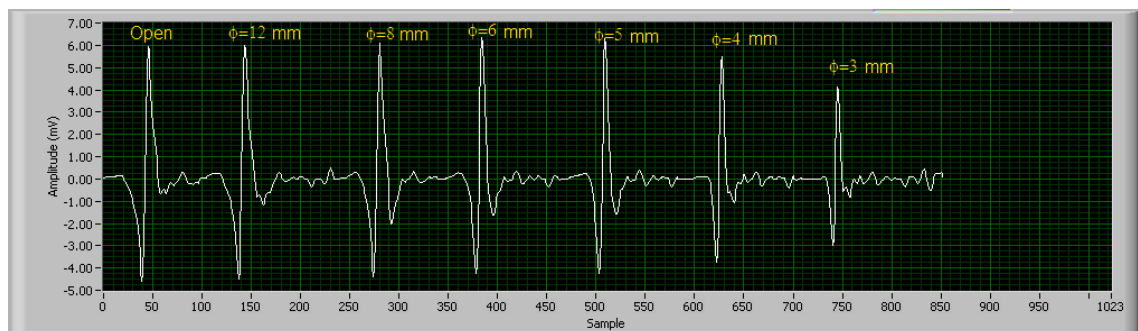
Figure 3-35. THz spike for different apertures of an iris diaphragm (diameter in mm).

One option to reduce the spot size would be to use parabolic mirrors with a shorter EFL. Currently, mirrors PM2 and PM3 have an EFL=17.7 mm. The spot size can be estimated by

$$y_2 = \theta_1 f \qquad\qquad (3\text{-}3)$$

Where θ_1 the divergence of the incoming beam, and f is the focal length (see Figure 3-36).
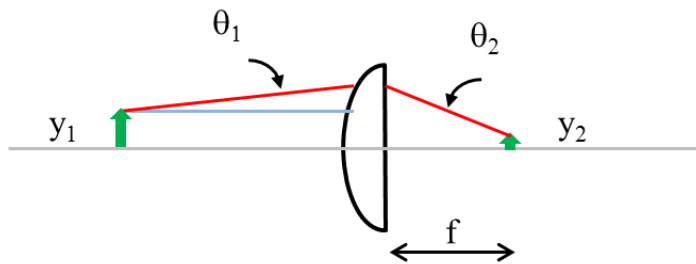
Figure 3-36. Focusing a collimated beam.

Therefore, by using a shorter focal length, magnitude of y_2 will be smaller. For example, in [86], a 4 mm THz spot size is reported, but authors used a pair of 50 mm EFL lenses. A knife edge test was performed later, and it is reported in chapter 5.

3.4.3   Low water vapour content chamber

In order to reduce the interference caused by water vapour absorption during a THz spectroscopy test, a Perspex box was built. The box is purged with a dry air supply. The laboratory at the Photon Science Institute has a compressed air supply installation. From it, a drying cylinder filled with calcium sulphate [87] was used to produce dry air. Air flow is controlled by a pressure regulator and monitored with an electronic flowmeter. The Perspex box covers the complete THz path, and is provided with holes to allow the laser beams and electrical connections to go through (see Figure 3-37).
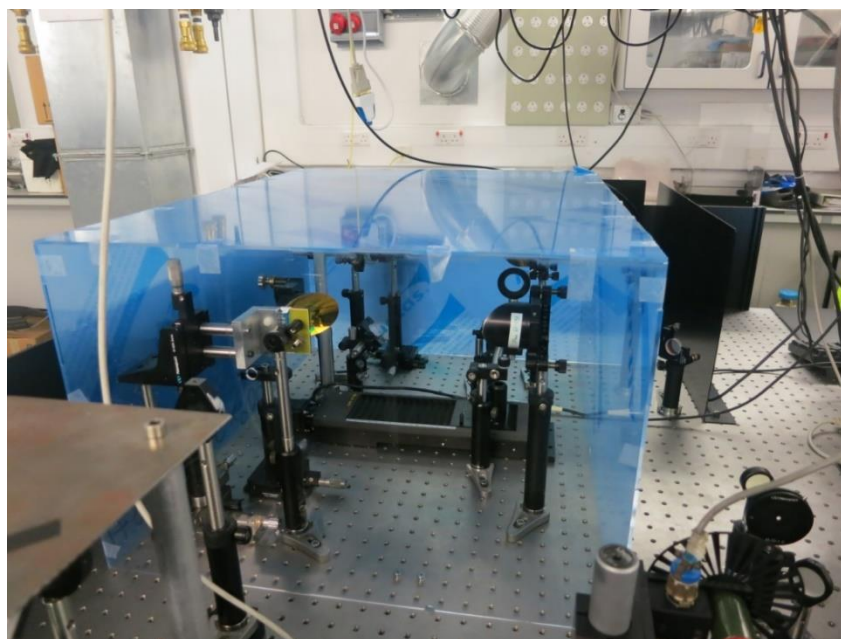
Figure 3-37. The Perspex box used to contain a volume with low water vapour content.

After a purging time of approximately 3 hrs, the system achieves a test atmosphere with a relative humidity RH≈10% (see Figure 3-38). The dry air supply was operated at a flow rate of 3L/min which agrees with the operating specifications of the drying cylinder (recommended flow rate is up to 200 litres per hour for maximum efficiency). An example spectrum test is shown in Figure 3-39. Since the atmosphere inside the chamber is not completely dry, some smaller absorption lines are still present.
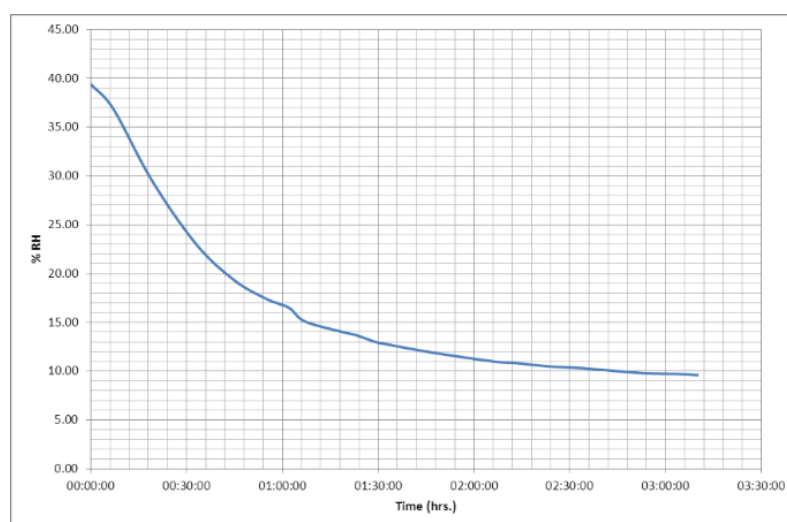
Figure 3-38. Relative humidity in the test chamber vs. purging time.
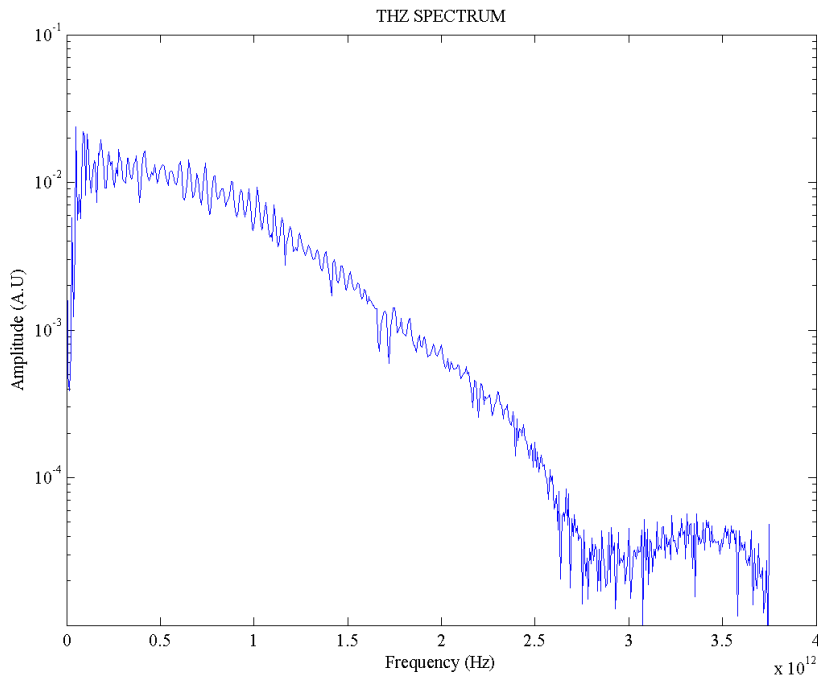
Figure 3-39. THz spectrum of air with RH=9.8% (Accuracy= ±3.5 %).

3.5 Signal-to-Noise analysis

Signal-to-noise ratio (SNR) is one of the most useful parameters for comparing instrument performance. SNR is commonly specified in THz literature but it is not always clear how the authors have measure it. A group at the National Physical Laboratory (UK) has been working in metrology issues regarding THz systems and a method for determining the SNR has been proposed [11]. The method estimates the SNR according to the following expression

$$SNR = \frac{mean\ magnitude\ of\ amplitude}{standard\ deviation\ of\ amplitude} \qquad (3\text{-}4)$$

The THz time-domain signal can be viewed as a random signal. Instead of calculating the mean magnitude of one scan, several scans are required and then an average is calculated for each scan position. The same procedure is used to calculate the standard deviation. The result is a graph where the mean (or the standard deviation) is a function of time. The system reported in [11] shows a SNR fluctuating between 0 dB and 150 dB (Figure 3-40),

90

but with a visual average of around 30 dB. Our system presents SNR excursions between 0 and 100 dB, and a visual average of around 60 dB (Figure 3-41). Therefore, it can be concluded that noise levels in our setup are similar or better to those reported in [11]. This procedure is supported by random data analysis literature [88], however is time consuming for a typical THz TDS system, and will give different values for each time sample (or frequency bin if applied to the spectrum signal), which may be difficult to interpret. Perhaps this is the reason why SNR is usually approximated by an alternative definition, and usually taken as the ratio between the maximum measured value to the noise floor (widely used with frequency responses).
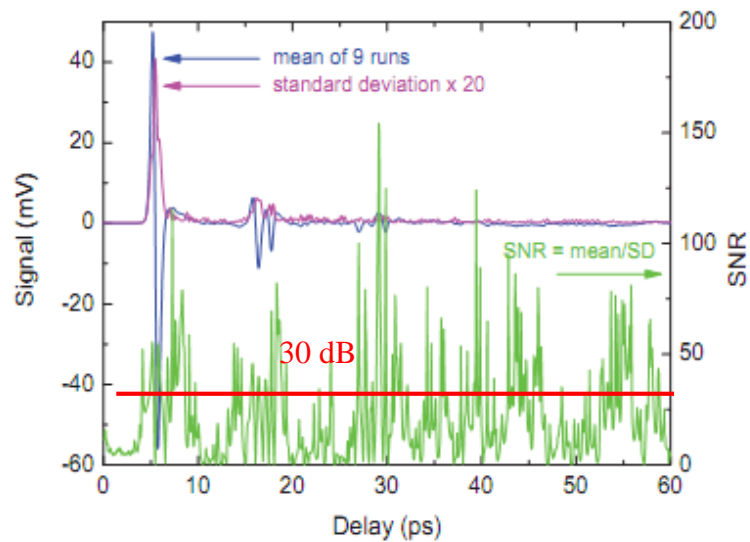
Figure 3-40. SNR of a THz-TDS as reported in [11].
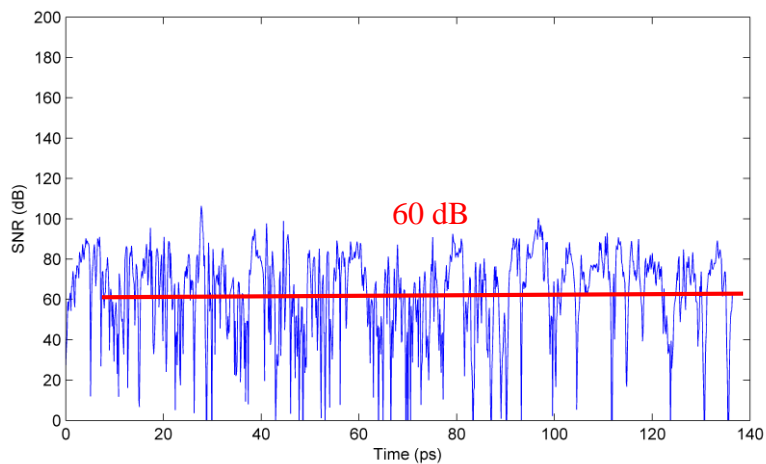
Figure 3-41. SNR of our THz-TDS system analysed according to equation (3-4).

3.6 Fast lock-in amplifier

The lock-in amplifier is a key element in many optical systems and this is also true for a THz TDS system. Its double function of demodulating a signal and filtering out the noise makes it very important. However, its operation introduces the most important bottleneck to the signal processing train. Its integration time, usually in the 100's of milliseconds for a THz system, produces more delay than the transition response of the mechanical delay line. Therefore, designing a lock-in amplifier capable of reducing integration time without sacrificing SNR performance was appealing.

The function of the low-pass filter in a lock-in amplifier is to eliminate the high frequency components produced during the synchronous demodulation, keeping only the DC component, which carries the information. An option to do that filtering is to use a simple linear averager, which can be modelled by

$$u = \frac{1}{T} \int_0^T v(t) dt \tag{3-5}$$

This ideal averager is considered an optimum solution for noise reduction problems in electronic instrumentation [89], since it minimizes noise equivalent bandwidth . The ideal averaging filter is difficult to approximate with analogue components due to DC errors, voltage drifting, and capacitance non-idealities such as leakage current and dielectric absorption [89, 90], but it is easy to implement with digital electronics.

In the digital domain, an ideal averager can be implemented by the following expression (rectangular approximation):

$$y_{avg} = \frac{1}{N} \sum_{n=0}^{N-1} x(n) \tag{3-6}$$

How good the approximation is will be determined by the dynamics of the signal and the sampling time used. A more detailed expression for the discrete averaging is

$$y_{avg} = \frac{1}{N \cdot \Delta t} \sum_{n=0}^{N-1} x(n) \cdot \Delta t \qquad (3\text{-}7)$$

where Δt is the sampling time. The product $x(n) \cdot \Delta t$ represents the area of a rectangle, as depicted in Figure 3-42. Therefore a better approximation will be produced if sampling time is reduced. Equation (3-6) can be rewritten as

$$y_{avg}(k) = \frac{1}{k+1} \sum_{i=0}^{k} x(i) \qquad (3\text{-}8)$$

which is also known as *cumulative averager* [91].
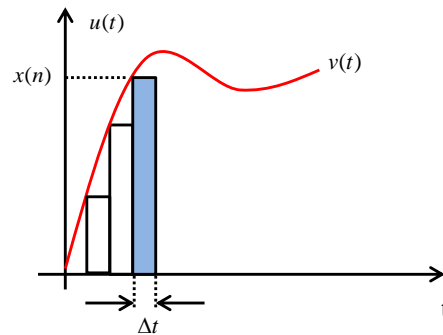
Figure 3-42. Discrete approximation of continuous integration.

An ideal averager based on (3-7) can be used as a filter in a lock-in amplifier as shown in Figure 3-43. Its operation was simulated using a sinusoidal input signal with added white noise (see Figure 3-44).
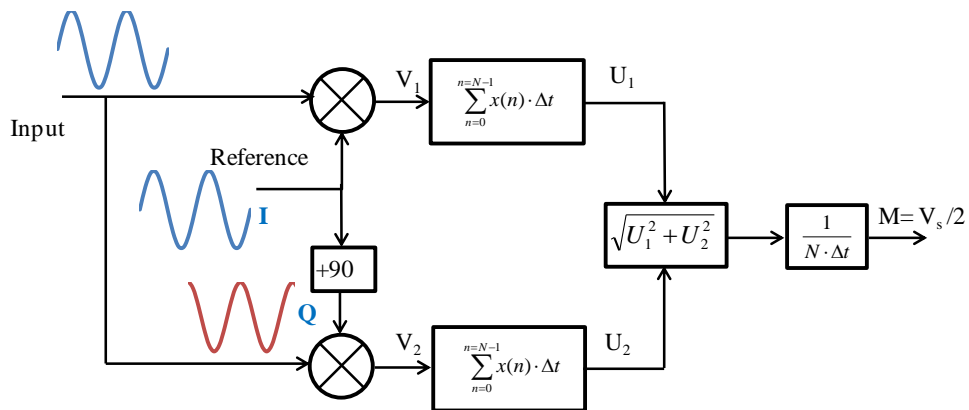
Figure 3-43. Block diagram of a lock-in amplifier indicating the influence of sampling time Δt.
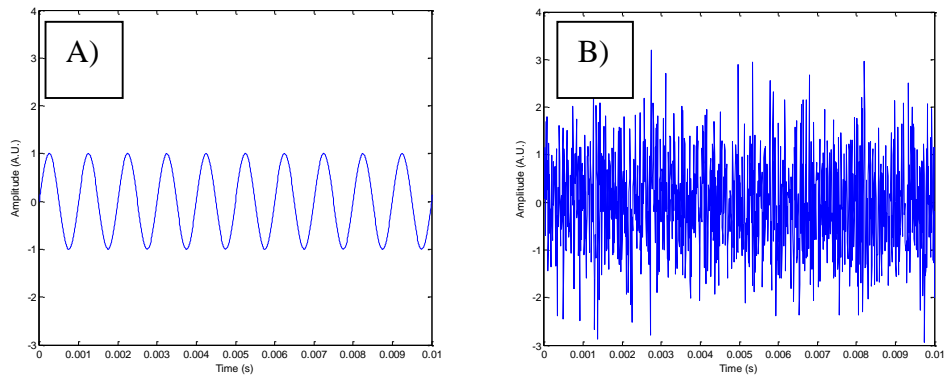
Figure 3-44. A) Input signal. B) Input signal with added noise.

A comparison of the operation of the lock-in amplifier using a first order low-pass filter (LPF, τ= 500 ms) vs. an ideal averager is shown in Figure 3-45. The modified lock-in output appears to be faster and with less noise content that the LPF lock-in. Due to its fast rise time, it was named "fast lock-in amplifier".
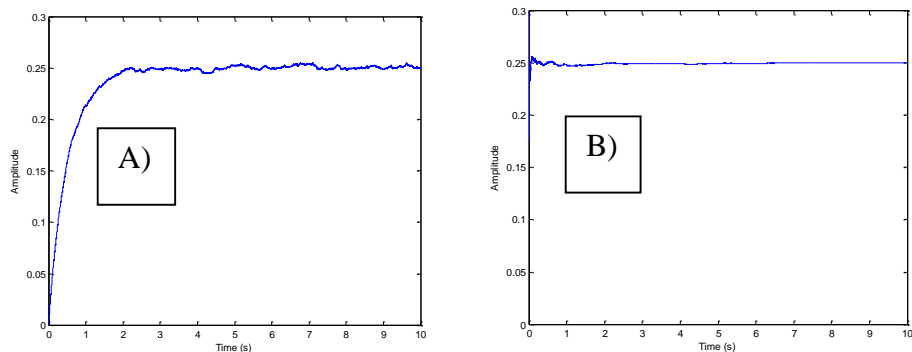
Figure 3-45. A) Lock-in output using a first order LPF (τ=500 ms). B) Output of ideal integrator lock-in amplifier.

Response time of the LPF can be improved by selecting a smaller time constant, for example τ= 50 ms. The rising time is better but at the expense of increasing the noise (see Figure 3-46).
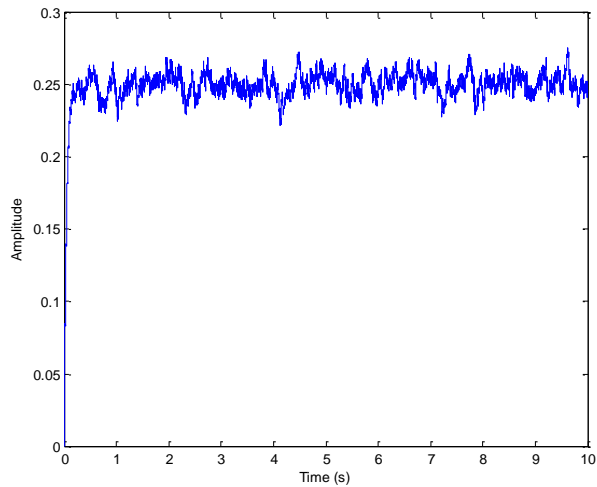
Figure 3-46. Dual phase lock-in with reduced time constant.

Operation of the ideal averager was simulated using the Simulink block diagram shown Figure 3-47. As a noise source, a random number generator is used. *Sine Wave 1* and *Sine Wave 2* are reference signals with a phase difference of 90º and the same operating frequency as *Sine Wave* (the input signal). A constant has been introduced in the division for avoiding a division by zero.
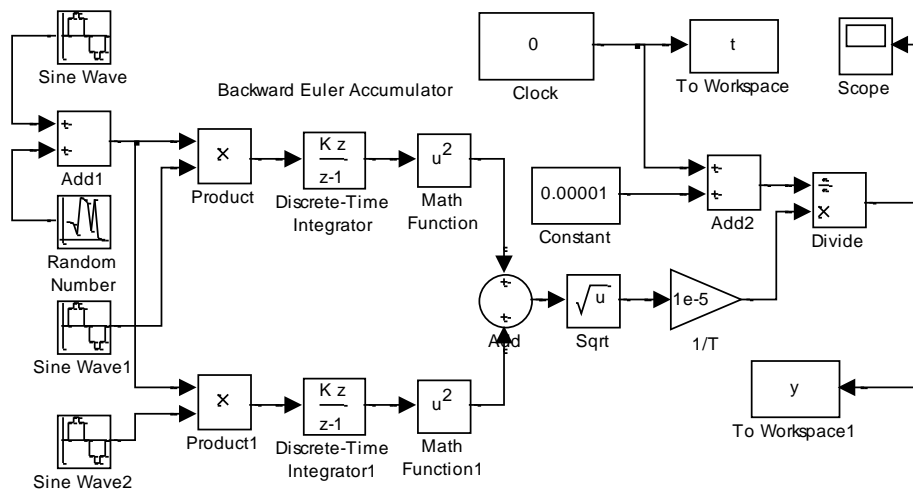
Figure 3-47. Simulink diagram of a discrete implementation of a lock-in amplifier.

A very common filter used in digital signal processing is the linear moving average [92], which is a very useful noise removing strategy because is simple, fast and always stable [93, 94] . A linear moving average can be expressed by

$$y_{avg}(k) = \frac{1}{N} \sum_{i=k-N+1}^{k} x(i) \qquad (3-9)$$

which is very similar to expression (3-8).

In Figure 3-48, a comparison between a lock-in amplifier with a linear moving average filter and a cumulative average is shown. Noise levels are similar for these two implementations as it can be seen in the detailed plot of Figure 3-48; nevertheless, in the case of the cumulative averager, noise keeps reducing as time increments.

The linear averager, the first order LPF and all low-pass filter implementations perform an integration to some extent. This integration will need some time to reach a result, and time depends on the number of taps and sampling time in a linear moving averager or on the time-constant τ in the case of a low-pass filter. For example, with a 50 000 taps linear averager, 50 000 samples are needed before getting a useful result, and in the case of the first-order LPF, response will stabilize after 5τ. On the contrary, the cumulative averager produces an output for each new sample; that is, it delivers an accurate average from the first couple of samples. With the use of a cumulative averager, the noise level at the beginning of the process is high, but decreases as the number of data points (n) increases, giving a noise improvement of $\sqrt{n}$ [95].
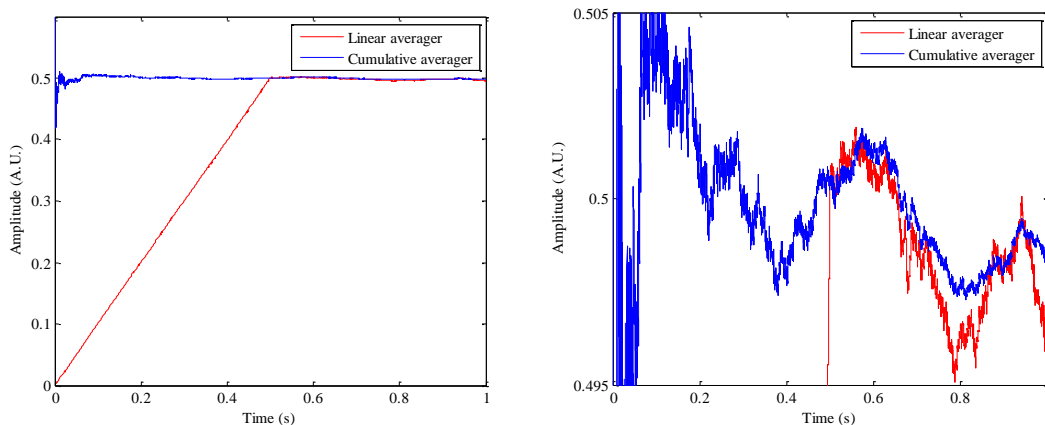
Figure 3-48. Time-response comparison between two lock-in amplifiers. A linear average vs. cumulative average filtering. Right: detail.

3.6.1 Limitations of the implementation

The cumulative averager lock-in amplifier was further tested using a DC signal with a step change at t=1 s, and the results are shown in Figure 3-49. After the step change, the output does not converge as fast as at the beginning of the simulation. This is due to the fact that the integrator has accumulated too many samples; it keeps 'remembering' all previous data. This effect will be worsened as more samples are taken, and it may be a problem unless some sort of resetting is added to the system. This does not represent a problem for a THz-TDS system since the lock-in amplifier filter can be reset after each step of the opto-mechanical delay line.
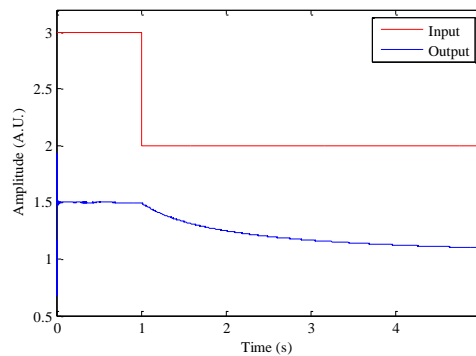
Figure 3-49. Lock-in amplifier response after an input step change at $t = 1$ s.

This problem doesn't occur with other filtering options which have a mechanism for 'forgetting' previous data. An example is given in Figure 3-50, where the responses for a first order LPF and a 50 000 tap moving average configurations are plotted (step change at t=2.5). It can be seen that these filters are capable of following the input after some transient. In fact, it could be easily shown that a first order LPF lock-in amplifier stabilizes $\Delta t = 5\tau$ after the transition, and a FIR (moving averager) after a time $\Delta t =$ (number of taps)·F_s, where F_s is the sampling frequency. This means that in this case, both filters have the same settling time.
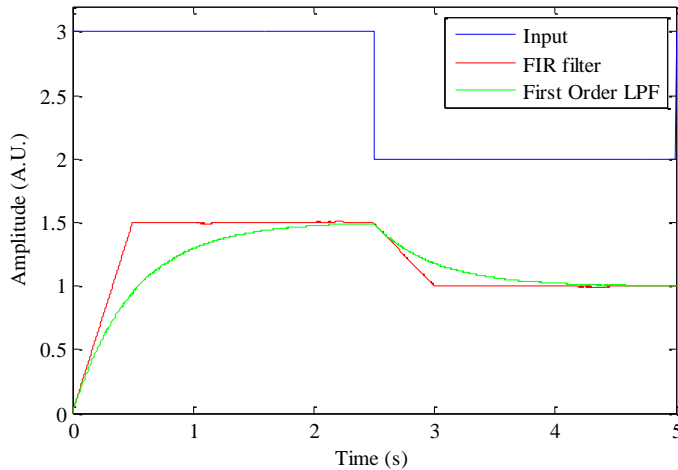
Figure 3-50. Response of a first order LPF and 50 000 taps lock-in amplifier to a step input change.

3.6.2 The box car averager

Another useful noise reduction technique is the box car averager, which performs signal integration over a time window (gated integration), as opposed to integration over the complete waveform that is required for the demodulation operation of a lock-in amplifier. In *static gate mode*, a box car integrator samples a particular point (defined by a delay) on a periodic signal (see Figure 3-51) [96], several of these samples are then averaged.

$$s_{avg} = \frac{s_1 + s_2 + s_3 + \cdots + s_N}{N} \tag{3-10}$$

In *waveform recovery mode*, samples are taken at a different point for each period of the signal (see Figure 3-52). A set of samples taken at the same relative delay are averaged in order to reconstruct that particular point on the waveform. This procedure, however, is time inefficient [96] and sensitive to low frequency drift caused by flicker noise, though this could be removed by using baseline resetting [97]. An interesting combination of gated integration with a lock-in amplifier with improved SNR is presented in [98].
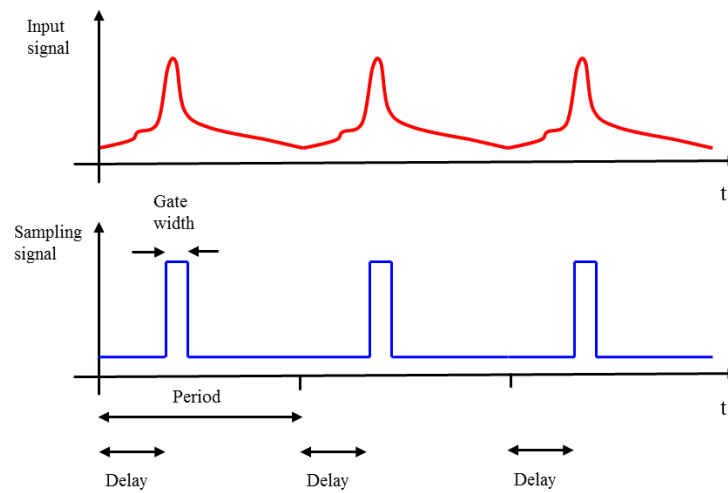
Figure 3-51. Box car averager operating in static mode.
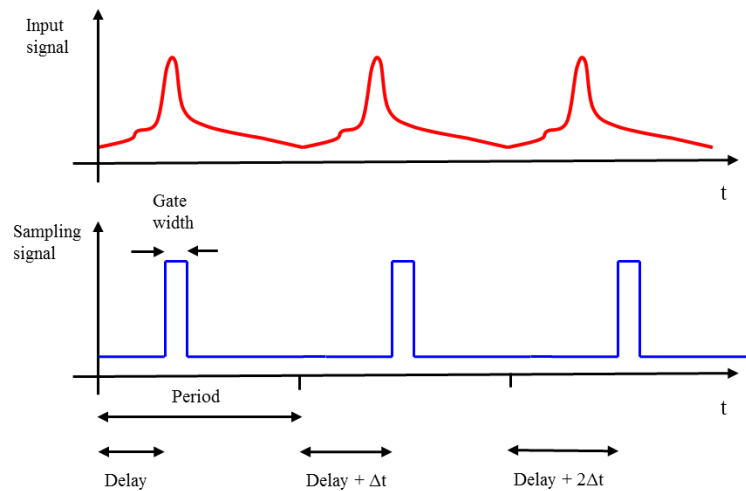
Figure 3-52. Box car averager operating in waveform recovery mode.

3.6.3   Performance comparison. The equivalent noise bandwidth.

The equivalent noise bandwidth (ENBW) is a figure of merit intended to measure the amount of noise that a filter is passing. It can be used to provide a comparison tool for filters used in a lock-in amplifier. If two filters have the same ENBW, then the one with the faster settling time can be selected.

The equivalent noise bandwidth (ENBW) is defined as the bandwidth of an ideal rectangular filter which passes the same amount of white noise power as the filter being characterized [99].
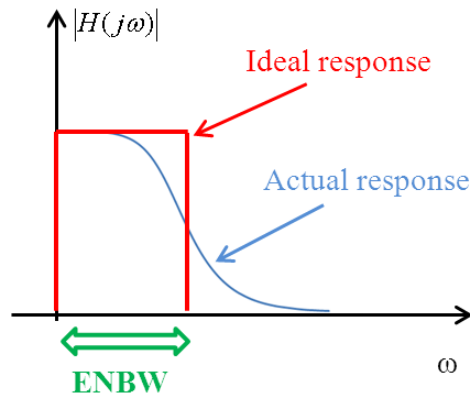
Figure 3-53. Equivalent noise figure of a filter.

For an analogue filter, the ENBW (in Hz) can be defined as [89]

$$\text{ENBW} = \frac{1}{2\pi} \frac{\int_0^\infty |H(j\omega)|^2 d\omega}{|H(j\omega_0)|^2} \qquad (3\text{-}11)$$

where $H(j\omega)$ is the transfer function of the filter and $H(j\omega_0)$ is the maximum value of $H(j\omega)$. Alternatively (3-11) can be expressed as

$$\text{ENBW} = \frac{1}{2\pi} \frac{\int_{-\infty}^\infty |H(j\omega)|^2 d\omega}{|H(j\omega_0)|^2}$$

which is intended for a two sided bandwidth definition ($-\infty < \omega < \infty$). As only positive frequencies are of interest, the latter equation can be rewritten as

$$\text{ENBW} = \frac{1}{4\pi} \frac{\int_{-\infty}^\infty |H(j\omega)|^2 d\omega}{|H(j\omega_0)|^2}$$

but in this case, it is valid for a one sided bandwidth.

For a first order low-pass filter with transfer function given by

$$H(j\omega) = \frac{1}{\tau j\omega + 1} \qquad (3\text{-}12)$$

100

and evaluating in (3-11),

$$\text{ENBW} = \frac{1}{4\tau} \qquad (3\text{-}13)$$

where τ is the time-constant given in seconds an ENBW is given in Hz. This shows the relation between the noise bandwidth and the time-constant of the filter, a longer time constant will give a lower ENBW, indicating that noise reduction comes at the expense of speed.

Equation (3-11) can also be expressed as [89]

$$ENBW = \frac{1}{2} \cdot \frac{\int_0^{T_0} |h(t)|^2 dt}{\left|\int_0^{T_0} h(t)\right|^2} \qquad (3\text{-}14)$$

with a discrete time equivalent given by

$$ENBW = \frac{1}{2} \cdot \frac{\sum_{i=1}^{N} |h(i)|^2 \cdot T_s}{\left|\sum_{i=1}^{N} h(i) \cdot T_s\right|^2} \qquad (3\text{-}15)$$

where T_s is the sampling time. Simplifying

$$ENBW = \frac{F_s}{2} \cdot \frac{\sum_{i=1}^{N} |h(i)|^2}{\left|\sum_{i=1}^{N} h(i)\right|^2} \qquad (3\text{-}16)$$

where F_S is the sample frequency, N the number of samples, and h(i) the impulse response of the filter.

The output of a moving average filter is given by [100]

$$y(n) = \frac{1}{M+1} \sum_{k=0}^{M} x(n-k) \qquad (3\text{-}17)$$

where $N=M+1$ is the number of averaged samples.

In discrete-time systems, any signal can be expressed by a sum of impulses

$$x(n) = \sum_{x=-\infty}^{\infty} x(k)\delta(n-k) \tag{3-18}$$

and for a linear system the output is given by

$$y(n) = \sum_{x=-\infty}^{\infty} x(k)h_k(n) \tag{3-19}$$

where x(k) is the input and h_k(n) is the impulse response of the system

$$\delta(n-k) \rightarrow h_k(n) \tag{3-20}$$

If the system is also time-invariant

$$h_k(n) = h_0(n-k) \tag{3-21}$$

and substituting in (3-19)

$$y(n) = \sum_{x=-\infty}^{\infty} x(k)h(n-k) \tag{3-22}$$

which is the convolution sum.

Using the convolution sum and (3-17)

$$y(n) = \sum_{k=0}^{M} \frac{x(n-k)}{M+1} = \sum_{k=-\infty}^{\infty} h(k)x(n-k) \tag{3-23}$$

The impulse response is given by

$$h(n) = \sum_{k=0}^{M} \frac{1}{M+1}\delta(n-k) \tag{3-24}$$

which has a finite number of terms and therefore belongs to a family of digital filters known as finite impulse response (FIR). One important property of this type of filters is that its response is always stable since the sum has a finite number of terms and cannot be divergent.

Substituting (3-24) in (3-16), and given $N=M+1$

$$\text{ENBW} = \frac{F_s \sum_{i=1}^{N} \left|\frac{1}{M+1}\right|^2}{2 \cdot \left|\sum_{i=1}^{N} \frac{1}{M+1}\right|^2} = \frac{F_s \cdot N \cdot {}^{1}/_{N^2}}{2 \cdot \left|{}^{N}/_{N}\right|^2} = \frac{F_s}{2N} \qquad (3\text{-}25)$$

ENBW is proportional to the sampling frequency F_s and inversely proportional to the number of samples. However, if the sampling frequency is increased, but the total acquisition time remains constant, the number of samples will be increased in the same proportion and the ENBW will remain constant. In a lock-in amplifier application, a low ENBW is needed, this is commonly achieved by increasing the number of samples at a given sampling rate, which in turn means a longer acquisition time.

For a linear averager with N=50 000 samples and operating at a F_s= 100 kHz,

$$\text{ENBW} = \frac{100\ 000}{2 \cdot (50\ 000)} = 1\ \text{Hz} \qquad (3\text{-}26)$$

The effect of the number of samples in noise reduction is shown in Figure 3-54. As it should be expected, a higher number of samples (taps) produces a greater noise reduction but with a slower time-response.
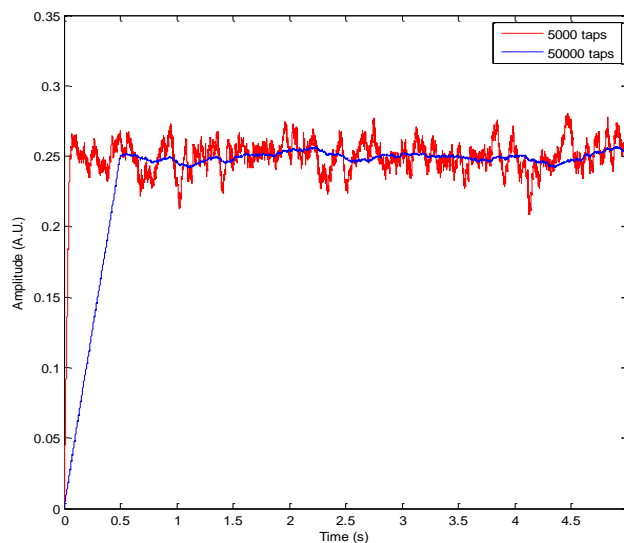
Figure 3-54. Dependence on noise reduction with different number of taps in a FIR linear averager lock-in amp at the same sampling frequency.

A 50 000 samples moving average has an ENBW= 1 Hz (@ 100 kS/s). With this result, an equivalent first order analogue filter can be found. From (3-13),

$$\tau = \frac{1}{4 \cdot \text{ENBW}} = \frac{1}{4 \cdot (1 \text{ Hz})} = 250 \text{ ms} \qquad (3\text{-}27)$$

A comparison between response of a lock-in amplifier with a LPF (τ= 250 ms) and a 50 000 taps linear averager FIR filter is shown in Figure 3-55. Output signals present a similar amount of noise but the FIR filter has a faster rise time. FIR settles in 250 ms, that is the time required to acquire its 50 000 samples, whereas the LPF requires five times its time-constant to settle (5τ=1.250 s).
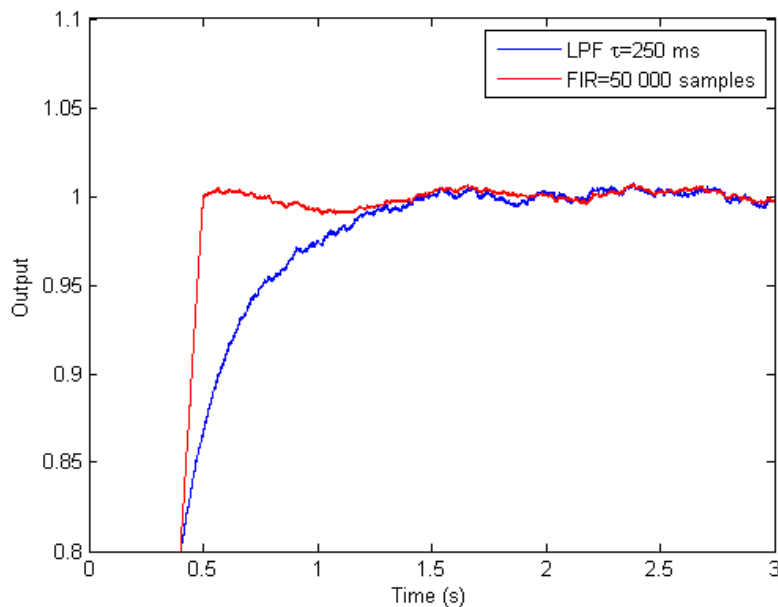
Figure 3-55. Noise performance. FIR filter (50 000 taps) vs LPF (τ= 250 ms).

The response of a linear averager lock-in amplifier can also be compared with higher order filters. In Figure 3-56, linear averager LIA is compared against a second order (H_1) and fourth order (H_2) Butterworth filters with a cutoff frequency equal to the first order filter, ω_c=1/τ=1/0.250=4 rad/s. Transfer functions are given by

$$H_1(s) = \frac{16}{s^2 + 5.6569s + 16} \qquad (3\text{-}28)$$

$$H_2(s) = \frac{256}{s^4 + 10.4525s^3 + 54.6274s^2 + 167.2401s + 256} \qquad (3\text{-}29)$$

With the Butterworth filters, the high frequency noise is attenuated but a low frequency oscillation persists. There is also an overshoot in the response, but that could be reduced by using a different approximation, for example, a Bessel filter.
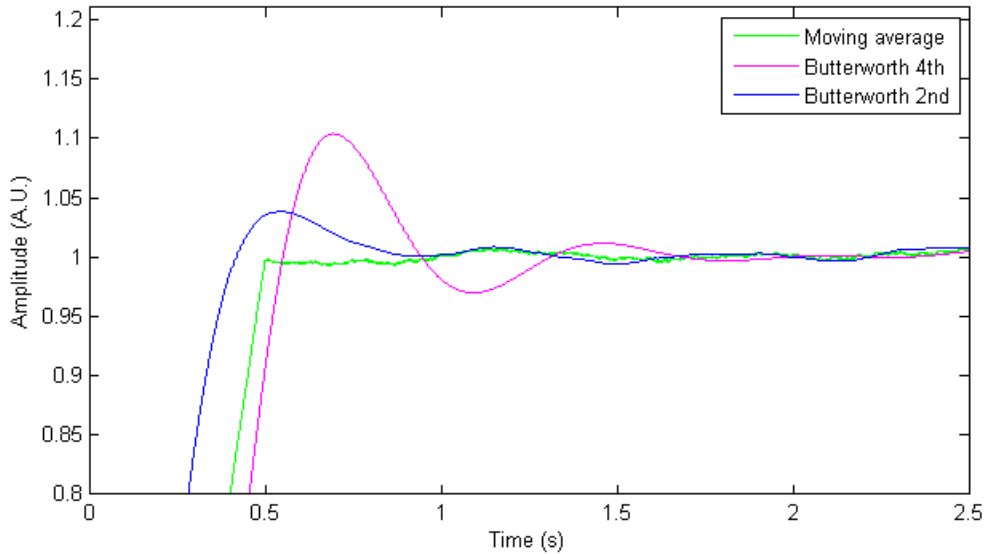
Figure 3-56. Comparison of FIR, 2nd order Butterworth and 4th order Butterworth filters in a lock-in amp.

3.6.4 Equivalence between cumulative average and moving average

It is difficult to obtain an expression for the ENBW of a cumulative averager, since it is a time-varying filter; however, for the case when N=k+1, both filters become

$$y(k) = \frac{1}{N}\sum_{i=0}^{N-1} x(i) \qquad (3\text{-}30)$$

It means that for that condition both filters are equivalent and will have the same ENBW (as given by (3-25)). This means that at any given time, the noise reduction achieved with any of them is the same. The difference is that the cumulative averager shows an

accurate result from the first sample, while in the Linear Averager case a whole set of samples (given by the number of taps) is required.

In Table 3-3, a comparison between different lock-in amplifier implementations, is presented.

	ANALOGUE LOCK-IN	DIGITAL LOCK-IN	MODIFIED LOCK-IN
Noise reduction technique	First order analogue averaging	Moving averager	Cumulative averager
Noise reduction depends on	Time constant τ $$ENBW = \frac{1}{4\tau}$$	Number of samples and sampling time $$ENBW = \frac{F_s}{2N}$$	Number of samples and sampling time $$ENBW = \frac{F_s}{2N}$$
Noise reduction is	Fixed by Time constant	Fixed by number of samples, given a certain F_s	*Dynamic. Depends on elapsed time.*
Response time	$$t_d = 5\tau$$	$$t_d = \frac{N}{F_s}$$	Depends on desired noise reduction
Digital implementation		Very fast. No need of multipliers No need of division if N is 2^n.	Needs a new division with each sample.
Hardware efficiency		Very high	Low
Acquisition time vs. Noise reduction		*The same* (Given the same sampling frequency)	

Table 3-3 Comparison between filtering techniques in a lock-in amplifier.

3.6.5 Hardware implementation

The fast lock-in amplifier was implemented using a data-acquisition module from National Instruments and its algorithm was programmed using LabVIEW. There is a program for implementing a lock-in amplifier available from the National Instruments webpage, however it is limited to a particular type of filters, this cannot be changed and

the code is protected, so it cannot be viewed nor modified. Therefore, a specific program was developed in order to implement the fast lock-in amplifier (cumulative averager). A moving average and a Butterworth low pass filters were also implemented as options for filtering. The data acquisition hardware is made of a NI cDAQ-9172 USB chassis, a NI 9401 8-channel TTL Digital I/O Module, and a NI 9205 32-channels (±200 mV to ±10 V) 16-Bit, 250 kS/s Analog Input Module [101-103].

The digital module is used to generate a 10 kHz square signal which modulates a high voltage power supply connected to the photoconductive antenna. This square signal also serves as trigger for the data acquisition. Since the voltage output of the balanced detector was around 10 mV, a ±200 mV input scale was selected for the analogue input channel. This limits the effective number of bits from the analogue-to-digital converter to 12-bits instead of 16-bits, but from previous experiments, a low dynamic range was already observed; therefore, it was decided not to include an amplifier at this point. 12 bits are equivalent to 72 dB dynamic range, which is more than it was observed with a commercial lock-in amplifier ($\approx$ 60 dB, with an 18-bit analogue-to-digital converter). Data acquisition was done at the highest sampling rate available (250 kS/s).
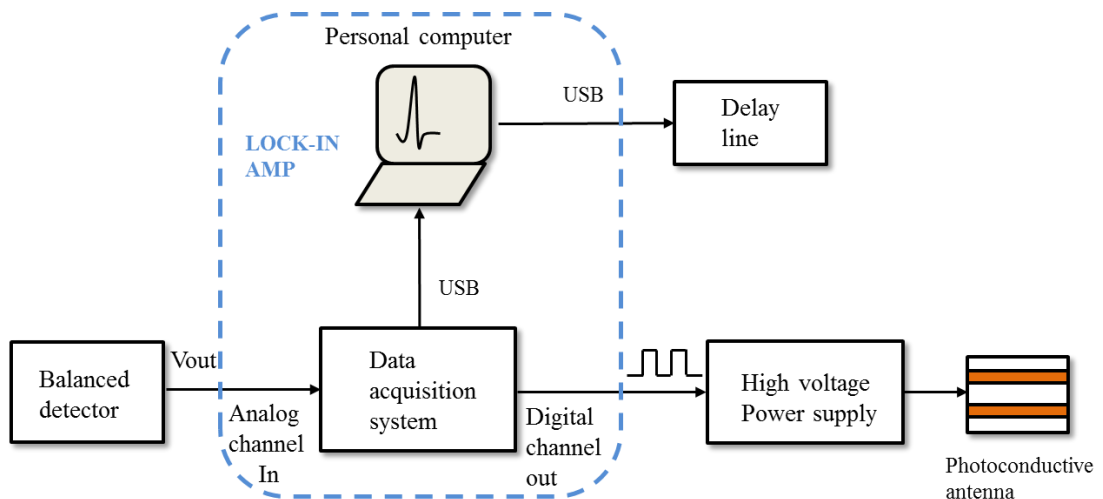
Figure 3-57. Block diagram of the THz-TDS instrumentation showing the computer based lock-in amplifier.

In Figure 3-58, an example of the program control window is presented. There are three plotting areas. From top to bottom: the time-domain THz signal, the lock-in amplifier

time response, and the THz spectrum. For the lock-in amplifier, there are three options for the filter: fast lock-in (cumulative averager), moving average, and second order Butterworth. An integration time can be set for the cumulative and moving averages, whereas the cut-off frequency can be adjusted for the Butterworth filter. Settling time for these three options can be monitored in the "Lock-in time response" chart window. A picture of the lock-in amplifier operating at The Photon Science Institute is shown in Figure 3-59.
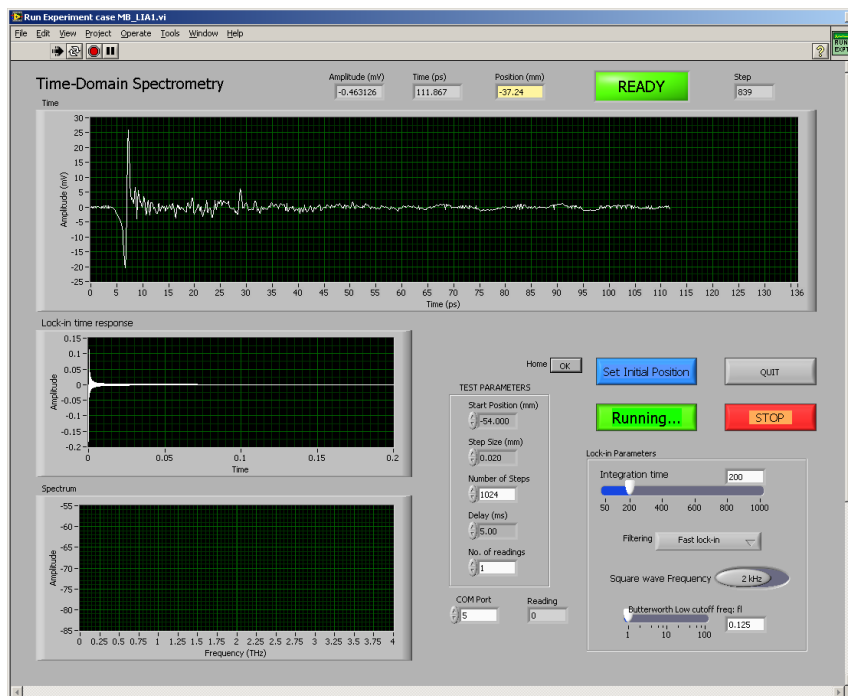
Figure 3-58. THz-TDS system control window showing the lock-in amplifier parameters configuration (bottom-right).
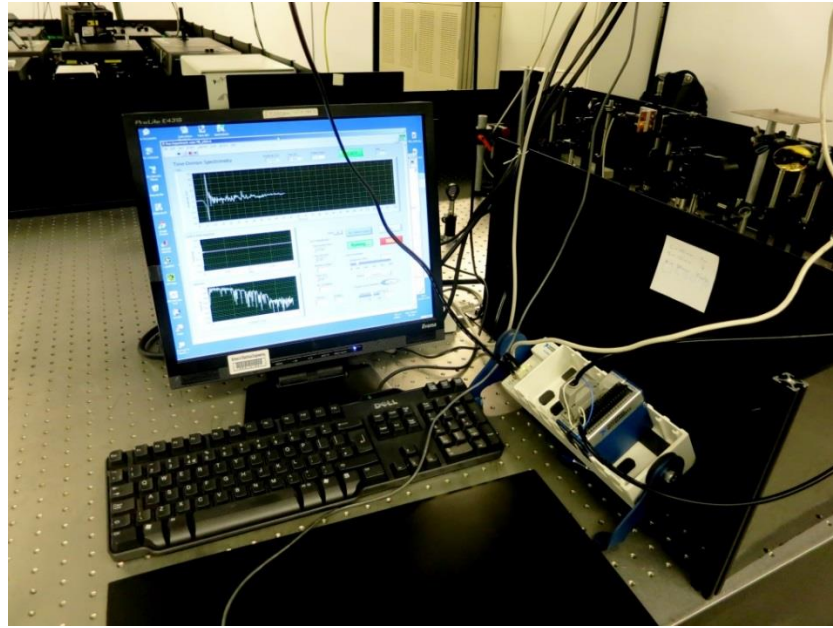
Figure 3-59. The fast lock-in amplifier installed at The Photon Science Institute.

The digital lock-in amplifier was tested using the THz-TDS system and some spectrums of air are shown in Figure 3-60 and Figure 3-61. There is no noticeable difference in performance for any of the implemented filters (Fast lock-in, moving average and Butterworth). Minor variations in the spectrum are observable but they can be attributed to the presence of noise in the system.
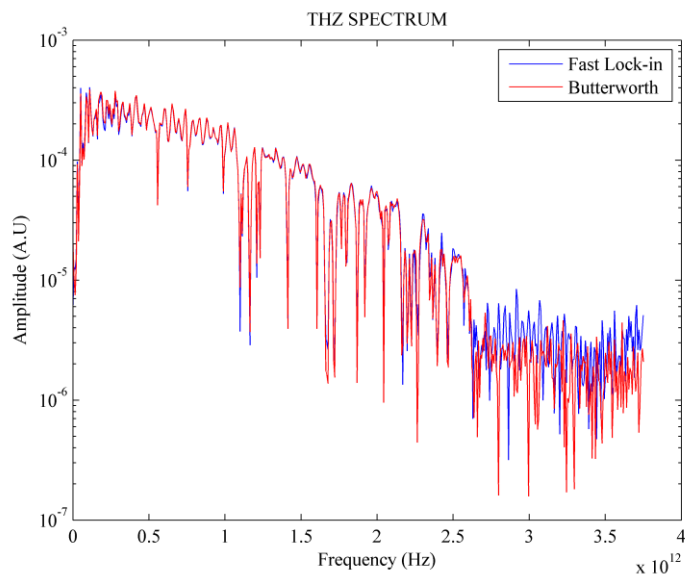
Figure 3-60. THz spectrum of air using a fast lock-in (cumulative averager) and a Butterworth filter.
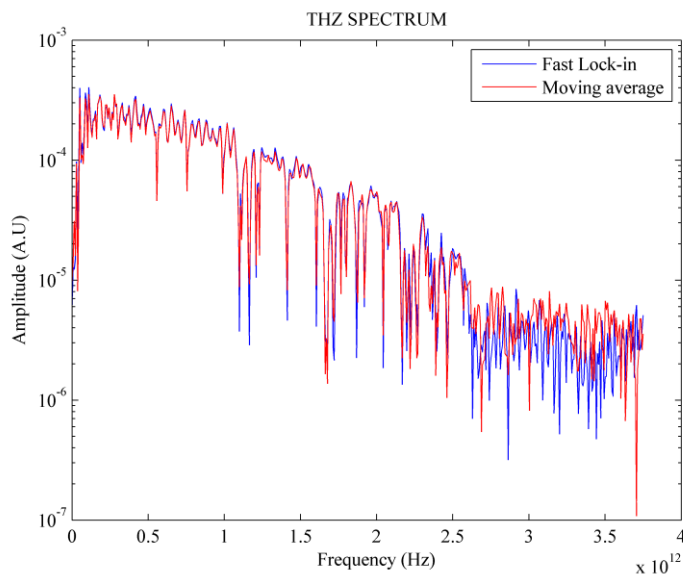
Figure 3-61. THz spectrum of air using a fast lock-in (cumulative averager) and a moving average filter.

Performance of the computer based fast lock-in amplifier is similar to a commercial lock-in amplifier (Signal Recovery model 7265), as it can be seen in Figure 3-62. Noise level is acquired whilst disconnecting the antenna bias voltage, therefore obtaining a reading without excitation applied to the transducer [88]. There is, however, a difference in the total acquisition time of the experiment. The computer based lock-in amplifier executes data acquisition, data transmission (to the PC) and data processing sequentially; this means, that all data is first acquired, then transmitted serially (through a USB port at 115.2 kbauds) and finally processed by the LabVIEW program. The commercial equipment has a Digital Signal Processor (DSP), it can operate in real-time and it has a parallel GP-IB communication port. With the computer hardware available, it takes twice as long to complete a THz-TDS test using the LabVIEW based lock-in amplifier.
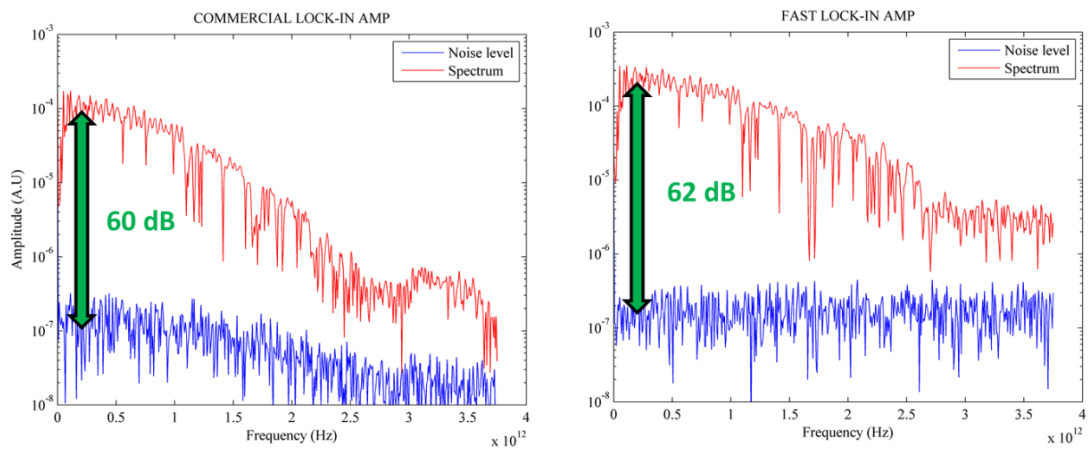
Figure 3-62. THz spectrum of air using a commercial lock-in and a LabVIEW based fast lock-in amplifier.

The noise floor level observed by the fast lock-in amplifier has a relatively flat frequency response, whereas the commercial lock-in shows a decaying response. The latter could be due to the actual implementation of the lock-in algorithm which is not available to the user as it is considered an industrial secret. It is not possible to know what is the sampling rate used by the lock-in amplifier nor the details of the implementation of the filtering stages, therefore a deeper comparison cannot be made. Nevertheless, both responses show a similar dynamic range vs. frequency behaviour.

3.7   Spectroscopy tests

The University of Manchester was involved in a project related to transformer oil aging, so this was an opportunity to test if the THz-TDS system could be useful. The first problem to be solved was to determine the sample size and cuvette material for containing the oil. A quick literature review on liquids with similar characteristics was made and results are summarized in Table 3-4 [104-110]. Where available, the table also includes information regarding THz optics. There are several examples in the literature [16, 104, 111], where an array of four parabolic mirrors is used to focus the THz beam on a sample. This agrees with our decision to build a four parabolic mirror setup, though an alternative

approach using two elliptic mirrors is used in [112, 113]. It was found that transformer oil has a density similar to that of diesel (see Table 3-5).

A Teflon container was used in [104], due to its low absorption and low refractive index, for measuring properties in petroleum with a THz-TDS system. Samples were 2 mm and 5 mm thick. A diesel-gasoline mixture was tested in [109], with a sample 10 mm thick. A cuvette made of 2 mm thick Teflon was used in [106]. Finally, it was decided to build two cuvettes with Teflon (PTFE) windows; one to hold a volume 5 mm thick and a second for a 10 mm thick.

Sample material	Sample thickness	Cuvette material	Construction	Num. of mirrors	Detector
Gasoline and xylene isomers	2 to 5 mm	HDPE bags	Holder with two 10 mm Teflon windows	4 Figure included	ZnTe 1 mm
Diesel-gasoline mix	10 mm	Not specified	Cuvette with two holes, one is for reference	4 Figure included	PCA
Polyglycol oil + water	0.5-0.8 mm	Cyclic Olefin copolymer window	Cuvette with replaceable spacer	2 ?	ZnTe 1 mm
Vegetable oil	5 mm	Quartz. 1.2 mm thickness	Focusing with 2 Si Lens	2 + Si Lens	ZnTe 0.5 mm
Oil + water		Polypropylene	QCL		Golay
Engine oil	10 mm	Polyethylene	Cell thickness <0.5 mm		ZnTe
Petroleum products and organic solvents	5 mm. 20 mm ϕ	Teflon (2 mm thick)	Homemade sample holder		

Table 3-4. Examples of cuvettes for oil testing with THz.

Gasoline	0.71–0.77 kg/l
Diesel	0.832 kg/l
Kerosene	0.78–0.81 kg/l
Benzene	0.8765 kg/l
Transformer oil	0.89 kg/l

Table 3-5. Density of some substances.

A cuvette suitable for THz was not available but some alternatives were found in the literature. An schematic diagram of a custom made liquid holder is presented in [106],

and a double cuvette capable of storing a sample and a reference simultaneously is proposed in [111]. It was decided to take that proposals further and to build a triple cuvette capable of having a sample, a reference and an empty cuvette for calibration. The position of the cuvette is adjusted by a linear translation stage inside the Perspex box, avoiding to purge separately to perform calibration, sample measurement, and reference measurement. A piece of acrylic was used as a spacer, and its design is shown in Figure 3-63. The cuvette is made of two 2 mm thick aluminium holders, two 1.5 mm thick PTFE windows, and an acrylic spacer (5mm or 10 mm thick) (see Figure 3-64). These five pieces are assembled together with 12 screws. By changing the spacer thickness, it is possible to modify the size of the oil sample. PTFE windows are mounted on the front and on the rear. The complete cuvette assembled and installed inside the Perspex box is shown in Figure 3-65.
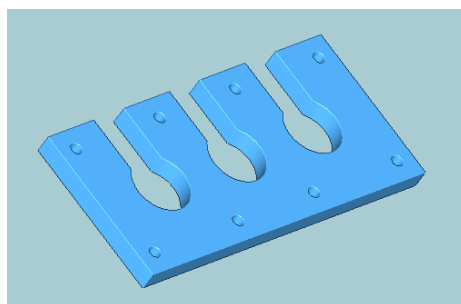
Figure 3-63. Spacer for the triple cuvette.
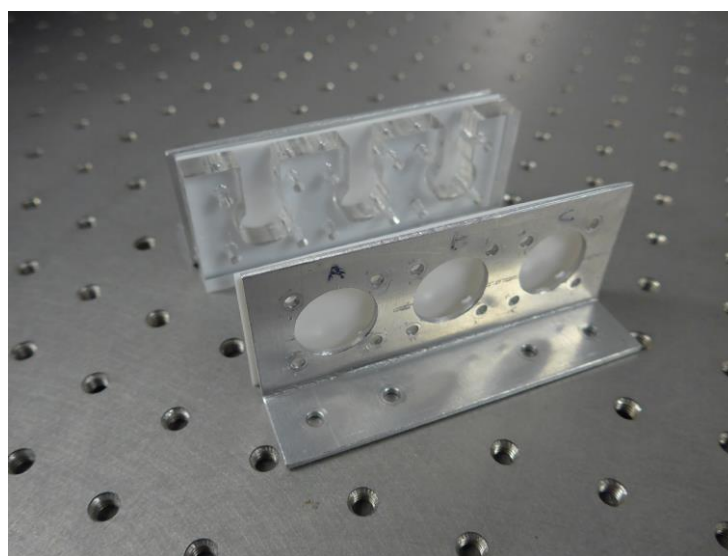
Figure 3-64. Components of the triple cuvette.

Figure 3-65. The triple cuvette mounted positioned inside the Perspex box.

An experiment was carried out for comparing two samples of transformer oil (5 mm thick). One sample consisted of virgin oil, whereas the second was a sample thermally aged for 7 weeks (oil was Nitro Gemini X [114]). Results are shown in Figure 3-66 for the spectrum, and Figure 3-67 for the time-domain THz signal. As it can be seen, both samples produce almost identical results, and minor differences can be attributed to system noise. After getting similar results with samples 10 mm thick, it was concluded that virgin oil is indistinguishable from 7 weeks thermally aged oil, in their spectral and time-domain THz responses. This may be corroborated by the study presented by [115], though it was done in the UV-visible spectrum, which concludes that optical properties of transformer oil are degraded more easily by partial discharge in comparison with arc or thermal ageing. In the last two cases, optical properties remained almost equal to that of virgin oil. A comparison between different types of organic oils, like sunflower, olive, brassica and groundnut oils gave similar results.

Alternatively, in order to enhance the differences between two spectra, a technique based on wavelets have been proposed in [116], but its use was out of the scope of the current research.
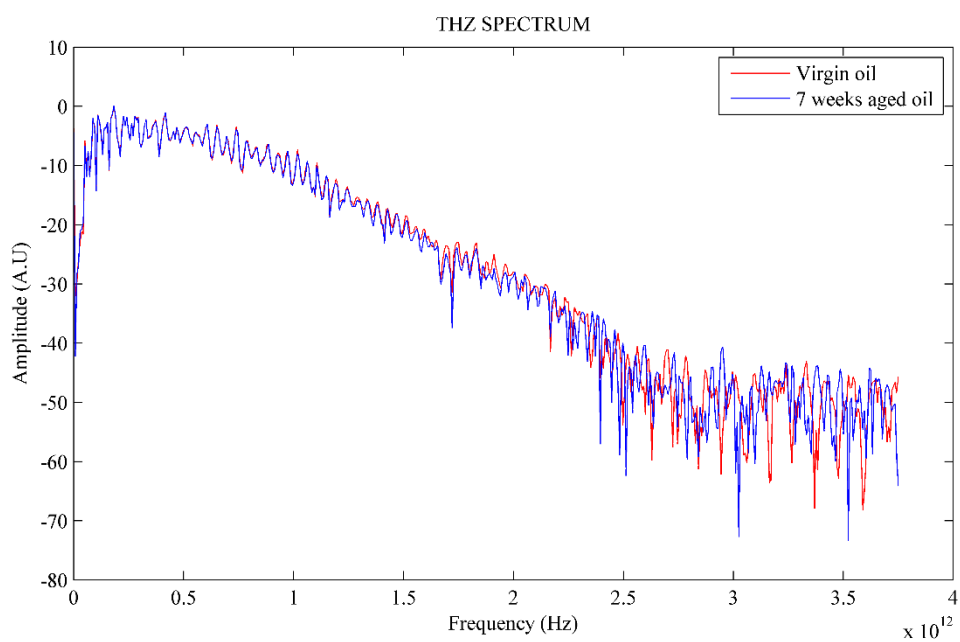
Figure 3-66. THz spectrum comparison. Virgin transformer oil vs. 7 weeks aged oil.
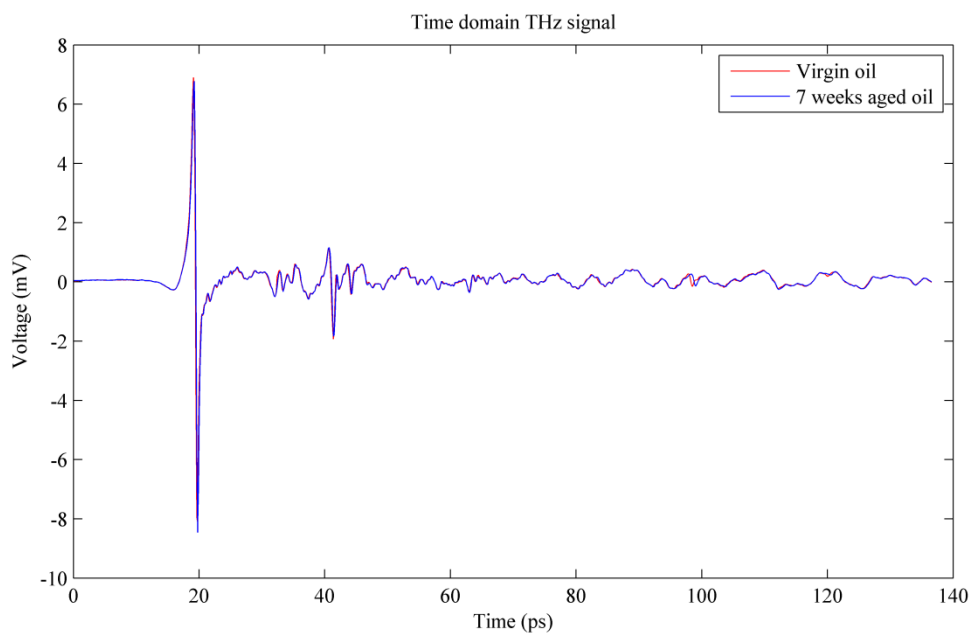
Figure 3-67. Time-domain THz signal. Virgin transformer oil vs. 7 weeks aged oil.

3.8 Alternative TDS configurations

Performance of the implemented THz-TDS system is similar to several examples reported in the literature, as has been shown in the previous sections. However, it was decided to explore some alternative configurations in order to improve the system operation. Our aim was centred in modifying the balance detection. At first there were two possibilities to be analysed: first, to propose a digital balance detection algorithm and second, to swap positions between the balance detection and the lock-in amplifier.

3.8.1 Modified balanced detection

As was explained in section 2.3.1, in an electro-optical sampling arrangement, a THz pulse is detected by analysing the change in polarization of the probe beam. Vertical and horizontal components of the beam are modulated by the THz electrical field, and the results are given by

$$
\begin{aligned}
I_x &\approx \frac{I_0(1 - \Delta\emptyset)}{2} \\
I_y &\approx \frac{I_0(1 + \Delta\emptyset)}{2}
\end{aligned}
\qquad (3\text{-}31)
$$

Where $\Delta\emptyset$ is proportional to the THz electrical field. Subtracting both components gives

$$
I_s = I_y - I_x = 2I_o\Delta\emptyset
\qquad (3\text{-}32)
$$

As was discussed above, the autobalanced operation performed by a Newfocus model 2017 Nirvana auto-balanced detector [117] is not suitable for a THz-TDS system and therefore experiments are performed in the "balance" mode. An example of a Nirvana detector used in balance mode in a THz setup can be found in [118]. A differential configuration, as it is the case in a balanced detector, is well known by its capability to reject common mode signals [119]; therefore, it will be able to reduce the influence of noise produced by an additive source.

116

If the term I_o in eq. (3-32) is affected by multiplicative noise, this will not be reduced by normal balanced operation. A simple modification to the balanced detection algorithm was made in order to reduce the influence of multiplicative noise. The idea is to divide the balanced detection signal by the signal present before the disbalance produced by the electro-optical sampling. Our idea was first simulated using LabVIEW and a simplified block diagram is shown in Figure 3-68. Signal V_{in} is made of a DC signal (representing the variable of interest) and some added noise (white-Gaussian). The two sum blocks at the centre are used to simulate the unbalance produced by the electro-optical sampling ($\Delta\emptyset$ term). The horizontal component (V_y) is incremented by the same amount that the vertical component (V_x) is decremented, and this quantity is derived from the initial V_{in}. This correctly represents equation (3-31), and reflects the fact that beam energy before and after the electro-optical sampling crystal should remain constant. The unbalance is given by the gain x and the output of the normal balanced detection (BD) operation is

$$BD = 2xV_{in} \tag{3-33}$$

which is equivalent to eq. (3-32). The output of the modified balanced detection (MBD) is

$$MBD = 2x \tag{3-34}$$

Ideally representing just the differential component without multiplicative noise.
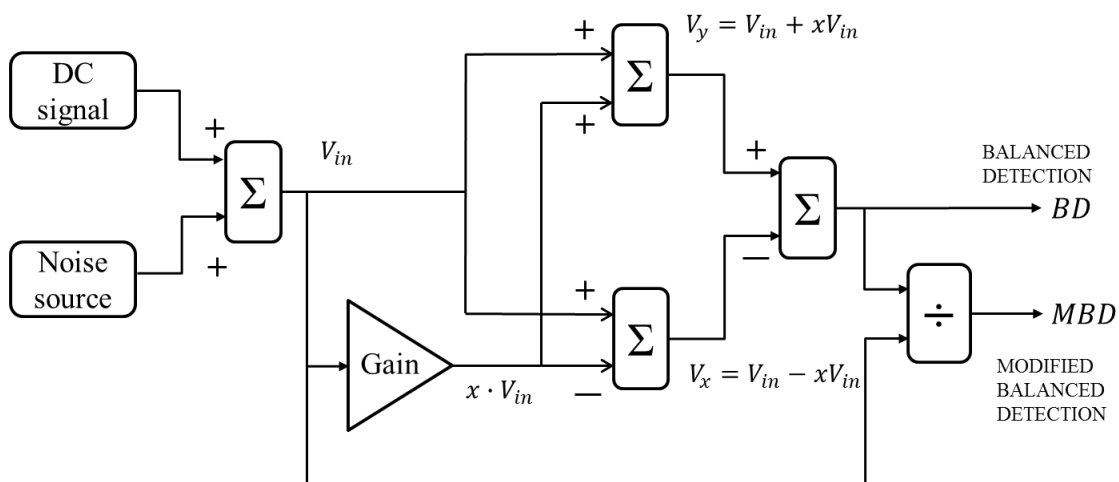
Figure 3-68. Block diagram of the simulation of a modified balanced detection algorithm.

Simulation results were encouraging and are shown in Figure 3-69. The output of the modified balanced detection clearly shows a lower noise content than the output of the normal balanced detection.

In order to bench test the MBD, a beam splitter (BS2) is added to the probe beam path, in order to get a sample of the beam before being modulated by the THz pulse in the electro-optical sampling crystal. The sampled beam is detected by a second balanced detector operating as single beam photodetector. The output of each balanced detector is connected to an input channel in a data acquisition system. Most multichannel data acquisition systems use a multiplexing method, that is, they acquire data from channels in a sequential fashion. However, it is highly unlikely that noise levels will remain constant between two consecutive samples, therefore, a simultaneous sampling data acquisition system is required. A simultaneous sampling analogue-to-digital converter module wasn't available, but its operation was approximated using two analogue-to-digital converter modules (NI 9205 32-channels (±200 mV to ±10 V) 16-Bit, 250 kS/s Analog Input Module), triggered by the same clock signal. A block diagram of the data acquisition system is presented in Figure 3-71. The lock-in amplifier is the fast-lock in version presented in section 3.6.
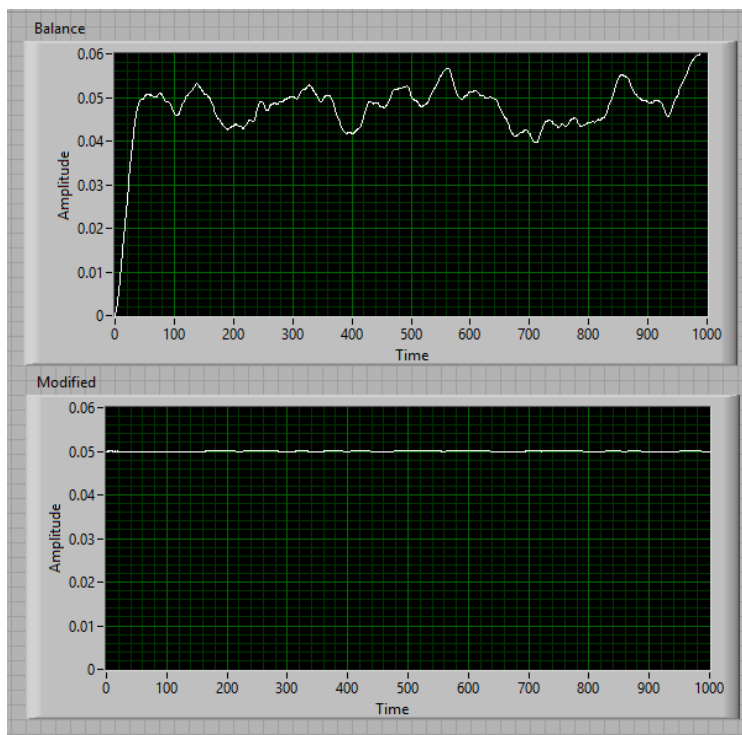
Figure 3-69. Simulation results of the BD and MBD algorithms.
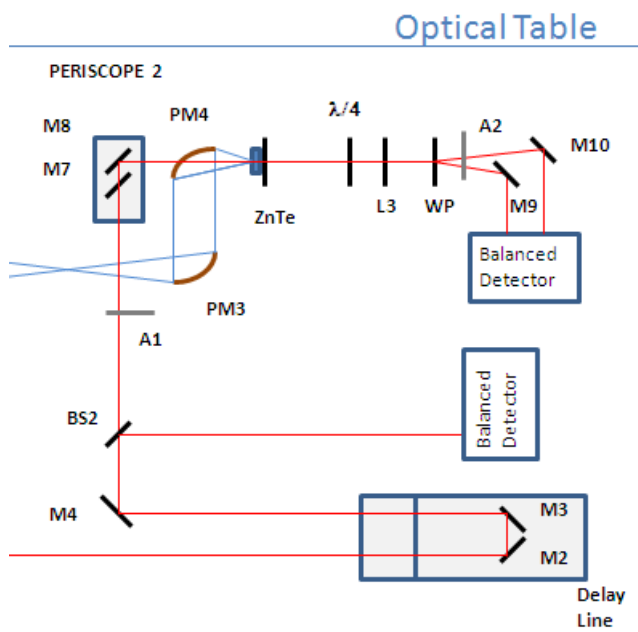
Figure 3-70. System modification for testing the modified balanced detection algorithm.
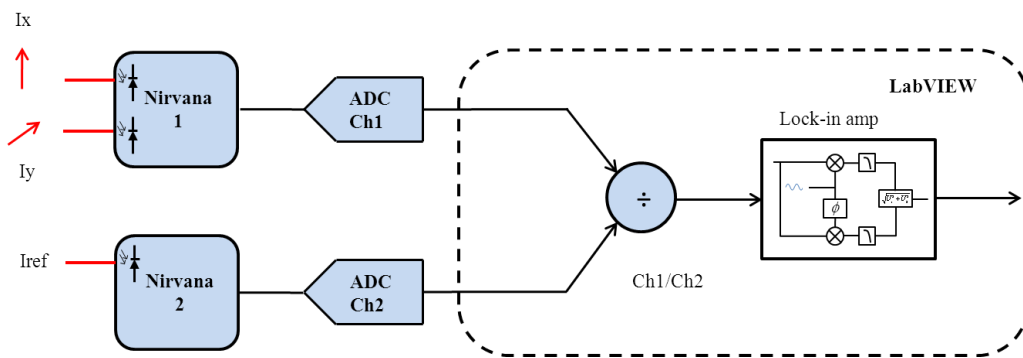
Figure 3-71. Block diagram of the data acquisition system for implementing a modified balanced detection algorithm (LIA2_BD2).

The spectral response performance is similar to the standard configuration using a single balanced detector, as it can be seen in Figure 3-72. A lower noise floor level and a higher dynamic range (DR) were expected. The experiment showed a 61 dB DR, which is similar to previous results, and minor variations on DR are normal in this type of tests.
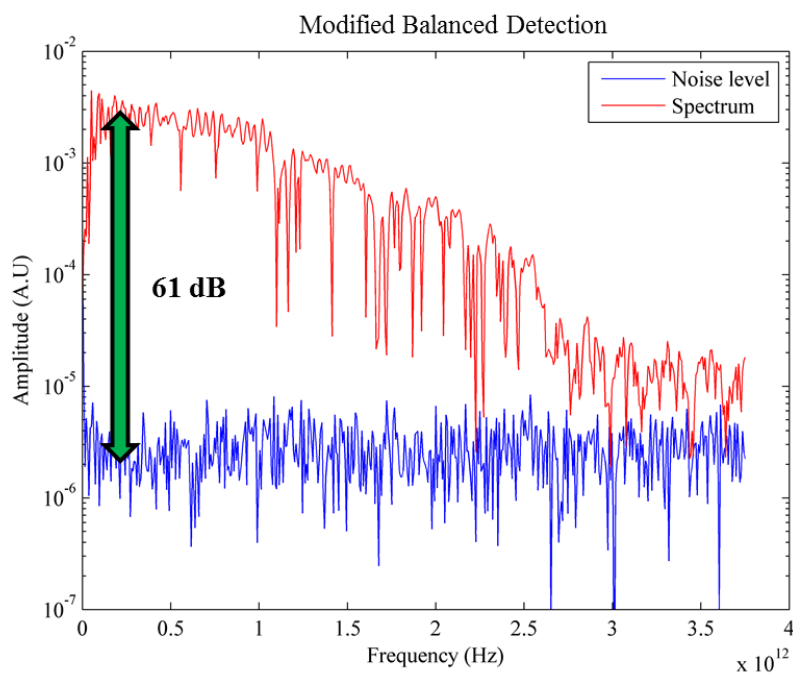
Figure 3-72. Spectral response for the modified balanced detection algorithm.

In Figure 3-73, spectral responses for a BD and a MBD are depicted. It is clear that both responses are practically the same, with minor variations attributable to system noise. If

they are compared against the noise floor level, it will be difficult to see any improvement since dynamic ranges present an almost identical profile as it can be seen in Figure 3-74.
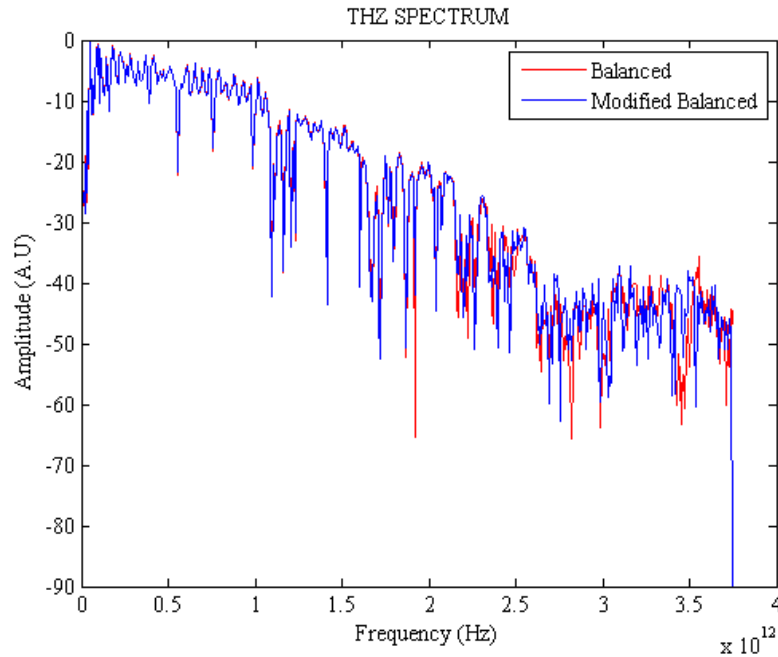
Figure 3-73. Spectral responses of a BD vs. MBD.
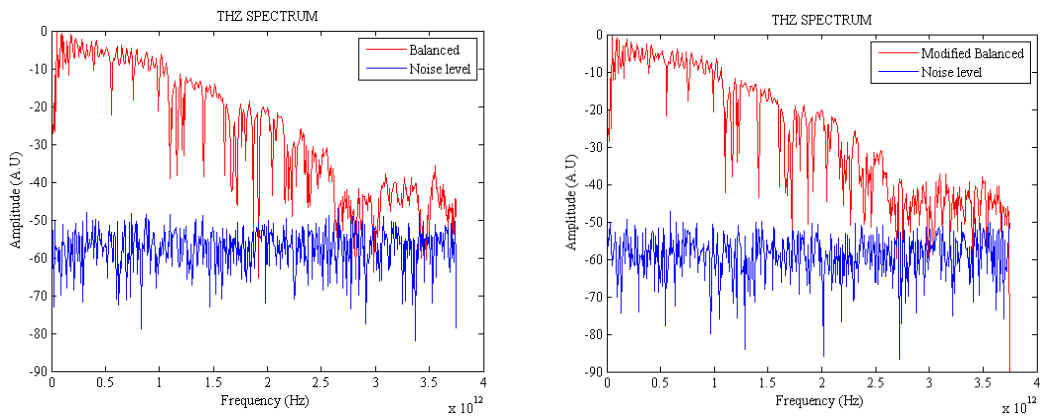
Figure 3-74. Spectral responses of BD (left) and MBD (right) vs. noise floor.

The beam sampled by BS2 is not affected by the THz beam, and that is why it was chosen in the first place, but if the noise source is in the THz emission, then it should be placed after the ZnTe crystal. A second arrangement was made changing the position of the beam sampler, as it is shown in Figure 3-75, but again no improvement was obtained. These results show that the proposed algorithm is not capable of any noise reduction, a possible explanation is that is not possible to obtain an accurate sample (copy) of the signal, whilst

in a computer simulaston this is perfectly doable. The simulation program made in LabVIEW tried to account for this effects and has options to simulate the frequency response of the detectors and to add a certain amount of mismatch, but accuracy in the end depends on having an exact copy of the input signal.
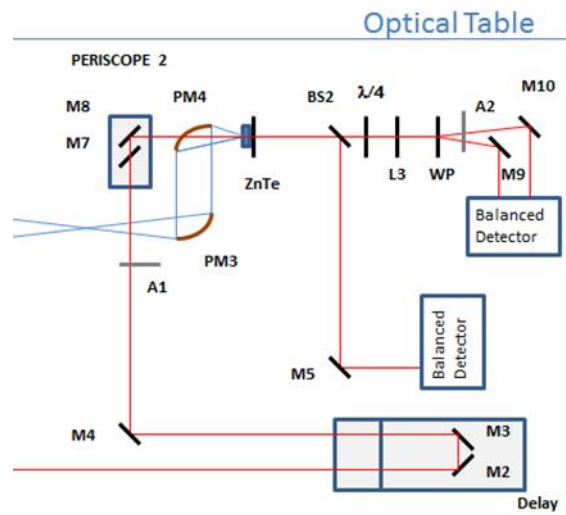
Figure 3-75. Sampling the beam after the ZnTe crystal.

3.8.2 Dual lock-in amplifier configuration

In a typical THz-TDS system, horizontal and vertical components of the probe beam are separated by a Wollaston prism and then processed by a balance detector. Signal is modulated by applying an optical chopper to the beam or by using an electronic chopper at the voltage bias of the GaAs emitter antenna. After the balance detection, demodulation is carried out by a lock-in amplifier. It was an open question whether detection could be improved by performing first the demodulation, using two lock-in amplifiers, and then applying a balance detection algorithm. During its operation, the lock-in amplifier not only demodulates the signal, but improves the signal-to-noise ratio. Having a cleaner signal before performing the key operation of balance detection appeared to be an attractive idea. In a typical balance detector, to photodiodes are connected together to subtract their photocurrents. In an alternative configuration, two independent photodetectors would be required, and each of them would have an associated lock-in amplifier as it is illustrated in Figure 3-76. The subtraction or any other form of balancing

would be performed after both signals were demodulated and filtrated. The setup was slightly modified, as shown in Figure 3-77, where two balanced detectors are used as single beam photoreceivers.
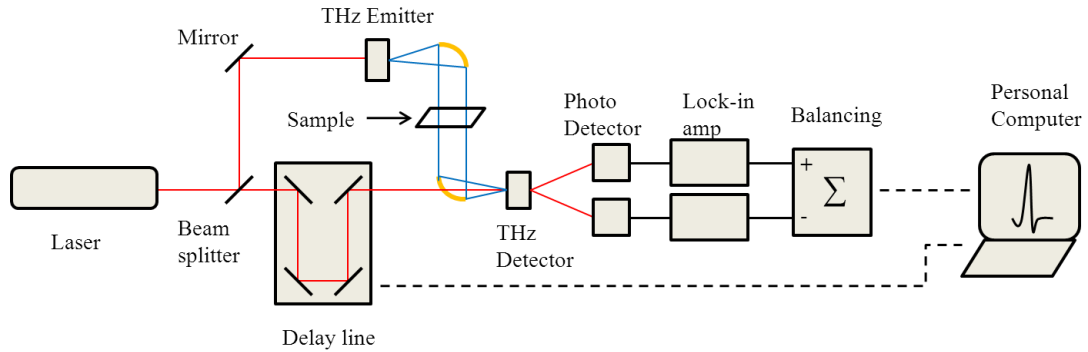
Figure 3-76. A THz-TDS system in post balancing configuration.
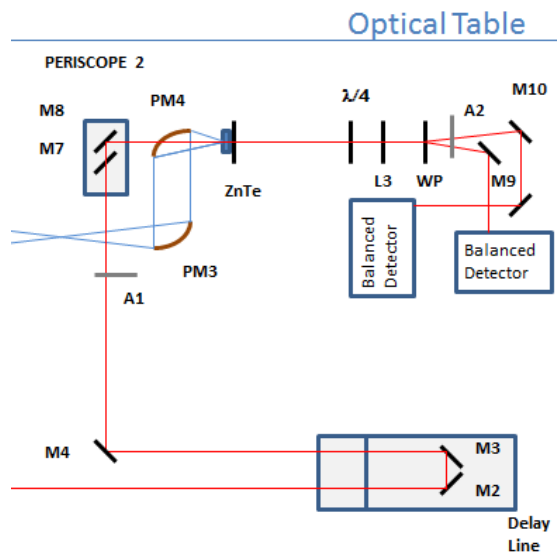
Figure 3-77. Setup with two independent photodetectors.

Each detector is connected to an analogue-to-digital converter and an independent digital lock-in amplifier before performing the balanced or modified balanced detection (see Figure 3-78). In order to further reduce the noise, an optional filter was added before the lock-in operation. The lock-in amp still can be configured to operate with a cumulative average (fast lock-in), a moving average or a Butterworth filter.
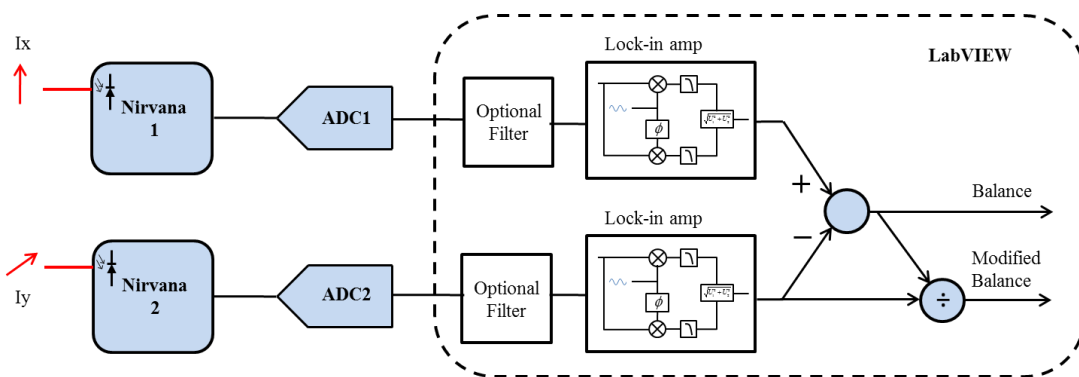
Figure 3-78. Dual lock-in amplifier detection system.

A comparison between a standard single lock-in amplifier and the proposed dual lock-in is presented in Figure 3-79. The dual lock-in version fails to detect major absorption lines. This could be caused by a reduction in dynamic range. When balance detection is performed first (subtraction operation), most of the common mode voltage is rejected, leaving only the smaller differential signal. In the THz TDS system, this differential signal is 1000 times smaller than the common mode. The input to the analogue-to-digital converter (ADC) has a large noise component and a smaller signal component (see Figure 3-80). On the one hand, in the case of the dual lock-in amplifier the added signal must enter the ADC, therefore, a great part of the dynamic range is wasted in digitizing the noise. On the other hand, after a differential detection (balanced detection), the signal component is isolated from the common mode noise and the signal can be amplified to make use of the complete dynamic range of the ADC.
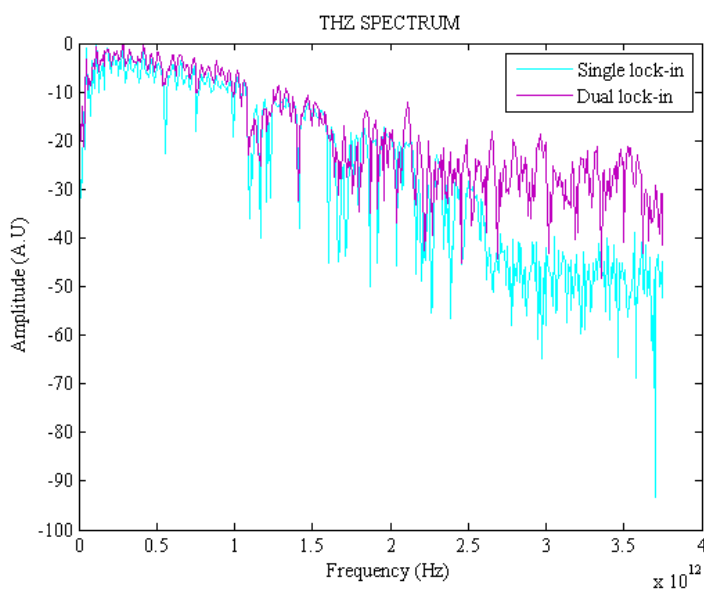
Figure 3-79. Spectral responses of a dual and single lock-in.

124
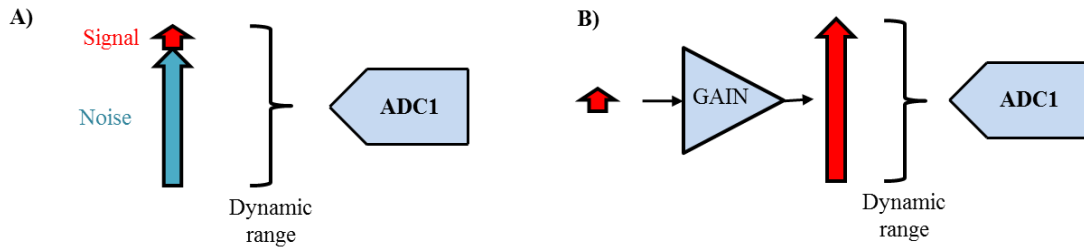
Figure 3-80. The influence of noise in the limitation of dynamic range.

3.9   Summary

The THz-TDS has been successfully characterized and modified. Dynamic range and SNR are comparable to those reported in the literature. The spectrum presents a spurious oscillation which is generated by an Etalon in the GaAs emitter antenna.

The power at several points in the setup was measured, and this information can be useful to make a new installation of the system or to monitor its operation. Tests were performed to obtain a better understanding of the system, like changing the pump beam polarization or varying the positions of a focusing lens for the probe beam. It was concluded that the polarization of the pump beam has no influence in the generation of the pulse, and it was possible to optimize the position of the focusing lens. A series of tests with different parabolic mirrors with and without Si lens in the PCA showed that placing a 2 in mirror with no antenna lens collects a similar amount of THz radiation that a 0.5 in mirror with antenna lens installed.

In several types of experiments, like measuring the refractive index of a material or in THz imaging, it is of interest to measure the time delay of the pulse. With this in mind, a method using parabolic interpolation was used to process data from a sooty flame experiment.

One critical aspect for THz detection is the quality of the polarization; therefore the use of a Glen Thompson polarizer for the probe beam could improve the system performance [120].

Two parabolic mirrors were added to the system in order to spectroscopy tests. Its alignment was difficult and time consuming, but a spot size of 4 mm was obtained which is comparable to similar systems. If a smaller spot is required parabolic mirrors with shorter EFL could be used. A Perspex box was made to provide a low water vapour content atmosphere as it is required by some tests.

A new approach for implementing a lock-in amplifier was proposed and tested using a data acquisition systems and a tailor made program in LabVIEW. The use of a cumulative average for performing the filtering operation inside the LIA was introduced for the first time. Initial tests showed a fast rising time, but further analysis proved that its noise performance is equivalent to the ubiquitous linear moving averager. Substituting the low pass filter in a lock-in amplifier for a cumulative averager gives very good results for an input occurring at t=0. However, if the input changes at any other time (t>0) then the system will not be able to follow the input within a practical amount of time. This can be solved if we introduce some sort of resetting to the averager. In the case of a TDS system, this is easily achieved since each reading should be synchronized to the displacement of the optical delay line: a reset can be signalized each time that the delay line is repositioned. The lock-in amplifier showed a performance in the THz-TDS system equivalent to a commercial instrument in terms of noise reduction, but real-time operation is not possible and a THz scan took twice as much time to be completed with our lock-in amplifier.

The THz-TDS system was used to determine whether it was possible to measure any spectral or time-domain difference between samples of new and aged transformer oil, but results were negative. This means that for the particular type of transformer oil, there is no optical difference in the THz region measurable with the current setup.

In an attempt to improve the SNR performance of the system two ideas were tested. First a digital balanced detection algorithm and second a dual lock-in amplifier configuration capable of demodulating the signal before performing the balanced detection. None of these ideas were successful, which suggest that the system can only be improved by changing the quality of some components. In particular, better results have been reported using a dipole antenna coupled with a silicon lens. (instead of the large aperture that is installed) [121] .

4   TERAHERTZ GENERATION BY PHOTOMIXING TECHNIQUES

4.1 Introduction

Continuous wave (CW) THz sources present an alternative to ultrashort laser systems and can also be used for spectroscopy and imaging [122]. Tunable CW lasers are used with photoconductive (photomixing) antennas to provide high frequency resolution (<1GHz) THz spectrometry, which represents a key advantage over other THz techniques. However, photoconductive (PC) switch antennas produce more average power (~100 times higher optical-to-THz conversion efficiency) and broader spectrum than photomixers [123]. One factor that limits the maximum amount of THz power is the thermal threshold of the antenna [46].

The development of the photomixing technique has been pushed forward by three important technological achievements [124]:

- Semiconductor materials with photocarrier lifetime lower than 1 ps
- Microfabrication techniques capable of sub-micron features
- Compact planar antenna integration with photomixer elements (for example, an interdigitated antenna)

The THz-TDS system described in the previous chapters has a footprint of around 2-3 m^2. CW laser sources are less expensive than ultrashort lasers and also have a smaller size. Miniaturizing a THz system if more applications are to be developed; therefore it was considered of interest to explore the generation and detection of THz radiation using CW photomixing techniques.

Photomixing is a technique were two CW single mode laser beams of slightly different frequency focused and pointed to the same spot on a photomixing antenna, producing and optical heterodyne down conversion. The optical power applied is given by [46]

$$P_i = P_0 + 2\sqrt{mP_1P_2}\left[cos(\omega_1 - \omega_2)t + cos(\omega_1 + \omega_2)t\right] \qquad (4\text{-}1)$$

where P_1 and P_2 are the laser power, operating at frequencies ω_1 and ω_2 respectively, $P_0 = P_1 + P_2$ is the total laser beam power averaged over a long period, and *m* is the mixing efficiency (0<m<1). The second cosine term has a frequency that is approximately the double of the optical frequency and is too fast to contribute significantly with the THz generation, therefore the radiation output depends on the frequency difference (Figure 4-1).
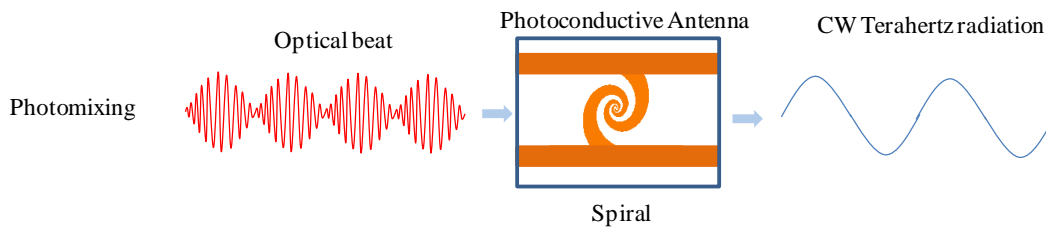
Figure 4-1. Terahertz generation by photomixing.
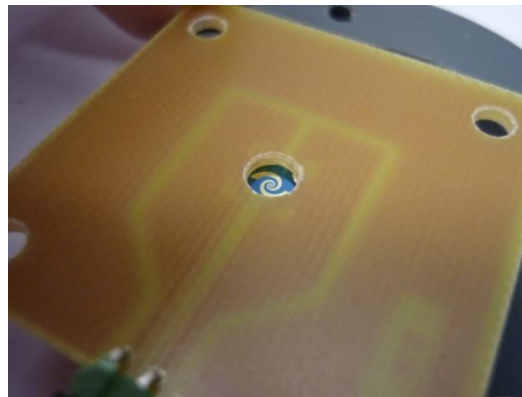
Figure 4-2. Photograph of the spiral PCA.

The THz radiation power is given by

$$P_{THz}(\omega) = \frac{I_{ph}^2 R_A}{2[1 + (\omega\tau)^2][1 + (\omega R_A C)^2]} \qquad (4\text{-}2)$$

where R_A is the antenna radiation resistance, C is the antenna gap capacitance, τ is the carrier lifetime and the DC photocurrent is

$$I_{ph} = G_0 V_b \qquad (4\text{-}3)$$

G_0 is the antenna DC photoconductance for a P_0 average power, and V_b is the antenna operating DC bias voltage.

4.2   Experiment setup

The schematic diagram of the first setup is shown in Figure 4-3. Two CW laser beams are made co-linear using a 50/50 beam splitter (BS). It is important to notice that THz emission efficiency depends on a precise collimation of both beams. Beam intensity is regulated with a neutral density filter attenuator (A) as it is important not to damage the antenna. A lens (L) is used to focus the beam on the photoconductive antenna and PTFE (Teflon) screen is used to prevent infrared laser radiation to reach the Golay detector. A Golay detector manufactured by QMC Instruments Ltd [125] was used, but it seems that is no longer available. An almost identical unit is now offered by Tydex [68]. A mechanical chopper is used to modulate the beam, and its operation is coupled to a lock-in amplifier. As was explained in the previous chapters, the beam is modulated to reduce flicker noise content, unfortunately, due to the slow response of the Golay detector, modulation must be maintained at a maximum of 15 Hz, limiting the noise reduction. An IEMN spiral LT-GaAs antenna model SP8 was used. Setup is completed by two Spectra Physics Matisse tuneable ring lasers [126], seeded by two Spectra Physics Millenia Pro solid state lasers [127].
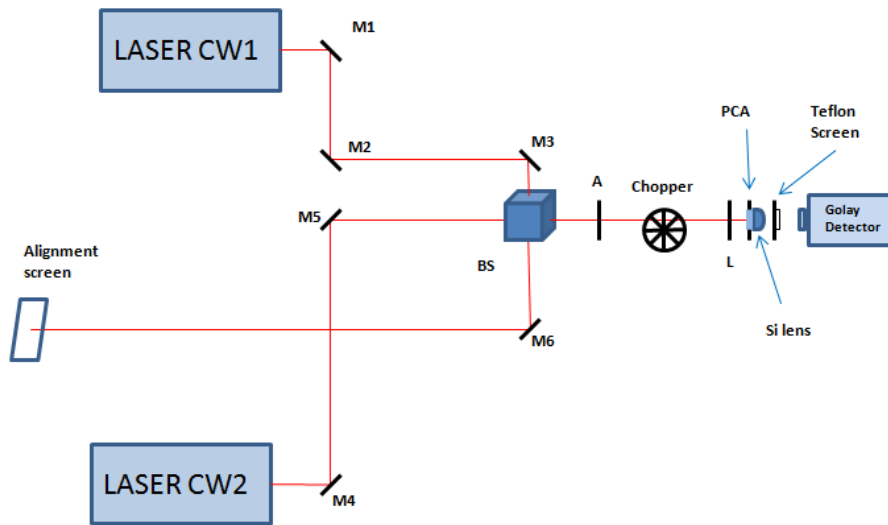
Figure 4-3. Photomixing setup 1.

4.2.1 Si lens positioning mechanism and mount

Operation of the photomixing antenna requires a silicon lens that is not attached, therefore a way of placing the lens had to be envisaged. The lens mounting should be able to make XYZ precision position adjustments whilst providing some spring mechanism in order to limit the amount of pressure posed on the antenna surface. The silicon lens positioning mechanism is based on a manual XYZ translation stage. A fibreglass ring serves as a holder, whilst a metallic computer slot bracket is used as a link between the holder and the translation stage. The bracket also provides a limited amount of pressure, enough to hold the lens in position, but not too much to damage the antenna (Figure 4-4). The photomixing antenna is mounted on a second XYZ translation stage, which facilitates alignment with the laser beam. A detail of the final arrangement, with the Si lens installed, is shown in **Error! Reference source not found.** The two XYZ mechanisms are shown in Figure 4-6.
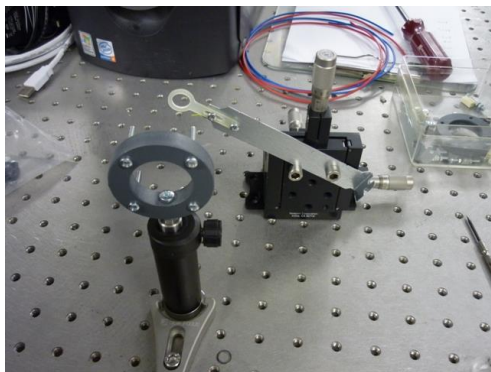
Figure 4-4. Si lens positioning mechanism.
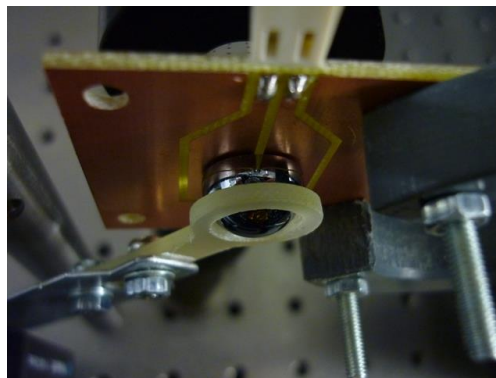
Figure 4-5. Si lens holder.
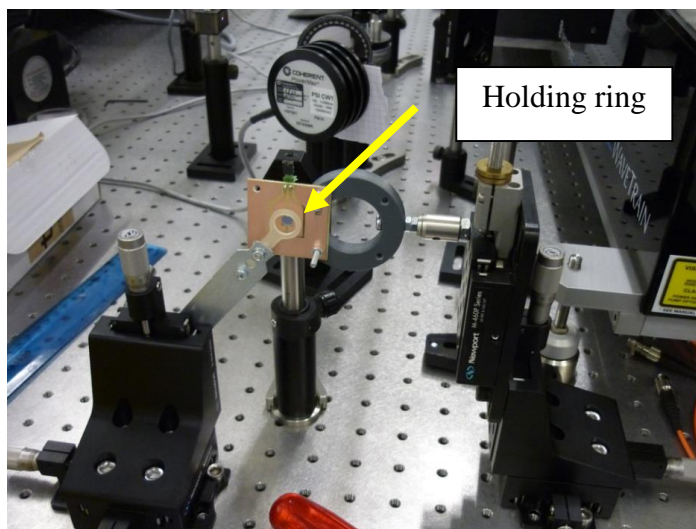
Figure 4-6. Photomixer antenna before installing the silicon lens.

4.2.2 Laser power adjust and alignment

Output power should be approximately the same on both lasers. This can be verified by placing a power meter after the chopper, and blocking alternatively each beam. Recommended operation power is 30 mW (average). Placing the power meter before the chopper should give a reading twice as high.

	Laser 1	Laser 2
Pump laser	6.75 W	8.19 W
Measured output power	750 mW	750 mW
Measured output power after attenuator (without chopper)	30 mW	30 mW

Table 4-1. Power adjust example.

Laser 1	380.184 THz
Laser 2	380.740 THz
Δf	556 GHz $\approx H_2O$ absorption

Table 4-2. Frequency mixing example.

Laser beams should be collinear, and they should be directed to the centre of the cube beam splitter. Alignment is verified by a two steps process at two different distances. In this way it can be guaranteed that the beams are overlapping instead of crossing in a single point.

A suggested procedure to verify alignment is as follows:

- Place a paper screen on M6 and then try to overlap the beam spot generated by laser 1 adjusting M2.
- Place a paper screen at the rear of the optical table (see
- Figure 4-3), then use M3 to do a finer adjustment.

For connecting the Photomixer the following procedure was followed:

- Turn on the DC Voltage Power Supply and adjust it to zero volts
- Connect it to the photomixer antenna. This is because of component sensitivity to electrostatic discharges
- Adjust DC Voltage to 15 V. Dark current < 10 nA @ 15 VDC
- The expected photocurrent is around 300 μA.

4.2.3   Antenna alignment

The antenna is mounted in a XYZ manual linear stage. Alignment is done by an iterative process:

- First XY (vertical plane, i.e. antenna's plane) should be varied for obtaining the highest amount of photocurrent
- Then a slight change in Z can be introduced. Wider movements of micrometres can be made in order to explore for a better region

It should be noticed that as the focal point is approached, the adjustment becomes more sensitive.

4.2.4   Terahertz generation test

In order to verify that Terahertz radiation is being generated, the bias voltage can be switched off and there should be an appreciable difference in the output measured with the Golay cell. Golay cells are very sensitive to vibration noise and they do not have a flat frequency response, mainly because of the transmission characteristics of the input window.

The Golay detector presented an intermittent response (on-off at slow frequency). The source of error was traced to be the overheating of integrated voltage regulators in the power supply unit, which entered in thermal shutdown. The solution was to open the power supply unit, to attach a couple of heat sinks and to place a fan above the unit (see Figure 4-7).
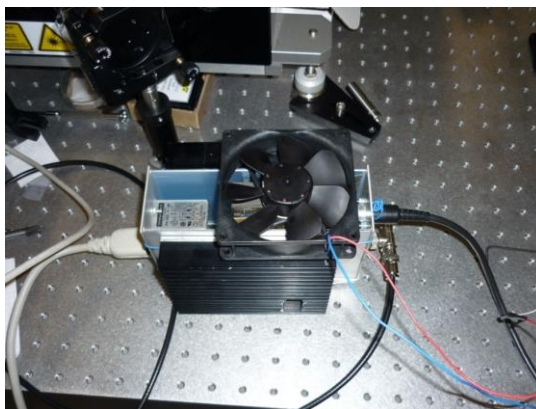
Figure 4-7. Cooling the Golay power supply.

Silicon lens are known to produce a virtual image between 10-20 mm behind the antenna plane. Taken this into account, the 101.2 mm EFL parabolic mirror is placed at approximately 90 mm from the antenna.

A screwdriver can be used to block some of the terahertz radiation (Figure 4-8), then an oscilloscope can be used to detect the maximum radiation point (minimal signal). The use of a low frequency time-base is convenient in this case. The screwdriver should be passed slowly in front of the mirror, both in vertical and horizontal position. The knobs in the mount are then adjusted to centre that point.
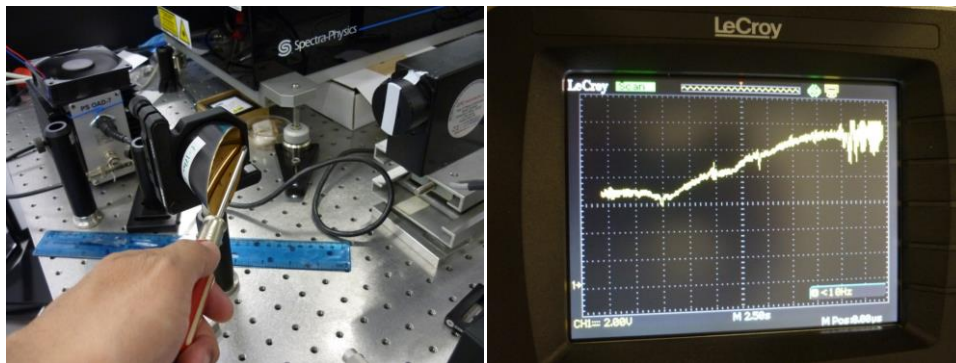
Figure 4-8. Aligning the parabolic mirrors.

It was explained in section 4.1 that the THz radiation produced will have a frequency equal to the difference frequency of the laser sources. The first experiment consisted in varying this difference frequency and measure the results. One laser was kept at a fixed 380.9301 THz and the other was progressively changed. The results are plotted in Figure 4-9. Output decays rolls-off as Δf increases, in agreement with equation (4-2), where THz power will decrease as ω increases.
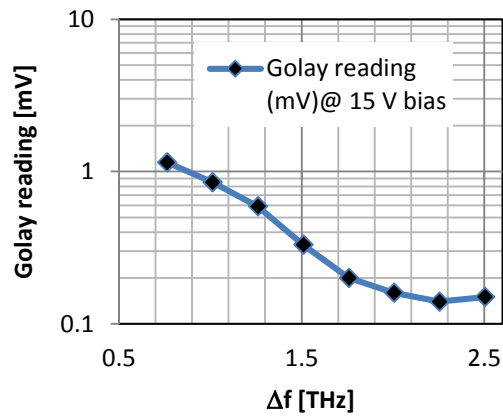
Figure 4-9. THz detection vs. Δf.

A second experiment was carried out using the setup shown of Figure 4-10. Two parabolic mirrors where used to modify the THz radiation path. In this case, the THz radiation versus the photocurrent was measured. Photocurrent was varied by changing the DC bias voltage between 0 and 15 V. Squared photocurrent vs. THz emission has been plotted in Figure 4-11, showing a linear relation which also agrees with equation (4-2).
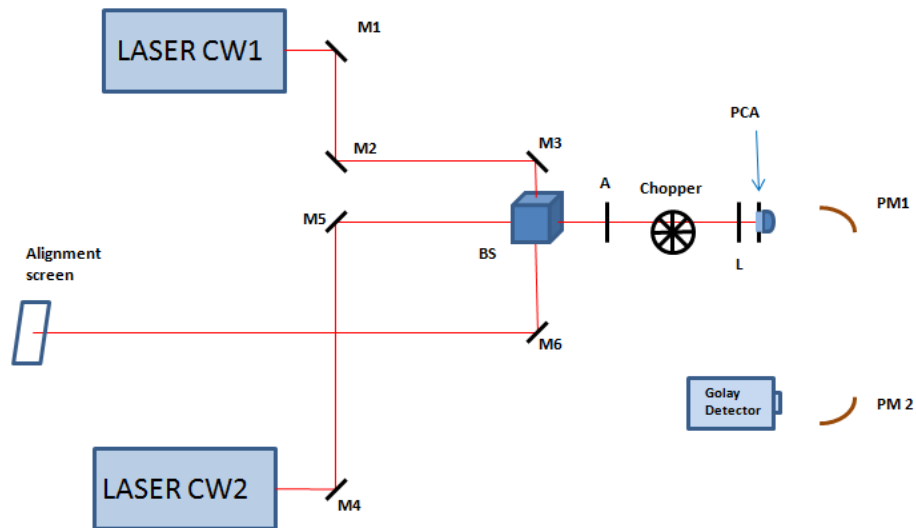
Figure 4-10. Photomixing setup 2.
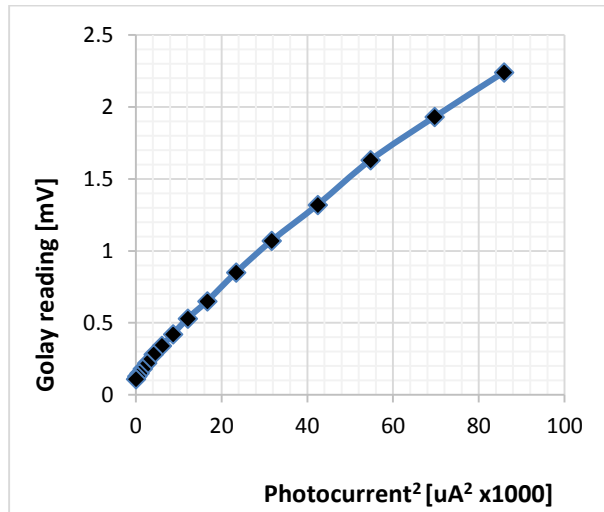
Figure 4-11. Squared photocurrent vs. THz emission.

The generation and detection of THz radiation using photomixing techniques has thus been demonstrated. THz generated power is lower than using a TDS system. A spectroscopy scan of a sample was not performed since it requires a time consuming manual adjustment of the lasers. On the other hand, a TDS system is able of perform it in a more automatic fashion.

THz generated by photomixing techniques are sensitive to laser thermal drifts which affect the absolute frequency value of the THz CW signal. In order to improve frequency accuracy, the relative phases between the two laser sources can be stabilized by using an optical phase-locked loop (OPLL) [128]. Stabilization of 1 MHz linewidth requires a delay below 2 ns and this is only possible using a photonic integration approach.

An example of this approach is presented in [129], where an optical frequency comb generator (OFCG) is used to produce a reference signal. Two lines of the OFCG, separated by the terahertz frequency that is required, are phase locked using two OPLLs. Each OPLL is based in an integrated twin distributed Bragg reflector laser. Their outputs are combined in a high-speed photodetector coupled to a suitable antenna (see Figure 4-12). This technique is able to produce high spectral purity signals with linewidths < 1 kHz, and its operation was demonstrated up to 300 GHz.
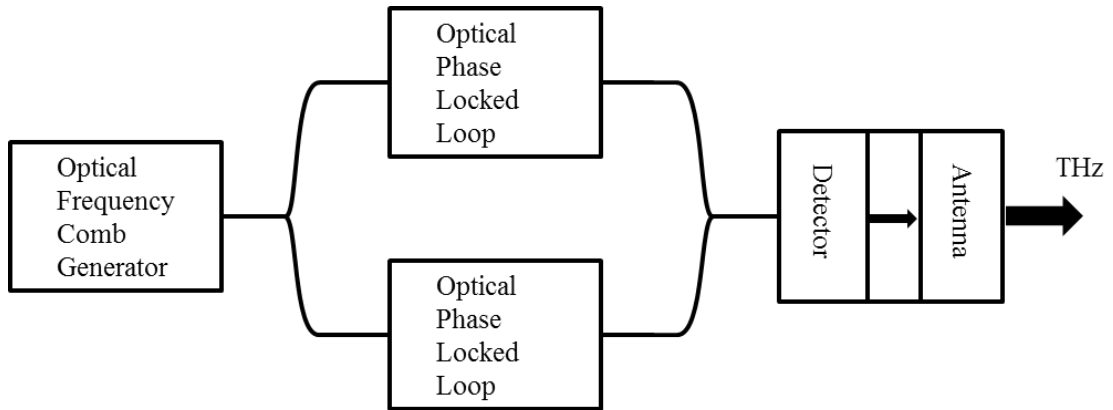
Figure 4-12. High spectral purity THz source [129].

The work in these THz photomixing experiments was done with the help of Dr. Francis Hindle from Laboratoire de Physico-Chimie de l'Atmosphère, Université du Littoral Côte d'Opale, France.

4.3 Summary

In order to gain insight in the operation of a CW THz system, a photomixing experiment was built and tested. A mount was designed to attach a Si lens to the antenna, whilst permitting enough movement for alignment. Two test were carried out: a frequency scan, and a antenna photocurrent scan. A frequency scan can be used to perform spectroscopy analysis, but given the lack of automation in the setting of operating frequencies of the two lasers, this operation was time-consuming. The squared antenna photocurrent showed a linear relation with THz power emission, in accordance with the theoretical model.

5 TERAHERTZ TOMOGRAPHY

5.1 Introduction

Since the early stages in the development of THz sources and detectors, there has been an interest in building imaging and tomography systems capable of operation at those frequencies [3, 130-132]. This development was motivated by potential industrial, medical and security applications [17, 133, 134]. Progress in these areas has been limited by the size, power and cost of THz sources [135, 136]. THz sources can produce pulsed or continuous waveforms (see chapter 2), but it can be envisaged that continuous wave (CW) THz sources, such as Quantum Cascade lasers (QCL) and photomixing techniques using diode fibre optic lasers will have an important role in tackling these problems [137-142]. Recently, a THz QCL operating at room temperature has been demonstrated [9].

A great part of THz imaging and tomography research has been done using pulsed THz sources [3-5, 48, 84, 143], exploiting its ability to produce images in time-of-flight contrast. However, in a THz-TDS system it is possible to separate the broadband frequency response of a THz pulse in its spectral components by using a Fast Fourier transform; therefore, the entire frequency response can be divided in individual frequency components that represent a portion of the original spectrum. These frequency components (frequency bins of limited bandwidth) can be used to study imaging in amplitude contrast, which is the only operational mode available to CW THz tomography systems. A THz-TDS system has the advantage that the information of all frequency components, in the THz system bandwidth, is obtained by acquiring a single radiation pulse, whereas performing a frequency scan using other techniques could take more time to be carried out. It is important to emphasize, that however small is the frequency content in a frequency bin, it still will be composed of a range of frequencies, whereas a CW THz system may produce a single frequency (narrow band). Besides this, in a THz-TDS system, the power is spread among all frequency components and for systems that only

require information on a narrow bandwidth a CW source would be a more efficient alternative. Previous work done at the University of Manchester on hard-field THz tomography [144], was used as a departure point to study the influence of frequency/wavelength on image quality.

5.2 Computerized tomography

Computerized tomography is a mathematical procedure where an image containing information on a property of the internal structure of an object is reconstructed from peripheral measurements. This reconstruction is done by measuring the transmission or reflection of some type of radiation in a cross-section plane of the object. A 3D reconstruction is possible if a set of measurements at different cross-sections over an axis are taken. The word tomography is derived from the Greek word τόμοζ, which means slice or section.

As an example of transmission tomography, consider a cylinder with an inner cylindrical bore and a cross-sectional measurement plane, as shown in Figure 5-1A. Both radiation source and detector are placed in the same plane that the selected cross-section. If radiation intensity is measured (amplitude contrast), then it is possible to reconstruct an image containing information on beam attenuation as it propagates through the object (Figure 5-1B). It is also possible to measure the time of arrival, and in this case and image mapping the refractive index of the object can be generated. A THz-TDS system is capable of performing measurements either on amplitude or time-of-flight, which is a flexibility that has been exploited in the development of THz tomography systems.

Most tomography systems employ an array of simultaneous parallel beams or an array of fan beams to speed up the data collection (a parallel beam array case is depicted in Figure 5-1C). In the implemented THz-TDS system, only one THz beam can be produced and detected, therefore the object must be displaced to generate the equivalent of a parallel beam array. Information collected from a set of parallel beams is called *projection*. In order to reconstruct an image, several projections at different rotation angles are required (Figure 5-1D). The internal structure of the object at the cross-sectional plane with axis

x, and y can be modelled by a function $f(x, y)$. In 1917, Radon demonstrated that a function in $\mathbb{R}^2$ is completely defined by the set of *all* possible projections [145]. In a practical case, it is only possible to get a measurement from a fixed the number of beams in a projection and from a fixed number of projections (at different rotation angles), imposing a limit to the quality of the reconstructed image, which therefore is always an approximation.
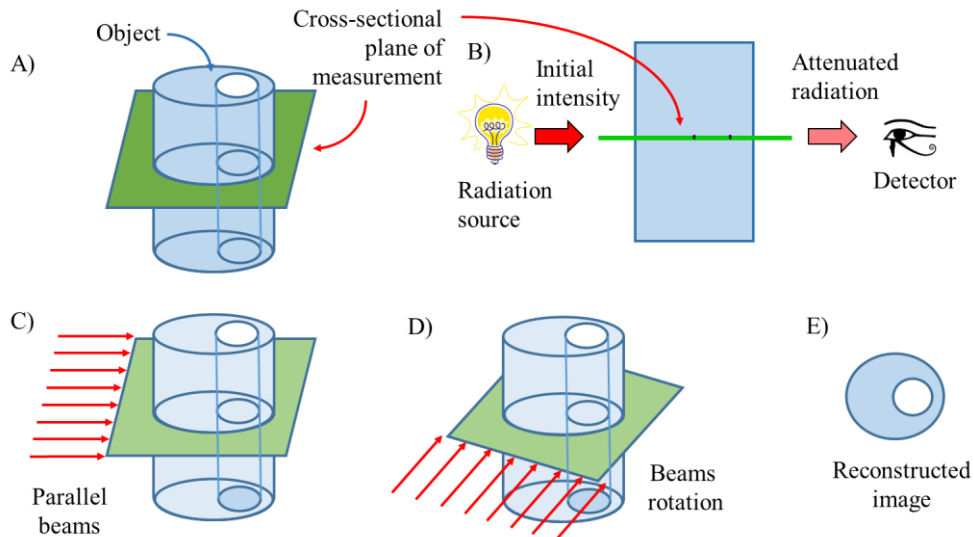
Figure 5-1. Tomography data collection process. A) Object and cross-sectional plane. B) Measurements are taken in the cross-sectional plane C) An array of parallel beams is applied to the object. D) The array of beams is applied at a different angle. E). Tomography reconstructed image.

The beams are partially attenuated as they go through the object, and this is the result of absorption and scattering. This attenuation can be model using the Beer-Lambert's law

$$I = I_0 e^{-\mu x} \tag{5-1}$$

Where I_0 is the initial beam intensity, I is the beam intensity after going through the object, x is the object thickness (beam path length through the object), and μ is the *attenuation coefficient*.

$$\mu = \mu_s + \mu_a \tag{5-2}$$

141

Where μ_s is the scattering attenuation coefficient and μ_a is the absorption coefficient [146].

Beer-Lambert's law can also be used for a material with a varying absorption coefficient (see Figure 5-2). In this case, considering a pixel of size Δx equation (5-1) can be generalized to

$$I = I_0 e^{-\mu_1 \Delta x} e^{-\mu_2 \Delta x} e^{-\mu_3 \Delta x} \cdots e^{-\mu_n \Delta x} = I_0 e^{-\sum_{n=1}^{N} \mu_n \Delta x} \qquad (5\text{-}3)$$

Which can be expressed as

$$p = -Ln\left(\frac{I}{I_0}\right) = \sum_{n=1}^{N} \mu_n \Delta x \qquad (5\text{-}4)$$

In the limit when $\Delta x \to 0$,

$$p = -Ln\left(\frac{I}{I_0}\right) = \int_L \mu(x) dx \qquad (5\text{-}5)$$

Where p is one point of the projection, defined as the line integral of absorption coefficients along the beam path.
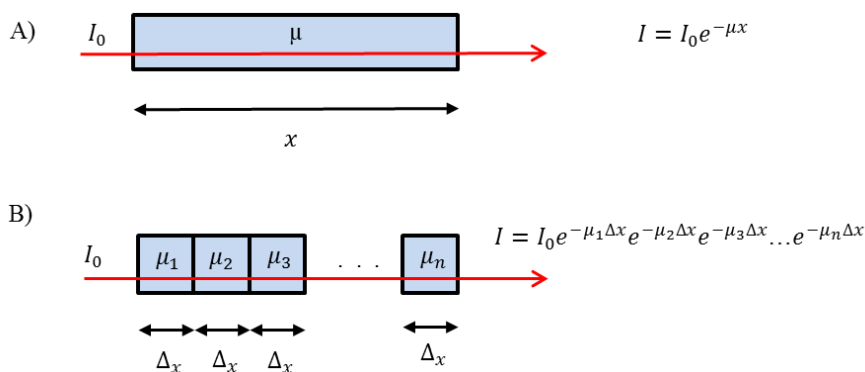
Figure 5-2. Beer-Lambert's law of absorption. A) Through a homogenous material. B) Through a material with varying absorption coefficient.

142

5.2.1 The Radon transform

In the previous section, it was mentioned that the tomography procedure requires the acquisition of several projections at different angles. Figure 5-3 shows how a projection is generated by lateral displacement of the probing beam relative to the object (scanning). A series of line integrals produce a projection which is a function of the displacement t, and each line trajectory is defined in polar coordinates by

$$x cos\theta + y sin\theta = t \tag{5-6}$$

where θ is the rotation angle, and t is the distance to the origin.
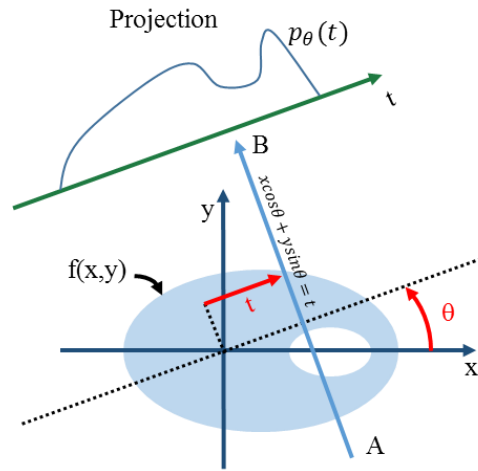
Figure 5-3. Details on the tomography procedure (adapted from [147]).

Then, the projection is defined by the set of line integrals

$$p(\theta, t) = \int_{(\theta,t)line} f(x,y)ds \tag{5-7}$$

and using a delta function

$$p(\theta, t) = \iint_{-\infty}^{\infty} f(x,y)\delta(x cos\theta - y sin\theta - t)dxdy \tag{5-8}$$

which defines the Radon transform of the object $f(x,y)$. The Radon transform is an integral transform and is a continuous map from $L^1(\mathbb{R}^2)$ to $L^1([0, 2\pi], \mathbb{R})$ spaces; this means that the object $f(x,y)$ will be mapped by the projections at all angles $\theta \in [0, 2\pi]$.

143

5.2.2 The reconstruction problem

The two dimensional Fourier transform of the object is given by

$$F(u,v) = \iint_{-\infty}^{\infty} f(x,y)e^{-j2\pi(ux+vy)}dxdy \qquad (5\text{-}9)$$

At this point, it is not possible to calculate the Fourier transform of the object, because the function $f(x,y)$ is unknown. The reconstruction approach is based on obtaining an estimation of $F(u,v)$ by experimental sampling and then apply an inverse Fourier transform to get $f(x,y)$ (see Figure 5-4)
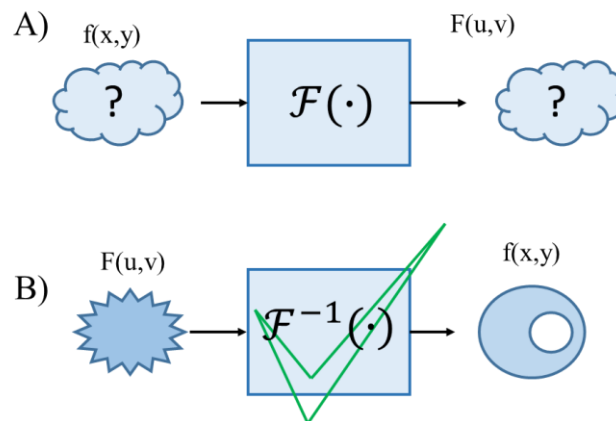
Figure 5-4. Reconstruction strategy is based on sampling the Fourier transform of the object and applying inverse Fourier transform. A) The object function is unknown so it is not possible to get F(u,v) directly. B) An under-sampled F(u,v) can be used to reconstruct the object function by using an inverse Fourier transform.

5.2.3 The Fourier slice theorem

Given an object $f(x,y)$ with a projection $p(\theta,t)$ at a fixed angle θ (see Figure 5-5) and its one-dimensional Fourier transform defined by

$$S_\theta(\omega) = \int_{-\infty}^{\infty} p_\theta(t)e^{-j2\pi\omega t}dt \qquad (5\text{-}10),$$

Consider a rotated coordinate system (t,s) defined by (see Figure 5-5)

$$\begin{bmatrix} t \\ s \end{bmatrix} = \begin{bmatrix} cos\theta & sin\theta \\ -sin\theta & cos\theta \end{bmatrix} \begin{bmatrix} x \\ y \end{bmatrix} \qquad (5\text{-}11)$$

In the new coordinate system a projection made of lines parallel to s-axis is given by

$$p_\theta(t) = \int_{-\infty}^{\infty} f(t,s)ds \tag{5-12}$$

Substituting in (5-10),

$$S_\theta(\omega) = \iint_{-\infty}^{\infty} f(t,s)\, e^{-j2\pi\omega t} ds dt \tag{5-13}$$

using (5-11)

$$S_\theta(\omega) = \iint_{-\infty}^{\infty} f(x,y)e^{-j2\pi\omega(x\cos\theta + y\sin\theta)}dxdy \tag{5-14}$$

and defining a change from Cartesian to polar coordinates

$$\begin{aligned} u &= \omega\cos\theta \\ v &= \omega\sin\theta \end{aligned} \tag{5-15}$$

$$S_\theta(\omega) = \iint_{-\infty}^{\infty} f(x,y)e^{-j2\pi\omega(ux + vy)}dxdy \tag{5-16}$$

which is equal to the definition of a two-dimensional Fourier transform given in (5-9). From this, the Fourier slice theorem can be stated as:

"The Fourier transform of a parallel projection of an object $f(x,y)$ obtained at an angle θ equals a line in a 2D Fourier transform of $f(x,y)$ taken at the same angle" [148]. That is

$$F(\omega\cos\theta, \omega\sin\theta) = S_\theta(\omega) \tag{5-17}$$
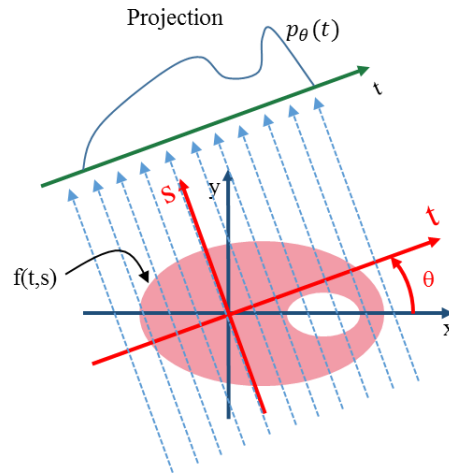
Figure 5-5. Projection on a rotated coordinate system.

A graphical representation is depicted in Figure 5-6. For each projection angle, a scan of the 2D Fourier Transform is made (a slice) and an accurate reconstruction is be possible if a large number of projections can be acquired.
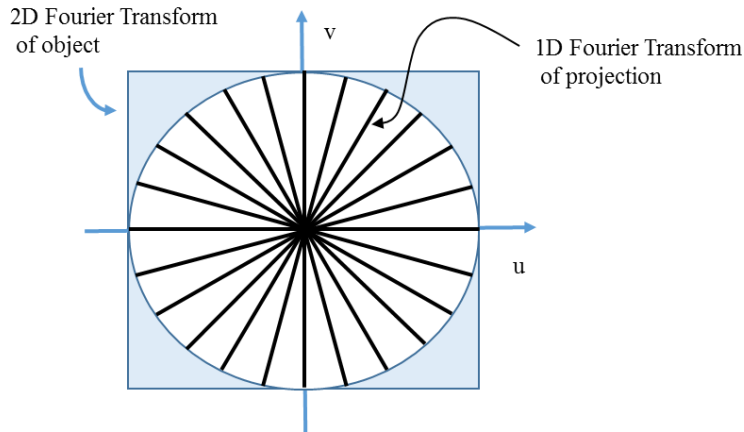
Figure 5-6. Graphical representation of the Fourier slice theorem.

5.2.4   The filtered back-projection algorithm

The object function $f(x, y)$ can be obtained by performing an inverse Fourier transform

$$f(x,y) = \iint_{-\infty}^{\infty} F(u,v)e^{j2\pi\omega(ux+vy)}\,du\,dv \qquad (5\text{-}18)$$

using a coordinate transformation given by (5-15), and calculating the new differential using the Jacobian determinant

$$du\,dv = \begin{vmatrix} \partial u/\partial\omega & \partial u/\partial\theta \\ \partial v/\partial\omega & \partial v/\partial\theta \end{vmatrix} d\omega\,d\theta = \omega\,d\omega\,d\theta \qquad (5\text{-}19)$$

$$\begin{aligned} &f(x,y) \\ &= \int_{0}^{2\pi} d\theta \int_{0}^{\infty} F(\omega cos\theta, \omega sin\theta)e^{j2\pi\omega(xcos\theta+ysin\theta)}\omega\,d\omega \end{aligned} \qquad (5\text{-}20)$$

Using the Fourier slice theorem

$$f(x,y) = \int_0^{2\pi} d\theta \int_0^\infty S_\theta(\omega) e^{j2\pi\omega(x\cos\theta+y\sin\theta)} \omega d\omega \qquad (5\text{-}21)$$

$$
\begin{aligned}
f(x,y) \\
= \int_0^\pi d\theta \int_0^\infty S_\theta(\omega) e^{j2\pi\omega(x\cos\theta+y\sin\theta)} \omega d\omega \\
+ \int_0^\pi d\theta \int_0^\infty S_{\theta+\pi}(\omega) e^{j2\pi\omega(x\cos(\theta+\pi)+y\sin(\theta+\pi))} \omega d\omega
\end{aligned}
\qquad (5\text{-}22)
$$

Projections present a symmetry property, which is explained graphically in Figure 5-7,

$$p_{\theta+\pi}(t) = p_\theta(-t) \qquad (5\text{-}23)$$
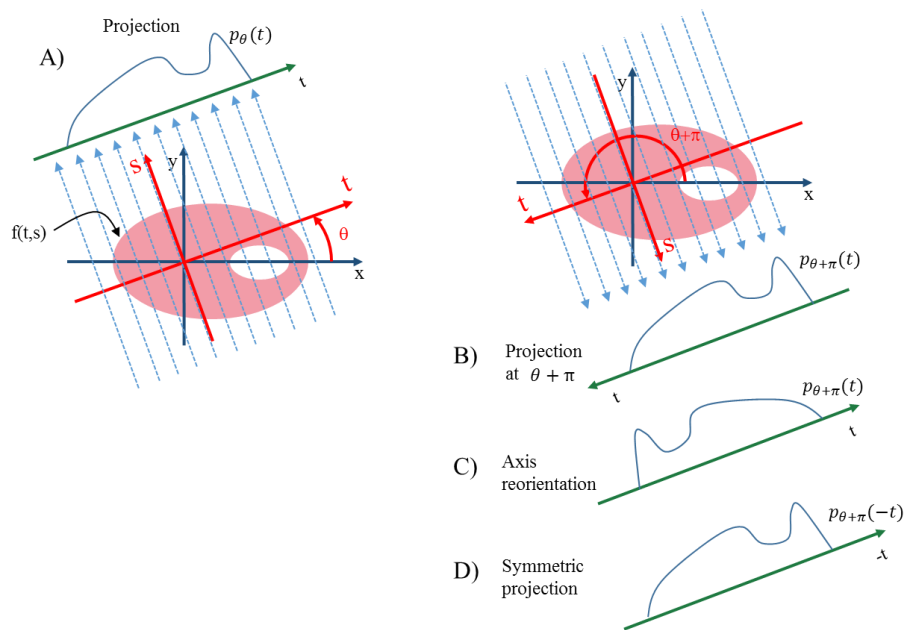
Figure 5-7. Symmetry of a projection. A) Original projection at angle θ. B) Projection at angle θ+π. C) Axis *t* is reoriented to match original projection. D) Symmetry is obtained if variable *t* is changed for –*t*.

and also in the Fourier domain

$$S_{\theta+\pi}(\omega) = S_\theta(-\omega) \qquad (5\text{-}24)$$

Therefore the same data is obtained by projections that are 180º apart. In the case of a Beer-Lambert attenuation law, this means that giving a line integral, attenuation is independent of the direction. From (5-22) and (5-24), it is possible to write

$$
\begin{aligned}
f(x,y) \\
= \int_0^\pi d\theta \int_0^\infty S_\theta(\omega)\omega e^{j2\pi\omega(x\cos\theta+y\sin\theta)}d\omega \\
+ \int_0^\pi d\theta \int_0^\infty S_\theta(-\omega)\omega e^{-j2\pi\omega(x\cos(\theta)+y\sin(\theta))}d\omega
\end{aligned}
\tag{5-25}
$$

Changing the integration limits

$$
\begin{aligned}
f(x,y) \\
= \int_0^\pi d\theta \int_0^\infty S_\theta(\omega)\omega e^{j2\pi\omega(x\cos\theta+y\sin\theta)}d\omega \\
+ \int_0^\pi d\theta \int_{-\infty}^0 S_\theta(\omega)(-\omega)e^{j2\pi\omega(x\cos\theta+y\sin\theta)}d\omega
\end{aligned}
\tag{5-26}
$$

and

$$
f(x,y) = \int_0^\pi d\theta \int_{-\infty}^\infty S_\theta(\omega)|\omega|e^{j2\pi\omega t}d\omega
\tag{5-27}
$$

where $S_\theta(\omega)$ is the Fourier transform of a projection at angle θ. The inner integral is the inverse Fourier transform of a product of two functions $S_\theta(\omega)$ and $|\omega|$. Since this product corresponds to the convolution of two functions in the space domain, the term $|\omega|$ constitutes a filter function which gives origin to the name "filtered projection". This filtered projection can be expressed as

$$
\begin{aligned}
g_\theta(t) = g_\theta(x\cos\theta + y\sin\theta) \\
= \int_{-\infty}^\infty S_\theta(\omega)|\omega|e^{j2\pi(ux+vy)}d\omega
\end{aligned}
\tag{5-28}
$$

and equation (5-27) can be rewritten as

$$
f(x,y) = \int_0^\pi g_\theta(x\cos\theta + y\sin\theta)d\theta
\tag{5-29,}
$$

which is known as the *backprojection operator*, where $x cos\theta + y sin\theta$ defines a projection line (see Figure 5-3); therefore, the reconstructed image at point (x,y) is the result of the integration (summation) of all projections ($0 \leq \theta \leq \pi$) that pass over that point.

The Fourier transform of a sample Radon projection is defined in polar coordinates, whereas the image is reconstructed in a space of Cartesian coordinates. A differential element of area in polar coordinates does not have a constant size, as it is the case in Cartesian coordinates (see Figure 5-8), this means that the central area is sampled heavier which incorrectly enhances the centre (low frequencies). This effect is compensated by the weighting function $|\omega|$ that appears in equation (5-27). A typical weighing function is

$$wf = 2\pi|\omega|/K \tag{5-30}$$

where K is the number of projections.
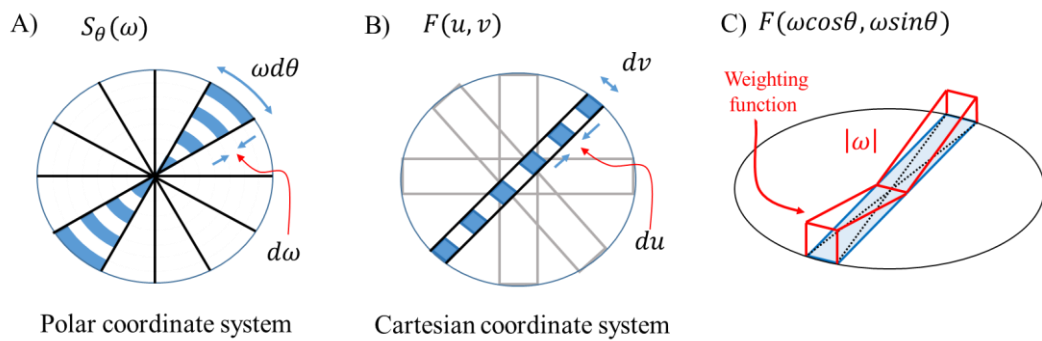
Figure 5-8. Filtered backprojection. A) Radon projection is defined in polar coordinates and a differential element of area is not constant. B) A differential element of area is constant in Cartesian coordinates. C) Changing the coordinate system introduces a weighting factor $|\omega|$ that compensates this difference and acts as a filter for the backprojection.
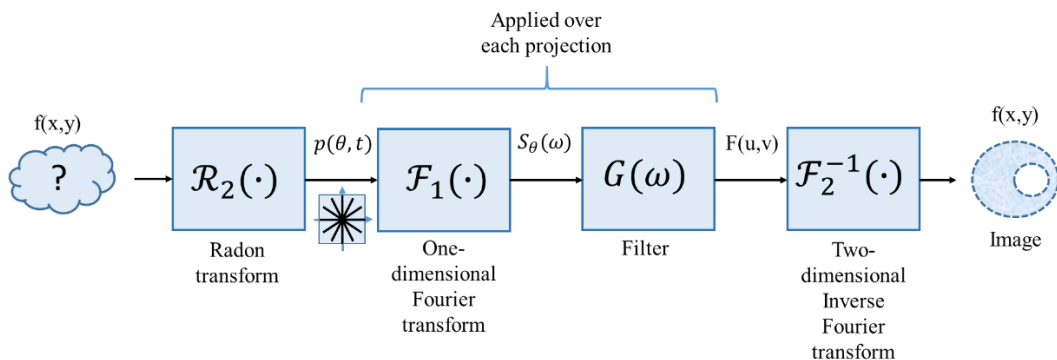
Figure 5-9. Block diagram of the filtered back-projection algorithm.

5.3 THz computerized tomography system

In chapter 3, the development of a THz system with four parabolic mirrors was presented. This mirror arrangement has the capacity of generating a focused THz beam which is useful for spectroscopy tests. The system is now further modified in order to make it capable of perform computerized tomography tests. A linear and a rotation table were added to perform object scans.

In hard-field tomography, the sensitivity of the detector must be independent of the parameter distribution in the system [149], therefore the beam must propagate in a straight line so any effect on the signal is only produced by its propagation along its path [150]. In order to reduce the detection of scattered beams, two iris diaphragms were introduced in the path to reduce the effects of scattering. A schematic diagram of the system is presented in Figure 5-10. The refractive index of the scanned object has a big influence in the quality of the images obtained by THz tomography in amplitude contrast; therefore the use of a low refractive index such as Styrofoam (n≈1.02) was preferred for the purposes of this research. A phantom composed of a small cylinder and a larger half cylinder was selected as prototype since there was previous work done with this configuration carried out at The University of Manchester [144].

As it was mentioned above, the THz-TDS system can only produce a single beam; therefore the object has to be translated using a motorized linear stage, and several measurements must be made to generate a single projection $p_\theta(t)$. In order to implement this, a Melles Griot linear stage capable of 100 mm displacement was used. A rotation stage was built using a DC servomotor, which is controlled by a National Instruments NI-DAQ chassis (NI cDAQ-9172) and a digital I/O module (NI 9401 8-Channel TTL). The rotation stage was calibrated to produce 7.5° degree steps over a 180° span. Filtered backprojection may present noise sensitivity and geometric degradation if a sufficient number of projection is not acquired [151]; however, a larger number of angular steps was not attempted in order to limit the duration of a tomography scan. In conjunction, these two stages provide for a working area of a circle of 100 mm diameter. The iris diaphragms before and after the object were placed as close as possible without interfering with the stages movement, in order to minimize the intensity drop that they produce. A

block diagram of the THz-TDS Tomography system is shown in Figure 5-10; at the centre, the two added stages for linear and rotation movement of the phantom are indicated. These stages tare controlled from a PC through USB links. A connection diagram of the instruments associated with the THz computerized tomography system is shown in Figure 5-11, and a picture of the optical table with the system installed is shown in Figure 5-12. With the exception of the computer screen and keyboard/mouse, all the instruments where installed in an overhead table for security reasons.
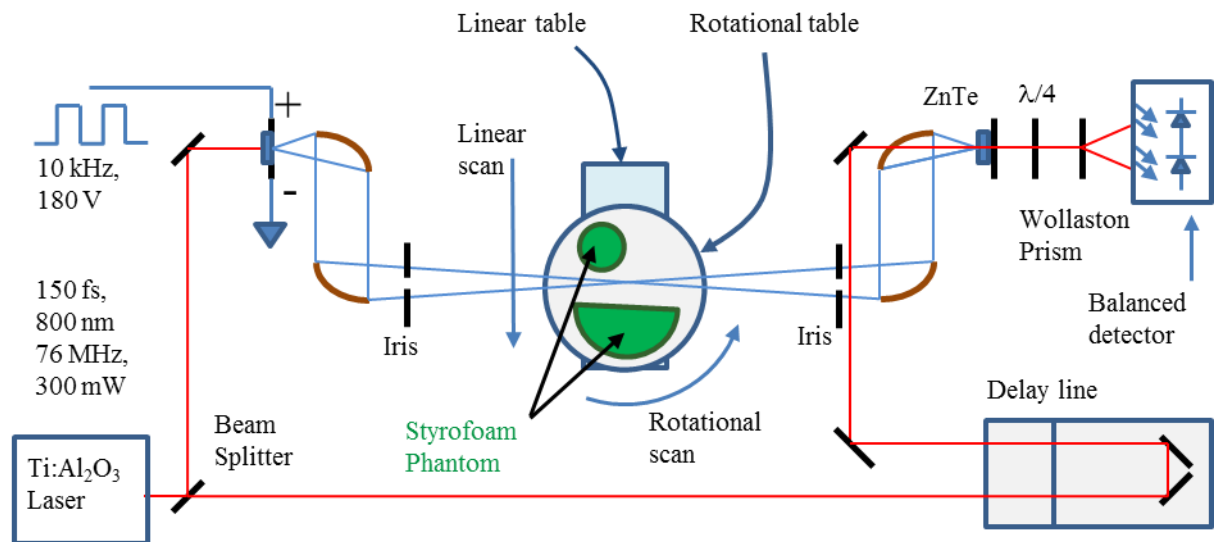
Figure 5-10. Schematic diagram of the THz tomography setup.
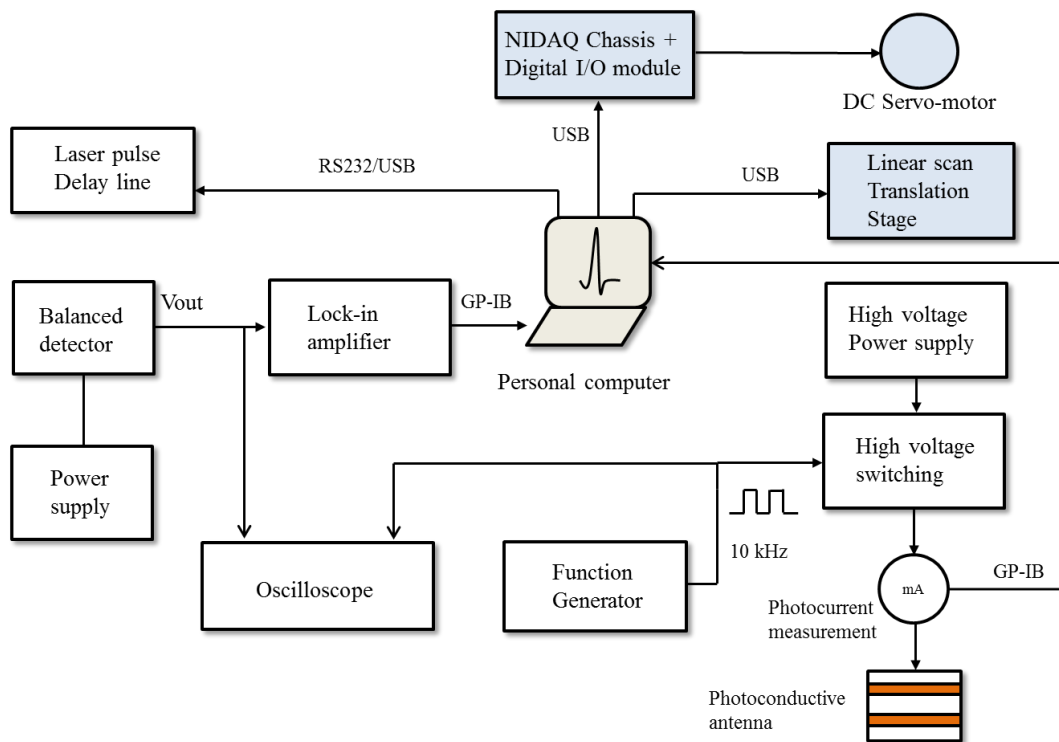
Figure 5-11. Block diagram of the instrumentation associated with the THz tomography system.
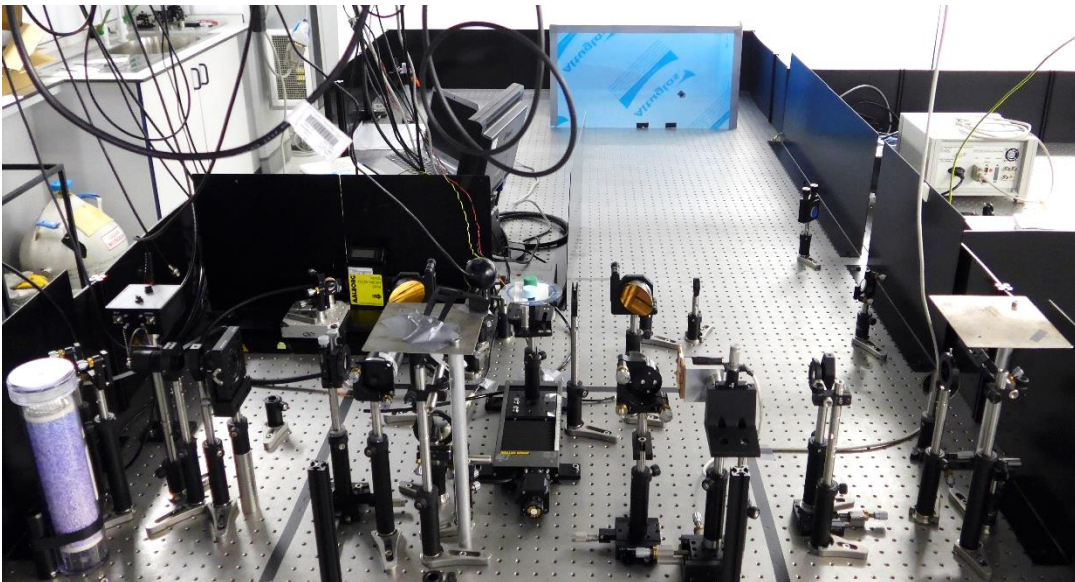
Figure 5-12. The THz tomography system installed at Photon Science Institute. The linear and rotation stages in charge of moving the phantom are at the centre.

5.4 Signal acquisition program

The control program for the THz-TDS system was modified to include the control of the two new motorized stages, and to store the collected data. The new program control window is shown in Figure 5-13. The controls for the linear and rotation stage are located in the lower right corner. Linear scans of down to 0.2 mm were tested (calibrated accuracy is 1 µm, and 15 µm uncalibrated), but most tomography scans were done with 1 mm linear steps and 7.5° angular increments (no accuracy data available). The window shows the current THz pulse acquisition, and the spectrum of the last complete scan. Data is saved in text format and several MATLAB programs were developed for their analysis and for image reconstruction. The program can control the full span of the linear stage (100 mm) at 50 nm resolution, and the full span of the rotation stage (180º) with angular increments in multiples of 7.5º. However, the working area was defined to be a circle of 60 mm diameter. The program registers the antenna photocurrent at the beginning of each pulse scan, which serves as a way of monitoring the laser power, along with the parameters of the test: initial position, step size, delay, and time-constant. The operation of the tomography system was monitored remotely using Microsoft remote desktop, which also has an Android application for mobile phones.
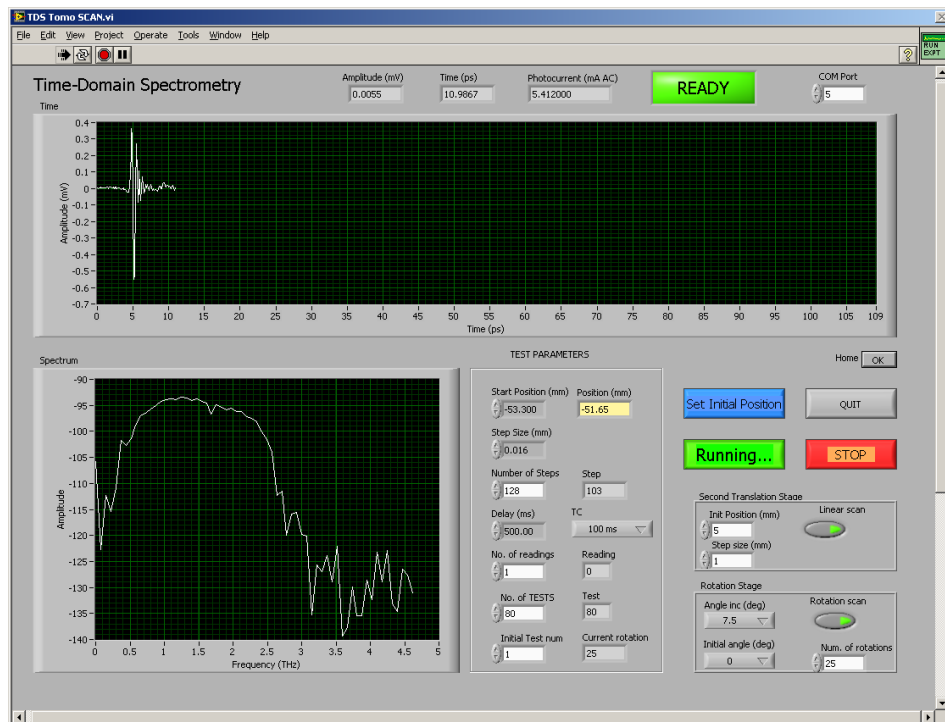
Figure 5-13. THz tomography program control window.

A simplified flow diagram of the program is shown in Figure 5-14. It consists of three nested loops for controlling the two linear stages and the rotation stage. A single pulse scan consists on the acquisition of a THz time-domain pulse at a single position. One projection is then made from a series of single pulse scans at different positions (typically between 40 and 80), which is controlled by the linear position stage. Once a projection has been acquired, the linear position stage is reset and the rotation stage angle is incremented. This procedure is repeated until the object has been rotated by180°.
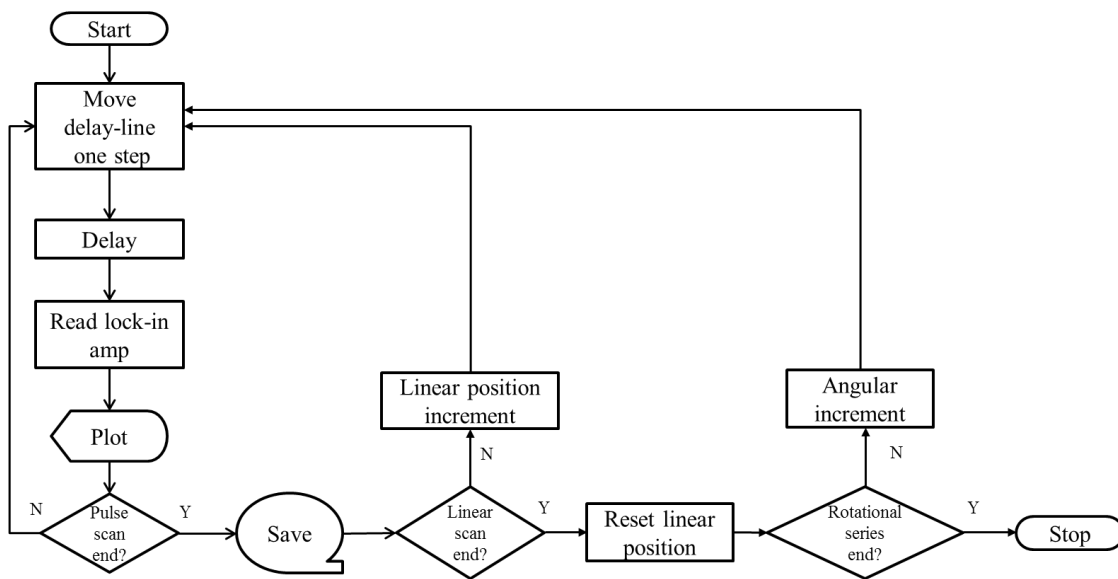
Figure 5-14. Simplified flow diagram of the THz computerized tomography program.

5.5 Beam apertures

For an appropriate image reconstruction, it is important that the beam keeps a constant profile. In order to determine if this condition is met, the Rayleigh range of the beam was experimentally determined. The Rayleigh range is an important parameter since it defines the length over which lateral resolution can be maintained [152].

The beam incident to the object comes from a metallic off-axis parabolic mirror which focuses the THz and it is then passed through a 4 mm circular aperture which is at 7 cm form the focal point. If the intensity profile is Gaussian, the beam will have a varying waist, as shown in Figure 5-15, and defined by

154

$$w(z) = w_0 \sqrt{1 + \left(\frac{z}{z_0}\right)^2} = w_0 \sqrt{1 + \left(\frac{z\lambda}{\pi w_0}\right)^2} \qquad (5\text{-}31)$$

where w_0 is the minimum radius, and z_0 is the *Rayleigh range*,

$$z_0 = \frac{\pi w_0^2}{\lambda} \qquad (5\text{-}32)$$

where z_0 defines the region where the beam approximates a plane wave and presents small divergence. This is also called the *near-field* or *confocal region* [153], and it defines a region where the size of the beam waist is lower than $w_0\sqrt{2} = 1.41w_0$. If the working area in a tomography system is centred on the minimum waist position ($z=0$), then the total working range will be given by twice the Rayleigh range ($2z_0$).
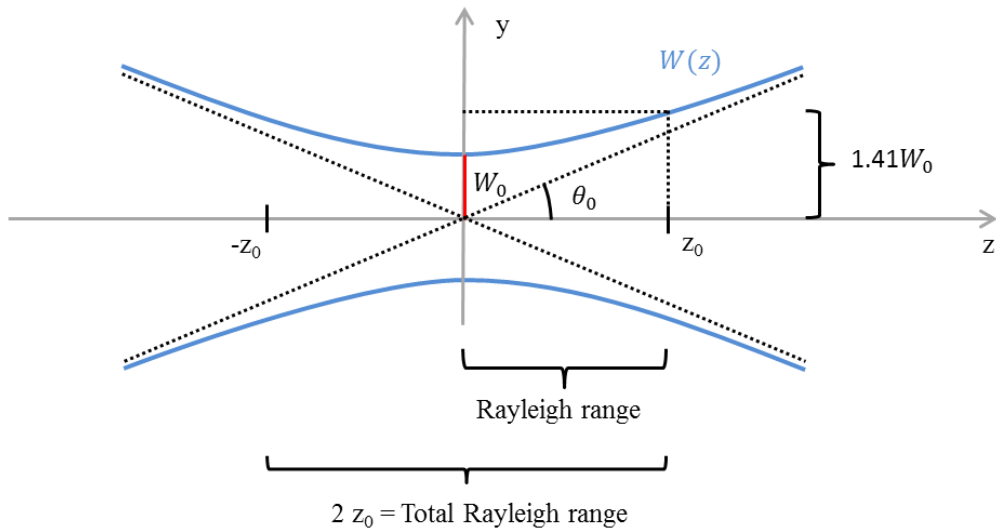
Figure 5-15. Beam waist and Rayleigh range of a Gaussian beam.

The phantom is placed in the middle of two off-axis parabolic mirrors as shown in Figure 5-16. Two apertures are placed in the beam path in order to limit the detection of scattered radiation. The use of apertures limits the beam waist which should increase the resolution of the image.
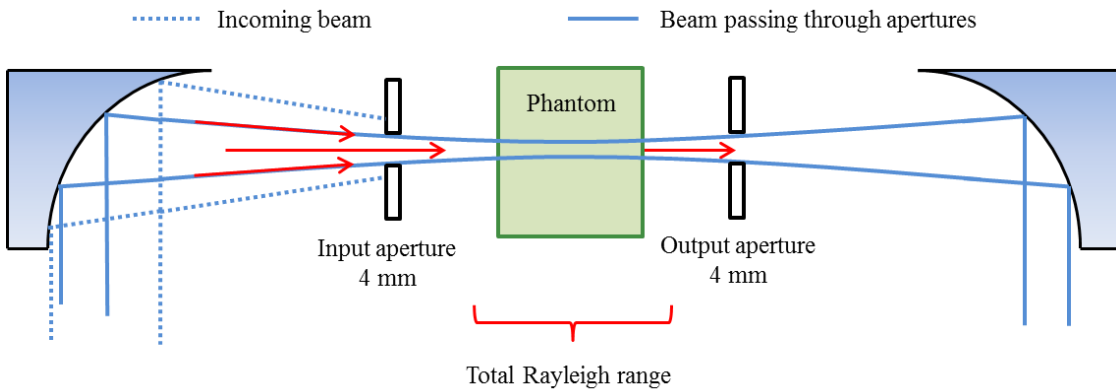
Figure 5-16. Schematic diagram showing beam trajectory, apertures and phantom.

In order to determine the Rayleigh range of the THz beam that is passing through an aperture of 4 mm diameter, a knife edge short test was performed [154]. A new 18 mm knife blade made of SK2 steel was used. The blade was mounted on a linear translation stage and it was moved in front of the THz beam at 0.2 mm steps, a THz pulse waveform was recorded for each position. The selected knife edge method estimates the waist by measuring the power when the knife is blocking 10% and 90% of beam power using the following expression

$$w_z = x_{10\%-90\%}/1.28 \tag{5-33}$$

Where $x_{10\%-90\%}$ is the position difference for a 10% and 90% blocked beam. A GUI was developed for determining the $x_{10\%-90\%}$ value, but the presence of noise makes difficult to define the 100% value and this can introduce some errors in the estimation of w_z (see Figure 5-17. The inset in that figure shows the blade knife mounted in the system. The GUI performs a normalization and a polynomial interpolation for improving the resolution. Values at 90% and 10% amplitude are taken manually using a cursor. Results for the Rayleigh range are plotted in Figure 5-18. The total working range is twice Z_0 (Total Rayleigh range) and for a working area of 60 mm diameter, a minimum $2Z_0=60$ mm is required. This condition is met only for a few frequencies between 0.5 THz and 1.0 THz. Out of that range the total Rayleigh range is around 30 mm, and for a 60 mm working range the beam waist would be $w_0\sqrt{5} = 2.24w_0$ which means that the image resolution may be degraded.

156
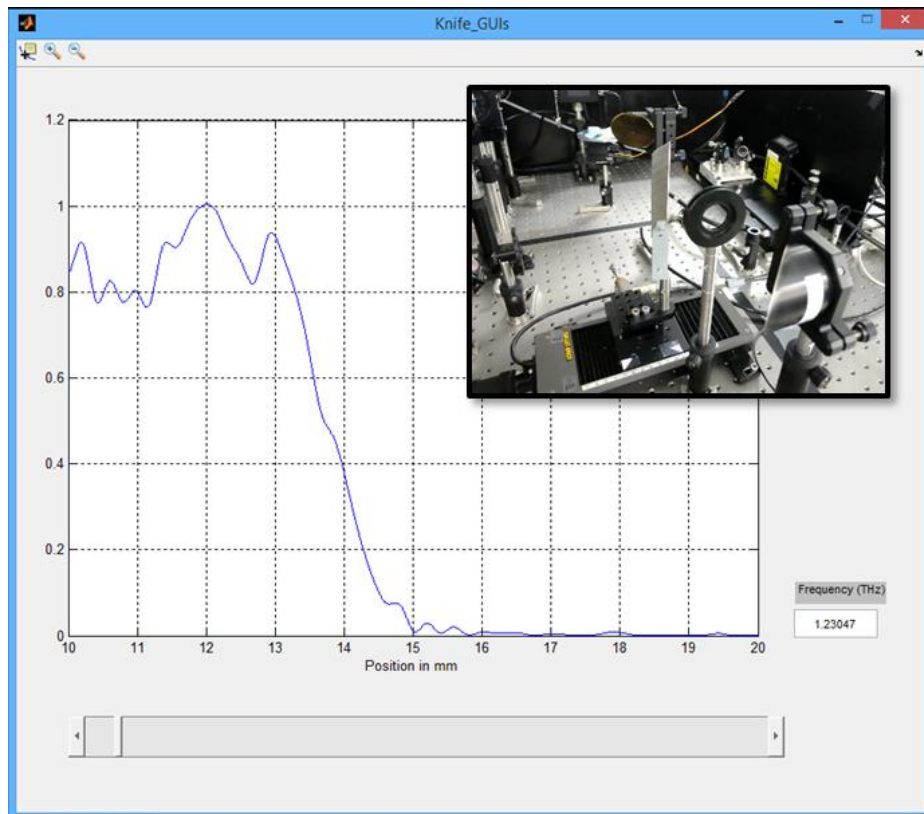
Figure 5-17. GUI for evaluating the $x_{10\%-90\%}$ value in a knife edge test. Inset: Picture of the blade knife installed in the system.
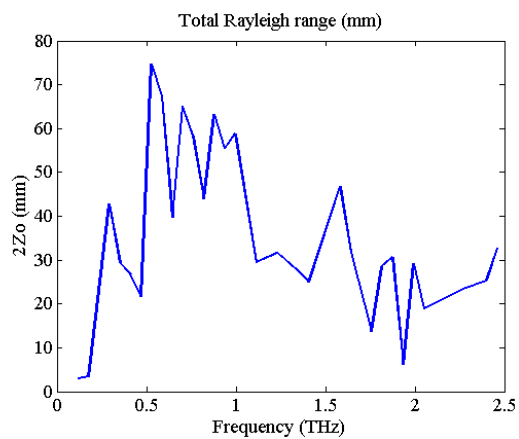
Figure 5-18. Rayleigh range with a 4 mm aperture.

F (THz)	$2 \cdot Z_0$ (mm)
0.586	67
0.703	65
0.996	59
1.231	32
1.582	47
1.758	14
1.992	29
2.461	33

Table 5-1. Total Rayleigh range for some representative frequencies.

The waist radius w_0 was also calculated and the results are plotted in Figure 5-19. The beam waist decreases as frequency increases, which corresponds to a shorter wavelength. The beam diameter is below 2.6 mm for frequencies above 0.5 THz, and this size represents the lateral resolution, that is, the resolution between adjacent projection points. At frequencies below 0.5 THz, lateral resolution degrades quickly as frequency is reduced.
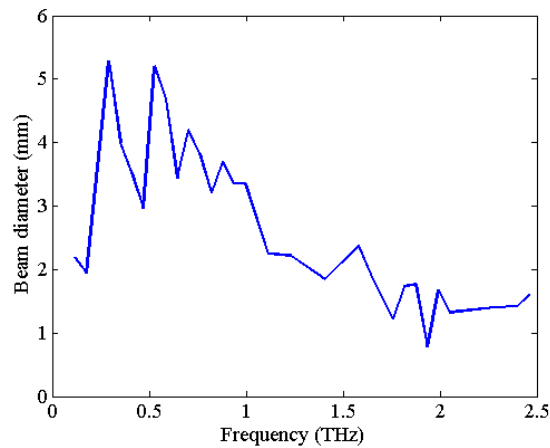
Figure 5-19. Waist radius after a 4 mm aperture.

It was found that the use of an aperture not only reduces the signal amplitude but also modifies the time-domain shape of the pulse, as it can be seen in Figure 5-20. By using a 4 mm aperture, the pulse amplitude has decayed from 7 mV to 0.7 mV, and its FWHM (Full width half maximum) is reduced from 0.3 ps to 0.2 ps. The aperture appears to be

operating as a *spatial filter* [155], blocking the longer wavelengths and filtering out the low frequency components, and the positive consequence is that the shorter pulse generates a broader frequency content.
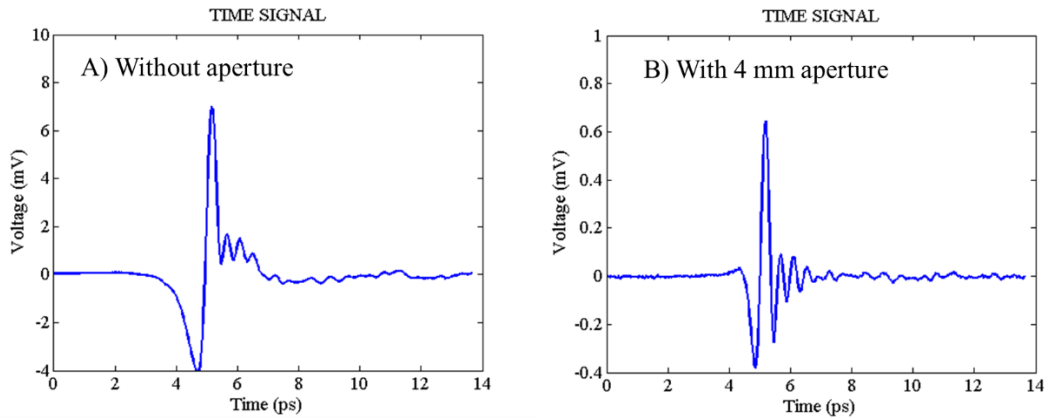
Figure 5-20. THz pulse. A) Without aperture. FWHM=0.3 ps. B) With a 4 mm aperture. FWHM=0.2 ps.

5.6 Data processing and image reconstruction in amplitude contrast

As it was presented in chapters 2 and 3, a THz time-domain spectrometry system is capable of measuring the spectral response of a material by using a broadband THz pulse. This frequency dependant information can be used to reconstruct a tomographic image, and it is possible to get as many images from an object, as calculated frequency components are available.

The tomography analysis was performed in ambient air, which means that water vapour absorption will influence the spectral analysis. During the computed tomography in amplitude contrast, the term I/I_0 is calculated and this reduces partially the influence of water vapour absorption lines; however, reconstruction may be severely distorted at certain frequencies.

A 47 mm diameter Styrofoam cylinder was used to generate the frequency plots shown in Figure 5-21. The red line represents the spectrum measured at a position of 5 mm, which is outside of the cylinder and can be used as a reference of the original signal. The blue line represents the spectrum obtained at a position of 30 mm, for a beam that goes

through the central region of the cylinder. Results show that attenuation increases with frequency, presenting a complete attenuation at frequencies higher than 1.5 THz. The spectral responses present the absorption lines produced by water vapour, and they appear broader than in a normal spectrum since only 128 points of the THz pulse waveform were acquired. This produced 65 frequency components, with an f_{BW}=58.6 GHz bin bandwidth (the bandwidth of each frequency component) if a step size of 20 µm is used, giving a lower resolution than in a typical spectrum, which is usually formed by 1024 or 2048 points (f_{BW}= 7.325 GHz and f_{BW}=3.66 GHz respectively, for the same step size conditions). The number of sampling points was reduced in order to minimize the acquisition time of each projection. Zero padding could be used if a higher resolution is required, though this will produce less information than the actual, longer measurement.

A complete projection of the cylinder is shown in Figure 5-22. The size of the THz beam is limited by two 4 mm diameter apertures situated before and after the cylinder. The projection was constructed with 70 scans at 1 mm displacement increments. The projection was done in free air, and the absorption lines produced by water vapour can be seen in the plot. At low frequencies, the central part of the cylinder produces a partial attenuation of the THz signal, and at high frequencies, the signal appears to be completely blocked.
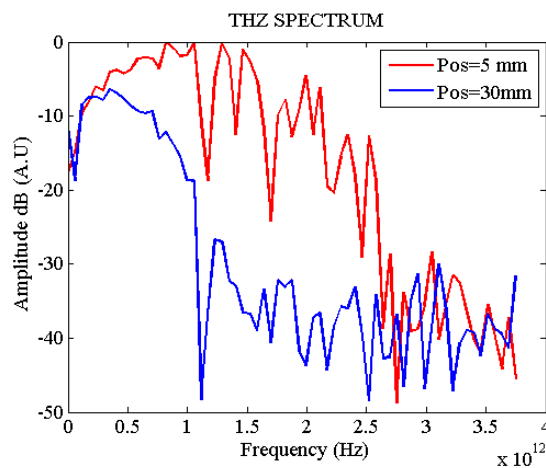
Figure 5-21. THz spectrum measured with and without a 47 mm cylinder Styrofoam phantom. Red line is without phantom. Blue line is measured through the centre (approximately) of phantom.
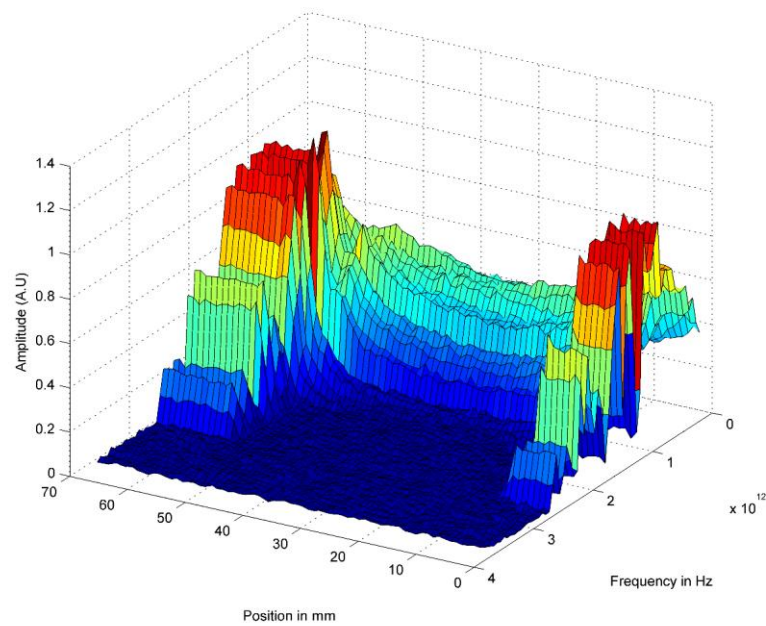
Figure 5-22. Spectrum of a single projection of a 47 mm diameter Styrofoam cylinder.

5.7   Tomography tests

One of the advantages of using a THz-TDS system in a tomography system is that each acquired projection can be separated in its frequency components, and this can be used to determine, for example, the difference between a projection at 1 THz and another at 2 THz. As a first approach, a graphical user interface (GUI) was developed in MATLAB for analysing normal projections.

First tests were carried out using cylindrical phantoms. A 22 mm diameter Styrofoam cylinder was scanned at a single view (no rotation) with 3 mm steps, which is equivalent to an array of parallel beams separated by 3 mm. In Figure 5-23, a projection analysed at 0.64 THz (λ=0.466 mm) is presented. The projection should present the effects of beam attenuation by Beer-Lambert law and generate a U-shaped profile, as it is indicated by the red dotted line. However the profile present a sharp attenuation at the edges, which indicates that an additional phenomenon is occurring and that will be analysed in the following sections.
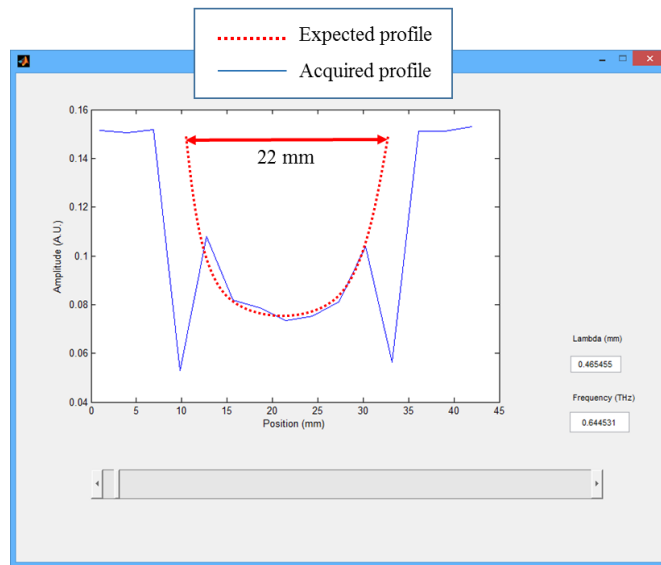
Figure 5-23. Projection of a 22 mm diameter Styrofoam cylinder at 0.64 THz.

A complete tomography image reconstruction is done using the MATLAB function *iradon,* which implements a filtered back-projection as explained in section 5.2. A second GUI was developed for visualizing the images at different THz frequencies (see Figure 5-25). The sliding control at the bottom allows the selection of the frequency/wavelength, and a second sliding control on the left side is used to set the gain. Two drop-down menus are located on the right and they permit the selection of several filtering and interpolation options, which are listed in Table 5-2, and Table 5-3. The normalized filter responses are plotted in Figure 5-24.

The Ram-Lak filter has a ramp frequency response as it was defined by expression (5-30). This type of response is prone to amplify high frequency noise components, therefore, some degree of gain reduction at high frequencies is desirable. MATLAB *iradon* function has a frequency scaling parameter to supress gain outside a threshold normalized value as it is shown in Figure 5-24B. The frequency response of the filter is compressed between the allowed range and outside it is replaced by zero gain. A frequency scaling of 0.85 and a Hamming filter was selected for the reconstruction of the images presented in this chapter, because it was considered that they provided the best setting in terms of image quality.

FILTER	Description
Ram-Lak	Ramp filter $|\omega|$
Shepp-Logan	Multiplies Ram-Lak by sinc function
Cosine	Multiplies Ram-Lak by cosine function
Hamming	Multiplies Ram-Lak by Hamming function
Hann	Multiplies Ram-Lak by Hann function
none	Unfiltered backprojection

Table 5-2. Inverse Radon filtering options.

INTERPOLATION	Description
Nearest	Nearest-neighbour interpolation
Linear	Linear interpolation
Spline	Spline interpolation
Pchip	Shape-preserving piecewise cubic interpolation
V5cubic	Cubic interpolation without extrapolation

Table 5-3. Inverse Radon interpolation options.

A) Frequency scaling=1   B) Frequency scaling=0.85
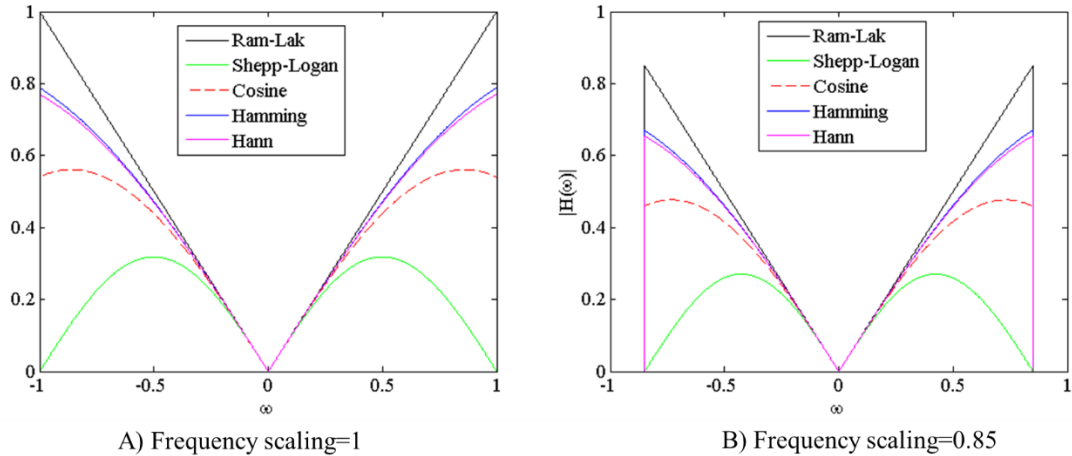
Figure 5-24. MATLAB backprojection normalized filtering functions.

A tomography image of a 63 mm diameter Styrofoam cylinder at 1.992 THz (λ=0.151 mm) is displayed in Figure 5-25. Since the acquired line-integrals are mapping the attenuation coefficient of the object, and the object is made of a homogenous material, the expected reconstructed image would be a plain circle. Instead of that, the image presents some deviations from the theoretical attenuation model. The strong contrast at the edges, which was already found in the profile presented in Figure 5-23, in this full

163

tomographic image produces a ring of heavy contrast at the border of the cylinder. There is also a varying degree of attenuation which is stronger in the outer part of the object and is reduced towards the centre, where contrast is minimal. Our first hypothesis was to think that the contrast at the surface was caused by beam deviation at high incidence angles (refraction losses), and it will be analysed in the following section.

Figure 5-25. Graphical user interface (GUI) for analysing THz tomography in amplitude contrast showing the image of a 63 mm Styrofoam cylinder.
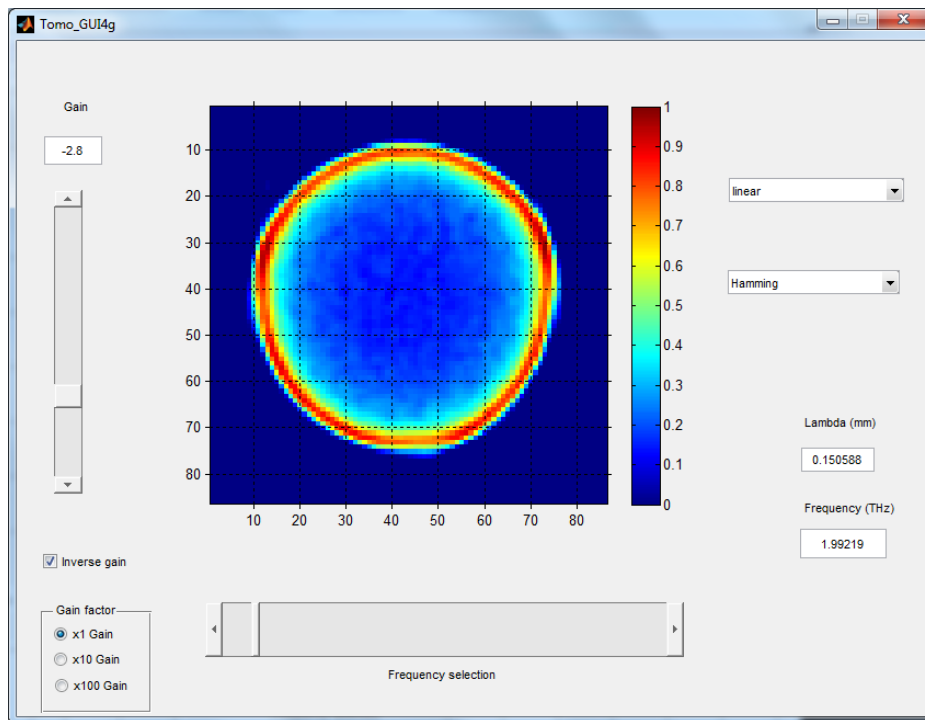
A complete frequency mapping was done for a crescent shaped Styrofoam phantom (see Figure 5-26), and the results for several aperture settings are presented in **Error! Reference source not found.**. The images show that a strong edge attenuation occurs in the convex side of the phantom and not in the concave side. The quality of the image varies with the frequency. As the phantom is made from a homogenous material, the expected images are a single colour shape, which is interpreted as a constant attenuation coefficient through the phantom volume. However, it appears that the image is better reconstructed at low frequencies, and shows increased edge contrast and errors in the reconstructed shape at higher frequencies. The shape's profile seems to be best detected by a combination of input and output open apertures, probably because of higher signal level, however some artifacts appear but are suppressed if an 4 mm input aperture is used.

164

The less accurate images come from the use of an open input aperture and a 4 mm output aperture. If a 4 mm input aperture is used, there is little difference in the images produced by using or not a 4 mm output aperture. Without using a 4 mm input aperture the shape presents a small shrinking effect as frequency increases which may be attributable to lower lateral resolution.

Figure 5-26. Crescent shape phantom.

In Table 5-5 shows a set of reconstructed images at different frequencies for 4 different phantoms: A) quarter of a cylinder, B) cylinder with hollow, C) Xbox control shape, and D) square; using 4 mm input and output apertures. Figure 5-27 shows a picture of these four phantoms. The phantoms were analysed by the THz tomography system using 1 mm steps for the linear scan and 7.5° angular increments for the rotation scan (from 0° to 180°). For each 1 mm step, a line integral (THz pulse waveform). Each pulse consisted of 128 points at the equivalent time sampling of 0.133 ps/point. A typical phantom required the acquisition of 80 line integrals at 25 different viewing angles, that is 2000 line integrals in total and it took 3 days and 6 hours to be scanned.

Reconstructed images in Table 5-5 show that as frequency increases, the first part of the phantom to be reconstructed is its border. At low frequencies the shapes are reconstructed with acceptable precision, and even it was possible to visualize the internal cylindrical bore in phantom B. However this internal detail is lost as frequency increases, as it is also

lost the ability to detect the concave sides of the Xbox control shape (phantom C). All phantoms produced rounded edges at higher frequencies.

Images were also reconstructed in time-of-flight contrast, using the same experimental data, but a different program to process it. Results are presented in Table 5-6. In this case, images don't suffer from the same problems that affect the reconstruction in amplitude contrast. The coherent detection of time-of-flight measurements produce clear images with only minor artifacts, showing that is less sensitive to scattering.
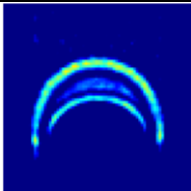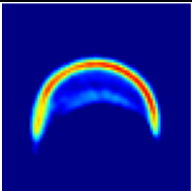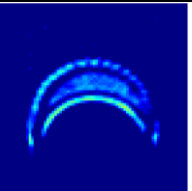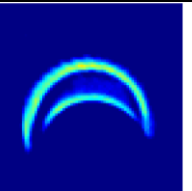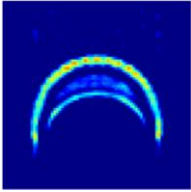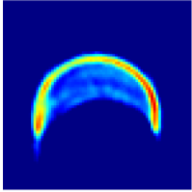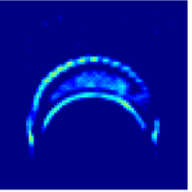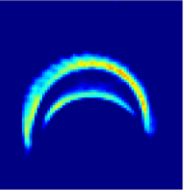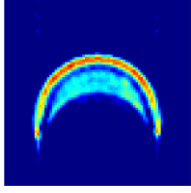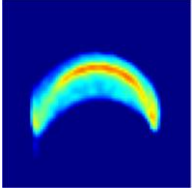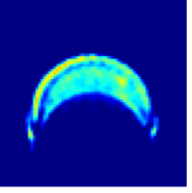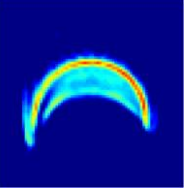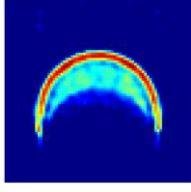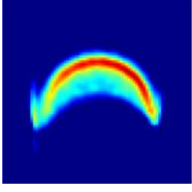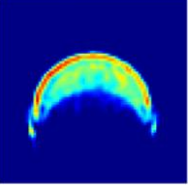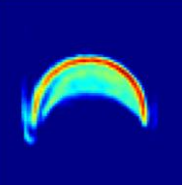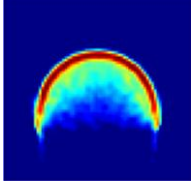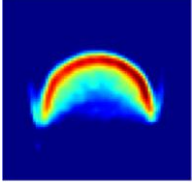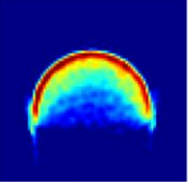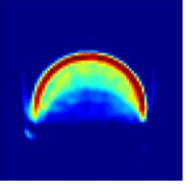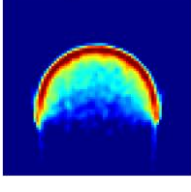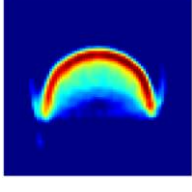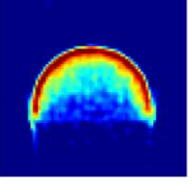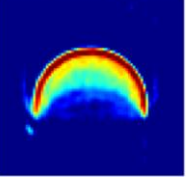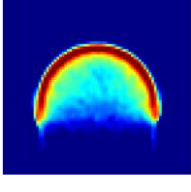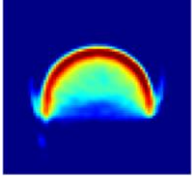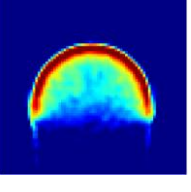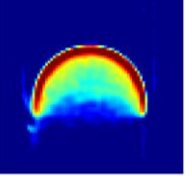
	Apertures			
Freq. and λ	In: 4 mm Out: 4 mm	In: open Out: 4 mm	In: 4 mm Out: open	In: open Out: open
f=0.586 THz λ=0.512 mm				
f=0.703 THz λ=0.427 mm				
f=0.996 THz λ=0.301 mm				
f=1.231 THz λ=0.244 mm				
f=1.582 THz λ=0.190 mm				
f=1.758 THz λ=0.170 mm				
f=1.992 THz λ=0.150 mm				

Table 5-4. Reconstruction of a crescent shape for different apertures.
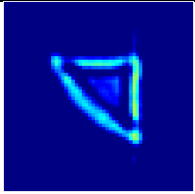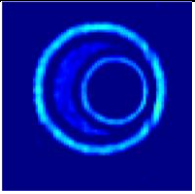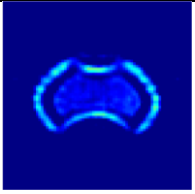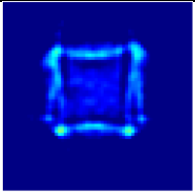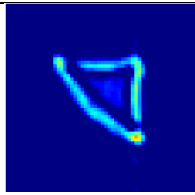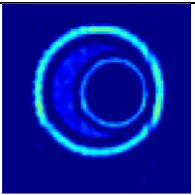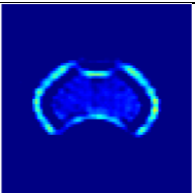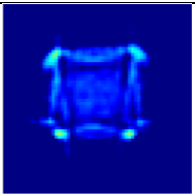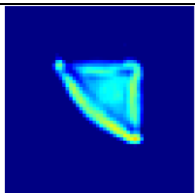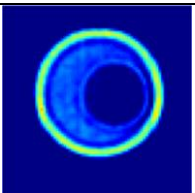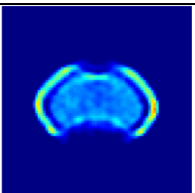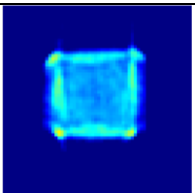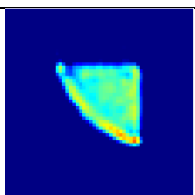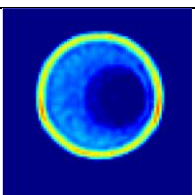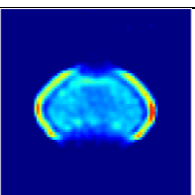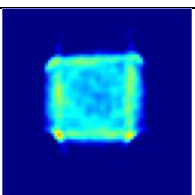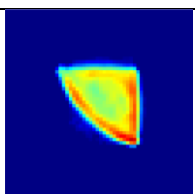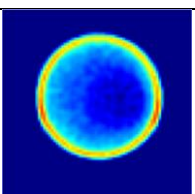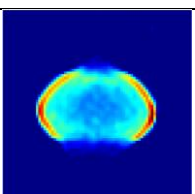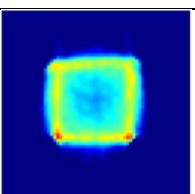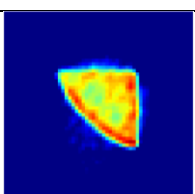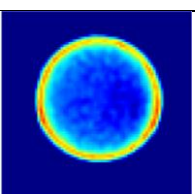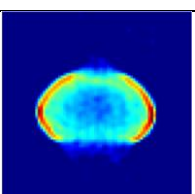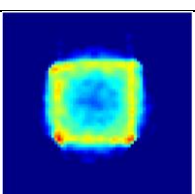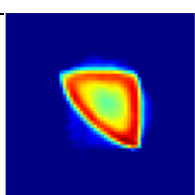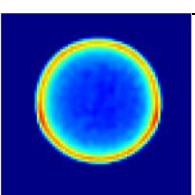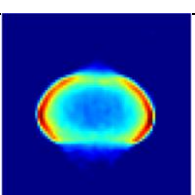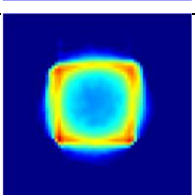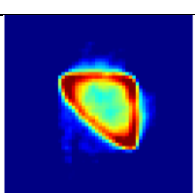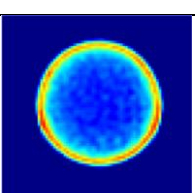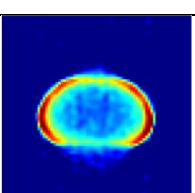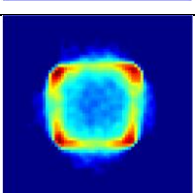
	A. Quarter of a cylinder r=22 mm	B. Cylinder with hollow	C. Xbox control shape	D. Square
f=0.586 THz λ=0.512 mm				
f=0.703 THz λ=0.427 mm				
f=0.996 THz λ=0.301 mm				
f=1.231 THz λ=0.244 mm				
f=1.582 THz λ=0.190 mm				
f=1.758 THz λ=0.170 mm				
f=1.992 THz λ=0.150 mm				
f=2.520 THz λ=0.119 mm				

Table 5-5. THz Tomography of other phantoms. A) Quarter of cylinder. B) Cylinder with cylindrical bore, C) Xbox control shape. D) Square.
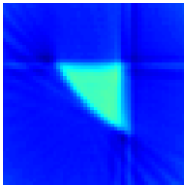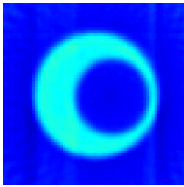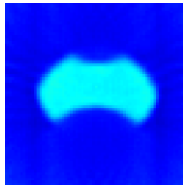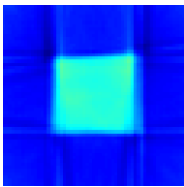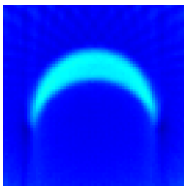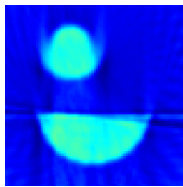
1/4 of a cylinder (r=22 mm)	Cylinder with hollow	Xbox control shape
26 mm square	Crescent shape	Composed phantom

Table 5-6. Imaging of phantoms in time-of-flight contrast.

Figure 5-27. Photography of the phantoms used for the images in Table 5-5 and for some of the images in Table 5-6.

5.8   Refraction losses

The high contrast found at the border of the reconstructed images may be caused by refraction losses, and a simulation of attenuation (modelled by Beer-Lambert law) and refraction losses (modelled by Fresnel law) will be presented in this section.

Refraction phenomena in THz tomography and imaging is a problem that has not been fully covered. A study of how a THz pulse is delayed as a cylindrical phantom is moved in front of the beam is presented in [156]. Authors show a tomography image of a 10 mm Teflon cylinder with a 3.4 mm circular hollow, similar in shape to the phantom B that we presented in Table 5-5, and they get a high contrast border similar to the one that we found when reconstructing an image in amplitude contrast. They conclude that this is the effect of refraction losses but didn't attempt to model the phenomena using Fresnel equations and Beer-Lambert law. In [157], a Plexiglas rod is analysed in a commercial THz tomography system at 0.15 THz. Authors present a model based on Fresnel equations and Beer-Lambert law for explaining the boundary artifacts that they get in a reconstructed image, and introduce a method for reducing the effects of refraction. Their reconstructed image show a similar high contrast edge to the type that we have found in our images. However, their analysis only uses a single frequency.

The effects of Beer-Lambert attenuation and refraction using the Fresnel equations will be used to simulate the projection of a cylindrical phantom. A simulation of a reconstructed tomography will be compared with the results of the Styrofoam cylinder of Figure 5-25. In order to make the simulations more accurate, the attenuation coefficient and the refractive index for two types of Styrofoam are determined experimentally. Measurements were carried out in the THz TDS system with standard spectrometry tests. For each type of Styrofoam, two samples with different thickness are placed in an air chamber with low humidity to limit the influence of water vapour absorption lines. The relative humidity (RH) inside the chamber was 8.5 % RH, and it was measured with a Sensirion SHT21 humidity and temperature sensor (typical accuracy= ±2.0 % RH).

5.8.1 Attenuation coefficient

In hard-field tomography in amplitude contrast, a beam propagating through an object is attenuated according to Beer-Lambert law. In order to identify such losses, the attenuation coefficient was experimentally determined. Two types of Styrofoam were used during our experiments, one with small porosity and other with large porosity.

For clarity, the Beer-Lambert law is repeated here

$$I = I_0 e^{-\mu x}$$

(5-34)

where I_0 is the initial intensity, x is the path length, and μ is the attenuation coefficient. In terms of the electrical field, (5-34) can be rewritten as

$$A^2 = A_0^2 e^{-\mu x}$$

(5-35)

Given two samples of the material with different thicknesses and analysed at normal incidence, the frequency dependant attenuation coefficient can be calculated by

$$\mu(v) = \frac{-2Ln\left(\frac{A_2(v)}{A_1(v)}\right)}{(x_2 - x_1)}$$

(5-36)

Where A_1, A_2 are the amplitude spectra responses of the samples, and x_1, x_2 are their respective thicknesses. Experimental results are shown in Figure 5-28. The sample with larger porosity presents a lower absorption as a result of a larger air pocket size. At high frequencies, noise and low dynamic range degrade the estimation. Both types of Styrofoam present an increase in attenuation as the frequency increases.
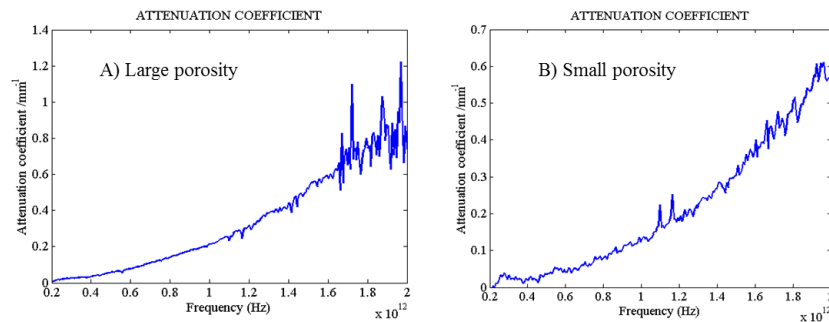
Figure 5-28. Attenuation coefficient of Styrofoam.

5.8.2   Refractive index

In order to estimate the refraction losses, the refractive index of the material has to be determined. To obtain the refractive index of the Styrofoam, we use two samples of the same material but with different thicknesses. The refractive index n as a function of frequency v can be estimated using the following equation [2, 85].

$$\Phi_2(v) - \Phi_1(v) = \frac{2\pi v}{c}(n(v) - 1)(x_2 - x_1) \qquad (\text{5-37})$$

where Φ_1 and Φ_2 are the phase shift as a function of frequency, obtained after applying a FFT on the time-domain data and performing a phase unwrapping. n is the refractive index, v is the frequency, c is the speed of light, and x_1, x_2 are the sample thicknesses. Solving for n, the frequency dependent refractive index is given by

$$n(v) = 1 + \frac{c(\Phi_2(v) - \Phi_1(v))}{2\pi v(x_2 - x_1)} \qquad (\text{5-38})$$

In Figure 5-29, the refractive index for the two types of Styrofoam is plotted. Both types present a low refractive index as it would be expected since the porous are filled with air (n=1). Again, at high frequencies, noise and low dynamic range degrade the validity of the estimation.
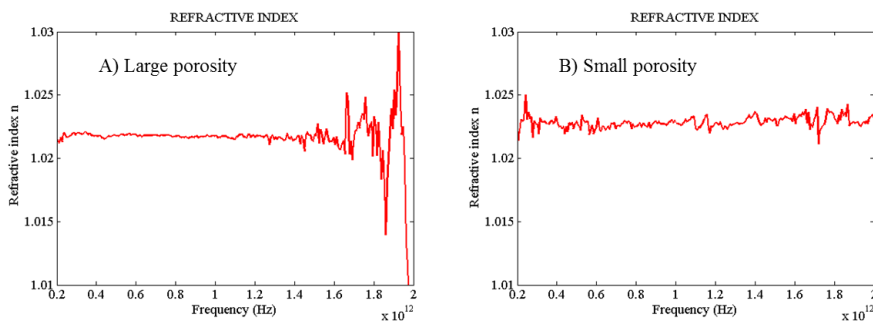
Figure 5-29. The refractive index of Styrofoam. A) Large porosity type presents an almost constant value of n≈1.022 from 0.3THz to 1.4 THz. B) Small porosity type presents n≈1.023 from 0.3THz to 2.0 THz.

5.8.3 Simulation of attenuation and refraction losses in a cylindrical phantom

The first step will be to consider the losses due to attenuation. This can be done by estimating the path length of the beam and by using the Beer-Lambert´s law. In a second step, the refraction losses using the Fresnel equations will be included.

ATTENUATION PATH

The cross sectional area of a cylindrical phantom is a circle. In Cartesian coordinates a circle centred at the origin is defined by

$$x^2 + y^2 = r^2$$

(5-39)

where r is the radius.

The path length L of a beam traversing a circular cross section in a direction parallel to the y-axis (see Figure 5-30) is given by

$$L = 2\sqrt{r^2 - x^2}$$

(5-40)
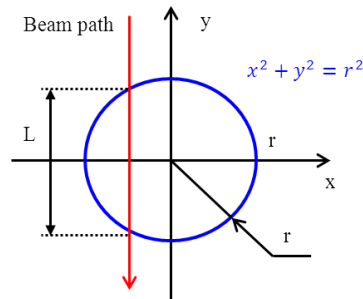
Figure 5-30. Path length of a beam traversing a circular cross sectional sample.

Then, using (5-34)

$$A = \sqrt{A_0^2 e^{-\mu L}}$$

(5-41)

As it is depicted in Figure 5-31, the angle of incidence θ_i of a beam crossing a cylindrical phantom is given by

$$\theta_i = angtan(1/m)$$

Or,

$$\theta_i = angtan\left(\frac{x_1}{\sqrt{r^2 - x_1^2}}\right) \qquad (5\text{-}42)$$
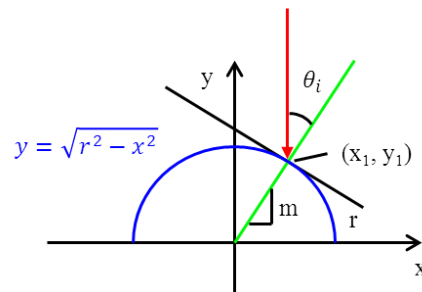
Figure 5-31. The angle of incidence $\boldsymbol{\theta_i}$ of a beam arriving to a cylindrical surface depends on the point of contact x_1.

Equation (5-42) is plotted in Figure 5-32, and it can be seen that the angle of incidence presents a sharp increase when the beam´s point of contact is close to the edge.
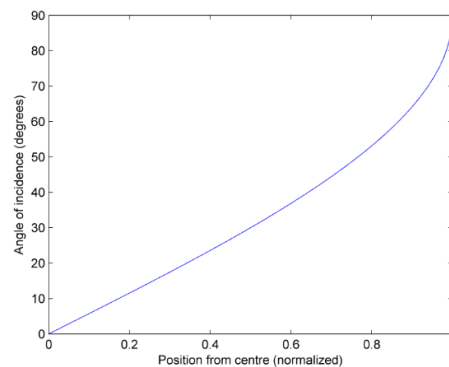
Figure 5-32. Angle of incidence to a circular surface vs. distance from centre (normalized).

According to Fresnel equations, the reflectance from a surface is given by

$$R_S = \left| \frac{n_1 cos\theta_i - n_2\sqrt{1 - \left(\frac{n_1}{n_2}sin\theta_i\right)^2}}{n_1 cos\theta_i + n_2\sqrt{1 - \left(\frac{n_1}{n_2}sin\theta_i\right)^2}} \right|^2$$

$$R_p = \left| \frac{-n_2 cos\theta_i + n_1\sqrt{1 - \left(\frac{n_1}{n_2}sin\theta_i\right)^2}}{n_2 cos\theta_i + n_1\sqrt{1 - \left(\frac{n_1}{n_2}sin\theta_i\right)^2}} \right|^2$$

(5-43)

where R_S and R_p are the reflectances for an s-polarized and p-polarized beam respectively, and n_1 and n_2 are the refractive indexes of the medium. A simulation for n=1.022 (Styrofoam) is shown in Figure 5-33. As it can be seen, there is a strong attenuation for angles of incidence greater than 85 degrees; this means that the transmitted beam intensity will be severely reduced for a beam incident to a point close to the edges of the cylindrical phantom.
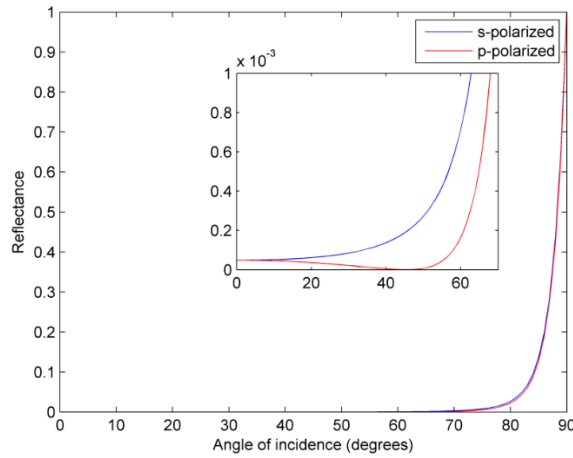
Figure 5-33. Reflectance vs. angle of incidence of Styrofoam (n=1.015). Inset: detail on the same axis.

Using equations (5-40), (5-41), (5-42) and (5-43), we can estimate the absorption of a beam crossing a cylindrical phantom, taking in to account just the Beer-Lambert law or both Beer-Lambert and Fresnel effects. A projection has been plotted in Figure 5-34 for a cylinder of 90 mm diameter. An array of parallel beams at 1 mm separation was simulated considering an attenuation coefficient of 0.21 mm^{-1} (@ 1 THz) and a refractive index n=1.022. The simulation shows that the Beer-Lambert law predicts a stronger

175

attenuation for a beam crossing the centre of the cylinder (blue dotted plot) and Fresnel equations show that a high level of attenuation is produced at the edges of the phantom (red plot). The two spikes present in the red plot of Figure 5-34, are similar (though thinner) to those presented in the projection of a cylinder shown in Figure 5-23, but the latter was reconstructed from beam measurements separated by a distance of 3 mm.
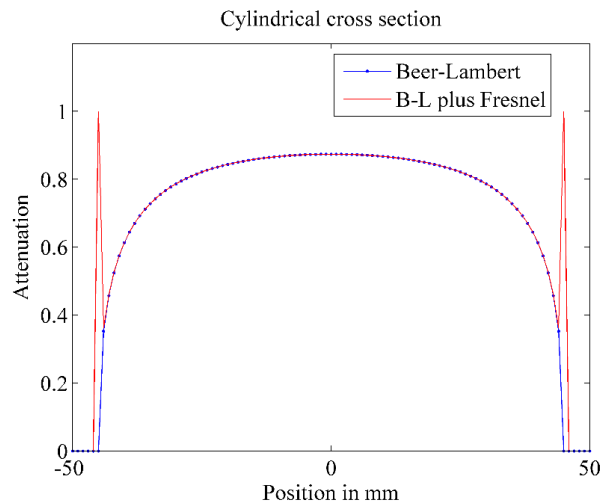
Figure 5-34. Beam absorption in a cylindrical Styrofoam phantom.

Since the simulated cylinder has radial symmetry, the profile plotted in Figure 5-34 can be used to reconstruct a tomography image by repeating the profile at 25 different rotation angles (7.5° increments). The MATLAB function *iradon* with Hamming filter and linear interpolation is used to generate the tomography image shown in Figure 5-35. The borderline presents a stronger attenuation than the rest of the cross sectional area, which clearly resembles the edge attenuation found in a cylindrical phantom and shown in Figure 5-25. However, the simulated border ring appears thinner than in an actual measurement, which suggests that additional phenomena may be occurring.
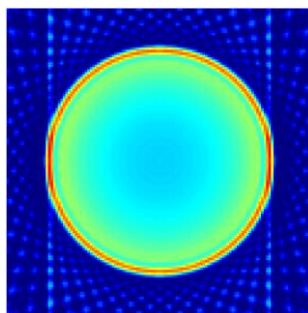
Figure 5-35. Phantom reconstruction using filtered back-projection.

176

5.9 Scattering analysis

In optics, it can be considered that scattering is a phenomenon that occurs when an electromagnetic wave interacts with matter, and this interaction produces a change in direction of the incident wave [158]. However, multiple scattering may occur producing a scattered wave going out in the same direction as the incident one. Under these assumptions, reflection and refraction are only a particular form of scattering, when the waves are deviated in such a way that can be accurately modelled by ray optics.

Scattering may be contributing to the edge contrast found in the tomography images that we obtained in amplitude contrast. It is considered that in many cases, scatter from optically smooth components can be treated as diffraction [159]. Diffraction would be a particular form of scattering where the deviated waves superimpose forming intensity ripples [160]. THz diffraction tomography was covered extensively in a paper by S. Wang *et al* [4]. They used the first Born and first Rytov approximation to estimate the solution to a scattered field. However, these approximations are valid only in the case of weakly scattering objects [22]. Our system is currently unable to perform diffraction tomography since it is not possible to acquire information about the scattered field as S. Wang *et al* did using a CCD camera.

In order to explore the effects of scattering, two phantoms with identical cross sections were made of two different types of Styrofoam, which is a porous material. The two types of Styrofoam have different porous size and different roughness. The phantoms consisted of a half cylinder and a small cylinder as shown in the pictures of Figure 5-36 and this was selected following previous work done at the University of Manchester [144],which used a similar Styrofoam phantom but of a smaller size (20x14mm). Details on the actual dimensions are indicated in Figure 5-37.
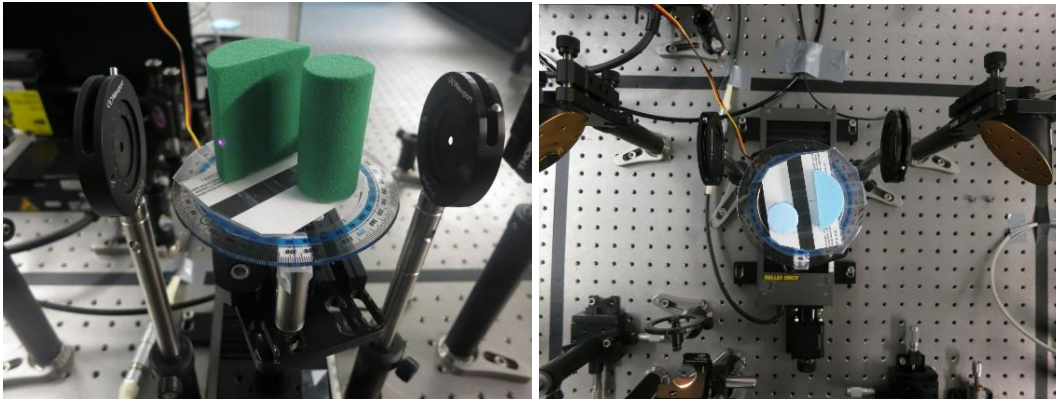
Figure 5-36. Photos of the Styrofoam phantoms mounted in the THz tomography system. Left) Large porosity type. Right) Small porosity type.
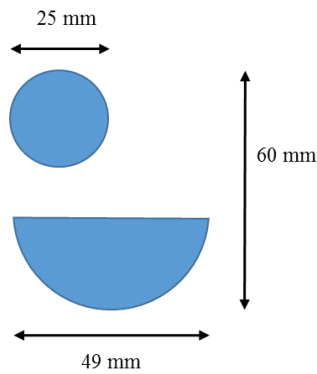
Figure 5-37. Details on the dimension of the phantoms.

In Table 5-7, a series of reconstructed images at some representative frequencies are presented. Frequencies were selected among those that weren't spoiled by water vapour absorption lines. The small porosity phantom presents a stronger edge contrast which could be caused by the larger number of cells per area unit (more scattering elements). At the lowest frequency both phantoms have a transparent volume and only their edges are detected. The small porosity material keeps showing a transparent interior up to 1.231 THz, whilst the interior of the large porosity phantom begins to lost transparency at frequencies above 0.586 THz, and that may be a product of volume scattering. The high contrast at the edges continues to increase with frequency until the quality of the image begins to deteriorate at frequencies above 2.5 THz.
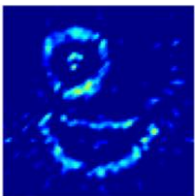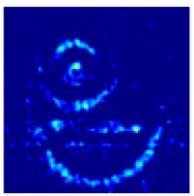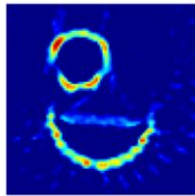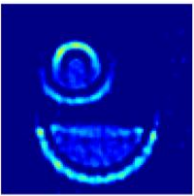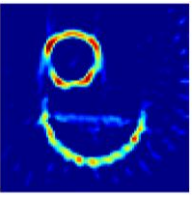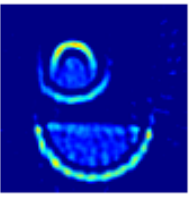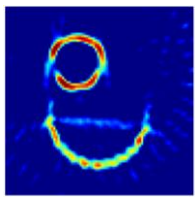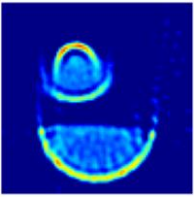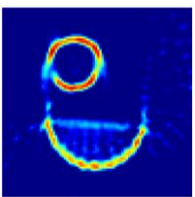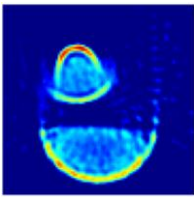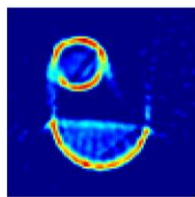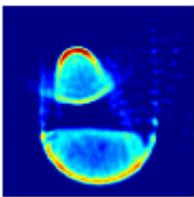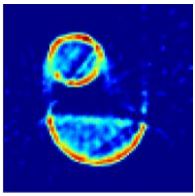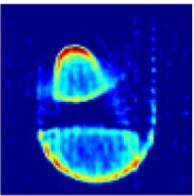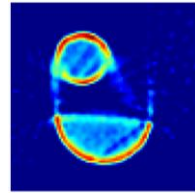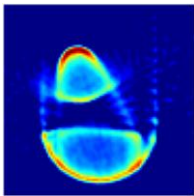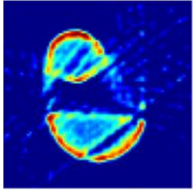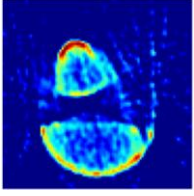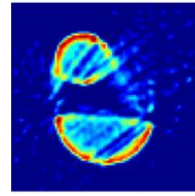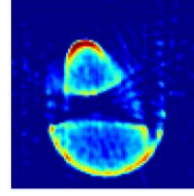
Small porosity	Large porosity	Small porosity	Large porosity
f=0.234 THz, λ=1.282 mm		f=0.586 THz, λ=0.512 mm	
f=0.703 THz, λ=0.427 mm		f=0.996 THz, λ=0.301 mm	
f=1.231 THz, λ=0.244 mm		f=1.582 THz, λ=0.190 mm	
f=1.758 THz, λ=0.170 mm		f=1.992 THz, λ=0.150 mm	
f=2.285 THz, λ=0.131 mm		f=2.520 THz, λ=0.119 mm	

Table 5-7. Image reconstruction for two phantoms with identical cross sections made from two types of Styrofoam.

5.9.1 Surface scattering

In a smooth surface, the low refractive index of Styrofoam, permits an incident beam to be transmitted with no appreciable deviation, even at moderate angles of incidence. However, in the case of a rough surface, some rays arrive at high angles of incidence (grazing angle) producing scattered rays (see Figure 5-38). The Fresnel equation can be modified to take into account this effect by introducing the Rayleigh roughness factor [161]
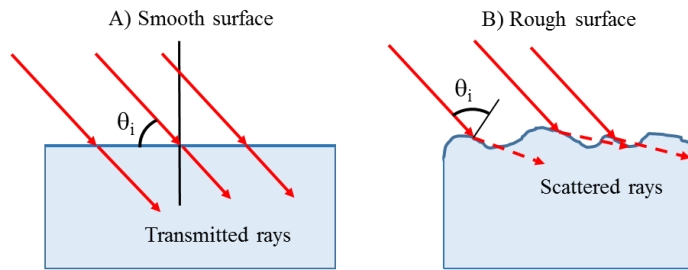
Figure 5-38. A) Transmission of beams is possible at moderate angle of incidence on a smooth surface. B) Rays may arrive at high angle of incidence on a rough surface producing scattered rays.

$$\rho = e^{-\frac{g}{2}} \qquad\qquad (5\text{-}44)$$

where

$$g = \left(\frac{4\pi\sigma cos\theta_i}{\lambda}\right)^2 \qquad\qquad (5\text{-}45)$$

where θ_i is the angle of incidence, σ is the standard deviation of the surface roughness and λ is the wavelength. The parameter g is a measure of the surface roughness and is derived from the mean square phase variations produced by the scattered reflection [162]. The roughness factor ρ represents the mean losses in a reflective surface [163]. Studies on scattering from rough surfaces are covered in depth for the case of reflective surfaces but not for the case of refracting materials. Since our tomography system works on transmitted radiation, we introduce the use of a 1-ρ factor to model these losses as a scaling factor for Fresnel equations.

Using the Fresnel equations, the transmittance of an s-polarized beam is given by

$$T_s = 1 - R_s \tag{5-46}$$

Where R_s is the reflectance as defined in (5-43). The modified Fresnel equation for an s-polarized beam then becomes

$$Tm_s = (1 - \rho)(1 - R_s) \tag{5-47}$$

where Tm_s is the modified transmission coefficient.

Pictures of the large porosity and small porosity Styrofoam are shown in Figure 5-39 and Figure 5-40 respectively. The pictures were taken with a digital compact camera Panasonic Lumix LF1 in macro focus mode (3 cm minimum distance focus) and then cropped. The size of the surface roughness has been sampled and measured with an evaluation version of an image measurement software. A needle was used as a calibration pattern (0.6 mm thickness). The standard deviation of the surface roughness was $\sigma_L = 0.12$ mm for the large porosity Styrofoam, and $\sigma_S = 0.06$ mm for the small porosity Styrofoam.

Figure 5-39. Measurement of porous size for the large porosity Styrofoam (Green). At the centre appears a needle. For the sampled porous, the average porous size is $X_L = 0.47$ mm, $\sigma_L = 0.12$ mm.

181
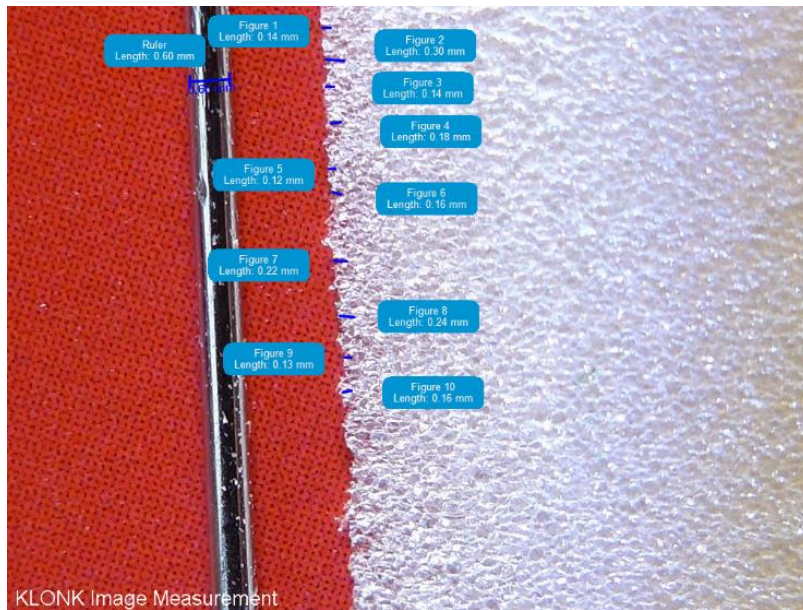
Figure 5-40. Measurement of porous size for the small porosity Styrofoam (White). At the centre appears a needle. For the sampled porous, the average porous size is X_S =0.18 mm, σ_S=0.06 mm.

The transmission scattering factor (1-ρ) has been plotted in Figure 5-41 for different angles of incidence. It can be seen that for small angles of incidence the transmitted beam is barely attenuated, whereas for large angles the scattering produces a loss in transmission. Therefore this can be used as an approach for modelling the strong attenuation presented at the surface of the images in Table 5-7.
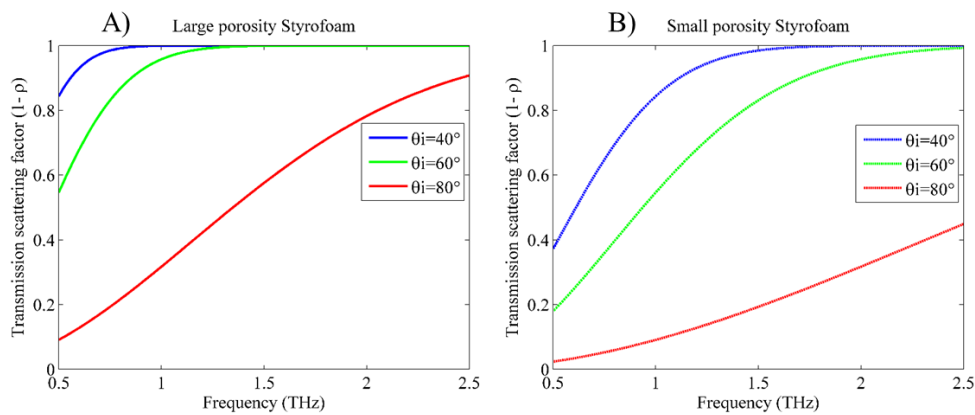
Figure 5-41. Scattering transmission factor (1-ρ) plotted for different angles of incidence. A) Large porosity Styrofoam. B) Small porosity Styrofoam.

Surface roughness, along with the attenuation coefficients and refractive indexes found in section 5.8 were used to simulate a projection of a Styrofoam cylinder using a MATLAB program. The results are presented in Figure 5-42 and for comparison purposes a tomography image of two Styrofoam cylinders is shown in Figure 5-43. Simulated profiles are similar to the results obtained in the tomography images, showing a higher edge contrast for the small Styrofoam cylinder, and producing higher internal attenuation in the large porosity phantom. The attenuation in the inner part of the phantom is mainly produced by the attenuation coefficient μ, which increases with frequency, and is higher for the low porosity Styrofoam, as it has a higher material density.
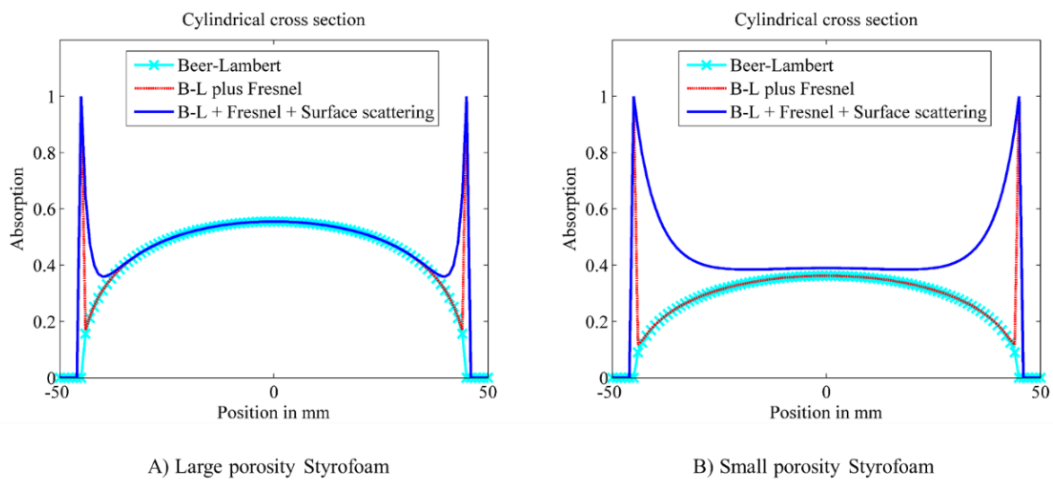
Figure 5-42. Simulation of a projection from a Styrofoam cylinder for f=1 THz. A) Large porosity. B) Small porosity.
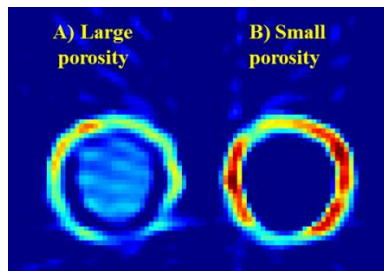
Figure 5-43. Tomography image of two Styrofoam cylinders at 1 THz. A) Large porosity. B) Small porosity.7

A simulation for three frequencies, along with a tomography image of a cylinder reconstructed at the same frequency is shown in Table 5-8. In the tomography images, it can be seen that the region affected by surface scattering is reduced as frequency increases and that effect is approximated by our model.

	Large porosity Styrofoam	Tomography example
f=0.586 THz, λ=0.512 mm		
f=1.099 THz, λ=0.273 mm		
f=1.538 THz, λ=0.195 mm		

Table 5-8. Simulation of an attenuation profile at different frequencies and comparison with actual tomography.

5.10 Results

It has been possible to reconstruct tomography images in amplitude contrast up to 2.5 THz and this is the result of good dynamic range and SNR, even when the apertures placed in front and behind the phantom reduced the signal by one order of magnitude. Graphs for the dynamic range and SNR are presented in Figure 5-44 and Figure 5-45 respectively. The THz tomography system presents good dynamic range and SNR for

frequencies below 2.5 THz; above that limit however, its specifications decay quickly. This shows why it has been possible to reconstruct images up to 2.5 THz.
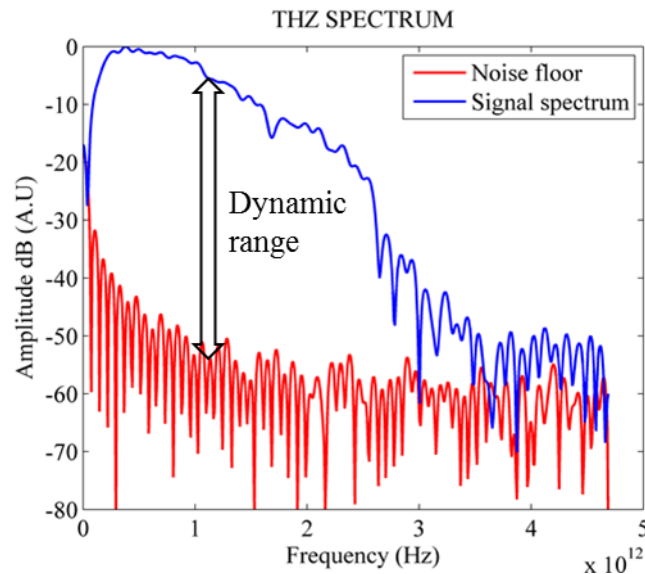
Figure 5-44. Spectral response and noise floor of the THz tomography system. $DR_{MAX} \approx 50$ dB.
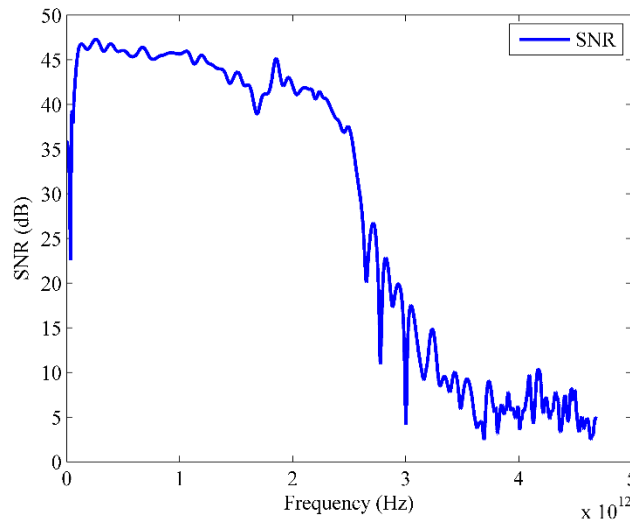
Figure 5-45. Signal-to-noise ratio of the THz tomography system. $SNR_{MAX} \approx 47$ dB.

The analysis that has been carried out allows to explain some of the changes in images reconstructed at different frequencies. In Table 5-9, some reconstructed images of a dual cylinder phantom are presented. The phantom is composed by two Styrofoam cylinders with identical cross-section but from different porosities. In this way, only one tomography experiment is required for comparing the two types of material, making the

185

test more reliable. It can be seen that at small frequencies, both cylinders have a transparent core, and this is the consequence of a low attenuation coefficient at such frequencies. However, the border of the shape is detected and this is due to surface scattering, which is stronger in the small porosity Styrofoam type due to a smoother surface that produces 'mirror like' reflection at high angles of incidence. This surface scattering was modelled using Rayleigh roughness factor and modified Fresnel equations. At intermediate frequencies, the core of the large porosity Styrofoam cylinder is visible whilst the core of the small porosity type remains almost transparent. This is due to the higher attenuation coefficient of the large porosity type. An initial hypothesis considered this as part of volume scattering but the simulations showed that the attenuation coefficient is taking into account of this effect. The attenuation coefficient, as it was explained in equation (5-2), comprises an absorption component and a scattering component. These components cannot be separated at this time, since the built system is not suitable for scattering measurements. Also at intermediate frequencies, the edge high contrast is incremented due to a higher attenuation coefficient. At high frequencies, the increase in attenuation has made the core of the small porosity Styrofoam cylinder visible, and the quality of the images for both cylinders begins to deteriorate due to lower dynamic range.
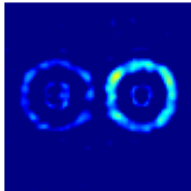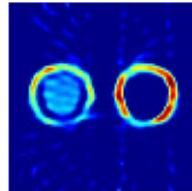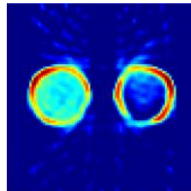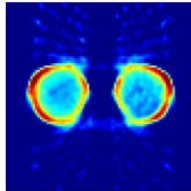
Porosity		Porosity		Porosity		Porosity	
Large	Small	Large	Small	Large	Small	Large	Small
f=0.336 THz, λ=0.893 mm		f=1.099 THz, λ=0.273 mm		f=1.758 THz, λ=0.170 mm		f=2.564 THz, λ=0.117 mm	

Table 5-9. Reconstructed images of a dual cylinder phantom made of two Styrofoam cylinders with different porosity.

Beam scattering is associated with a large number of variables, including: roughness, shape, polarization, angle of incidence, bulk defects and wavelength [159]. Therefore, the model presented here can only be considered as a first approximation towards a further understanding of the scattering phenomena at THz frequencies. For example, when a beam is scattered, not only its amplitude and direction is changed, but also its polarization [159, 164], and no attempt to consider such effects was made in our model.

Since the THz beam applied to the sample is linearly polarized, it is possible to think that some materials will present a varying attenuation depending on the polarization angle. However, we think that this would not be the case for Styrofoam since it is made of an array of cells with a random orientation. Materials with an internal structure showing a predominant orientation may be sensitive to beam orientation as can be interpreted from [165].

Finally, an alternative explanation to the high edge contrast can be found by using the concept of pseudocoherence [166]. This phenomenon occurs when the sample does not have a perfect parallel form, therefore its thickness varies across beam aperture. As a consequence, the resulting interferogram is composed by the sum of elemental interferograms crossing at different elemental apertures of the sample, and this may produce a zero transmission, even with transparent materials. An example of pseudocoherence applied to the transmission measurement of leaf water content using THz radiation is given in [167], and analysis distortion produced by cross-polarized components is given in [168]. Also, boundary effects between two different materials with wedged interfaces is presented in [169].

5.11 Summary

In this chapter, a THz tomography system in amplitude contrast based on THz-TDS has been presented. Its implementation required the assembly of optical components, motorized stages and measurement equipment. A rotation motorized stage was designed and built using a DC servo motor and a digital module interface. A program in LabVIEW was developed to control the rotation stage and a linear stage, in order to acquire the line integrals of the object under test. Without this level of automation, scanning an image

would have been very difficult given the large amount of measurements involved. A typical phantom scan, 80 mm long at 1 mm step size and 25 angular projections at 7.5° increments, took 3 days and 6 hours to complete, which is a typical value for this type of systems. For this conditions, a total of 2000 pulse measurements are acquired.

Image reconstruction was made using a MATLAB program which made use of the included *iradon* function, for implementing a filtered backprojection. A graphical user interface (GUI) was programed to visualize the images at their different frequency components. Several phantom shapes were reconstructed including: cylinder, quarter of a cylinder, crescent shape, cylinder with cylindrical hollow, Xbox control shape, square and a composed phantom made by a half cylinder and a small cylinder. Images were reconstructed at several frequencies in amplitude contrast, and for comparison purposes some images were reconstructed in time-of-flight contrast. Images in time-of-flight contrast presented no deviation from an expected reconstruction showing that the technique is robust. Images reconstructed using amplitude contrast showed strong attenuation at the border and a varying degree of transparency as frequency changed. It was found that the former is caused by a combination of Fresnel refraction and scattering losses, whereas the latter is due to the frequency dependence of attenuation coefficient of the material. In order to analyse the scattering losses, two types of Styrofoam were used to test similar shaped phantoms. Styrofoam types differed in the porous size which was measured using a photograph and an image measurement software. Despite the fact that scattering analysis from rough surfaces has been almost exclusively developed for reflective surfaces, a model was introduced to account for the scattering losses in a refractive material (transmission mode) and simulated using MATLAB. Results show an improvement over the Fresnel refraction losses model, but also suggest that further work needs to be done to produce a more accurate model.

6 CONCLUSIONS AND FUTURE WORK

A THz computerized tomography equipment, based on a time-domain spectroscopy system, was built from scratch, as a platform for working on the fulfilment of the objectives of this research. Our objectives were twofold: First, we were interested in improving the signal-to-noise ratio of the system as a way to facilitate the implementation of faster systems; and second, to determine advantages and limitations of a THz tomography system working in amplitude contrast, as these results are potentially applicable to CW THz imaging systems, which are expected to represent a better alternative than pulsed systems in terms of smaller size, higher power, and possibly lower cost.

6.1 Conclusions

Our first objective was to improve the SNR in a THz-TDS system, this objective was not accomplished, but the experience gained during this part of the research makes it possible to formulate some conclusions:

The optical balanced detection used as part of an electro-optical sampling in a THz-TDS system is an optimal approach. Balanced detection relies on the idea of differential amplification which is of widespread use in electronic instrumentation. A figure of merit for differential amplifiers is the common mode rejection ratio (CMRR) and this can only be improved by a careful selection of its internal components. However, laser systems have relatively high levels of noise, which means that simple balanced detectors with modest values of CMRR are usually enough.

Autobalance optical detection is not suitable for electro-optical sampling in THz detection. Autobalance optical detection is intended for optical unbalanced systems in

which a measurement is made by balancing the two branches of a split laser beam, usually by the use of a neutral density filter. Autobalance detectors automate this operation by introducing the equivalent to an electronic neutral density filter, which is in fact a controlled-gain amplifier. An electro-optical detection in a THz-TDS system produces a balanced signal, because information on THz electrical field is proportional to a differential signal; therefore, using an autobalanced scheme may deteriorate the detection.

THz time-domain signals may present echoes which produce spurious oscillations it the spectral analysis but which carry information on absorption lines. In some THz-TDS systems may appear one or multiple echoes of the main THz pulse, this is produced by Etalon phenomena caused by system optics or by the sample being analysed. One could be tempted to simply erase (manually of with a computer program) such echoes from the time-domain data, but this can affect the spectral absorption lines. We introduced a method of local apodization which reduces the spurious oscillations in the spectrum with minimal effect on spectral absorption lines.

The equivalent noise bandwidth (ENBW) can be applied to digital lock-in amplifiers. ENBW is a figure of merit that was extensively used to analyse the performance of analogue lock-in amplifiers; however, as digital lock-in amplifiers began to appear, this figure of merit stopped being used. Nevertheless, we used the ENBW for evaluating the performance of a digital lock-in amplifier and this allowed to compare the performance of analogue and digital implementations. This is important, since linear averager filters, which are easily implemented digitally, have no a direct equivalent in the analogue electronics domain.

A cumulative averager can be used to implement the filtering stage of a lock-in amplifier. We have introduced the use of a cumulative averager as a filter in a digital lock-in amplifier. In terms of noise reduction and speed of response is equivalent to a linear averager. There is a limitation however to the use of a cumulative averager in that it requires to be reset. For systems that may accept or require a timed reset, this implementation offers an alternative to the prior art.

A cumulative averager lock-in amplifier could be more efficient in terms of hardware against a moving average, since the former only requires to store one sample of data, whilst the moving average may require several thousands to perform the same filtering task, as it was explained in chapter 3. A trade-off has to be made between the amount of memory and the cost of implementing a division and a counter, which are required by the cumulative averager.

A cumulative averager has a relative advantage over an equivalent linear averager. A linear averager is 'blind' during a time lapse equal to the number of samples times the sampling time ($N \cdot t_s$) that need to be acquired before performing the averaging. This is not the case with a cumulative averager which presents an average with every acquired sample (the equivalent of a partial result) that could be useful in some applications. For example, it was easier to detect programing errors whilst developing a digital lock-in amplifier using a cumulative averager.

SNR, is the missing specification. In many commercial THz spectroscopy and imaging systems, there is one specification missing in their datasheets: the SNR. Manufacturers try to avoid the inclusion of this specification by including the dynamic range, but in my point of view, SNR is a more important specification, because it is a measure of system's precision. Of course, for many THz systems, to have an acceptable SNR specification requires the use of long integration times, which would be not very convenient for systems that otherwise are presented as 'fast'.

A mechanical delay line may not be the slowest component in a THz-TDS system. It has been usually considered that acquisition speed in a THz-TDS is limited by a slow moving mechanical delay line. However, in our experience, this is not necessarily the case. Most experiments (spectrometry and imaging) required to set the lock-in amplifier time constant to 100 ms, and to allow a 500 ms integration time for the reading to be accurate; in other words, the systems needs to wait 500 ms between samples. This setting is quite common for this type of systems. The mechanical delay line requires some milliseconds to move and settle, but even if that could be made instantaneously, the system still would require almost the same 500 ms integration time in order to reduce the system's noise to adequate levels.

Work in the development of THz antennas has been carried out at The University of Manchester by Prof. Mohamed Missous and his group. They have designed and fabricated antennas. Their devices have achieved a 60 dB DR in THz-TDS with 40 dB DR @ 1 THz [170]. This values are similar to the results presented by our system.

THz CW systems have presented a great advance in signal characteristics, and portability. For example, Toptica (Germany) commercializes systems with 80 dB DR @ 100 GHz, and 60 dB @ 1 THz [171]. Our system has 50 dB DR @ 1 THz, but it is fair to remember that the measurement was performed whilst using the 4 mm apertures. Operation without the apertures improved in terms of DR and SNR. Also, we experienced a decay in SNR once that we introduced the second set of parabolic mirrors. In other words, a system working with only two parabolic mirrors presented a better noise response that the system with four mirrors. This can be due to signal losses introduced by the extra optical components and the difficult involved in their alignment. In a typical configuration, the use of two extra parabolic mirrors is avoided by using Si collimating lenses attached to the antennas, which are mounted at the factory, preventing a possible misalignment.

Recently, vector network analyser extension modules have shown operation range from 50 GHz to 1.1 THz, with 120 dB DR @ 200 GHz and 70 dB @ 1 THz [172]. These devices are mainly used for device characterization in the mm band frequencies, but may also be used in general THz applications.

Our second objective was to define rules of operation suitable for pulsed THz tomography in amplitude contrast, which could be also useful for the operation of THz CW imaging systems. Our results in this topic can be summarized as follows:

THz tomography images in amplitude contrast presented strong edge contrast caused by refraction and scattering losses. This effect was not found, however, when images were reconstructed in time-of-flight contrast, because its coherent method of detection is less sensitive to these losses.

The use of apertures may improve image quality. It was found that the use of apertures was useful to limit some artifacts that appeared when the images were scanned without any apertures installed. The use of a second aperture placed after the phantom didn't contribute significantly to improve the image.

Refraction losses are present even at very low refractive indexes. We used Styrofoam for fabricating our phantoms. This material is probably among the most 'THz friendly' that are available, since it is almost transparent at low THz frequencies and has a very low refractive index (n=1.024). But even with this nearly optimal characteristics images were characterized by a strong edge contrast, which is partially caused by refractive losses at high angles of incidence.

Attenuation coefficients correctly approximate volume losses. Attenuation coefficient of Styrofoam increases with frequency and this is reflected in the reconstructed images which show a higher volume contrast at higher frequencies. After reviewing the first tomography images, we thought that there was some volume scattering phenomena, but later we discovered that such effect is approximated by the attenuation coefficient, which includes losses by absorption and scattering. Currently, we have no means available to measure those components separately.

An explanation on how refraction losses and surface scattering are responsible of the edge high contrast has been introduced for the first time. We introduced a modified Rayleigh factor which was used in conjunction with Fresnel equations as a way to approximate the scattered transmission. A simulation of the model was done using MATLAB and it was compared with actual tomography images. It was found that our model does approximate some of the high edge contrast phenomena found in real THz tomography images.

Reconstruction in amplitude contrast may be difficult for materials with higher refractive indexes or higher attenuation coefficients. Fresnel equations predict that if a material has a high refractive index, the refraction losses will increase, which in turn will have an effect in the quality of the reconstructed images. Just a few centimetres of a high attenuation coefficient material and a THz beam may be completely blocked. The latter is also valid for tomography in time-of-flight contrast.

Smoothness of object's surface or internal interfaces needs to be taken into consideration, as it may contribute to the scattering of THz radiation. We have shown that even a phantom with roughness in the order of hundreds of microns may produce high contrast edges due to scattering.

Size of samples are limited by the Rayleigh range. Laws of optics impose a limit on the size of objects that can be analysed by a THz tomography system. For the implemented system, it was found that the maximum working length is around 60 mm but this value is frequency dependent. An improvement could be achieved by a proper selection of THz optical components. This suggest the use of a small collimated beam before a focusing lens (or focusing parabolic mirror) but this could introduce some diffraction. The size of the object will also be limited its attenuation coefficient. A material can quickly become thick enough as to block all incident THz radiation. Attenuation is lower at low THz frequencies, therefore it may be easier to generate tomography images in that range.

6.2 Further work

It was been shown that surface scattering and refraction losses can produce increased attenuation at the edges of a tomography image in amplitude contrast. However, this is not necessarily a bad result. Edge detection is important in tomography, and several algorithms have been developed to generate or increase edge detection in general or specific conditions. In THz tomography in amplitude contrast, the dependency of scattering on wavelength could be used to selectively enhance the detection of a property inside the object. The same phenomenon can be used to enhance volume detection of otherwise transparent objects. Of course, this will require a careful analysis of the imaging scenario, since factors such as relative refractive index at the volume interfaces, and scattering levels at THz frequencies must be considered.

The Rayleigh range in the tomography system could be improved by using a different set of components. For example, if the parabolic mirror used to collect the radiation form the emitter antenna is chosen to have a smaller diameter, for example 12.5 mm instead of the 50 mm that it was used, this will produce a smaller beam before the second parabolic mirror which acts as a focusing mirror. This may require the use of a Si lens placed on the emitter antenna, since in our experience, the use of a smaller collecting parabolic mirror limited severely the amount of power collected in the case of an antenna without Si lens, which is the case for the implemented system. During our previous work in the THz spectrometry version of the system, we found that the combination of a Si lens and a 12.5 mm diameter collecting parabolic mirror worked fine.

In order to gain further understanding of the scattering phenomena at THz frequencies, an experiment for measuring scattering could be built. Such type of measurements require that the detector can be positioned at different angles to measure the beam scattered in different directions. That is not possible with our THz-TDS system and perhaps is very difficult to implement with an electro-optical detection scheme. A Golay cell or a Pyroelectric detector would be more suitable for such tasks.

The model that we have introduced, based on the Rayleigh roughness factor, to model scattering losses in transmitted beams, should be regarded as a first approximation, and further research is recommended in order to make it more accurate. This may require the use of a scattering measurement system, and a more elaborate method for measuring surface roughness. Among the phenomena that is not currently modelled is the partial loss in polarization as the beam is scattered. A study over a wider range of surface characteristics is also suggested.

In the actual tomography system, rotation of the phantom is done using a DC servomotor, which has been configured to provide 7.5° steps, if higher resolutions is required, then a new characterization procedure will be required. If better repeatability is needed then perhaps it should be changed by a commercial rotation stage.

Currently, acquired data is post processed in MATLAB for reconstructing the tomography images. However, this process can be embedded in the LabVIEW program if it is required.

System layout may not be optimal and could be improved. The THz-TDS system was installed at Photon Science Institute, and the ultrashort pulse laser that we used is mounted in a shared optical table, in a configuration that puts severe restrictions to the proximity of our setup. The THz antenna is situated more than 5 m away from the laser source, and this is not the most desirable condition, since it makes the system more sensitive to mechanical vibrations and it makes alignment more difficult. In an ideal situation, the THz antenna should be installed as close as possible to the laser source.

System integration will be a key factor towards portability of THz spectrometry and imaging systems. This will probably rule out electro-optical sampling since it requires several components: quarter-wave plate, focusing lens, Wollaston prism, two mirrors, a balanced detector and a power source; which may be substituted by a photoconductive antenna as THz sensor device. Currently, many commercial systems have followed this approach. In addition, the footprint required by a lock-in amplifier could be reduced if a computer-based approach is used. We designed a usable digital lock-in amplifier, but its performance was limited because the bottleneck introduced by USB communications. If a different hardware could be used, for example, a PCI card, that could be a better platform for developing a computer-based lock-in amplifier.

We have proposed a method based on local apodization to reduce the spurious oscillations that appear in some spectra. We tested the method using rectangular apodization, but it could be extended to other functions like, triangular, hamming, etc. Proper selection of the optimal parameters is difficult but this problem could be solved using some form of soft-computing, like artificial neural networks, or genetic algorithms.

Interpretation of THz images is a field open to research and to the development of applications. It is possible to think that once established back in Mexico, I could collaborate with some groups doing research on tomography images, such as the ones in the Universidad Nacional Autónoma de México, but it would be interesting to explore how the work done by Dr. Bayro Chorrochano, form the Universidad de Guadalajara, on geometric neural computing [173] and Clifford support vector machines [174] could be applied to object or feature recognition, and classification on THz images.

REFERENCES

[1]   D. H. Auston, K. P. Cheung, and P. R. Smith, "Picosecond photoconducting Hertzian dipoles," *Applied Physics Letters,* vol. 45, pp. 284-286, 1984.

[2]   M. Naftaly and R. E. Miles, "Terahertz time-domain spectroscopy for material characterization," *Proceedings of the IEEE,* vol. 95, pp. 1658-1665, 2007.

[3]   D. M. Mittleman, R. H. Jacobsen, and M. C. Nuss, "T-ray imaging," *Selected Topics in Quantum Electronics, IEEE Journal of,* vol. 2, pp. 679-692, 1996.

[4]   S. Wang and X. C. Zhang, "Pulsed terahertz tomography," *Journal of Physics D: Applied Physics,* vol. 37, p. R1, 2004.

[5]   J. P. Guillet, B. Recur, L. Frederique, B. Bousquet, L. Canioni, I. Manek-Hönninger*, et al.*, "Review of Terahertz Tomography Techniques," *Journal of Infrared, Millimeter, and Terahertz Waves,* vol. 35, pp. 382-411, 2014.

[6]   Teraview. (2014, 22-May-2014). *Terahertz applications*. Available: http://www.teraview.com/applications/index.html

[7]   B. Research. (2013, 22-May-2014). *Terahertz radiation systems: Technologies and global markets*. Available: http://www.bccresearch.com/market-research/instrumentation-and-sensors/terahertz-radiation-systems-technologies-ias029c.html

[8]   D. Grischkowsky, S. Keiding, M. v. Exter, and C. Fattinger, "Far-infrared time-domain spectroscopy with terahertz beams of dielectrics and semiconductors," *Journal of the Optical Society of America B,* vol. 7, pp. 2006-2015, 1990.

[9]   M. Razeghi, Q. Y. Lu, N. Bandyopadhyay, S. Slivken, and Y. Bai, "Room temperature compact THz sources based on quantum cascade laser technology," in *Proceedings of SPIE -Terahertz emitters, receivers and applications IV*, 2013, pp. 884602-1 884602-7.

[10]   X. C. Zhang and J. Xu, *Introduction to THz Wave Photonics*: Springer, 2009.

[11]   M. Naftaly, "Metrology Issues and Solutions in THz Time-Domain Spectroscopy: Noise, Errors, Calibration," *Sensors Journal, IEEE,* vol. 13, pp. 8-17, 2013.

[12]   EKSPLA. (2011, 25-Jun-2014). *T-Spec series THz spectrometer*. Available: http://www.ekspla.com/wp-content/uploads/2011/05/t-spec-series-real-time-terahertz-spectrometer1.pdf

[13]   D. W. Ball, *The Basics of Spectroscopy*: SPIE- The International Society for Optical Engineering, 2001.

[14]   D. Pavia, G. Lampman, G. Kriz, and J. Vyvyan, *Introduction to Spectroscopy*: Cengage Learning, 2008.

[15]   M. Theuer, S. S. Harsha, D. Molter, G. Torosyan, and R. Beigang, "Terahertz Time-Domain Spectroscopy of Gases, Liquids, and Solids," *ChemPhysChem,* vol. 12, pp. 2695-2705, 2011.

[16]   B. Ferguson and X. C. Zhang, "Materials for terahertz science and technology," *Nature Materials,* vol. 1, pp. 26-33, 2002.

[17]   P. De Maagt, "Terahertz applications and technology," in *IET Conference Publications*, 2009, pp. 8-11.

[18]   D. Mittleman, "Terahertz imaging," in *Sensing with terahertz radiation*, D. Mittleman, Ed., ed: Springer, 2003, p. 377.

[19] S. L. Dexheimer, *Terahertz spectroscopy: principles and applications*. Boca Raton, Fla: CRC, 2007.

[20] R. M. Woodward, "Terahertz technology in global homeland security," in *Proceedings of SPIE - The International Society for Optical Engineering*, 2005, pp. 22-31.

[21] M. R. Stringer, J. Bassi, R. E. Miles, Z. Yang, and K. Ozanyan, "THz spectroscopy through a high-pressure combustion system," in *IRMMW-THz 2008. 33rd International Conference on*, 2008, pp. 1-2.

[22] S. Wang, B. Ferguson, D. Abbott, and X. C. Zhang, "T-ray imaging and tomography," *Journal of Biological Physics,* vol. 29, pp. 247-256, 2003.

[23] C. M. Armstrong, "The truth about terahertz," *Spectrum, IEEE,* vol. 49, pp. 36-41, 2012.

[24] M. Nuss and J. Orenstein, "Terahertz time-domain spectroscopy," in *Millimeter and Submillimeter Wave Spectroscopy of Solids*. vol. 74, G. Grüner, Ed., ed: Springer Berlin / Heidelberg, 1998, pp. 7-50.

[25] Y.-S. Lee, "Introduction," in *Principles of Terahertz Science and Technology*, ed: Springer US, 2009, pp. 1-9.

[26] M. Tani, Y. Hirota, C. T. Que, S. Tanaka, R. Hattori, M. Yamaguchi*, et al.*, "Novel terahertz photoconductive antennas," *International Journal of Infrared and Millimeter Waves,* vol. 27, pp. 531-546, 2006.

[27] Z. Jiang and X.-C. Zhang, "Free-space electro-optic techniques," in *Sensing with Terahertz radiation*, D. Mittleman, Ed., ed: Springer, 2003, p. 353.

[28] Q. Chen, M. Tani, Z. Jiang, and X. C. Zhang, "Electro-optic transceivers for terahertz-wave applications," *Journal of the Optical Society of America B: Optical Physics,* vol. 18, pp. 823-831, 2001.

[29] M. Van Exter, C. Fattinger, and D. Grischkowsky, "High-brightness terahertz beams characterized with an ultrafast detector," *Applied Physics Letters,* vol. 55, pp. 337-339, 1989.

[30] K. Sakai and M. Tani, "Introduction to Terahertz Pulses," in *Terahertz Optoelectronics*. vol. 97, ed: Springer Berlin / Heidelberg, 2005, pp. 1-30.

[31] D. Mittleman and R. Cheville, "Terahertz generation and applications," in *Ultrafast Optics*, R. Trebino and J. Squier, Eds., ed, In press.

[32] M. Tani, S. Matsuura, K. Sakai, and S. I. Nakashima, "Emission characteristics of photoconductive antennas based on low-temperature-grown GaAs and semi-insulating GaAs," *Applied Optics,* vol. 36, pp. 7853-7859, 1997.

[33] H. Dyball, "Tuning into terahertz," *Electronics Letters,* vol. 46, p. 602, 2010.

[34] Batop. (2014). *Photoconductive antenna for Terahertz waves*. Available: http://www.batop.com/products/terahertz/photoconductive-antenna/photoconductive-terahertz-antenna.html

[35] Hamamatsu. (2011). Available: http://sales.hamamatsu.com/en/produkte/laser-group/Terahertz.php

[36] Y. Cai, I. Brener, J. Lopata, J. Wynn, L. Pfeiffer, and J. Federici, "Design and performance of singular electric field terahertz photoconducting antennas," *Applied Physics Letters,* vol. 71, pp. 2076-2078, 1997.

[37] A. Dreyhaupt, S. Winnerl, M. Helm, and T. Dekorsy, "Optimum excitation conditions for the generation of high-electric-field terahertz radiation from an oscillator-driven photoconductive device," *Opt. Lett.,* vol. 31, pp. 1546-1548, 2006.

References

[38]   M. Missous, I. Kostakis, and D. Saeedkia, "Arsenide-based terahertz materials and devices for 800 and 1550 nm excitations," 2012, pp. 63-70.

[39]   Y.-S. Lee, "Generation and detection of broadband Terahertz pulses," in *Principles of Terahertz Science and Technology*, ed: Springer US, 2009, pp. 1-66.

[40]   T.-A. Liu, M. Tani, M. Nakajima, M. Hangyo, K. Sakai, S.-i. Nakashima*, et al.*, "Ultrabroadband terahertz field detection by proton-bombarded InP photoconductive antennas," *Optics Express,* vol. 12, pp. 2954-2959, 2004/06/28 2004.

[41]   Q. Wu, M. Litz, and X. C. Zhang, "Broadband detection capability of ZnTe electro-optic field detectors," *Applied Physics Letters,* vol. 68, pp. 2924-2926, 1996.

[42]   P. L. Richards, "Bolometers for infrared and millimeter waves," *Journal of Applied Physics,* vol. 76, pp. 1-24, 1994.

[43]   Infra-Tec, "Pyroelectric detectors," Infra Tec GmbH2004.

[44]   I. Brener, Q. Wu, Y. Cai, X. C. Zhang, J. Lopata, J. Wynn*, et al.*, "Coherent terahertz detection: free space electro-optic sampling versus antenna detection," in *Lasers and Electro-Optics, 1997. CLEO '97., Summaries of Papers Presented at the Conference on*, 1997, pp. 136-137.

[45]   X.-C. Zhang and J. Xu, "Terahertz radiation," in *Introduction to THz Wave Photonics*, ed: Springer US, 2010, pp. 1-26.

[46]   K. Sakai, *Terahertz Optoelectronics*. Berlin Heidelberg: Springer-Verlag GmbH., 2005.

[47]   M. Nazeri and R. Massudi, "Study on the effect of dispersion of the probe pulse on measuring the THz pulse propagating in a ZnTe crystal," *Measurement Science and Technology,* vol. 21, 2010.

[48]   S. P. Mickan and X. C. Zhang, "T-ray sensing and imaging," *International Journal of High Speed Electronics and Systems,* vol. 13, pp. 601-676, 2003.

[49]   I. Thorlabs. (2011). *Off-axis parabolic mirror*. Available: http://www.thorlabs.de/NewGroupPage9.cfm?ObjectGroup_ID=5447

[50]   Newport, "10B20UF.25 Broadband 45° mirror," ed: Newport Corp.

[51]   I. Matsuda, K. Misawa, and R. Lang, "Femtosecond chirp-variable apparatus using a chirped mirror pair for quantum coherent control," *Optics Communications,* vol. 239, pp. 181-186, 2004.

[52]   Newport, "Model: 10RQ00UB.2 Ultrafast Laser Beamsplitter, S Polarized, 25.4 mm, 700-950 nm," 2014.

[53]   U. Fuchs and U. D. Zeitner, "Focusing ultrashort laser pulses," in *Ultrafast Optics*, R. Trebino and J. Squier, Eds., ed, In press.

[54]   Newport, "Application note 19. Prism compressor for ultrashort laser pulses," Newport Corporation2006.

[55]   E. Hecht, *Optics (4th Edition)*: Addison Wesley, 2001.

[56]   P. C. D. Hobbs, "REACHING THE SHOT NOISE LIMIT FOR $10," *Opt. Photon. News,* vol. 2, pp. 17-23, 1991.

[57]   S. Pal, P. Wright, and H. McCann, "Digital gain balancing technique for sensitive detection of minor gas concentrations," in *Proceedings of the 15th IEEE International Conference on Electronics, Circuits and Systems, ICECS 2008*, 2008, pp. 858-861.

[58]   P. C. D. Hobbs, "Shot noise limited optical measurements at baseband with noisy lasers," in *Proceedings of SPIE - The International Society for Optical Engineering*, 1991, pp. 216-221.

[59] P. C. D. Hobbs, "Noise cancelling circuitry for optical systems with signal dividing and combining means," United States of America Patent 5134276, Jul. 28, 1992, 1992.

[60] P. C. D. Hobbs, "Ultrasensitive laser measurements without tears," *Applied Optics,* vol. 36, pp. 903-920, 1997.

[61] Bentham. *Lock-in amplifiers*. Available: http://www.bentham.co.uk/pdf/F225.pdf

[62] G. Vasilescu, *Electronic Noise and Interfering Signals: Principles and Applications*: Springer, 2005.

[63] R. Alonso, F. Villuendas, J. Borja, L. A. Barragán, and I. Salinas, "Low-cost, digital lock-in module with external reference for coating glass transmission/reflection spectrophotometer," *Measurement Science and Technology,* vol. 14, pp. 551-557, 2003.

[64] S. Garcia-Castillo and K. B. Ozanyan, "Field-programmable data acquisition and processing channel for optical tomography systems," *Review of Scientific Instruments,* vol. 76, 2005.

[65] S. C. Corzo-Garcia, R. J. Medina-Lopez, S. Anderson, E. Castro-Camus, R. Carriles, and A. Ruiz-Marquez, "Reliable and economical method to join optical tables," *Optics and Lasers in Engineering,* vol. 49, pp. 1251-1253, 2011.

[66] P. V. Mitchel, "Fast steering mirror technology: Active beam stabilization. Application note 2," Newport Corporation.

[67] Newport, "Active beam stabilization between optical tables. Application note 23," Newport Corporation AN 23, 2006.

[68] Tydex. (2014, 14-Feb-2014). *Golay cells*. Available: http://www.tydexoptics.com/products/thz_optics/golay_cell/

[69] M. van Exter and D. R. Grischkowsky, "Characterization of an optoelectronic terahertz beam system," *IEEE Transactions on Microwave Theory and Techniques,* vol. 38, pp. 1684-1691, 1990.

[70] M. Hangyo, M. Tani, and T. Nagashima, "Terahertz Time-Domain Spectroscopy of Solids: A Review," *International Journal of Infrared and Millimeter Waves,* vol. 26, pp. 1661-1690, 2005/12/01 2005.

[71] M. v. Exter, C. Fattinger, and D. Grischkowsky, "Terahertz time-domain spectroscopy of water vapor," *Opt. Lett.,* vol. 14, pp. 1128-1130, 1989.

[72] P. U. Jepsen, R. H. Jacobsen, and S. R. Keiding, "Generation and detection of terahertz pulses from biased semiconductor antennas," *J. Opt. Soc. Am. B,* vol. 13, pp. 2424-2436, 1996.

[73] L. Duvillaret, F. Garet, and J. L. Coutaz, "Caractérisation de matériaux et autres applications de la spectroscopie térahertz dans le domaine temporel," *REE, Revue de L'Electricite et de L'Electronique* vol. 2003, pp. 63-68, 2003.

[74] NPL, "Terahertz emitter datasheet," National Physical Laboratory, UK.

[75] M. Naftaly and R. E. Miles, "An algorithm for the removal of spurious oscillations from spectra derived from THz time-domain data," in *IRMMW-THz. Joint 32nd International Conference on*, 2007, pp. 478-479.

[76] Filmetrix. (2014, 31-Jan-2014). *Refractive Index of GaAs*. Available: http://www.filmetrics.com/refractive-index-database/GaAs/Gallium-Arsenide

[77] R. K. H. Galvão, S. Hadjiloucas, A. Zafiropoulos, G. C. Walker, J. W. Bowen, and R. Dudley, "Optimization of apodization functions in terahertz transient spectrometry," *Optics Letters,* vol. 32, pp. 3008-3010, 2007/10/15 2007.

[78] R. K. H. Galvão, S. Hadjiloucas, and J. W. Bowen, "Use of the statistical properties of the wavelet-transform coefficients for optimization of integration

time in Fourier transform spectrometry," *Optics Letters,* vol. 27, pp. 643-645, 2002/04/15 2002.

[79]   Batop. *Photoconductive Antenna for THz Applications*. Available: http://www.batop.de/information/PCA_infos.html

[80]   Newport, "Optical delay line kits," Newport Corporation 2004.

[81]   P. H. Siegel, "Terahertz technology," *Microwave Theory and Techniques, IEEE Transactions on,* vol. 50, pp. 910-928, 2002.

[82]   P. Y. Han and X. C. Zhang, "Free-space coherent broadband terahertz time-domain spectroscopy," *Measurement Science and Technology,* vol. 12, pp. 1747-1756, 2001.

[83]   W. L. Chan, J. Deibel, and D. M. Mittleman, "Imaging with terahertz radiation," *Reports on Progress in Physics,* vol. 70, pp. 1325-1379, 2007.

[84]   B. Ferguson, S. Wang, D. Gray, D. Abbot, and X. C. Zhang, "T-ray computed tomography," *Opt. Lett.,* vol. 27, pp. 1312-1314, 2002.

[85]   M. R. Stringer, M. Naftaly, N. Marakgos, R. E. Miles, E. Linfield, and A. G. Davies, "An investigation of beam focusing perturbations in THz spectroscopy measurements," in *IRMMW-THz 2005. The Joint 30th International Conference on*, 2005, pp. 421-422 vol. 2.

[86]   C. P. Chiou, J. L. Blackshire, and R. B. Thompson, "Terahertz ray system calibration and material characterizations," 2009, pp. 410-417.

[87]   Drierite. (3-Feb-2014). *Laboratory gas drying unit*. Available: https://secure.drierite.com/catalog3/page5.cfm

[88]   J. S. Bendat and A. G. Piersol, *Random Data: Analysis and Measurement Procedures*: Wiley, 2011.

[89]   J. B. Grimbleby, "The ideal averaging filter: Its applications and realizations," *Radio and Electronic Engineer,* vol. 49, pp. 530-534, 1979.

[90]   R. A. Pease, *Troubleshooting Analog Circuits*: Newnes, 1991.

[91]   Wikipedia. (27/Jan/2014). *Moving average*. Available: http://en.wikipedia.org/wiki/Moving_average

[92]   S. W. Smith, *The scientist and engineer's guide to digital signal processing*: California Technical Publishing, 1997.

[93]   S. W. Smith, *Digital Signal Processing: A Practical Guide for Engineers and Scientists*: Newnes, 2003.

[94]   V. R. Kaluri and K. M. Ranjan, *Digital Signal Processing: A Practitioner's Approach*: Wiley, 2006.

[95]   G. M. Hieftje, "Signal-to-Noise Enhancement Through Instrumental Techniques part II," *Analytical Chemistry,* vol. 44, pp. 69A-78A, 1972.

[96]   R. Burdett, "Box car and signal averagers," in *Handbook of measuring system design*, P. H. Sydenham and R. Thorn, Eds., ed: John Wiley & Sons, Ltd., 2005, pp. 1209-1216.

[97]   T. H. Wilmshurst, *Signal Recovery from Noise in Electronic Instrumentation, Second Edition*: Taylor & Francis, 1990.

[98]   S. Efthymiou and K. B. Ozanyan, "Pulse Detection by Gated Synchronous Demodulation," *Sensors Journal, IEEE,* vol. 13, pp. 3349-3360, 2013.

[99]   E. C. Ifeachor and B. W. Jervis, *Digital signal processing: a practical approach*: Prentice Hall, 2002.

[100]   D. G. Manolakis and V. K. Ingle, *Applied Digital Signal Processing: Theory and Practice*: Cambridge University Press, 2011.

[101]   National-Instruments, "NI 9205 Operating Instructions and Specifications," 2008.

[102] National-Instruments, "NI cDAQ-9172 User Guide and Specifications," 2008.

[103] National-Instruments, "NI 9401 Operating Instructions and Specifications," 2012.

[104] F. M. Al-Douseri, Y. Chen, and X. C. Zhang, "THz wave sensing for petroleum industrial applications," *International Journal of Infrared and Millimeter Waves,* vol. 27, pp. 481-503, 2006.

[105] R. Cunnell, T. Luce, J. Collins, R. Rungsawang, J. R. Freeman, H. E. Beere*, et al.*, "Quantification of emulsified water content in oil using a terahertz quantum cascade laser," in *Infrared, Millimeter, and Terahertz Waves, 2009. IRMMW-THz 2009. 34th International Conference on*, 2009, pp. 1-2.

[106] K. Geun-Ju, J. Seok-Gy, K. Jung-Il, and J. Yun-Sik, "Terahertz time domain spectroscopy of petroleum products and organic solvents," in *Infrared, Millimeter and Terahertz Waves, 2008. IRMMW-THz 2008. 33rd International Conference on*, 2008, pp. 1-2.

[107] S. Gorenflo, U. Tauer, I. Hinkov, A. Lambrecht, R. Buchner, and H. Helm, "Dielectric properties of oil and water complexes using terahertz transmission spectroscopy," *Chemical Physics Letters,* vol. 421, pp. 494-498, 2006.

[108] L. Jiusheng, "Optical Parameters of Vegetable Oil Studied by Terahertz Time-Domain Spectroscopy," *Appl. Spectrosc.,* vol. 64, pp. 231-234, 2010.

[109] J.-s. Li, X.-l. Zhao, and D. Xu, "Optical parameter determination of seed oil with terahertz time-domain spectroscopy," pp. 73850N-73850N, 2009.

[110] S. Zhu, K. Zhao, T. Lu, S. Zhao, Q. Zhou, Y. Shi*, et al.*, "Terahertz spectroscopy properties of the selected engine oils," *Proc. of SPIE,* vol. 7854, pp. 78540A-78540A, 2010.

[111] Y. N. Li, J. Li, Z. M. Zeng, Z. Tian, and W. K. Wang, "Terahertz spectroscopy for quantifying refined oil mixtures," *Applied Optics,* vol. 51, pp. 5885-5889, 2012.

[112] P. Kuzel and J. Petzelt, "Time-resolved terahertz transmission spectroscopy of dielectrics," *Ferroelectrics,* vol. 239, pp. 79-86, 2000.

[113] S. Gorenflo, I. Hinkov, and A. Lambrecht, "Terahertz-Time-Domain-Spektroskopie mit einem leistungsoptimierten elektrooptishcen detektionsverfahren," *Technisches Messen,* vol. 72, pp. 430-439, 2005.

[114] Nynas. (2012, 4-Feb-2014). *Nytro Gemini X Product datasheet*. Available: https://nyport.nynas.com/Apps/1112.nsf/wnpds/Nytro_Gemini_X_IEC/$File/PD S_Nytro_Gemini_X_EN.pdf

[115] S. Karmakar, N. K. Roy, and P. Kumbhakar, "Effect of ageing in transformer oil using UV-visible spectrophotometeric technique," *Journal of Optics,* vol. 40, pp. 33-38, 2011.

[116] R. Galvão, S. Hadjiloucas, J. Bowen, and C. Coelho, "Optimal discrimination and classification of THz spectra in the wavelet domain," *Optics Express,* vol. 11, pp. 1462-1473, 2003/06/16 2003.

[117] NewFocus, "Nirvana autobalanced photoreceivers. Model 2007 & 2017 user's manual," ed. USA: New Focus, Inc., 2002, p. 36.

[118] Newport, "AN44 Terahertz spectrometer based on generation of ultrafast Terahertz pulses in air plasma," Newport Corporation2011.

[119] *Design With Operational Amplifiers And Analog Integrated Circuits*: McGraw-Hill Education (India) Pvt Limited, 2002.

[120] B. Schulkin and X.-C. Zhang. (2006) TERAHERTZ SPECTROMETRY: Time-domain spectrometers expand toward new horizons. *Laser Focus World*. Available: http://www.laserfocusworld.com/articles/print/volume-42/issue-

202

11/features/terahertz-spectrometry-time-domain-spectrometers-expand-toward-new-horizons.html

[121] Batop, "PCA-44-06-10-800-x Instruction manual and datasheet," Batop Optoelectronics.

[122] S. Preu, G. H. Dhler, S. Malzer, L. J. Wang, and A. C. Gossard, "Tunable, continuous-wave Terahertz photomixer sources and applications," *Journal of Applied Physics,* vol. 109, 2011.

[123] E. R. Brown, "Advancements in photomixing and photoconductive switching for THz spectroscopy and imaging," in *SPIE Proceedings: Terahertz technology and applications IV*, 2011, pp. 793802-1 793802-16.

[124] E. R. Brown, "THz Generation by Photomixing in Ultrafast Photoconductors," *International Journal of High Speed Electronics and Systems,* vol. 13, pp. 497-545, 2003.

[125] QMC. (2014, 14-Feb-2014). *Terahertz Companies*. Available: http://www.terahertz.co.uk/

[126] Spectra-Physics, "Matisse Ultra-narrow linewidth tunable ring laser datasheet," 2014.

[127] Spectra-Physics, "Millennia Pro S solid-state laser datasheet," p. 2, 2004.

[128] K. Balakier, M. J. Fice, L. Ponnampalam, A. J. Seeds, and C. C. Renaud, "Tuneability of monolithically integrated optical phase lock loop for THz generation," in *Microwave Photonics (MWP), 2013 International Topical Meeting on*, 2013, pp. 182-185.

[129] R. J. Steed, L. Ponnampalam, M. J. Fice, C. C. Renaud, D. C. Rogers, D. G. Moodie*, et al.*, "Hybrid Integrated Optical Phase-Lock Loops for Photonic Terahertz Sources," *Selected Topics in Quantum Electronics, IEEE Journal of,* vol. 17, pp. 210-217, 2011.

[130] D. M. Mittleman and M. C. Nuss, "T-ray tomography," 1997, pp. 62-63.

[131] Z. Jiang and X.-C. Zhang, "Terahertz imaging via electrooptic effect," *IEEE Transactions on microwave theory and techniques,* vol. 47, pp. 2644-2650, 1999.

[132] B. B. Hu and M. C. Nuss, "Imaging with terahertz waves," *Opt. Lett.,* vol. 20, pp. 1716-1718, 1995.

[133] W. Withayachumnankul, G. M. Png, Y. Xiaoxia, S. Atakaramians, I. Jones, L. Hungyen*, et al.*, "T-Ray Sensing and Imaging," *Proceedings of the IEEE,* vol. 95, pp. 1528-1558, 2007.

[134] K. Kawase, Y. Ogawa, Y. Watanabe, and H. Inoue, "Non-destructive terahertz imaging of illicit drugs using spectral fingerprints," *Optics Express,* vol. 11, pp. 2549-2554, 2003.

[135] X. C. Zhang, "Terahertz wave imaging: horizons and hurdles," *Physics in Medicine and Biology,* vol. 47, p. 3667, 2002.

[136] R. Bogue, "Terahertz imaging: A report on progress," *Sensor Review,* vol. 29, pp. 6-12, 2009.

[137] B. S. Williams, "Terahertz quantum-cascade lasers," *Nature Photonics,* vol. 1, pp. 517-525, 2007.

[138] M. Chamberlain, "Applied terahertz science: The technology of the future, and always will be?," in *Terahertz frequency detection and identification of materials and objects*, R. E. Miles, Ed., ed: Springer, 2007, pp. 341-352.

[139] K. Shibuya, M. Tani, M. Hangyo, O. Morikawa, and H. Kan, "Compact and inexpensive continuous-wave subterahertz imaging system with a fiber-coupled multimode laser diode," *Applied Physics Letters,* vol. 90, pp. -, 2007.

[140] K. L. Nguyen, M. L. Johns, L. Gladden, C. H. Worrall, P. Alexander, H. E. Beere, *et al.*, "Three-dimensional imaging with a terahertz quantum cascade laser," *Optics Express,* vol. 14, pp. 2123-2129, 2006.

[141] N. Rothbart, H. Richter, M. Wienold, L. Schrottke, H. T. Grahn, and H. W. Hubers, "Fast 2-D and 3-D terahertz imaging with a quantum-cascade laser and a scanning mirror," *IEEE Transactions on Terahertz Science and Technology,* vol. 3, pp. 617-624, 2013.

[142] N. Karpowicz, H. Zhong, J. Xu, K.-I. Lin, J.-S. Hwang, and X.-C. Zhang, "Comparison between pulsed terahertz time-domain imaging and continuous wave terahertz imaging," *Semiconductor Science and Technology,* vol. 20, p. S293, 2005.

[143] P. U. Jepsen, D. G. Cooke, and M. Koch, "Terahertz spectroscopy and imaging – Modern techniques and applications," *Laser & Photonics Reviews,* vol. 5, pp. 124-166, 2011.

[144] K. B. Ozanyan, P. Wright, M. R. Stringer, and R. E. Miles, "Hard-field THz tomography," *IEEE Sensors Journal,* vol. 11, pp. 2507-2513, 2011.

[145] J. Radon, "On the determination of functions from their integral values along certain manifolds," *Reports on the proceedings of the Royal Saxonian Academy of Sciences at Leipzig,* vol. 69, pp. 262–277, 1917.

[146] A. Plaskowski, S. Beck, R. Thorn, and T. Dyakowski, *Imaging Industrial Flows: Applications of Electrical Process Tomography*: Taylor & Francis, 1995.

[147] A. C. Kak and M. Slaney, *Principles of computerized tomographic imaging*: Society for Industrial and Applied Mathematics, 2001.

[148] J. Hsieh, *Computed Tomography: Principles, Design, Artifacts, and Recent Advances*: SPIE Press, 2003.

[149] I. Øyvind, "A review of reconstruction techniques for capacitance tomography," *Measurement Science and Technology,* vol. 7, p. 325, 1996.

[150] D. S. Holder, *Electrical Impedance Tomography: Methods, History and Applications*: Taylor & Francis, 2010.

[151] B. Recur, A. Younus, S. Salort, P. Mounaix, B. Chassagne, P. Desbarats, *et al.*, "Investigation on reconstruction methods applied to 3D terahertz computed tomography," *Optics Express,* vol. 19, pp. 5105-5117, 2011.

[152] J. Mo, M. de Groot, and J. F. de Boer, "Focus-extension by depth-encoded synthetic aperture in Optical Coherence Tomography," *Optics Express,* vol. 21, pp. 10048-10061, 2013.

[153] R. A. Lewis, *Terahertz Physics*: Cambridge University Press, 2013.

[154] Unknown. (30/Apr/2014). *Gaussian Beams and the Knife-Edge Measurement*. Available: massey.dur.ac.uk/resources/grad_skills/KnifeEdge.pdf

[155] T. Hattori, M. Sakamoto, and R. Rungsawang, "Spatial frequency filter for real-time THz imaging," in *IRMMW-THz 2005. The Joint 30th International Conference on*, 2005, pp. 333-334 vol. 2.

[156] E. Abraham, A. Younus, C. Aguerre, P. Desbarats, and P. Mounaix, "Refraction losses in terahertz computed tomography," *Optics Communications,* vol. 283, pp. 2050-2055, 2010.

[157] S. Mukherjee, J. Federici, P. Lopes, and M. Cabral, "Elimination of Fresnel Reflection Boundary Effects and Beam Steering in Pulsed Terahertz Computed Tomography," *Journal of Infrared, Millimeter, and Terahertz Waves,* vol. 34, pp. 539-555, 2013.

[158] P. Laven, "Separating diffraction from scattering: the million-dollar challenge," *Journal of Nanophotonics,* vol. 4, pp. 041593-041593-18, 2010.

[159] J. C. Stover, *Optical Scattering: Measurements and Analysis*: Society of Photo Optical, 2012.

[160] Y. Soskind, *Field Guide to Diffractive Optics*: SPIE Press, 2011.

[161] R. Piesiewicz, C. Jansen, D. Mittleman, T. Kleine-Ostmann, M. Koch, and T. Kürner, "Scattering analysis for the modeling of THz communication systems," *IEEE Transactions on Antennas and Propagation,* vol. 55, pp. 3002-3009, 2007.

[162] J. A. Ogilvy, *Theory of wave scattering from random rough surfaces*: A. Hilger, 1991.

[163] P. Beckmann and A. Spizzichino, *The scattering of electromagnetic waves from rough surfaces*: Pergamon Press; [distributed in the Western Hemisphere by Macmillan, New York], 1963.

[164] M. Zerrad, J. Sorrentini, G. Soriano, and C. Amra, "Gradual loss of polarization in light scattered from rough surfaces: Electromagnetic prediction," *Optics Express,* vol. 18, pp. 15832-15843, 2010.

[165] M. Beruete, M. N. Cia, I. Campillo, P. Goy, and M. Sorolla, "Quasioptical Polarizer Based on Self-Complementary Sub-Wavelength Hole Arrays," *Microwave and Wireless Components Letters, IEEE,* vol. 17, pp. 834-836, 2007.

[166] J. R. Birch, "Pseudocoherence in dispersive Fourier transform spectroscopy," *Infrared Physics,* vol. 28, pp. 345-352, 1988.

[167] S. Hadjiloucas, L. S. Karatzas, and J. W. Bowen, "Measurements of leaf water content using terahertz radiation," *Microwave Theory and Techniques, IEEE Transactions on,* vol. 47, pp. 142-149, 1999.

[168] J. W. Bowen, G. C. Walker, and S. Hadjiloucas, "Sample-induced beam distortions in terahertz time domain spectroscopy and imaging systems," in *IRMMW-THz. Joint 32nd International Conference on*, 2007, pp. 208-209.

[169] G. C. Walker, J. W. Bowen, S. Hadjiloucas, A. Zafiropoulos, T. Hadlington, and J. M. Chamberlain, "Quantification of boundary definition using pulsed terahertz radiation for wedged geometries," in *IRMMW-THz. Joint 32nd International Conference on*, 2007, pp. 512-513.

[170] I. Kostakis, D. Saeedkia, and M. Missous, "Terahertz Generation and Detection Using Low Temperature Grown InGaAs-InAlAs Photoconductive Antennas at 1.55 um pulse excitation," *Terahertz Science and Technology, IEEE Transactions on,* vol. 2, pp. 617-622, 2012.

[171] Toptica. (2014). *CW THz packages*. Available: http://www.toptica.com/products/terahertz_generation/lasers_and_photomixers_for_cw_terahertz_generation/cw_terahertz_spectroscopy_extension.html

[172] VDI. (2014). *Vector Network Analyzer extension modules*. Available: http://www.vadiodes.com/index.php/en/products/vector-network-analyzer

[173] E. J. Bayro-Corrochano, "Geometric neural computing," *Neural Networks, IEEE Transactions on,* vol. 12, pp. 968-986, 2001.

[174] E. J. Bayro-Corrochano and N. Arana-Daniel, "Clifford Support Vector Machines for Classification, Regression, and Recurrence," *Neural Networks, IEEE Transactions on,* vol. 21, pp. 1731-1746, 2010.

[175] Newport. (11-DIC-2013). *Introduction to positioning equipment*. Available: http://www.newport.com/Introduction-to-Positioning-Equipment/144535/1033/content.aspx

[176]   Batop, "Instruction manual and data sheet PCA-44-06-10-800-x," Batop optoelectronics.

[177]   M. Naftaly, M. R. Stringer, R. E. Miles, J. Bassi, and Y. Zhang, "Terahertz transmission spectroscopy of high-pressure flames," in *IRMMW-THz 2005. The Joint 30th International Conference on*, 2005, pp. 415-416 vol. 2.

[178]   K. J. Chau and A. Y. Elezzabi, "Ultra-wide bandwidth THz emission from a semiconductor irradiated with intense, radially-polarized, Bessel-Gauss pulses," vol. 79, ed, 2004, pp. 708-710.

[179]   H. G. Darabkhani, M. Banuelos-Saucedo, J. Young, M. Stringer, P. Wright, Q. Wang*, et al.*, "Sensing in sooting flames: THz time-domain spectroscopy and tomography," in *Proceedings of IEEE Sensors*, 2012, pp. 1-4.

A. APPENDIX

System setup alignment

The probe pulse must arrive synchronously with the Terahertz pulse; otherwise no signal will be detected. This means a time and space match between the two signals. Hence correct alignment of all components is indispensable for the system to work.

The laser source for the THz-TDS system is a Coherent Mira 900 mode-locked Ti-Sapphire laser, and according to health and safety regulations, pre-alignment procedures must be carried out with a low power laser. For that purpose a 650 nm 1mW laser module was used (Figure A-1).

Figure A-1. Laser module in a mirror mount.

First of all, we need to make both lasers co-aligned, so the adjustments made with the low power laser can be used with the Ti-Sapphire.

- Align the Ti-Sapphire laser beam so it is parallel to the optical table. A ruler can be used as reference (Figure A-2)
- Place two iris diaphragms in the beam path, separated at least 1 m from each other (Figure A-3)
- Place the laser module close to the Ti-Sapphire beam output and before the two irises. Since this module is going to be installed and removed several times, it is

convenient to leave a post holder in place and to fix a collar to the laser module post.

- Align the laser module so its beam passes through the irises
- In the above procedure a paper screen can be used as reference (Figure A-4)
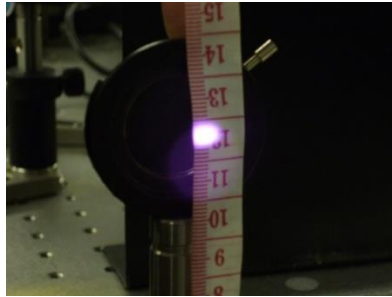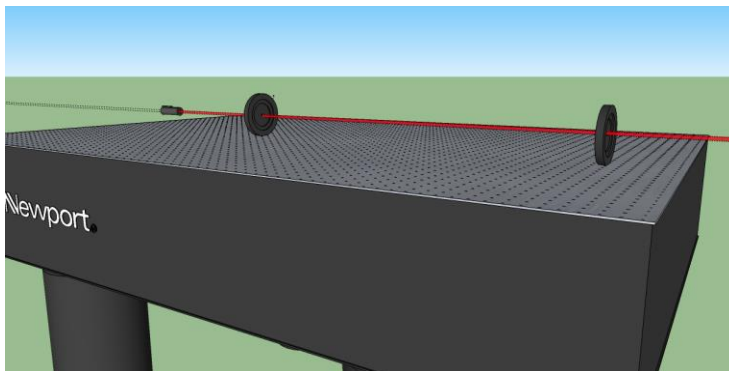

Figure A-2. Alignment of Ti-Sapphire laser.

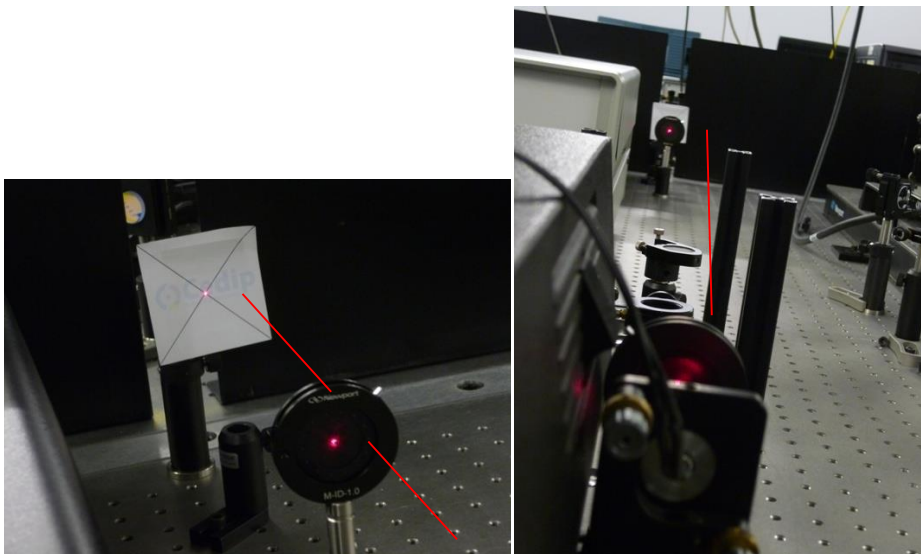Figure A-3. Laser alignment using two iris diaphragms.

Figure A-4. Alignment of the laser module beam.

For mounting the mirrors, kinematic type mounts were used. In standard kinematic (non-Gimbal) mounts, location and orientation of rotation axes are behind the optics [175]. Each mount has two adjustment knobs, and each knob is coupled with the other, so it is usually necessary to move both knobs to make the required adjust (Figure A-5). Furthermore, rotation of the mirror mount (over the post) produces a displacement of the mirror centre, which makes alignment more difficult (Figure A-6).
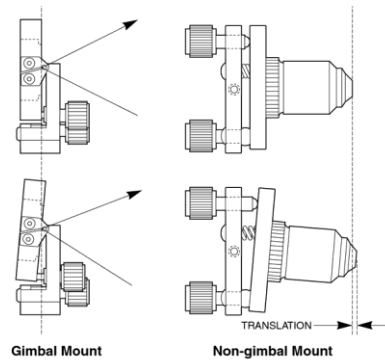

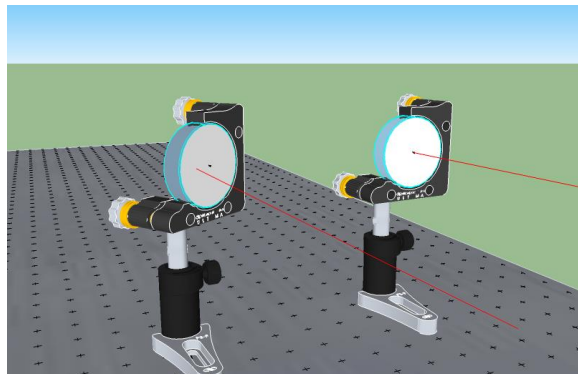Figure A-5. Comparison between Gimbal and non-Gimbal mounts [175].

Figure A-6. Effect of mount rotation centre on alignment.

One technique usually employed to reduce such effects is to maintain the beam centred in the mirror. Placing all mirror mounts at the same height is very important. For that purpose, a reference post was used while installing the mirror mounts (Figure A-7).
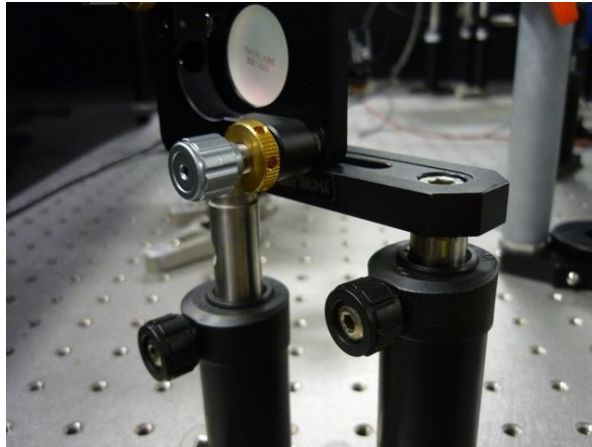
Figure A-7. Using a reference post to standardize mirror mount height.

The reflective surface of an ultrafast mirror is difficult to identify with the naked eye, but it is marked with a small arrow on the side, pointing to it (see Figure A-8).
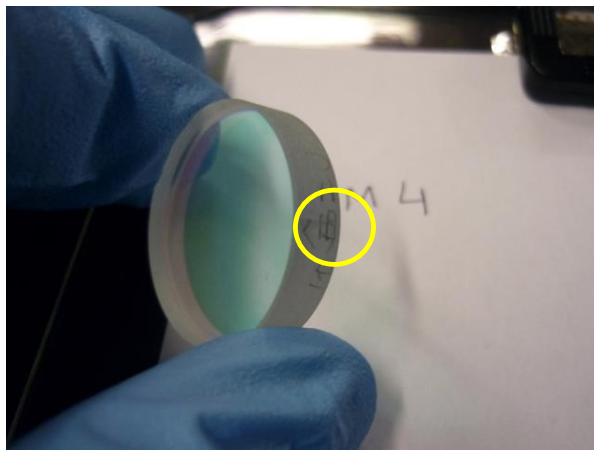
Figure A-8. Reflective surface of a mirror.

A.1 Delay line alignment

One of the key elements in the THz-TDS setup is the delay line. This subsystem is made by four mirrors, two fixed and two mounted on a linear translation stage. Its purpose is to introduce a path length change in the beam trajectory. As the linear stage moves, the alignment must be closed maintained, otherwise signal detection is compromised. The beam must be reflected at exactly 90 degrees angles and be kept in a horizontal plane (Figure A-9).

Figure A-9. Alignment restrictions for a delay line.

For aligning the delay line, we used the following procedure:

- Install the pre-alignment laser module
- The delay line should be installed in such a position as to have equal length paths for pump and probe beams. To the pump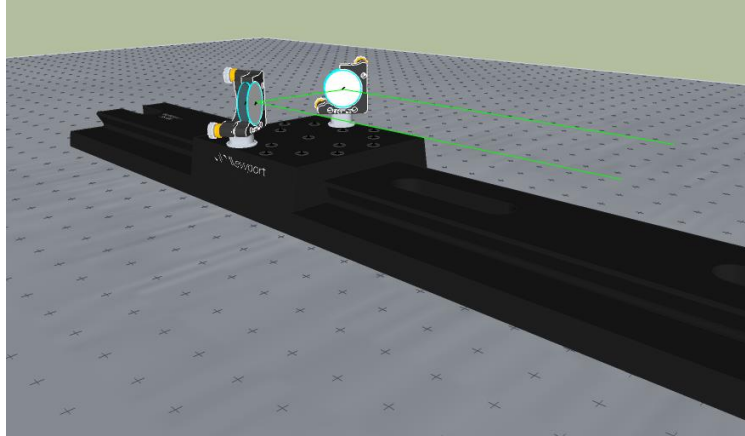 beam the THz ray trajectory should be added. As it can be seen in Figure A-10, this balanced is achieved when lengths a+e equals b+c. Since the translation stage has a 10 cm movement, b and c distances can be made shorter giving a b+c distance of 82 cm. Therefore, the THz spike should be detected at some middle point in the delay line movement.
- Install the delay line using a three point mount with flat washers [80], in this way any flatness irregularity of the optical table will not be transferred to the translation stage.
- Align mirror M3. This can be done with the help of a paper screen situated as far as possible to minimize angle errors (Figure A-11)
- *At all points*, verify that the beam keeps parallel to the optical table. This can be accomplish with an iris diaphragm
- *At all points,* verify that the beam is centred in the mirrors.
- The alignment beam should cross the centre of mirror M4. But this must be dismounted in order to align M3
- Mirrors M4 and M5 will have fixed positions because of their mount on the translation stage, therefore their centre can be estimated

- Since the centre position of mirror M4 is fixed, the orthogonality of the alignment beam should be achieved by moving M3

- Once mirror M3 has been aligned. Mount mirror M4 and dismount mirror M5

- Use a similar approach to align M4 thru M6, using a paper screen and the holes in the optical table as orthogonal reference

- Verify that relative angle between M4 and M5 is 90º (Figure A-12)

- Using the third layout is suggested to perform the alignment of the delay line with mirror M6 generating an outgoing horizontal beam, instead of the final layout. This should make easier to verify the alignment

- Make final adjustment of the delay line using a paper screen after mirror M6. Move translation stage to HOME position (longer path) and adjust M5, then move translation stage to END position and adjust M4. Repeat until a spot in the paper screen keeps stable between both positions of the translation stage

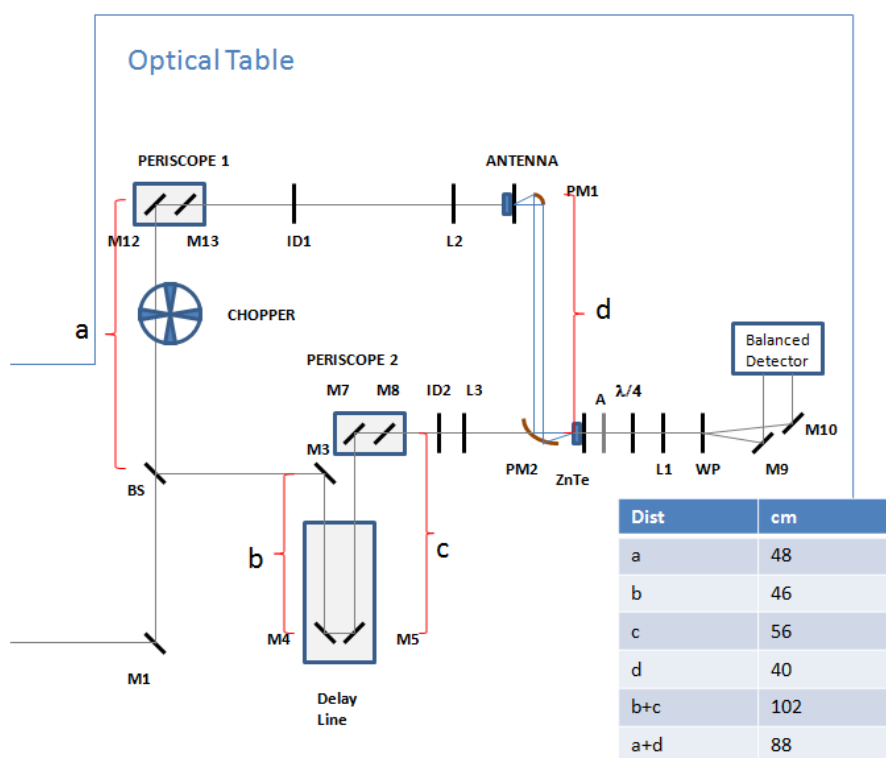| Dist	cm
a	48
b	46
c	56
d	40
b+c	102
a+d	88

Figure A-10. Calculating the beam path lengths.
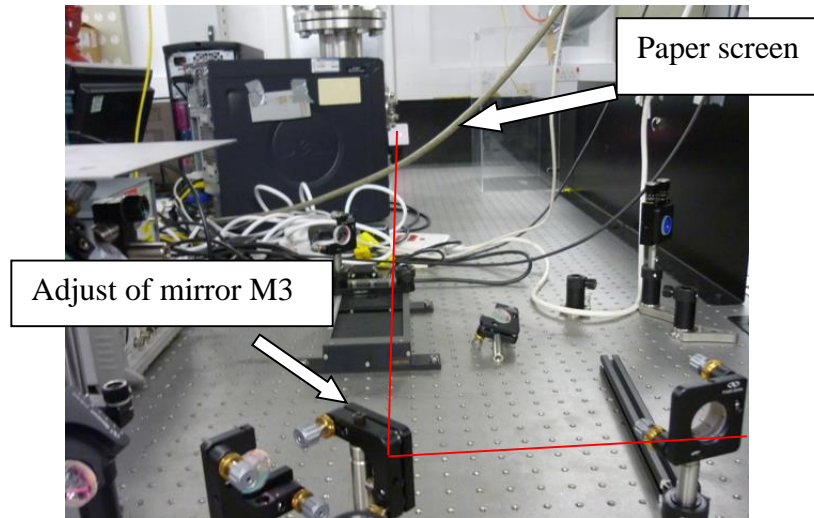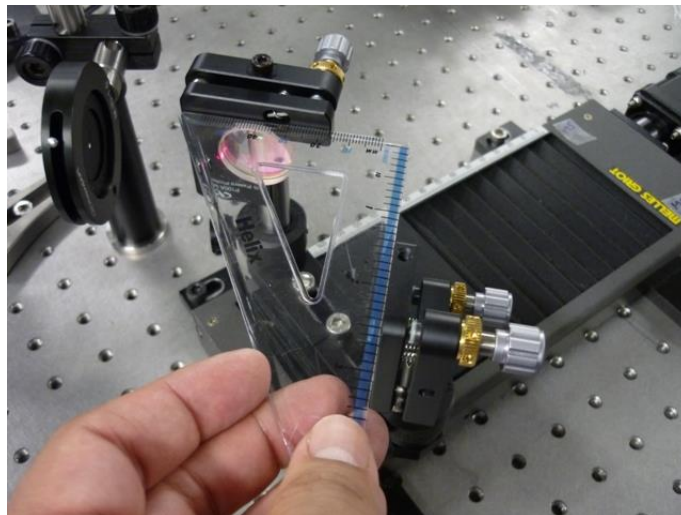
Figure A-11. Alignment procedures for a delay line.

Figure A-12. Using a set square for adjusting the relative angle between two mirrors.

Alignment across all the movement of the translation stage was also tested with a webcam. The webcam was mounted instead of the ZnTe crystal. Some screen shots are shown in Figure A-13. We can see that there is just a small translation of the beam spot.
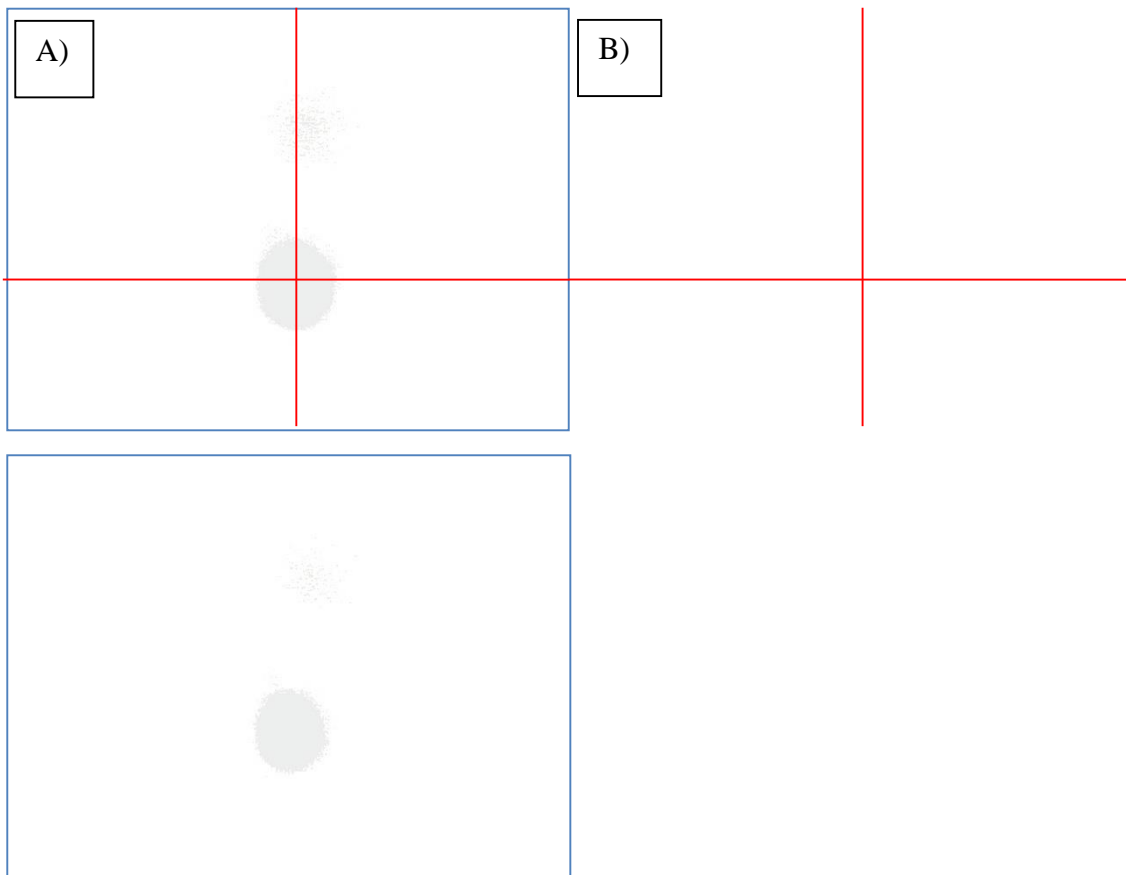
Figure A-13. Probe beam alignment test with a webcam. A) HOME position. B) END position.

A.1.1 Parabolic mirrors alignment

Alignment of the parabolic mirrors present a particular difficulty since they operate in the THz region, therefore there is no visible radiation. The proposed procedure is as follows:

- Mount the parabolic mirrors at the same height and one in front the other. A trajectory formed by 90° angles should be expected as shown in Figure A-14
- Dismount the PCA, since otherwise it will block the laser beam that it is going to be used as reference
- Install the pre-alignment laser
- Pump and probe beams should be at the same height. This will make easer to make them overlap on the ZnTe crystal. This procedure can be carried out with the help of a iris diaphragm.

214

- o For example, in a setup similar to Figure A-15, place the iris at some distance (20 cm) from the periscope, and adjust the upper mirror
- o Then place the iris close to the periscope and adjust the lower mirror
- o Repeat the last two steps until alignment is achieved

- Adjust position of parabolic mirror PM1 in order to get a spot close to its centre (Figure A-16)

- Adjust parabolic mirror PM1 orientation so the reflected beam targets the centre of parabolic mirror PM2

- Adjust parabolic mirror PM1 and PM2 so both beams target the same spot over the ZnTe crystal (Figure A-17). Control knobs of PM2 should not be adjusted too much, since that will block the probe beam that is coming across the hole that was drilled with that purpose. THz radiation is detected using the ZnTe crystal and a probe laser pulse; therefore the THz radiation must be focused over the crystal at the same spot where the probe pulse arrives.

- If one of the beams is too intense, an attenuator can be placed in its path

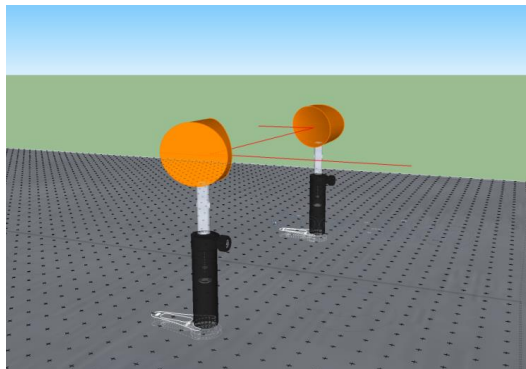- Verify alignment with the Ti-Sapphire laser

Figure A-14. Alignment of two parabolic mirrors.
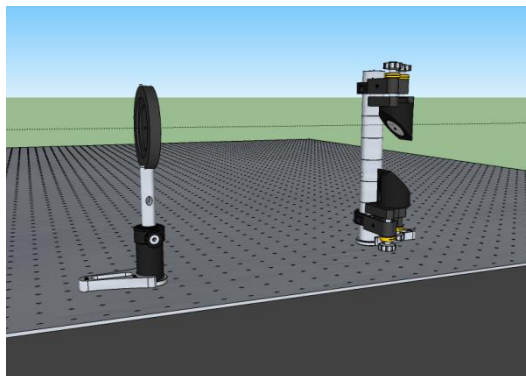
Figure A-15. Adjusting periscope to produce a horizontal beam.
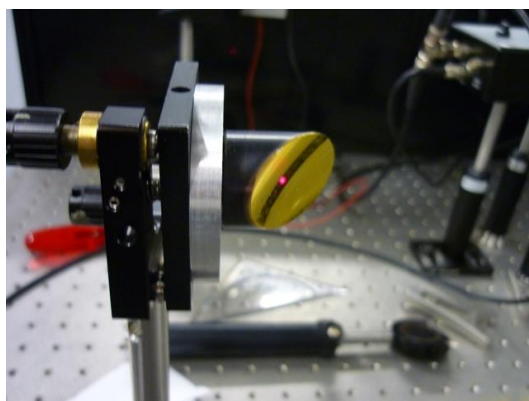
Figure A-16. Aligning the pump beam to the centre of parabolic mirror PM1 with the pre-alignment laser.

Figure A-17. Alignment of probe beam.

A.1.2 Placement of the photoconductive antenna and ZnTe crystal

The photoconductive antenna (PCA) must be placed in the pump beam path, just at a distance given by the EFL (equivalent focal length) of the off-axis parabolic mirror (PM1). In this case, EFL is 50.8 mm. As it can be seen in Figure A-18, as a lamp is placed close to the EFL of the parabolic mirror it begins to generate a collimated beam.

Figure A-18. Collimation of an incoming ray with an off-axis parabolic mirror.

For the same reason, ZnTe crystal should be placed at a distance equal to the EFL of the parabolic mirror PM2.

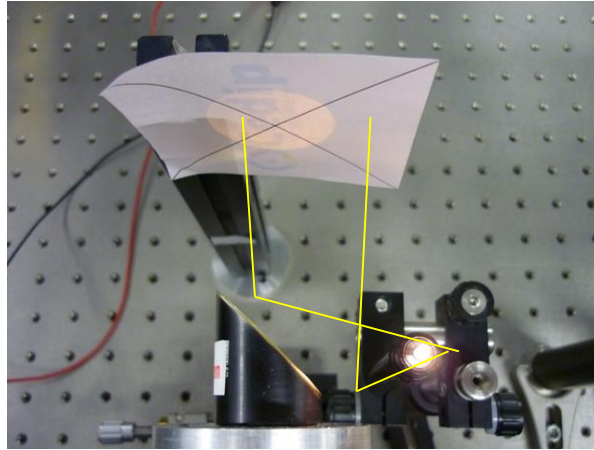### A.1.3   Alignment of photoconductive antenna

The PCA is mounted on a 3 axis translation base, and it should be connected to a 160 V DC power supply with its current monitored by a mili-ammeter. The alignment procedure followed is detailed below.

- Block the Ti-Sapphire laser beam
- Turn on the PCA power supply and verify that is set to zero Volts. An excess in photocurrent could lead to overheating and to a positive feedback situation where the amount of carriers increase, because of the temperature rise, and this in turn causes a further increment in photocurrent
- Unblock the Ti-Sapphire laser beam and increment the power supply voltage until 160 V, monitoring the photocurrent. Currents above 7 mA are not expected. Measured dark current was 1.65 mA
- Adjust PCA position using the vernier micrometers. The objective is to align the laser beam spot to the point where the maximum amount of carriers are produced. As the maximum photocurrent position is approached, the sensitivity to position variation increases. An adequate photocurrent level for this setup is 5 mA, without the beam being chopped.

- It is preferable to adjust the antenna only on its plane as any adjustment in the beam direction will modify its relative distance to the parabolic mirror
- Use lens L2, which is mounted on a small linear stage, to focus the pump beam
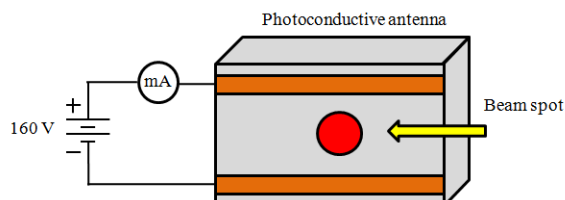

Figure A-19. Connection for the photoconductive antenna.

The datasheet for the PCA used was not available, but information from Batop Optoelectronics mention that an appropriate lens must be used to be focus the laser beam onto the antenna gap with a diameter of 6 µm to bridge the gap [176]. Lens L2 is used to focus the pump beam over the PCA. Contrary to what it was expected, moving the lens position did not produce appreciable changes in photocurrent.
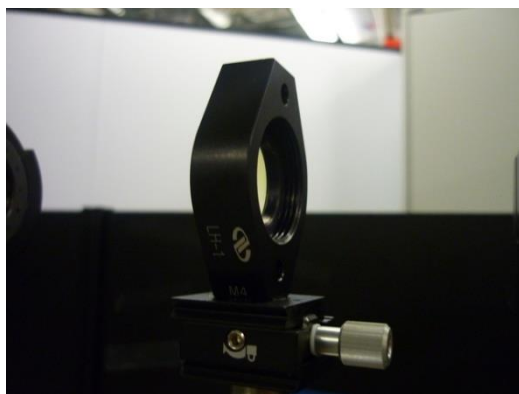
Figure A-20. Lens L2 mount showing its translation stage.

A.1.4 Special notes on using a 650 nm pre-alignment laser

Using a 650 nm 1 mW laser module for pre-alignment is extremely helpful since the Ti-Sapphire mode-locked laser generates an almost invisible radiation. Nevertheless, a problem was found while using it. Ultrafast mirror generated spurious reflections and the beam became split in multiple beams as shown in Figure A-21. These reflections are believed to be produced because the 650 nm wavelength is below the operating

218

specifications of the ultrafast mirror. As it can be seen in Figure A-22, typical operating wavelengths for a P polarized ray are between 730 and 880 nm [50].
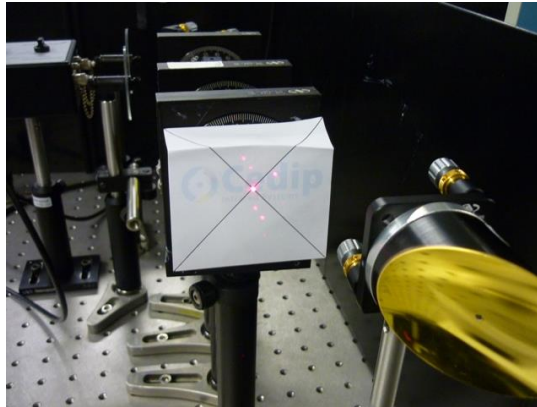

Figure A-21. Spurious reflections.
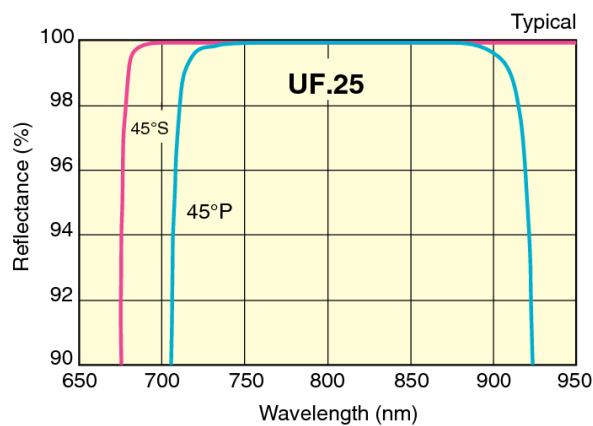
Figure A-22. Newport 10B20UF.25 broadband mirror operating wavelengths [50].

A.2 Balanced detector adjust

A Newport 2017 Nirvana Autobalanced photoreceiver is used as a balanced detector. An attenuator was placed after the ZnTe crystal in order to limit the amount of signal arriving to the balanced detector, since in that place it does not interfere with the balanced operation. A common arrangement is to place two attenuators: one in front of each one of the optical inputs of the balanced detector, but that can alter the balance of the signals. If the balanced detector is to be operated in the autobalaced mode, a second attenuator can be placed in front of mirror M10 (signal input), just to make sure that the reference

beam is greater than the signal beam (a factor of 2.2:1 is recommended by the datasheet in order to maximize Common mode rejection ratio).

The suggested calibration procedure is as follows:

- Install the pre-alignment laser module
- Verify that the two beams coming out of the Wollaston prism are horizontal, and target the detector optical inputs
- Modify the position of mirrors M9 and M10 so the beams became normal to the detector inputs
- Remove the pre-alignment laser module and use the Ti-Sapphire laser
- Set the Autobalanced detector in balanced mode and loop-gain to maximum
- Block the reference optical input. Adjust mirror M10 (signal) until maximum amplitude is obtained (seen in an oscilloscope). Test with both knobs
- Unblock the reference optical input and block the signal optical input. Adjust Mirror M9 (reference) until maximum amplitude is obtained
- If the output of the Nirvana detector gets saturated, attenuator "A" can rotated to reduce the amount of signal
- Unblock the signal optical input
- With no THz generation present (blocking pump beam or unbiasing the PCA), the quartewave plate is then rotated to null electrical output signal from the Nirvana detector. A DC signal with some modulating noise should be observed. Typical amplitudes are between 20 mV and 50 mV.
- Once the position of the THz pulse is known, the rotation of the quartewave plate should be carried out with the linear translation stage at a position close to the THz peak.

A.3 Final alignment

Final alignment is carried out with the Ti-Sapphire laser and using a fluorescing alignment disk (Figure A-23).

Lens L3 is used to focus the probe beam over the ZnTe crystal. This lens has a focal length of 200 mm, and that produces a very small spot over the ZnTe; however we found that it was better to move the lens a little away from the crystal and to have a spot of about 1.5 mm diameter. In the end the lens was placed at 235 mm from the ZnTe crystal. Once we did this adjust, we start to detect the THz peak.
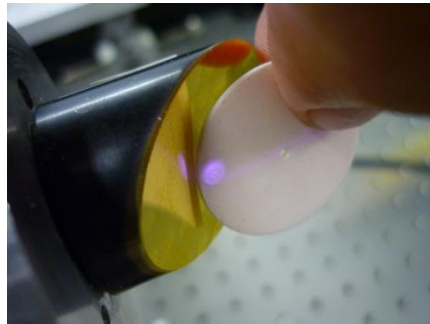

Figure A-23. Alignment verification with a fluorescing alignment disk.

B. APPENDIX

THz pulse delay measurement

A time-domain spectroscopy system is a powerful instrument for material characterization. In certain types of experiments, it is of interest to determine the time delay of the pulse. A method based on parabolic interpolation was implemented and used to analyse data from a sooty flame. THz beams are particularly useful since soot is transparent to THz radiation [177]. At the University of Manchester, a special burner was designed and built to perform THz-TDS experiments in flames. The flames are produced by a co-flow of dry air and gaseous methane. A series of experiments was carried out with different air flow whilst maintaining a constant methane flow (Table B-1). We gained access to the data, and we carried out the signal processing required to determine the delay between pulses, which is presented in this section.
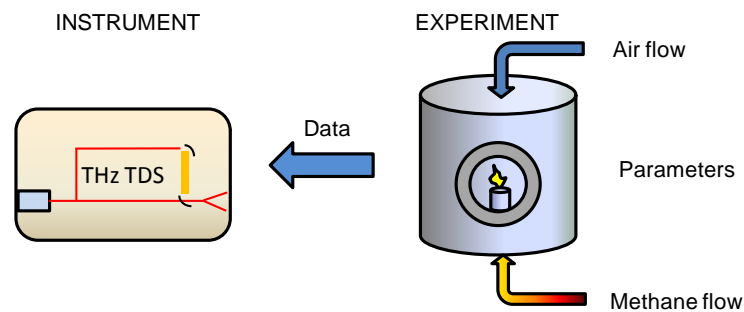
Figure B-1. THz-TDS analysis of sooty flames.

Experiment	Air flow (l/min)	Methane flow (l/min)
1	10	0
2	5.0	0.2
3	7.5	0.2
4	10.0	0.2
5	12.5	0.2
6	15.0	0.2

Table B-1. Experiment parameters.

A graph of the THz pulses for the reference and five different co-flow experiments is shown in Figure B-2. An amplitude reduction and a delay are observed as the air flow increases.
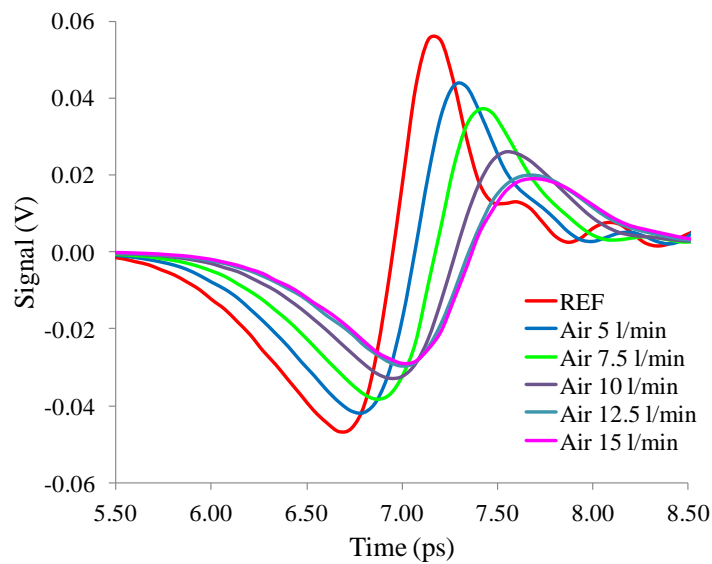

Figure B-2. Measured THz pulse.

B.1.1　Pulse integration as a method of delay estimation

A method for determining the delay between THz pulses has been proposed in [144]. THz emission is proportional to the time-domain derivative of antenna's current density [153, 178]. By integrating the detected THz pulse, it is possible map the "original" current density function. THz main pulses have a positive and a negative excursion peak, but performing an integration over that signal produces a function that has only one extremum, which can be easily used to estimate the time delay. The integrated THz pulses are shown in Figure B-3. Due to limitations in sampling-time, the resulting integration values don't guarantee a high resolution; however, this can be improved by using a parabolic interpolation.
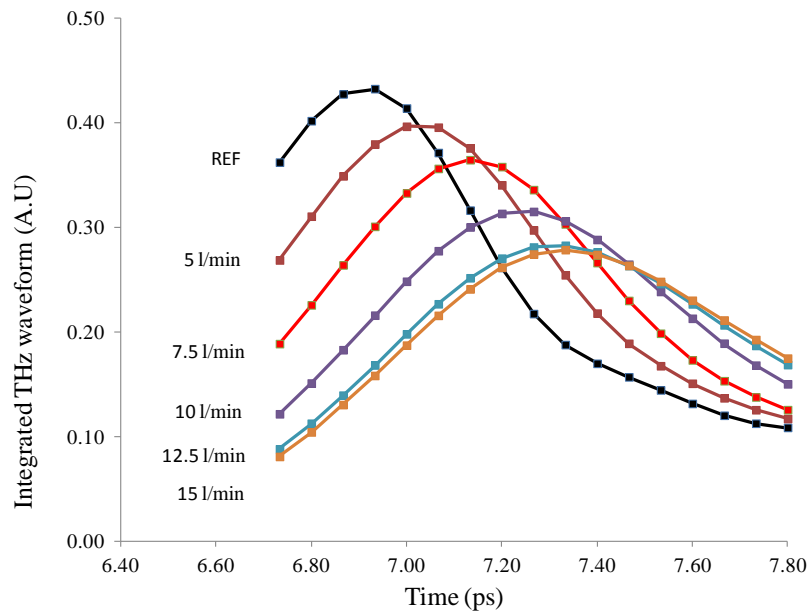

Figure B-3. Integrated THz pulses.

B.1.2　Parabolic interpolation

The interpolation method selected requires three points and uses a parabolic approximation. Given three points of a curve, a, b, and c (see Figure B-4), if the parabola has the form

$$y(x) = \alpha x^2 + \beta x + \gamma \qquad\qquad (\text{B-1})$$

225

it is possible to find the values of α, β and γ, by solving the following system

$$y(a) = \alpha a^2 + \beta a + \gamma$$
$$y(b) = \alpha b^2 + \beta b + \gamma$$
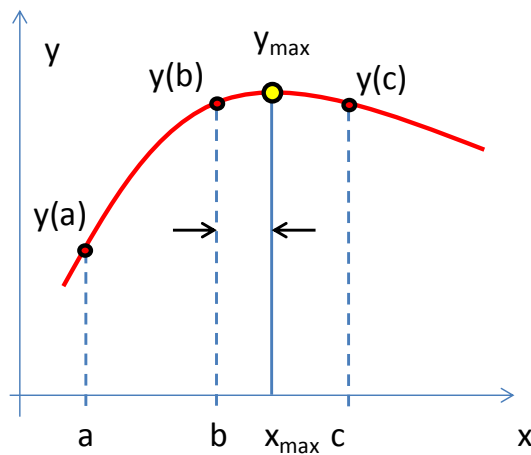$$y(c) = \alpha c^2 + \beta c + \gamma$$

(B-2)

Figure B-4. Parabolic interpolation from three points.

The parabola has a maximum or minimum at $f'(x) = 0$, that is

$$2\alpha x + \beta = 0$$

therefore,

$$x = -\beta/2\alpha$$

(B-3)

Rewriting equation (B-2)

$$y(a) = \alpha a^2 + \beta a + \gamma$$

(B-4)

$$y(b) = \alpha b^2 + \beta b + \gamma$$

(B-5)

$$y(c) = \alpha c^2 + \beta c + \gamma$$

(B-6)

Subtracting (B-5) from (B-4)

$$y(a) - y(b) = \alpha(a^2 - b^2) + \beta(a - b) \qquad \text{(B-7)}$$

Subtracting (B-6) from (B-5)

$$y(b) - y(c) = \alpha(b^2 - c^2) + \beta(b - c) \qquad \text{(B-8)}$$

Rewriting (B-7) and (B-8)

$$f_{ab} = \alpha x_1 + \beta x_2$$
$$f_{bc} = \alpha x_3 + \beta x_4 \qquad \text{(B-9)}$$

Where

$$f_{ab} = y(a) - y(b)$$
$$f_{bc} = y(b) - y(c)$$
$$x_1 = (a^2 - b^2)$$
$$x_2 = (a - b) \qquad \text{(B-10)}$$
$$x_3 = (b^2 - c^2)$$
$$x_4 = (b - c)$$

Using the Cramer's rule, we get

$$\alpha = \frac{\begin{vmatrix} f_{ab} & x_2 \\ f_{bc} & x_4 \end{vmatrix}}{\begin{vmatrix} x_1 & x_2 \\ x_3 & x_4 \end{vmatrix}} \qquad \text{(B-11)}$$

and

$$\beta = \frac{\begin{vmatrix} x_1 & f_{ab} \\ x_3 & f_{bc} \end{vmatrix}}{\begin{vmatrix} x_1 & x_2 \\ x_3 & x_4 \end{vmatrix}} \qquad \text{(B-12)}$$

Substituting in (B-3)

$$x = -\frac{\beta}{2\alpha} = -\frac{1}{2}\frac{\begin{vmatrix} x_1 & f_{ab} \\ x_3 & f_{bc} \end{vmatrix}}{\begin{vmatrix} f_{ab} & x_2 \\ f_{bc} & x_4 \end{vmatrix}} = -\frac{1}{2}\frac{x_1 f_{bc} - x_3 f_{ab}}{f_{ab} x_4 - f_{bc} x_2} \qquad \text{(B-13)}$$

Therefore

$$x = -\frac{1}{2}\frac{(a^2 - b^2)[f(b) - f(c)] - (b^2 - c^2)[f(a) - f(b)]}{(b - c)[f(a) - f(b)] - (a - b)[f(b) - f(c)]} \qquad \text{(B-14)}$$

Rearranging terms

$$x = \frac{1}{2}\frac{(b^2 - a^2)[f(b) - f(c)] - (b^2 - c^2)[f(b) - f(a)]}{(b - a)[f(b) - f(c)] - (b - c)[f(b) - f(a)]} \quad \text{(B-15)}$$

Since

$$\frac{1}{2}(b^2 - a^2) = b^2 - ab - \frac{b^2}{2} + \frac{2ab}{2} - \frac{a^2}{2} = b(b - a) - \frac{1}{2}(b - a)^2$$

and

$$-\frac{1}{2}(b^2 - c^2) = -b^2 + bc + \frac{b^2}{2} - \frac{2bc}{2} + \frac{c^2}{2} = -b(b - c) + \frac{1}{2}(b - c)^2$$

We can rearrange (B-15) as

$$x = b - \frac{1}{2}\frac{(b - a)^2[y(b - y(c)] - (b - c)^2[y(b) - y(a)]}{(b - a)[y(b) - y(c)] - (b - c)[y(b) - y(a)]} \quad \text{(B-16)}$$

If the points a, b, and c are equidistant then $b - a = c - b$, and

$$x = b - \frac{1}{2}\frac{(b - a)^2[y(b - y(c)] - (b - a)^2[y(b) - y(a)]}{(b - a)[y(b) - y(c)] + (b - a)[y(b) - y(a)]} \quad \text{(B-17)}$$

$$x = b - \frac{1}{2}\frac{(b - a)[y(b - y(c)] - (b - a)[y(b) - y(a)]}{y(b) - y(c) + y(b) - y(a)} \quad \text{(B-18)}$$

$$x = b - \frac{\frac{1}{2}(b - a)[y(b) - y(c) - y(b) + y(a)]}{y(b) - y(c) + y(b) - y(a)} \quad \text{(B-19)}$$

And finally,

$$x = b - \frac{\frac{1}{2}(b - a)[y(a) - y(c)]}{2y(b) - y(c) - y(a)} \quad \text{(B-20)}$$

228

B.1.3 Results

The calculated delays using parabolic interpolation are plotted in Figure B-5. The delay increases linearly with the air flow until 10 l/min. After that, the delay keeps increasing and reaches a saturation level at around 15 l/min. Delay increment and pulse broadening can be caused by a difference in the effective optical path length at increased co-flows. In this case, an increase in diffusion is expected, producing a reduction in the size of hot gas region [179].
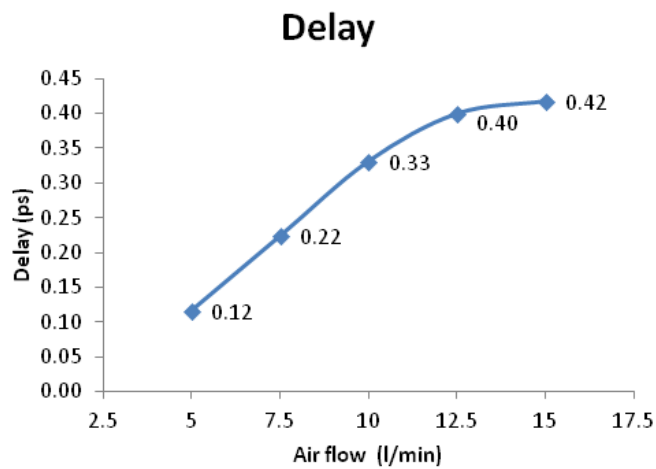

Figure B-5. Time delays for different air flow rates.